RUHR-UNIVERSITÄT BOCHUM

Abbas Farhat

Fluidization and erosion of cemented granular materials - Experimental characterization and micromechanical simulation

Bochum 2023

Heft 77

Schriftenreihe des Lehrstuhls für
Bodenmechanik, Grundbau und Umweltgeotechnik

Herausgeber: Torsten Wichtmann

ISSN 2699-1020

Fluidization and erosion of cemented granular materials Abbas Farhat 77

ISSN 2699-1020

Ruhr-Universität Bochum
Schriftenreihe Bodenmechanik, Grundbau und Umweltgeotechnik
Heft 77

Herausgeber:
Prof. Dr.-Ing. habil. Torsten Wichtmann
Ruhr-Universität Bochum
Fakultät für Bau- und Umweltingenieurwissenschaften
Lehrstuhl für Bodenmechanik, Grundbau und Umweltgeotechnik
44801 Bochum
Telefon: 0234/ 3226135
Telefax: 0234/ 3214236
Internet: www.bgu.ruhr-uni-bochum.de

ISSN 2699-1020

THÈSE DE DOCTORAT

NNT/NL : 2020AIXM0001/001ED000

Soutenue à Aix-Marseille Université
en cotutelle avec l'université de Bochum RUB
le 16 Mars 2023 par

Abbas FARHAT

Fluidization and erosion of cemented granular materials Experimental characterization and micromechanical simulation.

Discipline
Sciences pour l'Ingénieur

Spécialité
Doctorat Mécanique des solides

École doctorale
Ecole doctorale 353
Ruhr-Universität Bochum

Laboratoire/Partenaires de recherche
RECOVER, INRAE, Aix Marseille Univ.
BAM, Ruhr-Universität Bochum

Composition du jury

Vincent RICHEFEU MCF, UGA, France	Rapporteur
Valérie VIDAL DR, ENS Lyon, France	Rapporteure and Présidente
Vanessa MAGNANIMO Adj. Prof., Univ. of Twente, Netherlands	Examinatrice
Pierre PHILIPPE DR., INRAE, France	Directeur de thèse
Torsten WICHTMANN Prof., RUB, Germany	Codirecteur de thèse
Pablo CUÉLLAR Dr., Chargé de recherche, BAM, Germany	Encadrant

Preface of the editor

Inner erosion by pore fluid flow repeatedly led to failure of earthwork structures like dams or dikes in the past. Previous research was mainly restricted to granular soils without any bonding at the particle contacts. However, most natural granular soils exhibit some kind of cementation, e.g. due to calcite precipitation or the presence of cohesive fines. Considering the few information in the literature, the knowledge and understanding of erosion phenomena in cemented granular soils is limited so far.

This motivated the German Federal Institute for Materials Research and Testing (Bundesanstalt für Materialforschung und -prüfung, BAM) in Berlin and the French National Research Institute for Agriculture, Food and Environment (INRAE) in Aix-en-Provence to launch a scientific collaboration within the binational research project "Coupled micromechanical modelling for the analysis and prevention of erosion in hydraulic and offshore infrastructures" (COMET) funded by German Research Council (DFG) and French National Research Agency (ANR). Within this project two PhD theses have been prepared, one by Abbas Farhat at INRAE focussing on experimental research mainly supervised by Dr. Pierre Philippe, and another one by Mohammad Sanayei at BAM concentrating on numerical modeling under the main supervision of Dr. Pablo Cuéllar. The research was supported by Aix-Marseille University in France and Ruhr-Universität Bochum in Germany, leading to a binational PhD degree for both candidates.

Abbas Farhat has undertaken a thorough investigation on erosion phenomena in cemented granular soils, including mainly experiments on different scales but also some numerical simulations applying a coupled DEM-LBM framework. Artificial granular samples with controlled degree of bonding were prepared from glass beads mixed with liquid paraffin, which formed the bonds after cooling. The experiments comprised micro-scale tests on single bonds (i.e. pairs of cemented glass beads) under different kinds of loading (tensile, shear, bending, torsion), macro-scale tensile tests on larger samples with bi-conical shape, and model box tests in which a cemented granular layer was subjected to a localized fluid inflow with stepwise increased hydraulic gradient at the bottom. Mr. Farhat has significantly improved and extended the existing experimental setups, for example for studying all modes of loading in the micro-scale tests or applying the equipment in an X-ray tomography scanner. He also addresses problems encountered during the experiments together with applied remedies as well as methods that did not work out for the bonded glass beads, like e.g. the Refractive Index Matching (RIM) technique.

Mr. Farhat performed an impressive number of micro- and macro-scale tensile tests, with a variation of bead diameter, degree of cementation (paraffin content), sample size and loading rate. However, considering the large scatter of the measured

bond strength or yield stress values the large number of tests with similar boundary conditions is necessary to perform statistical analysis on the data and draw meaningful conclusions. Despite the scattering of the experimental data, Mr. Farhat is able to identify the most important influencing parameters and derive and validate theoretical equations for the bonding force in the micro-scale tests or the yield stress in the macro-scale experiments. From the model box tests he determines different modes of erosion depending on particle size, degree of bonding, height of the granular layer and applied hydraulic gradient. The 2D simulations of the box experiments with the coupled DEM-LBM approach considering bonding between the particles provide some additional insights into the micromechanics, in particular with respect to the development of the amount and position of broken bonds in the granular layer. For some boundary conditions the failure modes in the simulations still differ from those observed in the experiments, which could be partially attributed to the 2D simplification of the 3D problem and needs some further investigation.

Despite some open questions the PhD thesis of Abbas Farhat represents a valuable contribution towards a better understanding of erosion phenomena in cemented granular soils, and a step towards a safer design of earth structures like dams or dikes composed of such soils.

Torsten Wichtmann

Acknowledgement

Pursuing a Ph.D. is a life-changing event as well as an opportunity to improve our talents. This journey will not be without hurdles, which will need endurance and dedication in order to advance and achieve. It's just like climbing a high peak step by step, accompanied with hardships, frustration, encouragement, trust and so many people's kind help. Finally, success necessitates action, and it is determined by our ability to keep pushing forward in the face of adversity. It would always appear impossible until it was completed.

First of all, I would like to express my sincere gratitude to my thesis supervisors Dr. Pierre PHILIPPE and prof. Torsten WICHTMANN for their continuous support and encouragement over the last three years. Their patience and vast expertise, as well as the time they spent supplying me with relevant documents and guidance. Their trust and support in me for participation in international conferences helped me to get new experiences and knowledge. Also, I'm really grateful to Pierre because he significantly assisted my research work.

I'd like to give my sincere thanks to my co-supervisors Dr. Pablo CUELLAR, Dr. Nadia BENHAMED and Dr. Li Hua LUU. Thereafter, they offered me so much advice, patiently supervising me, and always guiding me in the right direction. I've learned a lot from them, without their help I could not have finished my thesis successfully.

I am grateful to the jury members, Professors Valerie VIDAL, Vincent Richefeu, Markus THEWES and Vanessa MAGNANIMO, for accepting to participate on my PhD Thesis Committee. I'd like to thank them for devoting their valuable time in evaluating this work. This is really appreciated, and it is a tremendous honor for me.

My sincere appreciation and gratitude are extended to my second family at INRAE Sylvie NICAISE, Faustine BYRON, Alexis DOGHMANE, Yves GRÉMEAUX, Naim CHAOUCH, and Julien AUBRIET for all their contribution to this work. I'll not forget to say thank you also to all the RECOVER members specially the team G2DR at INRAE, it was a pleasure to see great people like them. I am honored to be a member since 2019, for enriching my knowledge and experiences.

I am thankful for the French Agence Nationale de la Recherche (ANR) and the Deutsche Forschungs-gemeinschaft (DFG; German Research Foundation) for their confidence in funding this thesis. Also, I would like to thank UFA-DFH for the cotutelle grant.

My friends and cousins in France, the United States of America and Lebanon played also a crucial role in my motivation process. Thanks to Bilal ALTFAILY, Shadi YOUSSEf, Mohammad GHOSEIN, Ali HAMDAN, Nesrin AKEL, Ali ISSA, Majd HABIB, Mohammad OMAR, Abbas MOHAMMAD ALI, Kodor H. FARHAT, Dr. Mohammad K. FARHAT, Eng. Hussien K. FARHAT, Abbas H. FARHAT, Tarek TALAAT and Mazen EZZEDDINE.

All of them were important in this process more than they realize.

Finally, I want to express my heartfelt appreciation to my family for their unwavering love, assistance, and support during my PhD process and my life in general. Special thanks to my dear mother and father for believing in me and providing me with unconditional love and support in my ambition to discover and realize my potential. This achievement would not have been feasible without their assistance.

Thank you all...

Résumé

Dans le contexte général du risque lié à l'érosion des ouvrages hydrauliques en terre, cette thèse vise, à travers une approche multi-échelle, à étudier à la fois expérimentalement et numériquement, la déstabilisation des matériaux granulaires cémentés, c'est-à-dire comportant des ponts solides entre grains. Nous utilisons des matériaux artificiels, préparés au laboratoire à partir d'un mélange de paraffine et de billes de verre. Ces matériaux ont été testés à l'aide de dispositifs d'essais spécialement développées pour étudier leur résistance induite par cémentation à différentes échelles : résistance à la traction aux échelles micro et macro d'un échantillon ; seuil de rupture d'un pont solide sous cisaillement, flexion et torsion. Un modèle théorique 3D est proposé sur la base de l'hypothèse d'une adhésion de surface uniforme. Des expériences de fracturation hydraulique ont permis d'étudier le comportement hydromécanique de ces matériaux. Les conditions critiques de rupture d'une couche cémentée ont mis en évidence trois types de déstabilisation différents. Nous avons proposé de définir un nombre d'Archimède adhésif qui apparait directement relié au nombre de Reynolds. En utilisant un modèle micromécanique 2D, nous avons réalisé une étude paramétrique sur une configuration de déstabilisation similaire en faisant varier diamètre des particules, hauteur de l'échantillon et cémentation. Trois scénarios différents ont été observés et les résultats comparés aux expériences précédentes. Enfin, une simulation préliminaire sert à présenter brièvement l'extension 3D de cette étude numérique qui est en cours de développement via le code opensource waLBerla.

Mots clés: Matériaux granulaires cémentés, caractérisation mécanique, fluidification et instabilités hydromécaniques.

Abstract

Cemented granular materials constitute a special case, in which solid bridges link the particles to one another. In the general context of the safety of hydraulic earthworks under the risk of erosion (e.g. dams and embankments), this thesis aims to investigate, both experimentally and numerically, the hydromechanical destabilization of cemented granular materials using a multi-scale approach. Homemade artificial cemented granular materials, prepared from a mixture of paraffin and spherical glass beads, were tested with specially developed laboratory setups to investigate their cementation strength at different scales: tensile yield strength at the macro and microscale of a cemented sample, and micro yield strength for solid bonds ruptured by shear, bending, and torsion. A 3D theoretical model is provided based on the assumption of a uniform surface adhesion. Next, the hydromechanical behavior was investigated through localized underflow experiments. Under critical conditions, the cemented layer is hydraulically fractured and three different types of destabilization were observed. Defining an adhesive Archimedes number, we found a general relation with the Reynolds number. Using a 2D micromechanical model, we performed a parametric study on similar kind of destabilization by varying the particle diameter, the bed sample height, and the bond strength. Three different scenarios were observed and a discussion proposed to relate the 2D numerical simulation to the experiments. Lastly, we briefly present the forthcoming 3D extension of this numerical study, using the waLBerla open-code with a preliminary simulation.

Keywords: Cemented granular material, mechanical characterisation, fluidisation and hydromechanical instabilities.

Contents

List of Figures

List of Tables

General introduction

Context

Erosion is the gradual removal of solid matter under the action of an eroding agent. In other words, erosion is a phenomenon of natural origin causing the degradation of many types of soils and the generation of solid transport under the effect of wind, water, or ice. The eroded material can be rocks, snow, sand, clayey soils, etc. Erosion is a leading cause of sediment transport, resulting in a subsequent deposition that can cause many issues and challenges. Quantifying the amount of soil eroded is a major concern in a lot of environmental and engineering areas. The problem has been studied for many years in the field of meteorology, seabed degradation, coastline erosion, or morphological evolution of rivers and estuaries (Winterwerp and Van-Kesteren 2004; Van-Rijn et al. 1993). In civil engineering, erosion is an important issue to determine the sustainability and safety of many structures. Erosion and sediment transport can indeed interfere with human activities and constructions such as underwater structures (flow lines, tidal turbines), embankment dams, bridges or offshore structures. Some striking examples include the excavated holes caused by impinging water flow from dam spillways (Bollaert, Schleiss, Castillo, et al. 2007), bridges in rivers susceptible to failure due to subsoil scour at the foundations such as piers or abutments (Prendergast and Gavin 2014), or erosion degradation within hydraulic structures (Bonelli 2012; Van-Beek, Bezuijen, Sellmeijer, et al. 2013). Soil erosion is of importance also in a broader ecological context: it can spread heavy metals or radioactive particles through sediment transport and, focusing on agricultural soils, it has also been reported to have an impact on the global carbon cycle (Van-Oost, Quine, Govers, et al. 2007).

In France, there are around ten thousand dams, with about 500 classified as large, as well as several thousand kilometers of hydraulic structures such as river dikes or waterway embankments. Their main purpose is to retain water over time, but they are also used to produce hydro-electrical power and for irrigation systems during the dry season. Many of those hydraulic structures are more than half a century old, which makes them particularly susceptible to failure (Foster, Fell, and Spannagle 2000). More than 70 incidents have been reported by the International Commission On the Large Dams (ICOLD) in France, particularly during strong flood periods (i.e. Aude in 1999, Gard in 2002, and Rhône-Alpes in 2003). Such failure of an hydraulic earthwork structure can lead to dramatic consequences in terms of human lives and economic losses. There is a growing demand for improving safety management of the existing structures and building more resistant ones for the future.

Erosion is by far the most common cause of failure of earth dams. Two different situations can be distinguished: External erosion, the degradation of the outer surface of the hydraulic structure in the event of overflow or over-topping, and internal erosion which takes place inside the structure or the foundation by seepage flow. In the latter case there may therefore be no external evidence that erosion is taking place until the phenomenon has progressed sufficiently to be visible and detectable by measuring devices. The susceptibility of a soil to erosion can be assessed with dedicated devices developed for the purpose and based on mainly empirical interpretation models. The understanding of the intrinsic physics of the mechanism underlying the specific processes of soil erosion has been extensively studied for the specific case of granular materials, but very few for coherent soils, for which many questions are still open.

Objectives

This thesis deals with water flow induced erosion of geomaterials more complex than purely friction soil, which are often found in civil engineering hydraulic structures with significant socio-economic implications. More specifically, we focus here on cemented granular materials with solid inter-particle bonds. We aim to study the mechanical characterization of an artificial cemented granular system at different scales and the development of hydro-mechanical instabilities of this model soil, both by localized fluidization and hydraulic loading. This multidisciplinary research work involves different scientific communities, notably those of soil mechanics, geotechnics, and geophysics. This PhD thesis is part of a bilateral project funded by ANR-DFG, called COMET (Coupled micromechanical modeling for the analysis and prevention of erosion in hydraulic and offshore infrastructures).

Work Plan

This work is divided into four main chapters plus a conclusion.

Chapter 1 presents the state of the art as regards erosion/fluidization of soils. It consists firstly of the general context of erosion in hydraulic structures and secondly of a synthetic background on the different types of soils and their interaction with fluid flow, including some numerical methods capable of modeling soils erosion. Finally, we give a brief review of previous studies, both experimental and numerical, on the fluidization and degradation of materials, cemented or not, subjected to a localized inlet flow.

Chapter 2 first describes our complete experimental setup (including materials used and sample preparation) for multi-scale cohesion force measurements and, next, the different steps followed in the development of an original fluidization experimentation. A second part is dedicated to the numerical methods employed for the 2D and 3D micro mechanical modeling of a cemented granular soil driven to the critical conditions of localized hydraulic failure.

In Chapter 3, the experimental results obtained for micro-macro mechanical characterization of our artificial cemented granular material are presented. The first section consists of the micro characterization of the solid bonds strength at the particle scale, including some preliminary micro-tomography visualizations and a theoretical framework to interpret the cementation force measurements. As a continuation, the next section focuses on the tensile stress quantification at the macro scale. Finally, a discussion is provided to determine the possible roots for the observed huge intrinsic dispersion and to elaborate on the link between micro and macro scales.

Chapter 4 addresses the results achieved both experimentally and numerically from our study of localized hydraulic failure and fluidization of a cemented granular material. The first section is devoted to the experimental results while the second one presents several 2D simulations on its numerical counterparts, conducted as a parametric study that ends with a comparison between numerical and experimental results. Lastly, we briefly present the forthcoming 3D extension of this numerical study, using the WalBerla open-code.

To close this work, we give a general conclusion and provide some perspectives for future research.

1. State of the Art

Sommaire

Introduction

This chapter is intended to describe the general context of erosion in hydraulic structures, typically earthen embankment dams or levees, and to propose a synthesis of the general knowledge on the related field. Section 1.1 first distinguishes and further describes external and internal erosion, including the general concepts required for their study. Section 1.2 presents a synthetic background on the different types of soils constituting hydraulic structures with a specific interest on granular soils, especially cemented ones, and their interaction with an interstitial fluid flow, and ends with a presentation of current numerical models used to simulate this fluid-grains coupling. Finally, Section 1.3 focuses on a bibliographical review of previous experimental and numerical studies on hydro-mechanical instabilities within granular soils, either with or without cemented bonds.

1.1. General context of erosion in hydraulic structures

1.1.1. Concerned structures

On a global scale, there is an annual average of 25 billion tons of natural soil mass loss by erosion, mainly due to water (Girard, Walter, Rémy, et al. 2011). Amongst the numerous geological or technological earthen systems concerned with erosion, hydraulic structures such as embankment dams or levees play a critical role in flood protection systems. France has thousands of hydraulic structures. Most of them are small dams, meaning that their height is less than 15 m. But there are also about 500 large dams, and around 7000 km of defensive levees and 8000 km of waterways dikes. The great majority of these structures are more than a half-century old which increases the risk of failure. Erosion is known to contribute to about 90 to 95% of failure cases reported worldwide (Foster, Fell, and Spannagle 2000). Annually in France, we can estimate on average one dam rupture and one dike rupture, whose direct damage costs are estimated at over 100 million euros. This risk of hydraulic structure failure exists in the same way on a global scale, as illustrated in Figure 1.1 by two fairly recent examples concerning dams. Of particular interest in this PhD work is the internal flow caused by water within the foundation or the body of the structure, focusing specifically on embankment dams, levees, and dikes.

Embankment dams account for approximately 60% of world dams. These large structures are used as a barrier to retain water but also for other activities such as irrigation, human consumption of water, or electricity production. Earthen embankment dams are typically composed of soil and/or rocks. Most of them include a central core section that is made impervious by using very fine soils such as silt or clay. The stability of the whole structure is ensured by its own weight. To avoid overtopping or overflowing to cause surface degradation of these structures, a spillway is always provided. An archetypal example in France is the Serre-Ponçon dam, located in the

Figure 1.1. – Failure of the Algodoes dam (Piau, Brazil, 2009) (left), Failure of the Lianfeng dam (Urumqi, China, 2013) (right) [Oliveira 2018].

Alps on the Durance river, with a height of 124m, a core made of clay, and the capacity to retain up to 1,300 million of m^3 of water. There are other types of dams such as concrete gravity dams, reinforced concrete dams, or masonry dams. They are made up with concrete, bricks or stones mixed with mortar, and sometimes combined with earthen parts.

Levees and dikes are similar to earthen embankment dams in structure. They are usually built along the sea or rivers, as a protection of flood zones. Their main purpose is to prevent the course of the river from changing, to protect flood plains, and to prevent an inundation. It is also used for providing shipping lanes for maritime commerce and water to hydroelectric plants.

To conclude, dams and other hydraulic structures can be constituted by a wide variety of materials: from concrete to earthen soils and rocks, including mixed compositions. In this thesis, we are specifically interested in earthen structures that are threatened by water flow erosion.

1.1.2. Different types of soil's hydraulic erosion

Erosion of earthen hydraulic structures, more specifically embankment dams, can be divided into two distinct categories: external and internal erosion. The degradation of the outer surface of the hydraulic earthwork structure by entrainment of the constituting soil due to strong hydrodynamic stress, usually in overflowing or overtopping conditions, is called external erosion. Then, if the soil's sublayer is not resistant enough to erosion, a breach can be progressively created, eventually leading to the failure of the structure. This type of erosion represents about 50% of the reported earthen embankment failures (Foster, Fell, and Spannagle 2000).

Almost the same proportion of embankment dam failures, around 45%, are due to internal erosion by water seepage within the structure or through its foundations (see Figure 1.2). At the sample scale, internal erosion occurs when two conditions are met: the removal of particles by the seepage flow and their subsequent transport through the porous structure of the part of the soil remaining in place, i.e. coarse particles. Four different initiation mechanisms of internal erosion have been reported so far:

contact erosion, suffusion, concentrated leak erosion, and backward erosion (Fell and Fry 2007; Fry, Degoutte, and Goubet 1997; Van-Beek, Bezuijen, Sellmeijer, et al. 2013). Under critical conditions, hydraulic earthworks are susceptible to being eroded by one or more of these internal erosion processes, to final rupture in the most unfavourable and dramatic cases.

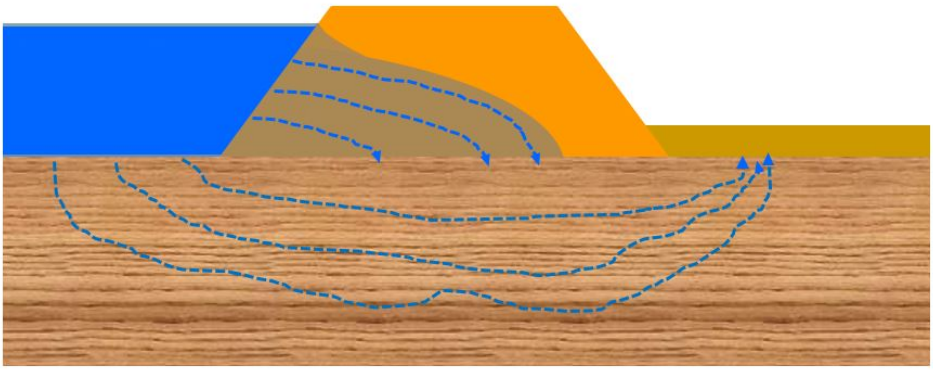

Figure 1.2. – Example of an internal flow in an embankment dam or a levee.

Contact erosion initiates when a coarse layer of soil is in contact with a fine layer of soil, creating a preferential flow path parallel along the two layers interface which, if strong enough, can detach and entrain particles from the fine soil's layer (i.e. removal and transport). Suffusion happens when the coarse fraction of soil is not able to prevent the loss of its finer fraction due to seepage flow. Suffusion within the core or the foundations may lead to settlement of the structure. Concentrated leak erosion may occur through an existing preferential flow path, as a crack (for instance caused by a differential settlement), pipes, animal burrows, tree roots rotting, or a hydraulic fracture due to water internal flow (L. Zhang, Peng, Chang, et al. 2016). Locally, the soil is eroded superficially by a tangential flow but this hydraulic flow is in charge compared to free surface flow inducing external erosion. Backward erosion, whose initiation will be described in more detail in forthcoming section 1.1.4, refers to the process by which seepage forces gradually erode material from the downstream part of the structure of the embankment dams and levees, thereby forming a growing tunnel within a soil layer or at an interface with a cohesive cover layer (see Figure 1.3).

The kinetics for these four mechanisms are initially rather slow and discontinuous (i.e. seasonal evolution over years), but they may progressively or intermittently accelerate, interacting with other processes (sinkholes, differential settlement, etc...), and also inducing new ones, possibly leading to an ultimate failure of the structure by a piping flow erosion, when a direct path exists between upstream and downstream. In this critical situation, the remaining time before rupture can often be counted in minutes or hours rather than days (Bonelli and Benahmed 2011).

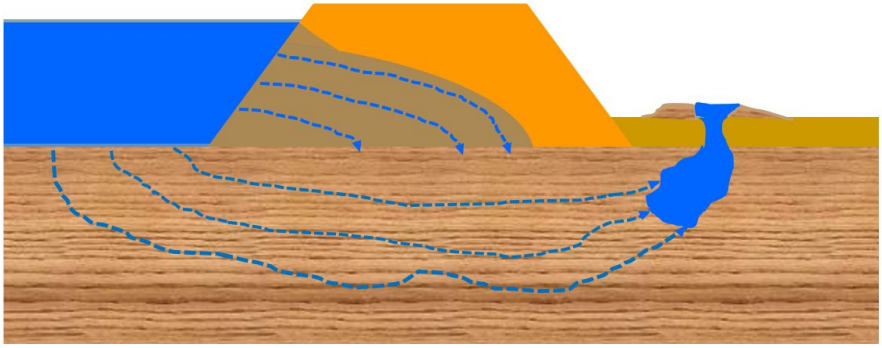

Figure 1.3. – Example of backward erosion.

1.1.3. General concepts for soil erosion modeling

As sketched in Figure 1.4, three conditions must meet to trigger internal erosion: material, mechanical, and hydraulic conditions. The material condition depends on several properties as the grain-size distribution, grain shape (angular, sub-angular, sub-rounded, rounded), void size distribution, void ratio, fines and water contents, etc. The mechanical condition is related to the stress state, the method of compaction used during the construction phase, etc. Finally, the hydraulic condition involves the hydraulic gradient, seepage velocity, seepage direction, etc. For example, the resistance of a soil to erosion is improved by soil compaction, a lower hydraulic gradient is required for the erosion of fine particles, and various mechanical conditions have an impact on the critical gradient for erosion onset (L. Zhang, Peng, Chang, et al. 2016).

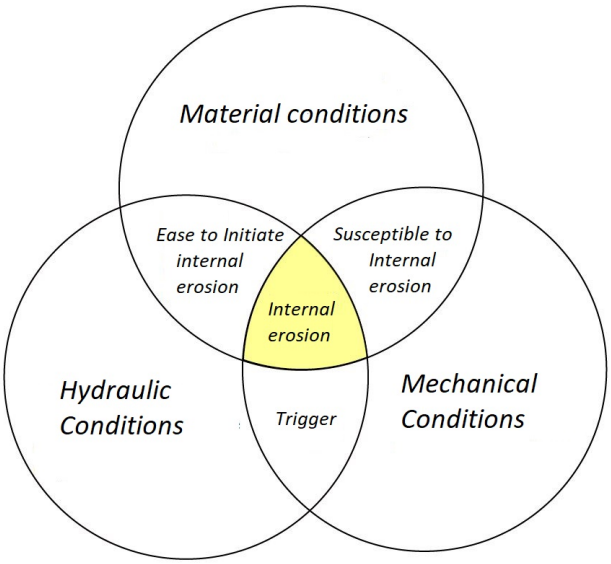

Figure 1.4. – Internal erosion conditions (L. Zhang, Peng, Chang, et al. 2016).

Quantifying the eroded mass also depends on the disciplinary field and the objects

under investigation since one needs first to fix the space scale, i.e. the dimension of study which can range from kilometers to microns or millimeters, and the time scale, i.e. the duration considered which can vary from seconds, which is the case of fully developed dam failures, to months, or even years in some geological phenomena. Another defining choice is that of the hydrodynamic quantity capable of accounting for the hydraulic load exerted on a soil. Many elements come into play here, such as the flow regime (laminar versus turbulent), the type of flow (free surface flow generated by rainfall or in charge flow), or the use of a single value (mean value) or an entire distribution.

In a soil mechanics perspective, the representative volume of a soil subjected to erosion is typically a cubic decimeter, for a characteristic evolution time of few seconds to minutes. Once this space-time frame is fixed, an additional uncertainty for the properties of a given elementary soil arises from the intrinsic heterogeneity of a soil at larger scale, from one location to another. In many practical cases, the fluid regime is no laminar but transitional or turbulent, which makes it difficult to quantify the hydrodynamic load since the fluid flow velocity and stress highly fluctuate in time and space. To overcome this obstacle, the most common solution is a crude averaging of the chosen quantity over time and/or space. Furthermore, it can be mentioned that external erosion but also several mechanisms of internal erosion involve local erosion at the surface of a soil exposed to a tangential water flow (either a free surface flow or a flow in charge): this generic situation is consequently called surface erosion.

Several empirical laws have been proposed to determine such a rate of erosion at the surface of a given soil as a function of the local flow stress. A famous empirical expression, first proposed by Partheniades (Partheniades 1965), is commonly used to relate the superficial rate of erosion to the hydrodynamic load, which is quantified here by the time average of the fluid shear stress. More precisely, the eroded mass per surface and time $\dot{m}$ (in kg m^2/s) is assumed to vary linearly with the fluid shear stress τ:

$$\dot{m} = \begin{cases} k_{er}\,(\tau - \tau_c) & \tau \geq \tau_c \\ 0 & \tau \langle \tau_c. \end{cases} \tag{1.1}$$

The two parameters introduced in this expression are τ_c, denoted critical shear stress (in Pa), and k_{er}, the so-called erosion coefficient (in s/m). Alternatively, dividing the previous expression by the dry soil density ρ_d, one gets the same relation for the eroded volume per surface and time, or equivalently the eroded depth per time, $\dot{\epsilon}$ (in m/s), provided that k_{er} is replaced by $k_d = k_{er}/\rho_d$ (in s m^2/kg). Obviously, τ_c is the erosion threshold above which the particles detach while k_{er}, or k_d, determines the kinetics of erosion when the shear stress threshold is exceeded.

After having presented the different conditions that must be simultaneously fulfilled for an internal erosion process to be initiated within a hydraulic structure, it is clear that the nature and properties of the constitutive soils are parameters of primary importance. It is therefore necessary to present in detail the different types of soils that constitute the earthen hydraulic structures (see section 1.2.1) as well as the

elementary physical mechanisms of the fluid-granular interaction at the particle and granular scale (see section 1.2.2). But just before, we will present a little bit further the trigger mechanisms of backward erosion, as these are at the heart of the motivations behind this work.

1.1.4. Specific scope on the initiation of backward erosion

Initiation of a backward erosion through the foundations of a hydraulic structure occurs when a transverse seepage flow creates an over-pressure at the foot of the structure, strong enough to locally destabilise the surface soil layer, reinforcing the leak. The level of resistance of the surface soil and the way it destabilises depends strongly on its nature.

For a granular top cover layer, the soil particles are put into motion by fluidization when the drag force exerted on the soil, or the corresponding hydraulic gradient, balances the soil's buoyant weight, which is equivalent to a cancellation of the effective stress in the material. Once fluidized, the particles float and lose their contact, being thus surrounded by a continuous liquid phase. More precisely, the internal underground flow follows a preferential path and creates locally a sufficiently high pressure gradient for soil's fluidization within one or several vertical chimneys. These are called "sand boils" or "sand volcanoes" (see Figure 1.5). This localized fluidization of the granular topsoil is a preliminary mechanism for forming a cavity that can then gradually develop from downstream to upstream and can ultimately lead to partial or total rupture of the structure.

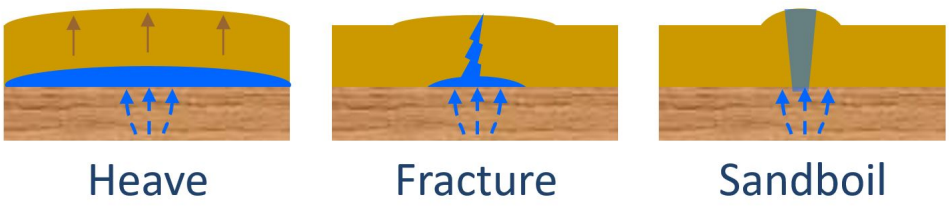

Figure 1.5. – Different types of hydraulic failure expected depending on the nature of soil.

The superficial destabilization by the flow is expected to be substantially different when the topsoil is no more sandy but either cohesive or cemented. However, apart from the purely granular case, there are few previous studies on this situation of destabilisation of the surface soil layer (see section 1.3 below). This flow-induced instability of the topsoil will be generically called "hydraulic failure". One of the main motivations of this work is to determine the specific critical conditions of occurrence and the different types of failure scenarios, among which we can envisage heave, when the soil expands and pushes the ground upward, fracture, when a crack propagates upward, and the previously described sandboil process (see Figure 1.5).

1.2. Synthetic background on hydraulic flow and soil interactions

1.2.1. Different types of soils

1.2.1.1. Granular soils

Soils are made up of different-sized particles, together with water and air. Soil texture refers to the size distribution of the particles that compose the soil and depends on the proportion of sand, silt, and clay. It can influence whether soils are more or less permeable and whether they can hold water. The soil texture will partially determine the properties of the soil, which are typically classified into categories and differentiated by the type of interactions occurring between the grains. Granular media are defined by grain sizes greater than 100 µm (R.-L. Brown 1970; Rao, Nott, and Sundaresan 2008; Duran 1997; Bear 1988) and are subject only to collisions and contact forces, including solid friction. These grains can range from fine sand to boulders. On a grain stack scale, the essential structural property is the solid volume fraction of a granular medium, which represents the solid volume ϕ occupied by the grains within a defined volume of soil:

$$\phi = \frac{V_g}{V_t} = \frac{V_t - V_v}{V_t}, \tag{1.2}$$

where V_v, V_g, and V_t stand for the volume of the inter-grain voids, the volume of the grains, and the total volume, respectively. Alternative quantities are more commonly used in soil mechanics: (i) the porosity ϵ [1], which represents the volume of the voids in the sample over the total volume of the sample and directly reads $\epsilon = 1-\phi$; (ii) the void ratio index e which represents the volume ratio between voids and solid. It comes:

$$e = \frac{1-\phi}{\phi} = \frac{\epsilon}{1-\epsilon}. \tag{1.3}$$

The solid fraction depends on the form, stiffness, and size distribution of the particles. By way of illustration, the solid fraction for a mono-size packing of perfectly rigid spherical particles varies from 0.55 (random loose packing) to 0.64 (random dense packing) for disordered structures, and up to a maximal limit of 0.74 for ordered ones (face-centred cubic or compact hexagonal arrangement). In the more realistic case where there is a particle size distribution, the small grains can fill part of the voids and higher solid fractions can be easily reached. The densest packing in 2D and 3D is accomplished by utilizing an Apollonian repartition with a power-law size distribution (Reis, Araújo, Andrade-jr, et al. 2012), with gradually smaller spheres filling the gaps of decreasing size in a hierarchical order. This principle is used for high-density concrete where different particle sizes are used, ranging from gravel to ash particles of sizes less than one micron.

1. in soil mechanics literature porosity is usually termed n

The volume fraction is an important factor to determine the mechanical resistance of soils. For instance, a loose granular soil under shearing will deform and get more compacted, showing a volume decrease. On the contrary, a dense frictional soil under shearing only slightly compacts initially before expanding with a substantial volume increase, what is referred to as the dilatant behaviour of soil.

1.2.1.2. From coherent to granular cohesive soils

Classification of cohesive soils properties A cohesive strength appears in the soil as soon as there exist attractive inter-particle interactions. For fine particles, these interactions are exclusively of microscopic origin (i.e. electrostatic and molecular forces). They develop only when two particles are close to each other within the same material (Israelachvili 2011) and generate an internal stress at the soil scale, denoted cohesion, that opposes shearing even for a vanishing normal stress. A soil constituted solely of fine particles is more appropriately described as coherent. For larger particles that become insensitive to electrostatic forces, other types of attractive interaction between grains may exist, mediated by a binder such as water or fine soil. Solid bonds can also exist between the particles in so-called cemented soils and a discussion about binder force will be presented later in section 1.2.1.3 (Lick, Jin, and Gailani 2004; Righetti and Lucarelli 2007). From this first description, we can already deduce that the size of the particles, and their relative distribution, as well as the water content of the soil will play an essential role in the degree of cohesion of the material. Classifications of particles by size are therefore commonly used, as the one presented in Figure 1.6.

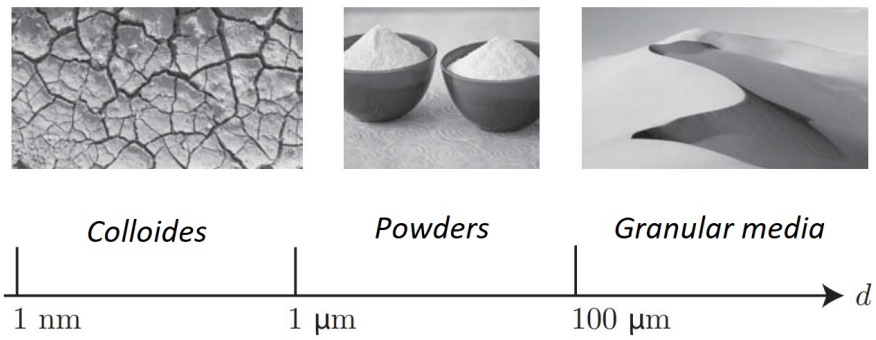

Figure 1.6. – Physical classification of divided media according to the size of the particles: colloids, powders and granular media (Pouliquen, Andreotti, and Forterre 2001).

Colloids are composed of particles smaller than 1 µm and they are highly sensitive to thermal agitation. This can be observed for example in clay which is primary responsible for cohesion in soils. For silts and fine sands, where the grains sizes range between 1 µm and 100 µm, Brownian motion (due to thermal agitation) becomes negligible and the dominant forces are the Van der Waals type molecular interaction forces, electrostatic forces and also capillary forces related to humidity.

In all cases, the degree of saturation plays an important role in determining the cohesion strength. For instance, the latter capillary cohesion is directly controlled by the degree of saturation of the material: starting from a purely granular behaviour at zero degree of saturation, the soil's cohesion builds up and increases with water content until a certain limit. Then cohesion stagnates before rapidly returning to zero in fully saturated conditions, recovering a frictional granular behaviour. The properties of coherent soils are also directly prescribed by the water content, from which four general soil states are defined: Solid, semi-solid, plastic, and liquid. These domains are determined by the so-called Atterberg limits which identify the water content limits specific to each state thus providing the liquid limit and plasticity index of soils.

Different origins of cohesion in a granular soil Thermal agitation and molecular interaction being negligible for particles that are greater than 100 µm, the only remaining interactions between two particles occur either by direct contact or via connection bonds involving an additional phase which can be liquid (i.e. capillary bridges mediated by a more or less viscous liquid) or solid (as coherent clay or calcite deposition).

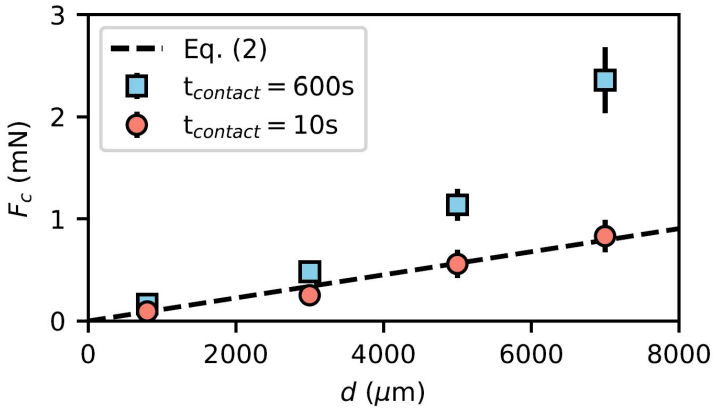

Figure 1.7. – Cementation force as a function of the particle diameter and for short and long contact time. Figure extracted from (Gans, Pouliquen, and Nicolas 2020).

The case of attractive forces existing through direct contact and adhesion between millimeter-sized particles is rare, if not almost absent in nature. A recent example can however be reported and concerns the obtaining of grains with tunable cohesion. Gans and co-workers (Gans, Pouliquen, and Nicolas 2020) indeed developed a controlled cohesive granular material, made of spherical particles coated by a thin layer of polymer, namely Polyborosiloxane (PBS). Adhesive strength is created between the particles, due to the contact between polymeric chains, and depends on the PBS coating thickness, with an additional impact of the pre-compressed contact time which eventually saturates for a long time. Figure 1.7 shows the effect of the contact time and

the particle diameter: both particle diameter and contact time increase the adhesive force. Note that the bond failure for this particular type of cohesion is reversible since the adhesive contact between polymeric chains spontaneously rebuilds after being removed. Tunable cohesion has been achieved in a quite similar way by glass surface silanization to induce a cohesive force between dry glass particles which is controlled by varying the duration of the chemical silanization reaction (Jarray, Shi, Scheper, et al. 2019).

Considering now the most common case of granular cohesion mediated by binder bonding, and before focusing more in depth on cemented granular soils in the next section, the case of capillary cohesion in granular soils can be briefly presented here. Capillary bridges, as the one sketched in Figure 1.8, are created due to the difference in surface energy between the 3 phases present (air, water, solid) from competition between solid/air, liquid/air, and solid/liquid surface energies. The equilibrium state is defined by the liquid/air surface tension, often denoted simply as the liquid surface tension γ_l, and by the wetting angle θ which derives from the three surface energies. There consequently exists a difference in pressure between the inside and outside of the capillary bridge which is given by Laplace's law:

$$\Delta P = \gamma_l \Big(\frac{1}{C_1} - \frac{1}{C_2} \Big), \tag{1.4}$$

where C_1 and C_2 are the two radii of curvature of the liquid bridge.

If gravity contribution can be neglected (typically for small liquid volume), the resulting static force of the bridge that brings two identical spherical particles of radius R together can be written as the sum of the capillary force of the meniscus and the axial component of the surface tension force (Fisher 1926; Pitois, Moucheront, and Chateau 2001):

$$F_{cap} = 2\pi R \gamma_l \sin(\varphi) \sin(\varphi - \theta) - \Delta P \pi R^2 \sin^2(\varphi), \tag{1.5}$$

with φ the half-filling angle (see Fig. 1.8).

The water content in a granular soil will have an essential impact on capillary cohesion by controlling the volumes of water trapped in capillary bridges (**mitarai2006**). According to Kohonen (Kohonen, Geromichalos, Scheel, et al. 2004), a minimum amount of water content around 0.03% for mono-disperse spheres is required to promote the formation of the first capillary bridges. Fournier et al. (Fournier, Geromichalos, Herminghaus, et al. 2005) observed that all capillary bridges are formed at 0.07% water content. The range between these two values being rather narrow, the number of capillary bridges is expected to increase sharply until there are no more intergranular constrictions available. Then, above 0.07%, the water bridges that were pendular, i.e. connecting pairs of grains, grow and progressively turn to pendular bonds connecting now at least 3 particles. Increasing further the water content makes the pendular bridges merge together, filling almost all the pores by regions between which liquid surfaces with menisci still exist, holding cohesion. This is the so-called capillary regime. Finally, at very high water content above 90% (**mitarai2006**), the granular

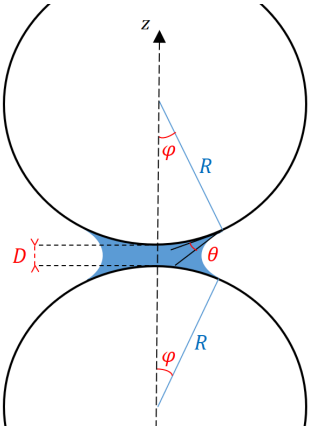

Figure 1.8. – Shape of a pendular liquid bridge between two identical spherical particles (radius R) separated by a gap D. θ and ϕ are the wetting angle and the half-filling angle, respectively.

medium gets almost totally saturated and cohesion is rapidly lost.

1.2.1.3. Focus on cemented granular soils

Different types of cemented soils Cemented soils are characterized by the presence of a solid binder that connects their constituent particles to each other, thus conferring to the medium rather specific mechanical properties, somewhere between hard soils and soft rocks. Indeed, a soil's strength is enhanced by cementation, its macroscopic behaviour at low stress also deviates from that of a frictional soil, as it deforms, the internal structure of a cemented soil can gradually degrade by brittle rupture of the microscopic connections, then generating fractures on a larger scale. It appears essential to fully understand this type of mechanical behaviour given that cemented materials are very common in our environment, either of natural origin or man-made by addition of a binding agent.

Many geological landforms all over the world consist indeed of several varieties of cemented soils as sandstones, breccias, carbonate sands, or coarse-grained sediments (Asghari, Toll, and Haeri 2003; Collins and Sitar 2011; Tengattini, Andò, Einav, et al. 2022). The high shear strength of these geomaterials often creates a spectacular landscape, characterized by cliffs with very steep slopes, shaped by sudden and possibly repeated failures (Collins and Sitar 2011). Sandstone is also abundant in the deep seabed, explaining a growing interest from the offshore community seeking to operate at greater depths (Marques, Festugato, and Consoli 2021). Such natural cementation has mainly an inorganic origin from precipitation and deposition of mineral compounds as carbonates, commonly carried by underground flows (Ismail, Joer, Sim, et al. 2002; Michlmayr, Cohen, and Or 2012). Hydrate-bearing sediments are another example of natural cementation (Waite, Santamarina, Cortes, et al. 2009; Jung and Santamarina 2011). There are alternative cementing agents of biogenic origin, induced by biological activity (roots, microbes, bacteria, fungi) (Michlmayr, Cohen,

and Or 2012; Terzis and Laloui 2018). Natural cementation is often accompanied by a substantial variability in strength observed on a large but also on a small scale (Asghari, Toll, and Haeri 2003). Some examples of natural cemented granular soils are presented in Figure 1.9.

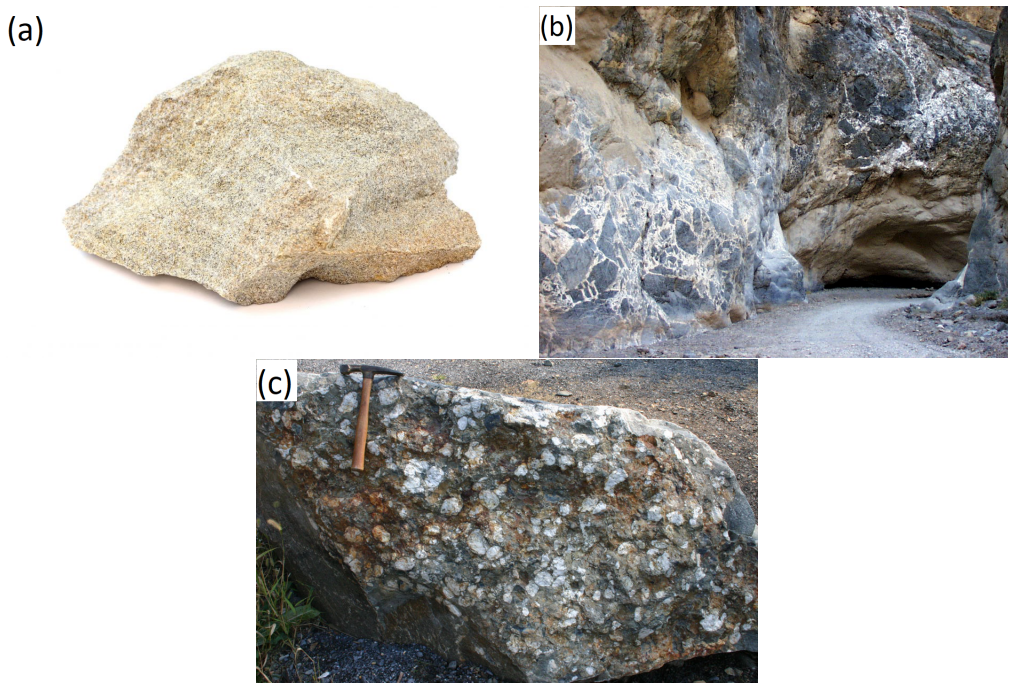

Figure 1.9. – Examples of natural cemented granular soils: (a) Sandstone, (b) Boulder of conglomerate and (c) Fault breccia of grey limestone. Reference: National Park Service.

Particles binding is also obtained from artificial cementation in several construction materials (mortar, asphalt) (Tengattini, Andò, Einav, et al. 2022) and is commonly implemented on-site for soil improvement (Powrie 2004). Binding agents are typically cement, lime, bitumen, or polymeric organic stabiliser (Ingles 1962; Powrie 2004) but, due to energy cost and greenhouse gas emission (Mikulčić, Klemeš, Vujanović, et al. 2016), alternative techniques are emerging, such as industrial waste residue-based binding (Kou, Jing, Wu, et al. 2022) or microbially induced cementation (Terzis and Laloui 2019). These soil treatments provide increased shear strength, prevent scouring (for instance around a pipeline (R. Hu, X. Wang, H. Liu, et al. 2022) or inhibit sediment transport (particularly critical for polluting or radioactive particles). Many other industries (mineral, agricultural, food, chemical, pharmaceutical) besides civil engineering produce and handle binded particulate materials, usually in the form of agglomerates or granules whose attrition and breakage properties are essential to properly comprehend the many processes involving this type of material (Topin, J.-Y. Delenne, Radjai, et al. 2007; Ge, Ghadiri, Bonakdar, et al. 2018; X. Chen, L.-G. Wang, Morrissey, et al. 2020). The range of cemented materials is anyway quite wide and other examples may also include sintered ceramics, snow, or certain grains such as

wheat (Topin, J.-Y. Delenne, Radjai, et al. 2007; Tengattini, Andò, Einav, et al. 2022). Some examples of artificial cemented granular soil are presented in Figure 1.10.

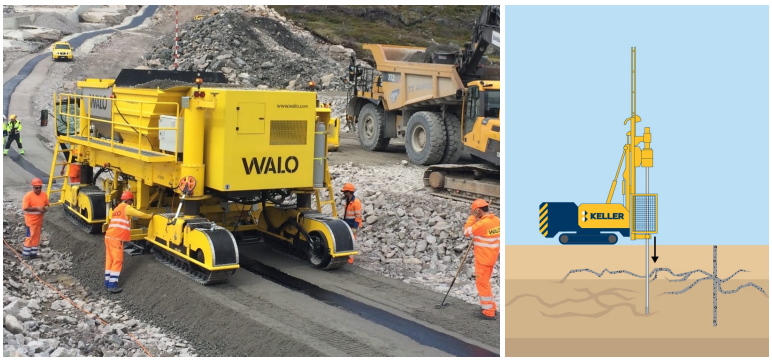

Figure 1.10. – Example of artificial cemented granular soils: Asphalt core dam, cement grouting soil improvement. Reference: https://walo.com.

Solid bonds at contact scale The type of cemented soil of interest in the present study involves coarse soil particles bonded by solid bridges at grain contacts. In the literature, the vast majority of the experimental investigations focusing on this type of material have been carried out with artificially cemented models, on the one hand because the extraction of intact materials on site is a very delicate operation (Asghari, Toll, and Haeri 2003) and, on the other hand, because the use of a versatile model material allows a wide and controlled exploration of its properties and related behaviours, particularly its mechanical strengthening provided by cementation. The preparation of these different artificial cemented materials requires the addition of a binder which must be able to be intimately mixed with the base granular material. The solution implemented in most studies consists in using a workable binder easy to blend and which often hardens after mixing, such as cement, clay, hydrated lime, polymeric solution, epoxy resin, etc. An alternative is to directly induce the precipitation of a crystallised solid, typically calcite of microbial origin (Lin, Suleiman, D.-G. Brown, et al. 2016; Terzis and Laloui 2019; Ham, Martinez, G. Han, et al. 2022), within the soil grains. The final spatial distribution of the binder in the material can then differ, ranging from a quasi-uniform coating of the surface of the grains to a very localised distribution of the cementing binder at the contacts (Ingles 1962; Lin, Suleiman, D.-G. Brown, et al. 2016; Terzis and Laloui 2018; Theocharis, Roux, and Langlois 2020; Tengattini, Andò, Einav, et al. 2022). Note that we are only interested here in the case where solid bridges exist between the grains, thus discarding the reversible contact adhesion presented before (Gans, Pouliquen, and Nicolas 2020; Jarray, Shi, Scheper, et al. 2019).

There are two types of cemented contacts as sketched in Figure 1.11. In the first case, the cemented contacts are issued from prior grains coating, where the subsequent failure of a bridge requires the occurrence of a fracture within the solid binder. We will exclusively focus in the present study to the second case, where an isolated solid bridge formed between the two particles without the whole surface of the particles

being coated by the binder. Then, as sketched in Figure 1.12, several modes of rupture are possible for an isolated solid bond: cohesive (i.e. internal failure within the binder), adhesive (i.e. debonding failure at the interface between the binder and one of the grains), or mixed (i.e. combination of the two previous modes) (Schmeink, Goehring, and Hemmerle 2017; Ham, Martinez, G. Han, et al. 2022). Progressive bond damage was also reported in some cases (Tengattini, Andò, Einav, et al. 2022). Together with the elastic properties of the bond, a critical parameter is its adherence, or adhesive strength, to the grain surface (Topin, J.-Y. Delenne, Radjai, et al. 2007), which depends on the microscopic interaction between the molecules of the two solid bodies in contact. This adhesive strength is to be compared to the internal cohesive strength of the bond itself, or ultimate tensile yield stress, which is an intrinsic property of a material corresponding to its elastic limit.

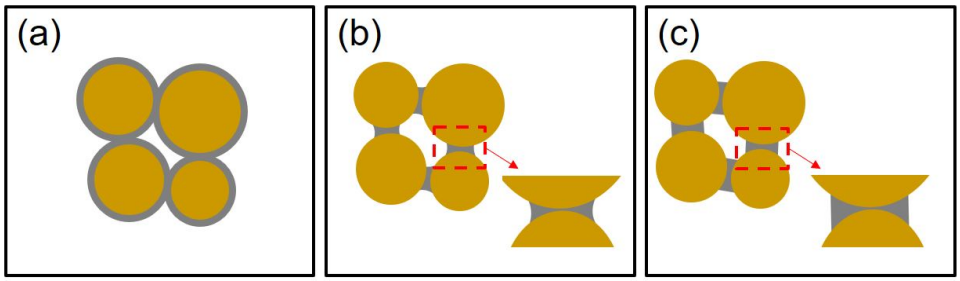

Figure 1.11. – Different types of cemented contacts: (a) Grain coating contact; (b) Bridging cementation type meniscus; and (c) Bridging cementation type flat torus-filling. Insets a close view of the bond. After (Schmeink, Goehring, and Hemmerle 2017; Ham, Martinez, G. Han, et al. 2022).

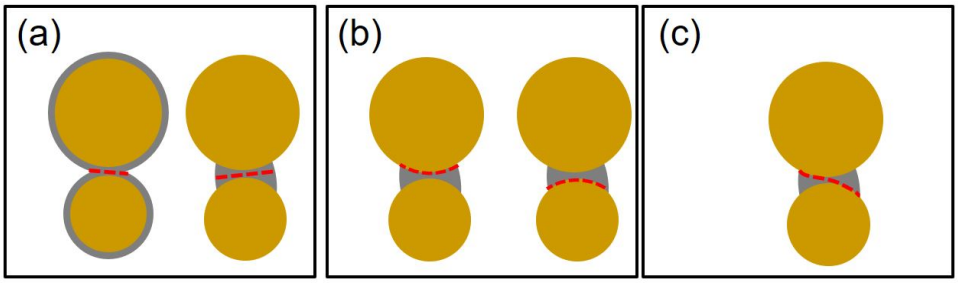

Figure 1.12. – Different types of bond rupture for the two different cases: (a) Cohesive rupture, (b) Adhesive rupture, and (c) Mixed Rupture. After (Tengattini, Andò, Einav, et al. 2022).

Bond strength measurements In order to be able to understand the behaviour of such artificial cemented soils at a sample scale, a first essential step is the microscopic characterization of the mechanical strength of a cementing bridge between two neighboring grains. From an experimental point of view, some studies have been

carried out to measure the yield strength of an individual bridge in tension, shear, more occasionally, in bending and torsion (Fan, Ten, Clarke, et al. 2003; J.-Y. Delenne, El Youssoufi, Cherblanc, et al. 2004; Söderholm 2009; Kirsch, Bröckel, Brendel, et al. 2011; Jung and Santamarina 2011; Ham, Martinez, G. Han, et al. 2022; Jarray, Shi, Scheper, et al. 2019).

Ham et al. (Ham, Martinez, G. Han, et al. 2022) performed experiments to determine the strength of a bond, made by microbially induced calcium carbonate precipitation MICP (i.e. by solidification of calcite crystals), between two spherical grains of 3 mm diameter. The experimental setup is presented in Figure 1.13. The three types of cemented contacts previously introduced were obtained depending on the calcite content but without prior control: grain coating, meniscus-filling, and flat torus-filling models (see Figure 1.11). The minimum cross-sectional area and the contact radius can be determined by the calcite content. Micro tensile and shear tests were implemented on a pair of beads as follows: bead 1 is glued with epoxy to a quartz disc connected to a micrometer by a rod while bead 2 is epoxy-glued to another quartz disc connected to a cantilever beam whose deflection is instrumented with strain gauges for the purpose of measuring the horizontal force between the two beads, either in tension or shear depending on the bond orientation. Figure 1.14 shows the micro tensile and shear results with the different types of ruptures obtained, i.e. mixed, adhesive and cohesive. Highly disperse tensile and shear stress values are observed for a same calcite content and no clear distinction can be made between the three rupture types as regards calcite content. However, a trend seems to be emerging when considering the tensile stress: The strength values for the adhesive failure mode are roughly higher than those of the mixed mode, which are themselves higher than those of the cohesive mode. Furthermore, the mean tensile stress values are greater by a factor of 2.7 than the shear ones. Note that the MICP process occurs here in only a few days to weeks, which much probably makes the strength of the material weaker than for the same geological process in the field which takes thousand to millions of years (Budd 1988; Casella, Griesshaber, X. Yin, et al. 2017).

Approximately the same type of device has been used previously to measure the adhesive force between ice particles in the air or in a sucrose solution by micro-manipulation (Fan, Ten, Clarke, et al. 2003). This setup is able to characterize the very weak adhesive force for very small particles from 10 to hundreds of microns. A micro-balance setup and a micro-positioner driven by a DC motor with adjustable speed were used to measure somehow stronger forces in the previously mentioned case of direct adhesive contact for silanized glass beads (Jarray, Shi, Scheper, et al. 2019). Our micro-mechanical characterization setup which will be presented later in chapter 2 is rather close to the latter.

Other measurements at solid bond scale are interesting to present as they were conducted in quasi-bidimensional geometry, the grains being cylindrical aluminum rods (8mm diameter, 60mm long) glued along their common edge by an epoxy resin (J.-Y. Delenne, El Youssoufi, Cherblanc, et al. 2004). Figure 1.15 shows the different experimental devices used to obtain tensile, shear, compression, and bending limits of the bond failure. It is worth noting that the bending test has an additional compressive

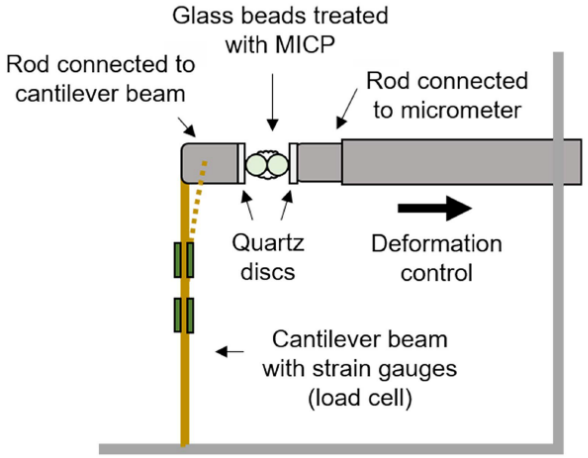

Figure 1.13. – Schematic drawing of the tensile setup used to characterize the strength of solid bonds created by MICP. Figure extracted from (Ham, Martinez, G. Han, et al. 2022).

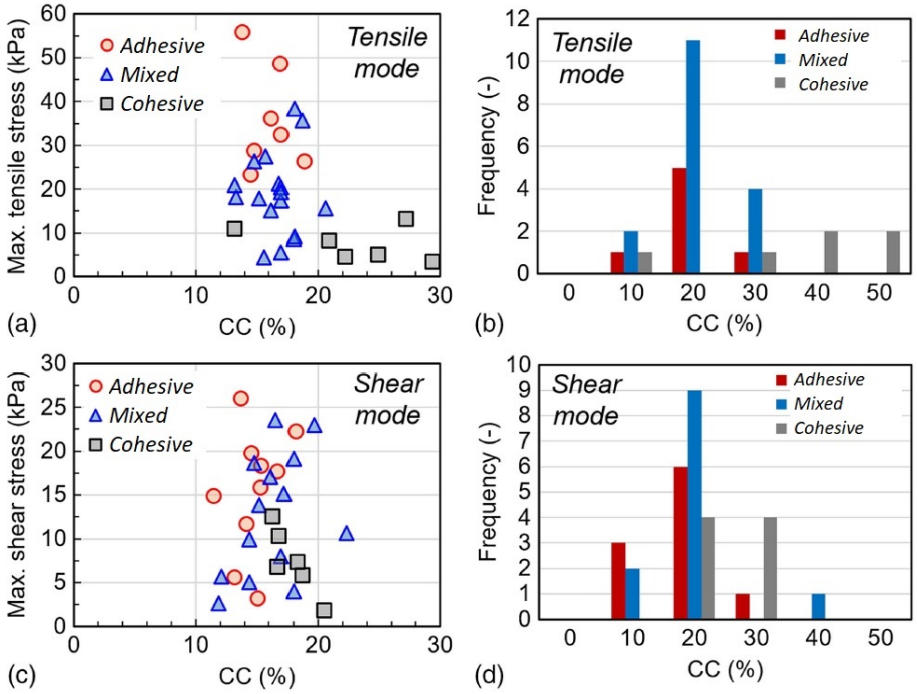

Figure 1.14. – (a) Tensile stress versus calcite concentration. (b) Frequency of bond rupture occurrence of each type of failure for tensile. (c) Shear stress versus calcite content. (d) Frequency of bond rupture occurrence of each type of failure for shear. Figure extracted from (Ham, Martinez, G. Han, et al. 2022).

force contribution which is however very small and negligible. From this unique

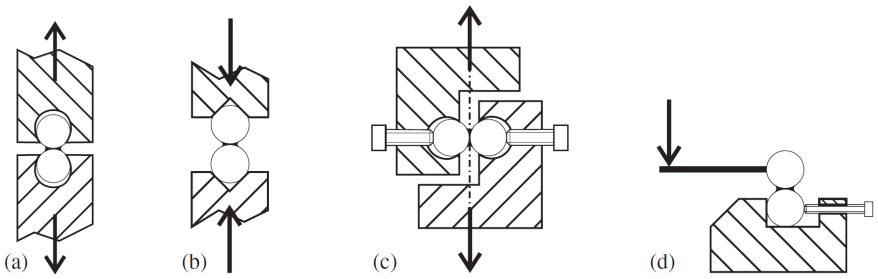

Figure 1.15. – Different experimental devices used to characterize the strength of a solid bond between two rods: (a) Tensile, (b) Compression, (c) shear, and (d) Bending. Figure extracted from (J.-Y. Delenne, El Youssoufi, Cherblanc, et al. 2004).

test series, three threshold values are found for tensile (normal), shear (tangential) and bending solicitation: C_n, C_t and C_b. From the 5 points corresponding to failure along the pure loading paths (i.e. 2 symmetric directions for shear and bending, no failure observed in compression), Delenne and co-authors proposed a yield surface of parabolic shape as detailed later (see section 1.2.3.1).

Homogenisation From an analytical point of view, the transition from the microscopic level to the macroscopic behaviour of a cemented material is done with the help of homogenisation laws, developed in the continuity of Rumpf's original work (Rumpf 1962; Ingles 1962; Pierrat and Caram 1997; Richefeu, El Youssoufi, and Radjaı 2006). In particular, Richefeu and co-authors (Richefeu, El Youssoufi, and Radjaı 2006) proposed considering the macroscopic stress as

$$\sigma_T = \frac{1}{2} n \langle f_t l \rangle, \tag{1.6}$$

where

— $\langle\ \rangle$ stands for the averaging over all bonds in the control volume,
— f_t is the normal component of the force at the particle contact,
— l is the length of the branch vector,
— n is the density of the bonds.

The latter quantity n can be expressed in terms of the coordination number Z_c, the volume of a particle V_p and the mean solid volume fraction ϕ:

$$n = \frac{\phi Z_c}{2 V_p}. \tag{1.7}$$

Inserting Equation 1.7 in Equation 1.6, results in:

$$\sigma_T = \frac{3 Z_c \phi}{2\pi} \frac{F_t}{d^2}. \tag{1.8}$$

Where F_t and d are the micro tensile force and the particle diameter, respectively.

1.2.2. Action of fluid on granular media

This section is devoted to a synthetic presentation of the interplay between grains and fluid in a flow situation. We will first consider two extreme cases, namely that of a single grain moving in a surrounding fluid and that of a fluid flowing through a static granular porous medium. The more complex case of granular suspensions, where both phases are in motion, will finally be considered.

1.2.2.1. Case of one particle in a fluid flow

The dynamics of grains in a fluid can be highly challenging, especially in the case of complex fluid flow configurations as turbulent flow regime with re-circulation of grains (Van-Dyke 1982), high pressure conditions which can deform the particles, or suspension sedimentation where contact interactions between the grains is known to play a key role. But before getting into the study of these intricate systems, it is first necessary to be aware of the elementary forces that can be exerted on a particle by a surrounding flowing fluid.

Let's consider an isolated spherical particle in a stationary and uniform flow. An essential dimensionless parameter is the Reynolds number, which is the ratio of inertial forces to viscous forces within a fluid. The expression of the Reynolds number of a moving spherical particle of diameter d with a velocity u^R relative to that of the fluid is given by:

$$Re_p = \frac{u^R d}{\nu}, \tag{1.9}$$

where ν is the kinematic viscosity, recalling that $\nu = \eta/\rho_f$ with ρ_f and η are the density and dynamic viscosity of the fluid, respectively.

The Reynolds number is used to identify the different flow regimes: laminar, transitional and turbulent regimes. The laminar regime occurs when the viscous forces are dominant, i.e. at small Reynolds numbers, and it is characterized by smooth and constant fluid motion. The turbulent regime occurs when the inertial forces are dominant, i.e. at high Reynolds numbers, and it is characterized by chaotic motion, eddies, vortices and other flow instabilities. Between the two is the transitional regime, i.e. at intermediate Reynolds numbers, characterised by localised instabilities, recirculation and intermittency.

The sum of the external forces applied on the grain is equal to the integral of the stress tensor $\tilde{\tilde{\sigma}}_f$ and the pressure of the fluid P over the outer surface of the grain, and it is expressed in the following form:

$$\sum \vec{F}_{ext} = \int_{S_g} (-P\vec{n} + \tilde{\tilde{\sigma}}_f.\vec{n})\,ds, \tag{1.10}$$

with $\vec{n}$ the normal vector to the outer surface area S_g of the particle.

Without going deep in explaining all the different types of interaction between the fluid and the grain, we will mainly focus here on the two most common hydrodynamic forces: buoyant and drag forces.

The buoyant force, first introduced by Archimedes, is an upward force exerted by the fluid on an object that is partially or fully immersed. This force is due to the pressure applied by the surrounding fluid. The resultant force is not zero because the fluid pressure increases with depth due to the effect of gravity. The pressure is thus stronger on the lower part of a submerged object than on the upper part, resulting in a generally vertical upward force, opposed to gravity:

$$\vec{F}_b = -\rho_f V_p \vec{g}, \tag{1.11}$$

where V_p is the submerged volume of the particle and $\vec{g}$ is the vector of gravity.

The buoyant weight of the particles is thus obtained by subtracting this buoyant force from the weight of the particle, such as:

$$\vec{W}_b = (\rho_p - \rho_f) V_p \vec{g}. \tag{1.12}$$

The drag force is generated by the high fluid shear in the immediate vicinity of the surface of the particle moving relative to the surrounding fluid with a velocity u^R (i.e. u^R is the difference between the velocity of the particle u^p and the velocity of the surrounding fluid u^f). It is expressed as:

$$\vec{F}_d = \frac{1}{2}\rho_f C_d(Re) S_a |u^R| \vec{u}^R, \tag{1.13}$$

where S_a is the cross-sectional area of the sphere particle and C_d is the so-called drag coefficient, which depends solely on the particle Reynolds number Re_p.

For $Re_p \ll 1$, the drag coefficient is equal to $24/Re_p$ as the drag force is known to coincide with the Stokes force:

$$\vec{F}_{d_{St}} = -3\pi\eta d \vec{u}^R. \tag{1.14}$$

For instance, regarding a particle settling in a fluid at rest, the equation of Stokes for the force provides for its terminal velocity, denoted Stokes velocity:

$$\vec{u}_{St} = \frac{(\rho_p - \rho_f)\vec{g}d^2}{18\eta}. \tag{1.15}$$

For $Re_p \gg 1$, the flow regime gets fully inertial and turbulent while the drag coefficient reaches a constant value which is $C_d \approx 0.44$ for a sphere up to $Re_p \approx 10^5$ (drag crisis).

In-between these two limits, many empirical laws have been proposed. Amongst them, a rather convenient expression by Dallavalle, even if not the most accurate one, allows to recover the two asymptotic behaviours (A.-D. Gibilaro 2001; Di-Felice 1994)

as shown in Figure 1.16. It reads:

$$C_d = \left(\sqrt{0.44} + \sqrt{\frac{24}{Re_p}}\right)^2. \tag{1.16}$$

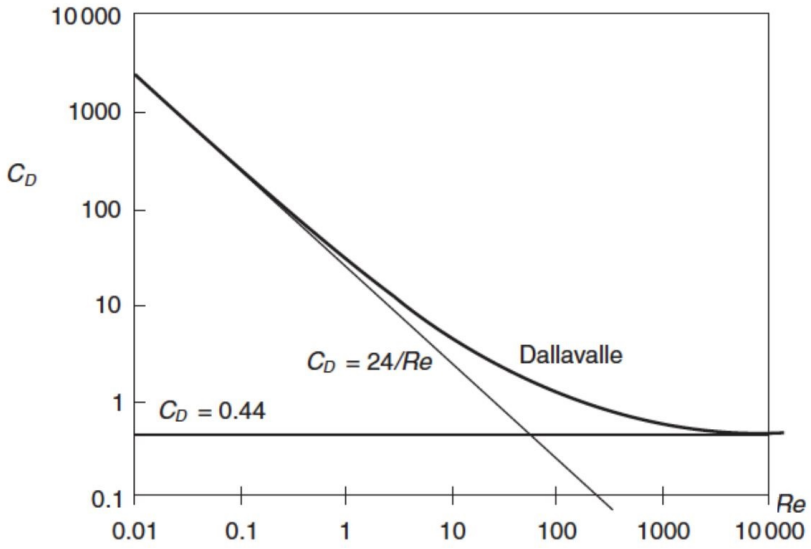

Figure 1.16. – Empirical expression from Dellavalle for C_d versus the particle Reynolds number. Figure extracted from (A.-D. Gibilaro 2001).

Other types of forces can act on a particle submerged in fluid, such as lift, virtual (or added-mass), lubrication, generalised buoyancy, Basset and Magnus forces. The lift force is induced by a velocity gradient of the fluid which causes the rotation of the particle and thus an asymmetry of the pressure field. The virtual force is the inertia added due to the acceleration or deceleration of the movement of the particle in the fluid, where in this motion the particle drags the surrounding fluid. The overpressure in the fluid during a collision between two particles leads to a repulsive force, called the lubrication force, which theoretically vanishes at contact (i.e. only in the ideal case of a perfectly smooth surface but no longer with some roughness). The previous buoyant force can be generalised to an accelerated flow owing that this local fluid acceleration is added to the gravity field. The Basset force accounts for the viscous effect and lagging boundary layer development as the relative velocity changes with time. The Magnus force is the sideways force on a rotating body when there is a relative motion between the rotating body and the fluid.

1.2.2.2. Granular porous flow

In this section, we are interested in porous media corresponding to granular and cemented granular soils, with a particle size typically greater than 100 µm. The voids of such a soil form a network of pores with constrictions. The voids are filled with

water, air, or any other type of liquid. The size of the constrictions makes it more or less difficult for a fluid to pass through, a geometrical property of the medium which is quantified by the permeability, or the hydraulic conductivity.

Strictly speaking, an unambiguous definition of permeability can only be obtained for a homogeneous and isotropic porous medium and in laminar flow regime, where Darcy's law holds. This empirical law, proposed by Henry Darcy (Darcy 1856) and later refined by Morris Muskat (Muskat 1937), proposes a linear relationship between the specific water flow rate (i.e. flow rate by unit area) and the hydraulic head difference based on measurements of water flow through sand beds. In the context of soil mechanics, where only hydraulic flows are considered, Darcy's law is written in a practical way as follows:

$$q = \frac{Q}{A} = Ki, \tag{1.17}$$

where q is the so-called Darcy's velocity, K is the hydraulic permeability (in m/s), Q is the flow rate through a cross section A, and i is the hydraulic gradient, equal to hydraulic head difference between two points along the flow divided by the distance between these points.

A more general expression of Darcy's law can be written, valid for any fluid, no longer neglecting gravity and depending only on the internal geometry of the porous medium:

$$\vec{q} = -\frac{k}{\eta}(\vec{\nabla}P - \rho_f \vec{g}), \tag{1.18}$$

where k is the geometrical permeability (in m^2) and $\vec{q}$ is the Darcy's velocity vector. The exact relationship between permeability and internal soil geometry is not straightforward, often requiring the use of empirical laws, with the exception of a few simple cases where an analytical expression exists such as the Kozeny-Carman law for disordered packings of spheres of the same size (Bear 1988).

Introducing a characteristic pore size, which is naturally the mean diameter for a granular porous medium, a porous Reynolds number can be calculated and used to determine the porous flow regimes. It was found that Darcy's law is valid for low flow velocity, namely for porous Reynolds numbers below 10.

Beyond this limit, the relationship between the pressure drop and the fluid velocity (i.e. Darcy's velocity) is no longer linear and several empirical laws exist to account for this, such as Forchheimer's laws or Ergün's law (Bear 1988). The latter considers two contributions to the pressure drop ΔP, the first of which, linear with the velocity, is formally identical to Darcy's law. The second contribution is quadratic with Darcy's velocity and accounts for the singular head losses within the medium. The final expression reads:

$$\frac{\Delta P}{L} = \frac{150\eta\phi^2}{d^2(1-\phi)^3}q + \frac{1.75\rho_f(1-\phi)}{d(1-\phi)^3}q^2, \tag{1.19}$$

where ϕ is the solid volume fraction of the porous medium and d is a relevant characteristic particle size.

The linear term of Ergün's law which is dominant at small porous Reynolds numbers

defines the permeability of the porous medium as follows:

$$k_E = \frac{\phi^3 d^2}{150(1-\phi)^2}. \tag{1.20}$$

This expression is very similar to the previously mentioned one by Kozeny-Carman, except the coefficient 150 which is replaced by 180 (Bear 1988).

If the porous flow velocity increases further, temporal fluctuations start to be observed for $Re_p = 80$ to 120, before a fully turbulent regime is finally reached from $Re_p = 300$ to 600 (Hlushkou and Tallarek 2006; Beguin, Philippe, and Faure 2013).

1.2.2.3. Dense granular suspensions

Suspensions of solid particles floating in a liquid are frequently encountered in nature, industry or everyday life. We consider here dense granular suspensions, whose particles are non-Brownian (i.e. not subject to thermal fluctuations) and whose concentration is high enough to ensure many contacts between particles. There are thus two types of interaction acting on the particles: direct contact with other grains and hydrodynamic interaction (Guazzelli and Morris 2012). Note that no physico-chemical interaction between the particles is considered here.

The concentration of the suspended load, quantified through the solid volume fraction ϕ, plays an essential role on the behavior and especially the rheology of the suspension (Guazzelli and Morris 2012). Due to the complexity of the hydrodynamics of suspension, the first studies were based on a simple approach to consider the sedimentation of particles in a dilute suspension for mono-disperse and finally bi-disperse particles. For a diluted suspension of spherical particles, of which $\phi \ll 1$, the sedimentation velocity in Stokes regime ($Re_p \ll 1$) is given by the following theoretical expression due to Batchelor (Batchelor 1972):

$$U_{St,\phi} = U_{St,0}(1 - 6.55\phi) \tag{1.21}$$

where $U_{St,0}$ is the terminal settling velocity of an isolated particle in a liquid, the so-called Stokes velocity given previously in Eq. 1.15, and $U_{St,\phi}$ is the macroscopic settling velocity of a suspension of same liquid and particles with concentration ϕ. Note that the decrease of the global sedimentation velocity is due to the counter flow created by the particles.

Following experimental findings, a generalized empirical formulation for the sedimentation velocity of a concentrated suspension was proposed by Richardson and Zaki (Richardson and Zaki 1954) and reads:

$$U_{s,\phi} = U_{St,0}(1-\phi)^n = U_{St,0}(\epsilon)^n. \tag{1.22}$$

As sketched in Figure 1.17, it was observed that the value of n is approximately limited to 4.8 for the viscous regime and 2.4 for the inertial regime. In-between, n is found to vary depending on the Reynolds number, or equivalently on the Archimedes number

which is defined as:

$$Ar = \frac{(\rho_p - \rho_f) g d^3}{\rho_f \nu^2}. \tag{1.23}$$

For instance, a widely used expression for the exponent n was proposed by Khan and Richardson (Khan and Richardson 1989) as follows:

$$\frac{4.8 - n}{n - 2.4} = 0.043 Ar^{0.57}. \tag{1.24}$$

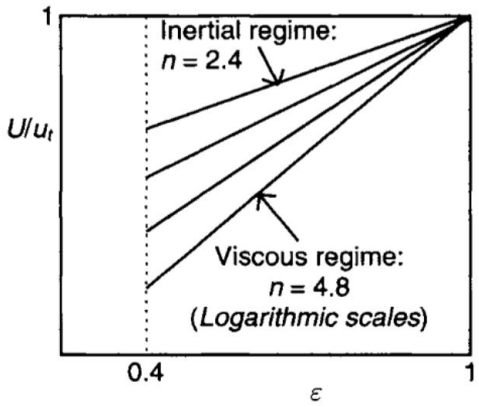

Figure 1.17. – Richardson-Zaki relation. Figure extracted from (A.-D. Gibilaro 2001).

Note that, by switching the reference frame from particles to liquid, it has been proposed to simply invert Richardson's relation to predict the concentration in a fluidized bed, giving good quantitative agreement with the experimental measurements (Garside and Al-Dibouni 1977; Rapagna, Felice, L.-G. Gibilaro, et al. 1989).

1.2.3. Numerical modeling of fluid-grains systems

After having presented the interactions between fluid and grains in concentrated phase, we will now describe how they can be numerically modeled. To this end, we will introduce the discrete modeling of the solid phase in grains, including the case of cemented granular soils, and then we will briefly present the numerical techniques for modeling fluid flows in porous media, with a focus on the LBM method.

1.2.3.1. Modeling of the solid phase by the Discrete Element Method

Presentation The Discrete Element Method (DEM) is a very popular numerical method in terms of granular material modeling, used to compute the motion of solid particles based on Newton's equations via explicit numerical schemes. This numerical method derived from molecular dynamics was first developed by Cundall and Strack (Cundall and Strack 1979). The particles are considered as perfectly rigid

but with a small interpenetration overlap which is used to calculate the interaction forces at contact. The motion of each particle (i.e. position, velocity and acceleration) is obtained by solving Newton's equations for translation and rotation:

$$\vec{F}_i = m_i \frac{d^2 \vec{x}_i}{dt^2} \quad \text{, and} \quad \vec{T}_i = I_i \frac{d\vec{\omega}_i}{dt}, \tag{1.25}$$

where m_i is the mass, I_i the moment of inertia, $\vec{x}_i$ the position vector, and $\vec{\omega}_i$ the angular velocity vector of a particle i. $\vec{F}_i$ and $\vec{T}_i$ are the total force and total torque acting on the particle i. The total force is equal to the sum of the contact force $\vec{F_{ij}}$ applied by grain j on grain i plus the resulting external force $\vec{F_{ext}}$ (for example hydraulic forces if the particle is subjected to hydraulic load, gravity, etc.). Each $\vec{F_{ij}}$ force is decomposed into two components, the normal and tangential forces acting at the contact surface between the two grains (see Figure 1.18). Hence, $\vec{F_{ij}}$ can be written as follows:

$$\vec{F_{ij}} = F_n \vec{n} + F_t \vec{t}, \tag{1.26}$$

where $\vec{n}$ and $\vec{t}$ are the normal and tangential unit vectors at the contact between the two particles.

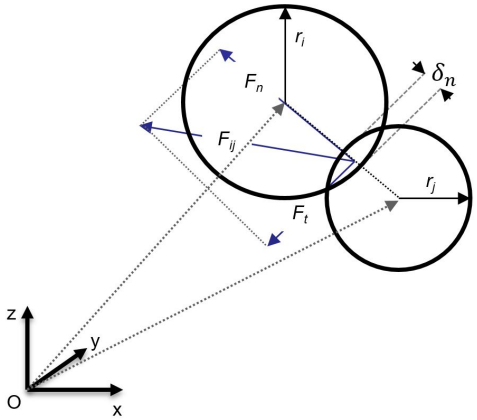

Figure 1.18. – Overlapping of two particles.

The normal overlap δ_n is equal to the distance between the two centers minus the two radii of the two particles:

$$\delta_n = \|\vec{x}_i - \vec{x}_j\| - r_i - r_j. \tag{1.27}$$

Frictional contact law The normal and tangential forces at the contact are often calculated based on a visco-elastic linear model. The normal force equation is written below:

$$f_n = -k_n \delta_n - \gamma_n v_n \quad , \quad F_n = \begin{cases} 0 & \text{for} \quad f_n \leq 0 \\ f_n & \text{for} \quad f_n > 0. \end{cases} \tag{1.28}$$

where k_n is the normal contact stiffness and v_n is the relative velocity in the normal direction between the two particles, i.e. $v_n = \|\vec{v}_i - \vec{v}_j\|$. γ_n is the normal viscous

damping to impose energy dissipation.

The tangential force is limited by Coulomb's friction criterion, namely $|F_t| \leq \mu_s F_n$, and thus reads:

$$f_t = -k_t \delta_t - \gamma_t \frac{d\delta_t}{dt} \quad , \quad F_t = \begin{cases} f_t & \text{for} \quad |f_t| < \mu F_n \\ sgn(F_t)\mu F_n & \text{for} \quad |f_t| \geq \mu F_n, \end{cases} \tag{1.29}$$

where k_t is the tangential contact stiffness, μ_s is the coefficient of friction, γ_t is the tangential viscous damping, and δ_t is the cumulative shear displacement which is integrated over time from the following equation (Zhou, Wright, Yang, et al. 1999):

$$\frac{d\delta_t}{dt} = v_t = (\vec{v}_i - \vec{v}_j).\vec{t} - (r_i\omega_i + r_j\omega_j). \tag{1.30}$$

A rolling resistance can be introduced to take into account the energy dissipation during relative rotation (Ai, J.-F. Chen, Rotter, et al. 2011). The rolling resistance can be introduced according to (Zhou, Wright, Yang, et al. 1999) as follows:

$$T_{roll} = -\frac{\omega_r}{|\omega_r|}\mu_r R_{eff} f_n, \tag{1.31}$$

With $\omega_r = \omega_i - \omega_j$ the rolling velocity equal to the difference between the two angular velocities, R_{eff} the corrected radius equal to $r_i r_j/(r_i + r_j)$, and μ_r the rolling coefficient.

Extension to cemented soil On the modeling side, several micro-mechanical contact laws exist for bonded grains, including yield conditions of bond rupture (in stress, force, or energy) derived from adhesion theory for elastic solids (Kendall 1971; Chung and Chaudhury 2005) or calibrated from experimental results in 2D (J.-Y. Delenne, El Youssoufi, Cherblanc, et al. 2004; M.-J. Jiang, J. Liu, Sun, et al. 2013) or 3D (Kirsch, Bröckel, Brendel, et al. 2011). These bonded contact laws provide the convenient possibility of direct implementation in numerical calculations based on the Discrete Element Method approach (Potyondy and Cundall 2004; Ergenzinger, Seifried, and Eberhard 2011; Brendel, Török, Kirsch, et al. 2011; M.-J. Jiang, H.-S. Yu, and Harris 2006; M.-J. Jiang, Yan, H.-H. Zhu, et al. 2011; Yamaguchi, Biswas, Hatano, et al. 2020; Horabik and Jozefaciuk 2021) to model the soil's behaviour at a representative scale.

For instance, Yamaguchi and co-authors have proposed a model based on energy considerations and designed around the Griffith failure criteria for fracture as bond rupture occurs when the internal elastic energy stored in the bonds exceeds the peeling energy (Yamaguchi, Biswas, Hatano, et al. 2020). An auto-adhesive contact law was developed by Thornton and co-authors (Thornton 1991; Thornton and Ning 1998), based on the JKR theory of soft adhesion of elastic spheres (Johnson, Kendall, and Roberts 1971; Chung and Chaudhury 2005) and parameterized by a single dimensionless parameter K.

Several models propose a mechanical description of a solid bond, considered as an

elastic body with typically a cylindrical shape (illustrated in Figure 1.19). These include the Bonded Particles Model (BPM) in 2D or 3D versions (Potyondy and Cundall 2004; Ergenzinger, Seifried, and Eberhard 2011; Horabik and Jozefaciuk 2021) or a rather similar model based on Tresca failure criterion with bonds represented by thin discs (Brendel, Török, Kirsch, et al. 2011).

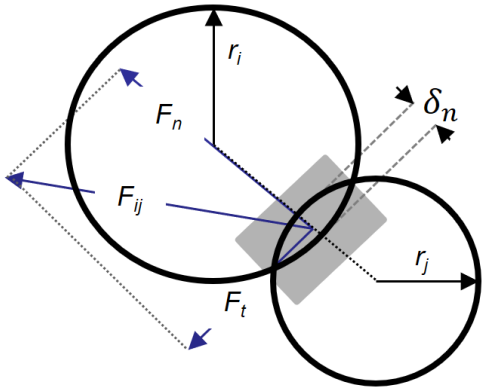

Figure 1.19. – Solid bond between two particles. Figure redrawn from (Potyondy and Cundall 2004).

When solely considering bond failure model from the applied contact forces, the simplest approach is to consider only the contact normal force and introduce a yield traction force. For example, Tran and co-authors have proposed the bond failure envelope presented in Figure 1.20, characterized by tensile and shear thresholds and given by (Tran, Prime, Froiio, et al. 2017):

$$F_n > -A \quad \text{and} \quad |F_t| < \mu F_n + C, \tag{1.32}$$

where A is the contact adhesion force and C is the contact cohesion force (C is greater than μA with μ the friction coefficient). A quite similar model was proposed earlier introducing normal and tangential bond strength additionally to friction as residual shear strength after bond breakage (M. Jiang, H.-S. Yu, and Leroueil 2007).

From experimental results, Jiang and co-authors also developed a bond failure criterion based on tension and shear force which reads (M.-J. Jiang, J. Liu, Sun, et al. 2013):

$$\left(\frac{F_t}{R_s}\right)^5 - \left(\frac{F_n}{R_t}\right) = 1, \tag{1.33}$$

where R_t and R_s are the yield force values in tension (normal) and shear (tangential), respectively.

Another model that we will examine in more detail here is the one proposed by Delenne and co-authors (J.-Y. Delenne, El Youssoufi, Cherblanc, et al. 2004). As already mentioned in section 1.2.1.3, this two-dimensional bond model introduces a

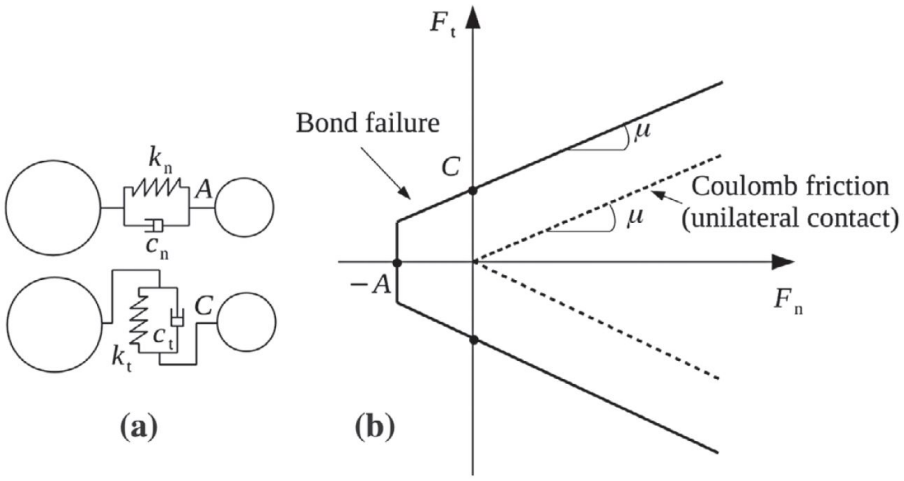

Figure 1.20. – DEM model used by Tran, Prime, Froiio, et al. 2017. (a) Rheological bond model; (b) Bond failure criterion. Extracted from Tran, Prime, Froiio, et al. 2017.

failure surface criterion complementing a visco-elastic rheology with three degrees of freedom: normal translation δ_n, tangential translation δ_t, and rotation γ, as sketched in Figure 1.21. It takes into consideration the combination of all types of loading acting on the bond at the same time: tension, compression (no more considered in the following as no bond rupture is observed in compression), shear, and bending. The normal translation δ_n is the one seen before in equation 1.27 while the two other degrees of freedom are defined as follows:

$$\delta_t = I_i\vec{I}_j.\vec{t}\gamma = \alpha_i - \alpha_j. \tag{1.34}$$

These forces are calculated only for small displacements and rotation via a linear elastic rheology, where the tensile, shear force and bending are associated by normal, shear and moment stiffness as presented below:

$$\begin{pmatrix} F_n \\ F_t \\ M_b \end{pmatrix} = \begin{pmatrix} k_{nb} & 0 & 0 \\ 0 & k_{tb} & 0 \\ 0 & 0 & k_\gamma \end{pmatrix} \begin{pmatrix} \delta_n \\ \delta_t \\ \gamma \end{pmatrix}$$

As sketched in Figure 1.22, the failure criterion is defined by the following equation:

$$\zeta = \left(\frac{F_n}{{F_n}^{rupt}}\right) + \left(\frac{F_t}{{F_t}^{rupt}}\right)^2 + \left(\frac{M_b}{{M_b}^{rupt}}\right)^2 - 1, \tag{1.35}$$

where ${F_n}^{\text{rupt}}$, ${F_t}^{\text{rupt}}$ and ${M_b}^{\text{rupt}}$ are the maximum experimental yield load in pure tensile, shear and bending conditions, respectively. The failure of the bond is obtained for $\zeta \geq 0$.

This model appears rather complete from a mechanical point of view and, in the

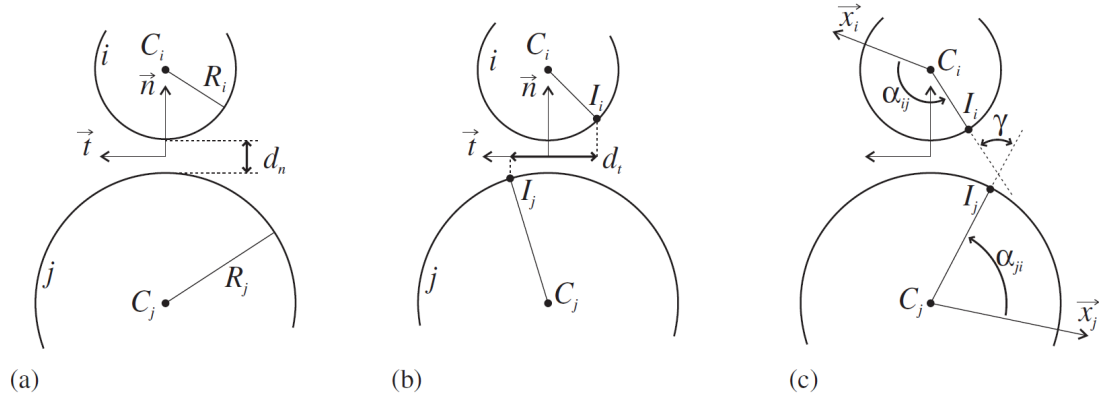

Figure 1.21. – Degree of freedom of the cohesive solid bond at the local scale: (a) Normal displacement, (b) Tangential displacement, (c) Rotation angle. Figure extracted from (J.-Y. Delenne, El Youssoufi, Cherblanc, et al. 2004).

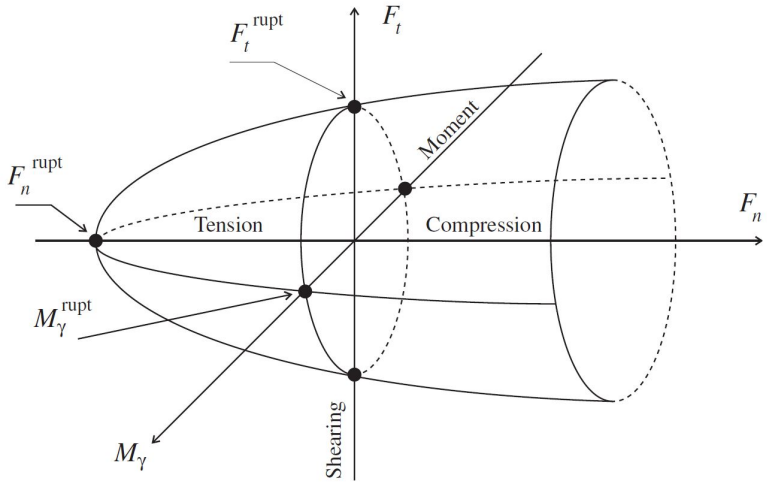

Figure 1.22. – Surface failure criterion. Figure extracted from (J.-Y. Delenne, El Youssoufi, Cherblanc, et al. 2004).

context of soil erosion, some preliminary studies have shown that interestingly it is able to produce a large variety of material behaviour from brittle damage to diffusive debonding (Philippe, Cuéllar, Brunier-Coulin, et al. 2017). For simplicity, the aspect ratios of the yield surface may be fixed to constant proportions, for instance in dependence of a single parameter C (Benseghier, Cuéllar, Luu, Bonelli, et al. 2020):

$$C = F_n^{rupt} = 2F_t^{rupt} = \frac{4}{d}M_b^{rupt}, \tag{1.36}$$

where C quantifies the cementation force of the bonded granular medium.

Finally, as with all bond models, it can also be enriched with a bond damage model

as developed by Benseghier and co-authors (Benseghier, Cuéllar, Luu, Bonelli, et al. 2020), where an additional homothetic envelope defines a damage zone where a progressive damage occurs and continuously degrades the yield value of the failure envelope.

Note that there are other studies where damage is considered, for instance the one including a progressive failure model for the adhesive bonds in the BPM approach in Christian et al. (Ergenzinger, Seifried, and Eberhard 2011).

1.2.3.2. Modeling of fluid phase by Computational Fluid Dynamics

The different existing approaches This section is devoted to the different numerical models used to simulate a fluid flow in a granular medium, possibly cemented, the challenge of such computations being to describe the coupled fluid-solid interactions accurately. Two strategies can be applied for this: Either to implement the discrete grain modeling presented in the previous section 1.2.3.1 by fully resolving the fluid flow at the grain scale, or to integrate the interactions between phases within a continuous model with mesoscopic laws, empirical or semi-empirical, governing exchanges between solid and fluid phase.

In brief, the latter continuum approach can be divided into three different types of models: monophasic, biphasic, and tri-phasic. The monophasic model solves the Navier-Stokes equations to model the fluid flow alone, a Lagrangian boundary being considered for the fluid particle interface (Mercier, Bonelli, Philippe, et al. 2014). The bi-phasic approach consists of two distinct phases, one to model the fluid with resolution of the Navier-Stokes equations, and another one for the solid phase with an adapted constitutive law, and an additional momentum contribution accounting for the interaction between the two phases, commonly a porous flow type relation as Darcy's law or Darcy-Brinkman's law (Lachouette, Golay, and Bonelli 2008). In the tri-phasic approach, an extra fluidized solid phase is considered to model directly the solid-fluid interaction, with a dedicated flux exchange law between solid static and solid fluidized phases (Vardoulakis, Stavropoulou, and Papanastasiou 1996).

Here, we are interested more in the second multi-scale approach, combining the Discrete Element Method by solving Newton's second law for grains motion and a continuous modeling of the fluid phase dynamics (T. Wang, F. Zhang, Furtney, et al. 2022), for which the main theoretical frameworks include the models based on the Navier-Stokes equations (CFD), the ones based on pore networks (PNM) as the Pore-scale Finite volume (PFV), and those in strong development based on the Boltzmann equation (LBM). Each of these models has advantages and drawbacks.

The CFD-DEM is a computational approach to modeling fluid particle systems, where the fluid flow is computed by solving the Navier-Stokes equation at a mesoscopic scale. It consists of discretizing the fluid zone into cells larger than the particle size, where several particles are held in one cell. Regarding the fluid, the porosity and drag force terms must be added through empirical relations (Di-Felice 1994; T. Wang, F. Zhang, Furtney, et al. 2022) while, in each mesoscopic cell, the solid particles are subjected to a mean flow with a constant drag force at this scale. This method is

computationally efficient but fails to model behaviors at particle scale and compact granular structures.

The PFV-DEM is a computational approach for the simulations of hydro-mechanical couplings. It is a method developed 10 years ago, which links the Discrete Element Method to a pore-scale finite volume (Tong, Catalano, and Chareyre 2012; Catalano, Chareyre, and Barthélémy 2013; Catalano, Chareyre, and Barthélemy 2014). The pore domain is discretized into a connected pore network, i.e. regular triangulation, and its dual Voronoi graph as seen in Figure 1.23. The pore volume is decomposed into tetrahedra (in 3D). The Navier-Stokes equations are integrated at the scale of each pore in which the pressure field is defined by the border pressure values on the Voronoi graph (Catalano, Chareyre, and Barthélemy 2014). Despite the advantage of a very low computational time, this method loses accuracy whenever large pores exist in the system and it is limited to simulate internal Stokes fluid flow within a compacted granular material.

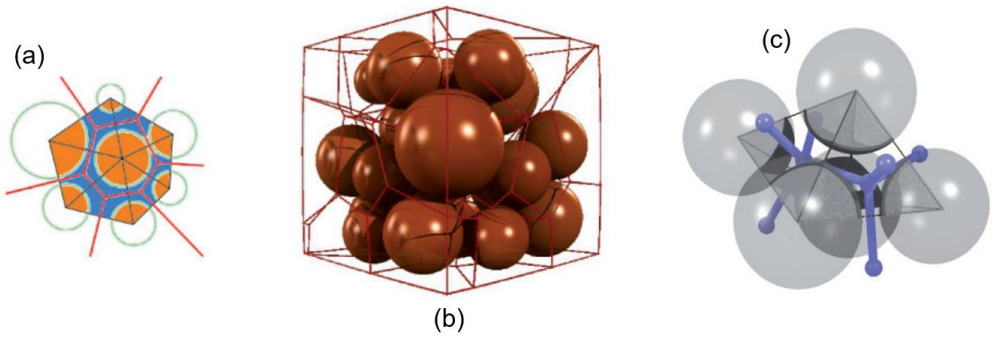

Figure 1.23. – PFV geometrical scheme: (a) Voronoi graph in 2D, (b) Voronoi graph in 3D and (c) 3D view of a pore and its connection. Figures extracted from (Tong, Catalano, and Chareyre 2012; Catalano, Chareyre, and Barthélémy 2013).

Before presenting in more detail the LBM method that will be used in this work, we can mention other more marginal methods to couple DEM with a fluid approach (T. Wang, F. Zhang, Furtney, et al. 2022): DNS (Direct Numerical Simulation) at sub-particular scale which is very accurate but far expensive in computational time and subject to huge mesh distortion for substantial particle motion, SPH (Smooth Particle Hydrodynamics) using a Lagrangian representation of the fluid (Potapov, Hunt, and Campbell 2001), or DFM (Dynamic Fluid Mesh) where the fluid mesh follows to deformation of the soil skeleton formed by the coarse particles.

Focus on the Lattice Boltzmann Method The Lattice Boltzmann Method is one of the most commonly used CFD methods for simulating fluid-solid coupling problems. Unlike the CFD model which depends on solving the Navier-Stokes equation for fluid, the LBM consists in solving a discretized version of the Boltzmann equation to simulate the fluid phase/behaviour which describes the statistical behaviour of

a thermodynamic system as a gas. The Boltzmann equation excluding the external forces is written as follows:

$$\frac{\partial f}{\partial t} + \vec{c}.\nabla_x f = \Omega(f), \tag{1.37}$$

where $f = f(x, \vec{c}, t)$ is the particle distribution function at time t, position x, velocity $\vec{c}$, and $\Omega(f)$ is the so-called collision operator.

The collision operator represents the relaxation of the particles towards an equilibrium state with a dependency on one or more relaxation times. The simplest collision model is the so-called Bhatnagar-Gross-Krook (BGK) model, based on a single relaxation time τ_0 for all hydrodynamic moments towards the thermodynamic equilibrium given by the Maxwell-Boltzmann distribution function f^{eq} (Benseghier, Cuéllar, Luu, Bonelli, et al. 2020). It reads:

$$\Omega(f) = -\frac{1}{\tau_0}(f - f^{eq}). \tag{1.38}$$

It has been proved that the incompressible Navier-Stokes equation can be recovered at small Mach numbers [2] from the Chapman-Enskog expansion (Chapman and Cowling 1970).

In the LBM, the fluid domain is discretized into a regular static grid where discrete populations of fluid particles propagate and collide. The lattice structure is composed of the space dimension d and the velocity directions q, denoted as DdQq models (Qian, d'Humières, and Lallemand 1992). The example of the D2Q9 model is shown in Figure 1.24.

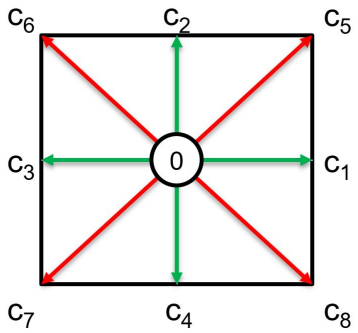

Figure 1.24. – 2D lattice model: D2Q9.

The Boltzmann equation (Eq. 1.39) is difficult to discretize numerically since a triple discretization is required for the particle distribution function f (i.e. in space, velocity, and time). As a result, some constraints are required. The velocity space c is first discretized into a limited collection of velocities c_i (in a direction i). As a result, by inserting a weight parameter ω_i linked with the velocity c_i, the discrete-velocity

2. Mach number is a dimensionless quantity representing the ratio between the maximum velocity in the system and the sound velocity c_s in LBM

distribution function may be constructed from the distribution function (Benseghier, Cuéllar, Luu, S. Delenne J.-Y. B., et al. 2020).

This LBM equation is solved in two main steps: Collision and streaming.

The collision step equation reads:

$$f_i^{out}(x + c_i\Delta t, t + \Delta t) = f_i(x, t) + \Omega_i(x, t), \tag{1.39}$$

where $\Omega_i(x, t)$ is the discretized form of the collision operator.

The streaming step equation, as depicted in Figure 1.25 for D2Q9 scheme, is given below:

$$f_i(x + c_i\Delta t, t + \Delta t) = f_i^{out}(x, t). \tag{1.40}$$

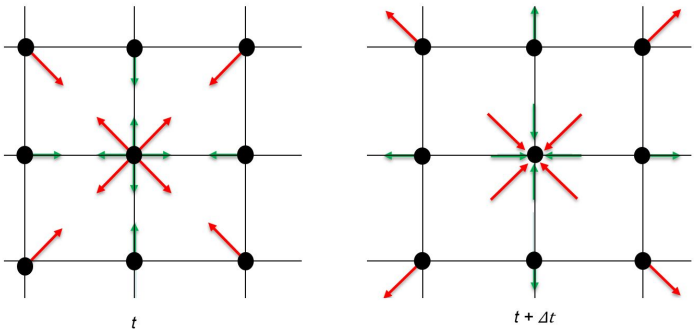

Figure 1.25. – Streaming step.

Several models exist for the collision operator such as the BGK model, which depends on a single relaxation time τ_0, another model with two relaxation times (TRT), and a third model where multiple relaxation times (MRT) are considered. For instance, the discretized BGK collision operator reads:

$$\Omega_i^{BGK}(f) = -\frac{1}{\tau}(f_i(x, t) - f_i eq(x, t)), \tag{1.41}$$

where $\tau = \tau_0/\Delta t$ and f_i^{eq} is the Maxwell-Boltzmann distribution function at equilibrium given by:

$$f_i^{eq}(\rho, u) = \rho\omega_i\left(1 + \frac{u.c_i}{c_s^2} + \frac{(u.c_i)^2}{2c_s^4} + \frac{u.u}{2c_s^2}\right), \tag{1.42}$$

with c_s the speed of sound in the lattice system ($c_s = c/\sqrt{3}$), c the lattice speed ($c = \frac{dx}{dt}$), and u the fluid velocity.

The density ρ_f of the fluid and its velocity u are calculated from the distribution function:

$$\rho_f = \sum_i f_i, \tag{1.43}$$

$$u = \frac{1}{\rho}\sum_i f_i c_i. \tag{1.44}$$

The relation between the relaxation time τ and the kinematic viscosity is as follows:

$$\tau = \frac{\nu}{\Delta t {c_s}^2} + \frac{1}{2}. \tag{1.45}$$

The fluid pressure is given by the following equation in terms of c_s and ρ_f:

$$p = \rho_f c_s^2. \tag{1.46}$$

We end this section by presenting the MRT model that will be used in this work. The MRT model represents the moments n of the distribution functions that can be relaxed with different relaxation times. In contrast to the BGK model presented previously, the collision step is carried out in the moment space. An invertible transformation matrix M links the distribution function vector f to their moment vector n, given by $n = Mf$. The equation in the D2Q9 scheme is presented below (Lallemand and Luo 2000):

$$\begin{pmatrix} \rho_f \\ e \\ \epsilon \\ j_x \\ q_x \\ j_y \\ q_y \\ P_{xx} \\ P_{xy} \end{pmatrix} = \begin{pmatrix} 1 & 1 & 1 & 1 & 1 & 1 & 1 & 1 & 1 \\ -4 & -1 & -1 & -1 & -1 & 2 & 2 & 2 & 2 \\ 4 & -2 & -2 & -2 & -2 & 1 & 1 & 1 & 1 \\ 0 & 1 & 0 & -1 & 0 & 1 & -1 & -1 & 1 \\ 0 & -2 & 0 & 2 & 0 & 1 & -1 & -1 & 1 \\ 0 & 0 & 1 & 0 & -1 & 1 & 1 & -1 & -1 \\ 0 & 0 & -2 & 0 & 2 & 1 & 1 & -1 & -1 \\ 0 & 1 & -1 & 1 & -1 & 0 & 0 & 0 & 0 \\ 0 & 0 & 0 & 0 & 0 & 1 & -1 & 1 & -1 \end{pmatrix} \begin{pmatrix} f_0 \\ f_1 \\ f_2 \\ f_3 \\ f_4 \\ f_5 \\ f_6 \\ f_7 \\ f_8 \end{pmatrix}$$

where ρ_f is the fluid density, e is the energy, ϵ is related to energy square, j_x and j_y are the momentum in x and y directions (i.e. $j_i = \rho_f u_i$), P_{xx} and P_{yy} are the diagonal and off-diagonal components of the stress tensor, q_x and q_y are the energy flux in x and y components.

The multi relaxation time lattice Boltzmann equation is given below:

$$f_i(c + c_i\Delta t, t + \Delta t) = f_i(x,t) - M^{-1}S\left[m_i(x,t) - m_i^{eq}(x,t)\right], \tag{1.47}$$

where S is a diagonal relaxation matrix.

1.2.4. Coupling DEM-LBM

As presented, the LBM divides the domain into a static grid, where all the nodes are regarded as fluid. To couple the DEM and LBM methods, we need to introduce the particle shapes to the LBM. This can raise several questions. How does the LBM deal with these shapes in static and in motion? How to couple LBM with the DEM? On this basis, several methods have been proposed such as the momentum exchange scheme due

to Bouzidi (Bouzidi, Firdaouss, and Lallemand 2001) or the Partial Saturation Method (PSM) to apply a non-slip boundary condition at the surface of an arbitrarily shaped particle with or without motion. They both proposed a solid domain implemented in the fluid domain by changing the state of the lattice node, i.e. to impose a solid node when occupied by a particle and a fluid node if not. Imposing the non-slip condition at the boundary nodes of a particle provides a momentum-exchange algorithm between the two phases (Benseghier, Cuéllar, Luu, Bonelli, et al. 2020), as sketched in Figure 1.26.

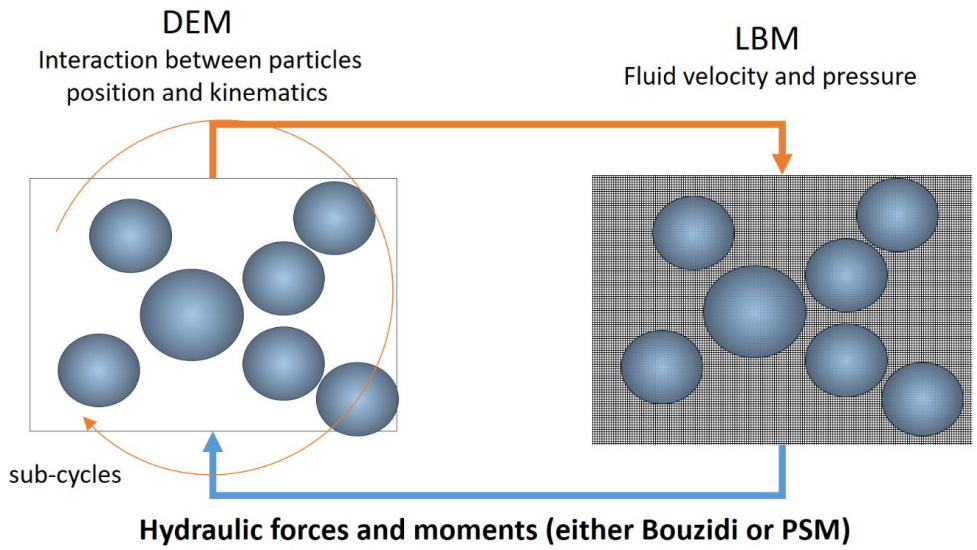

Figure 1.26. – DEM-LBM coupling

The space discretization of the LBM is usually based on the minimum diameter of the particles of the DEM, where the particle resolution is equal to $d_{min}/\Delta x$. This space resolution should be high enough to resolve the fluid flow around the particle with sufficient accuracy. It is usually recommended to use $d_{min}/\Delta x \geq 10$, where this ratio sets the discretization parameter Δx (D. Yu, Mei, Luo, et al. 2003).

Once the lattice speed is chosen and fixed, another important condition for modeling an incompressible fluid with Navier-Stokes equation is that the Mach number, which is equal to the maximum fluid velocity divided by the lattice speed c, remains small enough, usually less than 0.1.

For 2D simulations, the particles are often represented by circular particles. For a densely packed granular sample, the 2D particles in contact leave no open fluid path between them, preventing the fluid from passing through out the pores. This issue is often solved by introducing a slightly smaller hydraulic radius r_h for the grains in the LBM calculations but keeping the real radius value for the DEM calculations. The typical ratio r_h/r is usually fixed at 0.8 (Boutt, Cook, McPherson, et al. 2007; Cui, Li, Chan, et al. 2012).

Finally, it is possible to employ two different time steps in the DEM-LBM. Usually, the necessary DEM time step Δt_{DEM} is smaller than the LBM one Δt_{LBM} and the

concept of combined sub-cycles for the DEM was proposed (K. Han, Y.-T. Feng, and Owen 2007). In other words, we can perform several DEM sub-cycles during a given LBM cycle. The number n_p of DEM sub-cycles is fixed by the integer part of the ratio between the elementary DEM and LBM time steps. The value adopted for the simulations used in this work is $n_p = 2$.

1.3. Hydro-mechanical instability in granular or cemented granular material.

Instabilities induced in a granular soil by a hydraulic load is a broad topic that has motivated a large number of studies. In this last section, we restrict ourselves to our configuration of interest where a liquid flow is injected in a localized manner at the boundary of a granular soil layer in order to destabilize the material and set the particles in motion. A distinction will be made between experimental and numerical work, and between purely granular and cohesive or cemented soils. In the literature, there seems to be recent experimental works only regarding granular soils (Zoueshtiagh and Merlen 2007; Philippe and Badiane 2013; Mena, Luu, Cuéllar, et al. 2017; Mena, Brunier-Coulin, Curtis, et al. 2018), except one very limited study with bonded grains (Luu, Noury, Benseghier, et al. 2019), while some numerical simulations focused on either granular (Ngoma, Philippe, Bonelli, Radjaı, et al. 2018) or cemented soils (Cui 2013; Cui, Li, Chan, et al. 2012; Tran, Prime, Froiio, et al. 2017). In all these articles, a single localized inlet fluid injection or aspiration is imposed, apart from few preliminary studies where two localized inlets are used (Philippe and Badiane 2013; Ngoma, Philippe, Bonelli, J.-Y. Delenne, et al. 2014) and which will not be discussed here.

1.3.1. Previous experiments

Following an earlier study by Zoueshtiagh and co-authors (Zoueshtiagh and Merlen 2007), Philippe and Badiane conducted a thorough work on granular localized fluidization with an original device that allows the visualization inside the granular sample using combined optical techniques: Refractive Index Matching (RIM) between the liquid used and the particles and Planar Laser-Induced Fluorescence (PLIF), where a specific illumination inside a plane is obtained by means of fluorescent dye added to the liquid and re-emission of light from the plane of a laser sheet beam (Philippe and Badiane 2013). Figure 1.27 shows the experimental device applied, where a cell box is used with different inlet nozzles positions (A, B and C) and with different inlet diameters that can be chosen (6 mm or 14 mm). These three nozzles are connected to a gear pump to apply a constant flow rate over time, and the atmospheric pressure is only applied at the outlet surface of the cell. In their experiments, they used spherical glass beads with different particle diameters.

Three different fluidization regimes were observed: Static, when the bed behaves as a porous media at low flow rate; Fluidized cavity regime when grains fluidization is restricted to a cavity at the inlet ; Fluidized chimney regime, when the fluidized zone

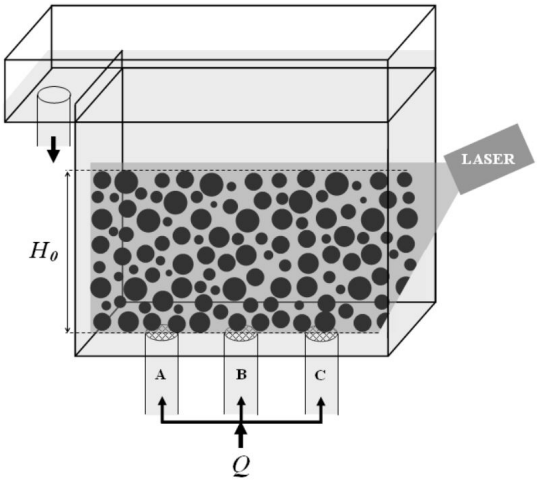

Figure 1.27. – Experimental device used by Philippe and Badiane (Philippe and Badiane 2013).

reaches the top surface of the layer. This study has confirmed the presence of the fluidized cavity after the dilation of the surface bed which was previously only speculated (Zoueshtiagh and Merlen 2007). Both studies showed that the fluidization threshold is independent of the injection diameter and the flow rate at the frontier between cavity and chimney regimes is found to vary approximately linear with the height of the sample. Additionally, a new hysteresis effect in the cavity regime was highlighted as presented in Figure 1.28: the flow rate determining the limit between static and cavity regimes has two very different values between an initial flow increase phase (fluidization threshold) and a reduction to zero phase (defluidization threshold). The cavity regime would exist at lower flow rate values than the one for prior fluidization Q_{cav} of the granular medium until a certain limit Q_{col} where the remaining cavity ultimately collapse.

The study of the steady fluidization regimes was completed by a systematic experimental campaign by changing the diameter of the particles, the nozzle diameter and the height of the granular layer (Mena, Luu, Cuéllar, et al. 2017). In particular, the dependency between critical chimney flow rate and sample height was found no more linear for thicker layers and a saturation was finally obtained. Starting from a previous theoretical model that predicted the linear behavior (Zoueshtiagh and Merlen 2007; Philippe and Badiane 2013), an extension was proposed to describe this saturation effect related to the lateral widening of the flow in the porous bed, as shown by the gathering of the data set in Figure 1.29 when the dimensionless velocity, which compares the critical uniform fluidization velocity to inlet velocity, is plotted versus sample height.

This analysis also showed that the critical condition for fluidization initiation was controlled by the Archimedes number Ar whose definition is given in Eq. 1.23. More precisely and as shown in Figure 1.30, provided that the uniform Reynolds number is replaced by a local particle Reynolds number within the fluidized chimney, the usual

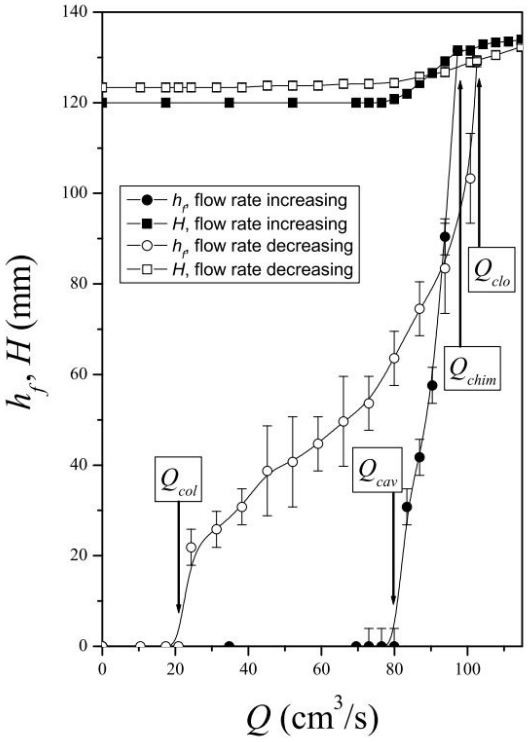

Figure 1.28. – The height of the fluidized zone h_f (circle symbols) and the total height H (square symbols) of the layer, in vertical alignment with the injection hole for a 5 mm bead layer of initial height 120 mm and with an injection hole of 14 mm. Extracted from Philippe and Badiane 2013.

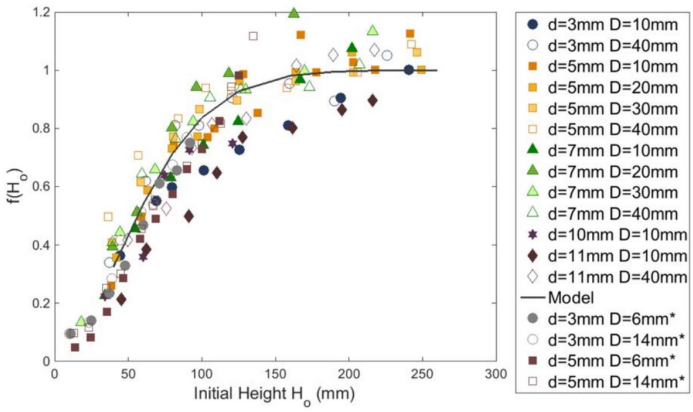

Figure 1.29. – Dimensionless velocity function versus initial bed height. Figure extracted from (Mena, Luu, Cuéllar, et al. 2017).

relation between the Archimedes and Reynolds numbers for uniform fluidization is recovered. Using the Kozeny-Carman expression of permeability (Bear 1988) with the

Darcy's law, this expression reads:

$$Ar = \frac{180\phi}{(1-\phi)^3} Re. \tag{1.48}$$

with ϕ the solid volume fraction of the granular sample, about 0.61 in these experiments. For higher Re numbers, Ergün's law can be preferentially used, simply meaning that the coefficient $(1 + \alpha Re)$ is added in the right term of the previous equation, with $\alpha \approx 0.02$.

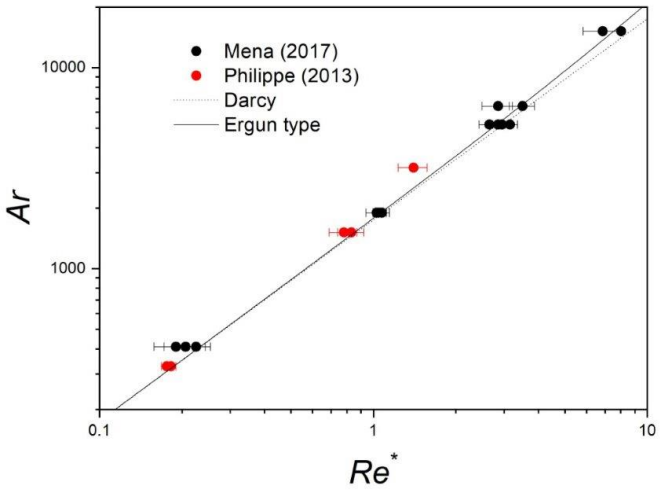

Figure 1.30. – Experimental relation between Archimedes number and local Reynolds number compared to the Darcy and Ergün's laws. Figure extracted from (Mena, Luu, Cuéllar, et al. 2017).

Finally, a complementary study on the transient regime of localized fluidization allowed to highlight the existence of two expansion regimes from cavity to chimney with far distinct kinetics (Mena, Brunier-Coulin, Curtis, et al. 2018).

Several other slightly different experiments can be ultimately cited, in variant configurations where the fluidized zone develops along a transparent wall allowing direct visualisation and possibly quantitative recording of the velocity of the moving grains by Particle Image Velocimetry (Alsaydalani and Clayton 2014; Y. He, D.-Z. Zhu, T. Zhang, et al. 2017; H.-E. Schulz, Zyl, T. Yu, et al. 2021; Akrami, Bezuijen, Tehrani, et al. 2022). However, these configurations are significantly affected by geometrical confinement and solid friction imposed by the presence of the side wall.

1.3.2. Previous numerical simulations

Case of a frictional material Cui and co-authors have modeled the effect of a localized inlet flow on both a granular and a cohesive granular layer using the

DEM-LBM coupling (Cui, Li, Chan, et al. 2012; Cui 2013). A 2D LES-LBM (LBM with the Smagorinsky turbulence model) model was used for the fluid phase (Cui, Li, Chan, et al. 2012; Cui 2013; Li 2013; Owen, Leonardi, and Y.-T. Feng 2011; Z.-G. Feng and Michaelides 2004; Y.-T. Feng, K. Han, and Owen 2007; Succi 2001). In the DEM approach, the auto-adhesive contact model by Thornton and co-authors was implemented (Thornton 1991; Thornton and Ning 1998), where the inter-particle force of adhesion is controlled by a single dimensionless parameter K. In this section we will only present the results obtained without adhesion, for $K = 0$.

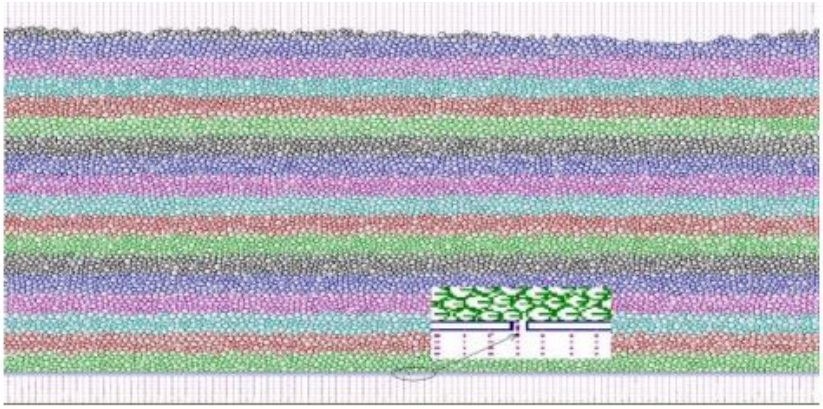

Figure 1.31. – 2D numerical model implemented to study the localized fluidization. Extracted from Cui 2013.

Figure 1.31 presents the 2D numerical model implemented to study the localized fluidization with a detailed view of the inlet. It is composed of 9997 circular discs with a poly-disperse distribution of the diameter (3, 4, 5 and 6 mm). The inlet nozzle of 3 mm is situated at the center of the bottom base, where a constant flow rate is imposed. The range of the flow rate was chosen between 0.25 to 6 l/s and was kept constant until the end of the duration of the simulation (t =20 s). In this study, either purely frictional grains or bonded grains were modeled, according to a dimensionless adhesive parameter K. For a frictional sample (i.e. $K = 0$), the same types of fluidization regimes as in the experiments were observed (Cui 2013; Cui, Li, Chan, et al. 2012): static, cavity, and chimney regime. An illustration is presented in Figure 1.32a while the other cases will be discussed in the next section.

Additionally, an analysis of the cavity volume expansion versus time and pressure profile at different heights versus the inlet flow rate has been carried out as shown in Figure 1.33.

More precisely, Figure 1.33 shows the variation of the excess pore pressure versus the inlet nozzle flow rate comparing the previous experimental data (Alsaydalani and Clayton 2014) (Fig. 1.33a) and the present numerical results (Fig. 1.33b). The numerical simulations are qualitatively in agreement with the experimental results, although the orders of magnitude are not the same. For the orifice, it is seen that the pressure builds up until it reaches a maximum value, then it drops, indicating that fluidization has occurred since the unlocking of the particles releases the pressure

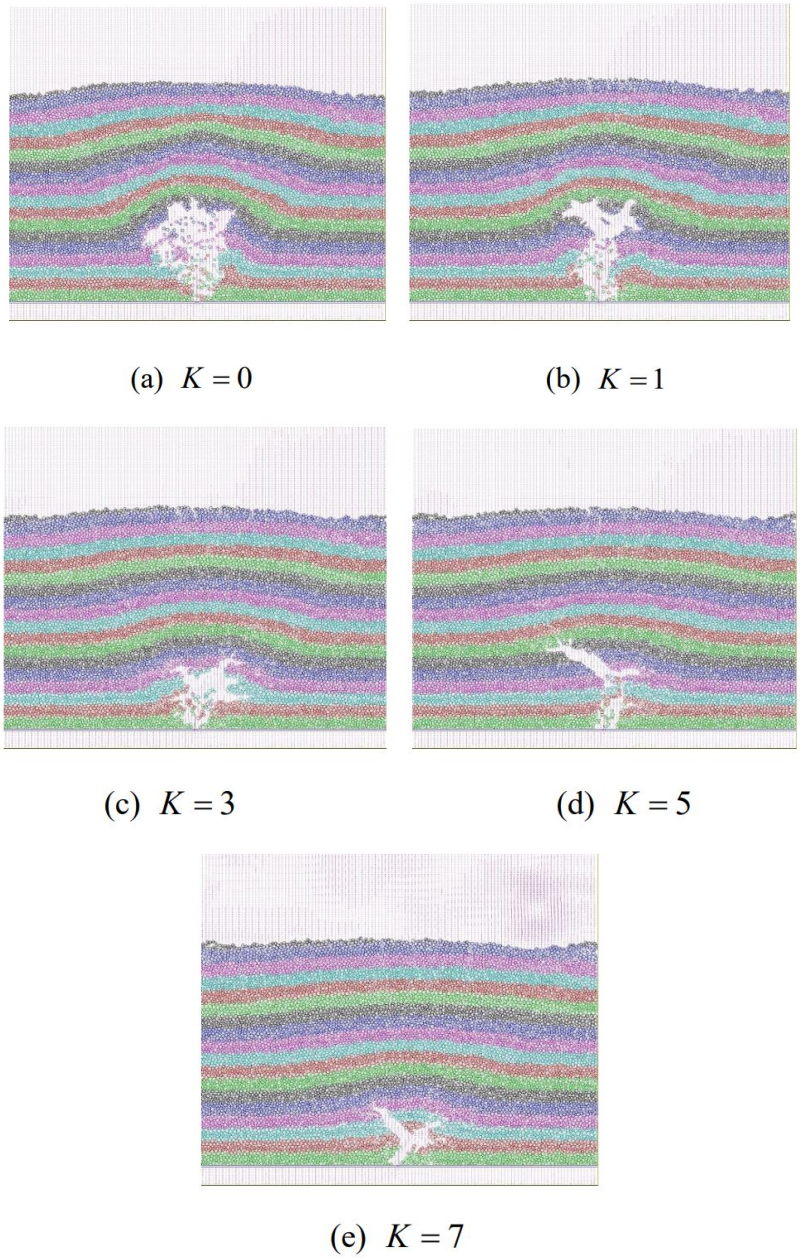

Figure 1.32. – Fluidization of an adhesive granular medium. Figure extracted from (Cui 2013).

and the hydraulic resistance is much lower, although the inlet flow rate continues to increase. It was also observed that the pressure builds up slowly as the distance from the orifice increases, and a slight pressure drop may be seen due to the occurrence of the fluidization phenomena.

Ngoma and co-authors have also modeled the localized fluidization of a granular medium using a 2D DEM-LBM coupling model (Ngoma, Philippe, Bonelli, Radjaı, et al. 2018). This model, whose general approach was already well detailed in section 1.2.3,

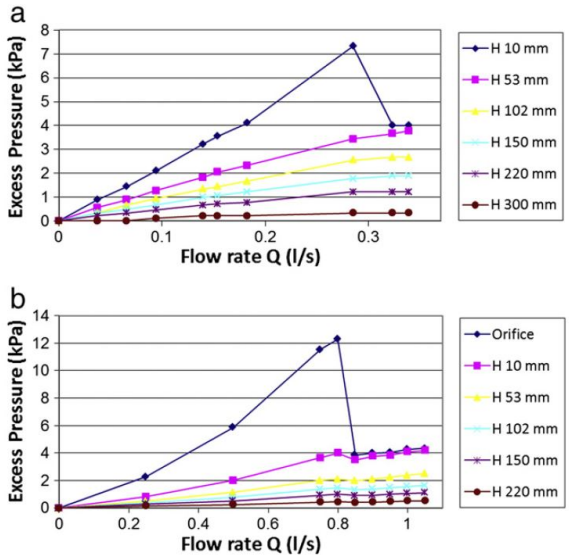

Figure 1.33. – Fluid pressure at different heights from the orifice (inlet nozzle): (a) Experimental data from Alsaydalani and Clayton 2014, (b) numerical results of Cui, Li, Chan, et al. 2014. Extracted from Cui, Li, Chan, et al. 2014; Alsaydalani and Clayton 2014.

imposed a non-slip boundary condition to the east and west walls, with a periodic boundary condition for the south boundary, and a localized inlet flow at the middle of the base (i.e. a velocity boundary is imposed). The same regimes of fluidization have been observed in the simulations as presented in Figure 1.34, consistently with both the experimental results and the previous simulations (Cui 2013; Cui, Li, Chan, et al. 2012). A study of the transient regime to cavity was also performed (Ngoma, Philippe, Bonelli, J.-Y. Delenne, et al. 2015), including an empirical power law dependency between the critical particle Reynolds number at chimney fluidization onset and the Archimedes number (see previous definition in Eq. 1.23), namely $Re \propto Ar^{3/4}$, that is very reminiscent of the experimental finding presented just above.

Case of cemented granular material Coming back to the simulations by Cui and co-authors (Cui 2013; Cui, Li, Chan, et al. 2012), let's now consider the case where the auto-adhesive force at inter-particle contact is included, through the dimensionless parameter K being strictly positive. However, only a very limited number of simulations with adhesion have been carried out and without thorough analysis of the results obtained. By changing the value of K, previous Figure 1.32 shows the effect of the adhesion force on the cavity expansion and mechanical behaviour through the type of failure. It can be clearly seen that increasing K values, the cavity expands more hardly, with progressive appearance of cracks.

More recently, Tran and co-authors have numerically modeled backward erosion based also on a 2D DEM-LBM coupling (Tran, Prime, Froiio, et al. 2017). The fluid phase is modeled using the MRT scheme of the LBM, as explained previously, and the

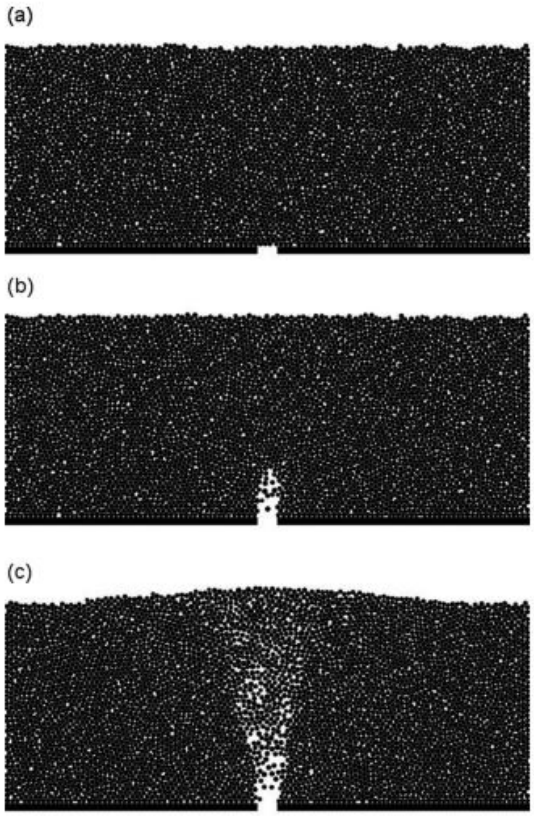

Figure 1.34. – Different regimes observed for a granular sample of height 85.8 mm: (a) static regime for u =0.10 m/s, (b) cavity regime for u =0.20 m/s, and (c) Chimney regime for u =0.30 m/s. Figure extracted from (Ngoma, Philippe, Bonelli, Radjaı, et al. 2018).

DEM part uses either a frictional contact law in the no bond case, or a bond model with the failure criterion already presented in section 1.2.3.1.

Figure 1.35a shows the granular sample located at the upstream side of the pipe face. The black particles are fixed ones while the ones in grey are capable of moving due to the hydraulic load. The sample is made of 800 particles with a geometrical length of 66.8 mm and a height of 33 mm. The grain sizes are randomly dispersed in the range from 0.75 to 0.95 mm. The sample is subjected to isotropic compaction until the confining pressure reaches 30 kN/m and the grains are in a nearly static equilibrium state, defining all the existing contacts as bonds. Then the right wall is removed and stresses applied by the top, left and bottom walls are released. For the boundary conditions implemented in the simulations of the LBM, a non-slip boundary condition is applied to the top and the bottom. The incompressible fluid flows through the sample due to the pressure difference between the inlet and the outlet, where pressure is imposed at the inlet (see Figure 1.35b).

For a sufficient flow intensity, erosion of grains occurs. With M_o the total mass of the 800 particles and M_{cr} the eroded mass (defined as the one that crossed the right

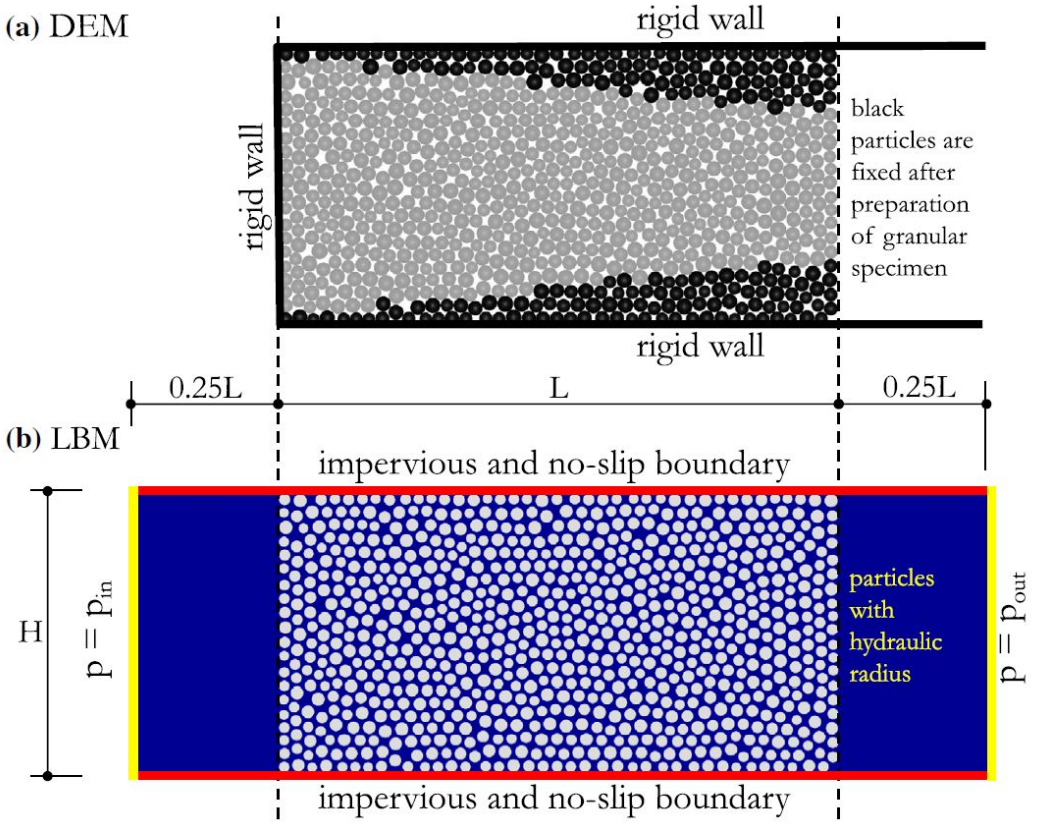

Figure 1.35. – Boundary configuration. Figures extracted from (Tran, Prime, Froiio, et al. 2017).

border), the ratio M_{cr}/M_0 is plotted in Figure 1.36 (top figure) as the imposed inlet pressure is increased linearly over time. When the time t is less than t_a, particles remain motionless, so there is no erosion. After this point, erosion starts and gradually increases with the pressure gradient. An arching effect is observed after around 2.5 s where no more erosion is found. Just after t_e, erosion restarts due to the destruction of the arch, as the concentration of the tensile and compressive force chains is released (see Figure 1.36). It should be noted that this modeling and specific boundary conditions impose the location of the eroded area and the preferential flow that is created.

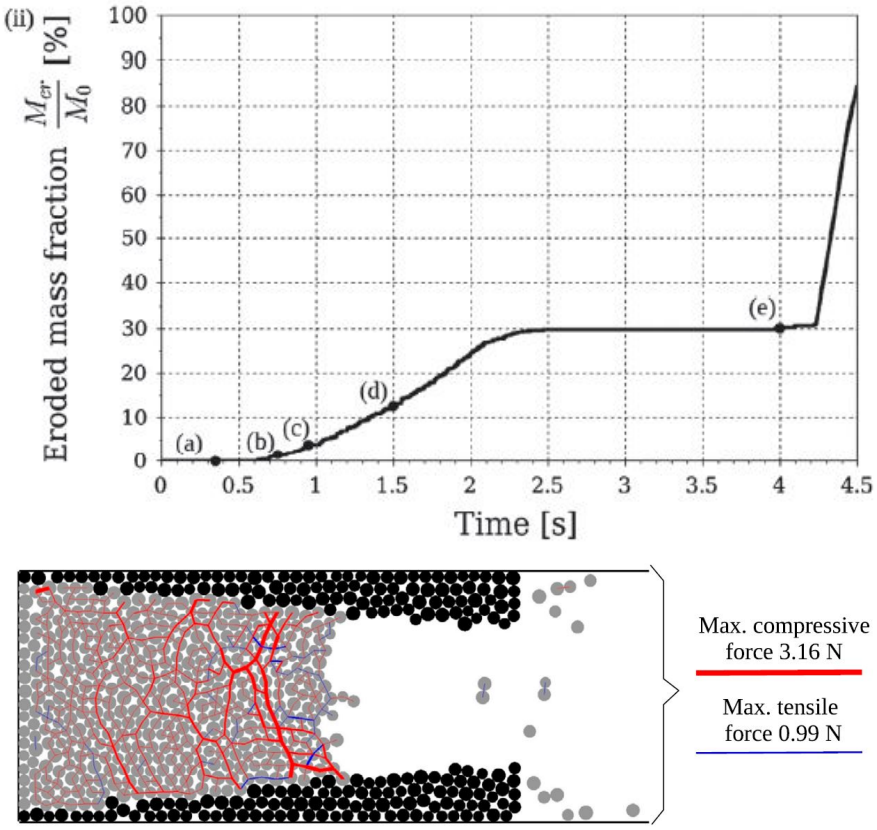

Figure 1.36. – (Top) Eroded mass fraction versus time t: (a) 0.35s, (b) 0.75s, (c) 0.95s, (d) 1.5s, and (e) 4.0s. (Bottom) Compressive and tensile force chains (blue and red colored, respectively), revealing the arching effect. Figures extracted from (Tran, Prime, Froiio, et al. 2017).

2. Experimental and numerical methodologies developed

Sommaire

Introduction

This chapter is divided into two parts, dedicated respectively to experimental developments and numerical modeling. The experimental section details the materials and the multiple setups used to study (i) the mechanical characterization of a home-made artificial cemented granular material, composed of grains bonded by a solid binder, and (ii) the hydraulic failure of a soil layer made of this particular material. This experimental section presents successively the materials used (grains, binder, liquid mixtures), the preparation and recycling methods, the micro-mechanical devices implemented to assess the strength of an individual bond between a pair of grains for different types of loading (tensile, shear, bending, and torsion), and the macro scale tensile setup developed to quantify the yield stress of the material. Then, we present the different steps followed for developing our hydraulic failure experimental setup, including the initial objective based on the Refractive-Index-Matching technique, the multiple challenges faced, and the final version of the experiment. The chapter ends with a section dedicated to the numerical simulation employed for the 2D modeling of cemented granular soil with application to hydraulic failure by a localized fluid flow and extension to a 3D approach.

2.1. Experimental part

2.1.1. Materials used

2.1.1.1. Spherical beads

Our experimental work is based on the use of artificial soils made of glass beads and therefore far from real geomaterials. However, this choice allows us to control and vary different properties (typically the particle size and the density), but also, as initially planned, to achieve the transparency of the medium. A direct visualization of the microstructure of the grains within a fully saturated particulate medium can indeed be obtained by the Refractive Index Matching (RIM) method, which consists in adjusting the refractive index of the interstitial liquid with that of the solid particles. Unfortunately, this optical technique was finally excluded due to experimental difficulties encountered, which will be explained later in section 2.1.5.1.

The beads are spherical in shape and made of either silicate glass type S or borosilicate glass type M (supplied by Sigmund-Lindner GmbH). The densities of the two different glasses are $\rho_{gs} = 2650\,\mathrm{kg/m^3}$ and $\rho_{gb} = 2230\,\mathrm{kg/m^3}$, respectively. Borosilicate glass was specifically chosen for its lower optical index, namely $n_b = 1.472$, which facilitates the RIM implementation. We used separate particle lots, each with a narrow particle size distribution around a mean value. The diameters considered are: $d = 0.60 \pm 0.13$ mm, $d = 1.40 \pm 0.15$ mm, $d = 3.0 \pm 0.3$ mm, and $d = 4.0 \pm 0.3$ mm for the silicate glass beads; $d = 5.0 \pm 0.2$ mm and $d = 7.0 \pm 0.3$ mm for the borosilicate glass beads. Also, the particles are produced with two different surface finishes: a rough texture called Matt (M) by the manufacturer and a smooth surface called Polished (P)

(see Figure 2.1). The typical Young's modulus is $E_{gs} \sim 70$ GPa and $E_{gb} \sim 65$ GPa for the silicate and borosilicate glass, respectively.

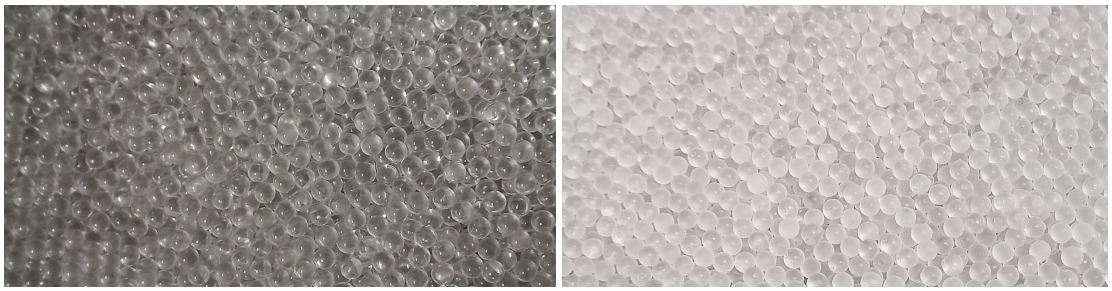

Figure 2.1. – Observed difference between Polished beads (left) and Matt beads (right).

2.1.1.2. Binder

The solid bonds intended to glue the beads together are made of a commercial paraffin (supplied by CHIMIE-PLUS Laboratoires) whose solid density was measured to 880 kg/m^3 and melting temperature between 40°C and 60°C. The volume reduction of liquid paraffin after cooling (i.e. solidification) is small (see Figure 2.2) and was measured to be less than 10 % (giving a liquid density around 800 kg/m^3). This is an alternative choice, which is an improvement over a similar system developed previously in our team but using polyurethane resin, whose high volume reduction on drying was suspected to weaken the solid bridge by generating pre-stress and micro-fractures (Brunier-Coulin, Cuéllar, and Philippe 2020). The young modulus of the (solid) paraffin was not evaluated but typical values in the literature give $E_p \sim 200$ MPa (DeSain, Brady, Metzler, et al. 2009), thus much smaller than the two glass moduli, indicating that only the bond is susceptible to deform during a tensile test and not the glass beads.

Figure 2.2. – Paraffin volume reduction from liquid to solid.

2.1.1.3. Liquid mixtures

RIM mixtures The RIM optical technique consists of using the same refractive index value for the liquid mixture and the glass beads, so that the interface between them becomes indistinguishable by suppressing the refraction of light. It was not easy to find a liquid with the same refractive index as the beads, with a viscosity not too high and that was compatible with both the paraffin and the beads (i.e. no undesired physico-chemical effects). For this, it is necessary to mix different liquids, miscible with each other. To adjust the refractive index, at least one of the selected liquids must have a refractive index higher, and a second one lower, than that of the solid beads, $n_b = 1.472$ (borosilicate glass). The first liquids chosen are distilled water and the dimethyl sulfoxide DMSO solvant (supplied by Sigma Aldrich). DMSO is a hygroscopic liquid that can absorb moisture from the atmosphere which decreases its refractive index from its initial value of 1.479 (pure DMSO). The corresponding mixture consists of 99.2 % DMSO and 0.8 % distilled water, with a density and viscosity equal to 1086 kg/m^3 and 2.0 cP [1] at 22°C. As there was a change in the refractive index (RI) of the mixture, regular measurements of the RI were carried out after each test. This mixture was conserved in a sealed tank and only opened during the experiments. The refractive index of this mixture still dropped to 1.469 after one month of experiments.

Since many difficulties were encountered with the latter first mixture as will be explained in section 2.1.5.1, another one has been tested which allows us to obtain a higher viscosity in order to generate a greater pressure gradient. This second mixture consists of mixing 49.75 % of DMSO, 49.75 % of glycerol (supplied by Sigma Aldrich), and 0.5 % of distilled water. The viscosity and density of this mixture are 24.5 cP and 1147 kg/m^3 at 22°C. Due to the hygroscopicity of both DMSO and glycerol, the RI and viscosity dropped to 1.470 and 23.3 cP at 22°C, respectively, after one month of experiments.

Non-RIM Mixture Removing the requirement for transparency of the medium, the selection is made this time on viscosity, miscibility, and compatibility with the paraffin and the beads. This last mixture, viscous enough to be capable of generating a high-pressure gradient as it flows across a sample, is composed of 65 % of glycerol and 35 % of distilled water, with a density 1179 kg/m^3 and a viscosity 24.0 cP at 22°C. The viscosity of the liquid dropped to 23.1 cP after 4 months due to the hygroscopicity of glycerol.

2.1.2. Sample preparation and recycling

Each artificial cemented granular material used in the following was fabricated from glass beads, as granular material, and liquid paraffin, as binder. First, the mass m_g of beads needed to fill the mold is weighed. Then, the mass m_p of solid paraffin is added according to the required quantity. The corresponding paraffin content in mass

1. Viscosity is measured at the end of each experiment using a falling ball viscometer from Gilmont instruments

is denoted $X_p = m_p/m_g$ and ranges from 0.2 % to 1 %, while the volume fraction in paraffin directly reads $\xi_p = X_p\,\rho_g/\rho_p$ with ρ_g the glass density [2]. The mixture is heated with an electric stove set at 240°C in order to reach a temperature in the medium high enough for the paraffin to be completely melted. At the same time, the sample is stirred carefully and continuously to distribute the liquid paraffin evenly, until the sample reaches a temperature of 90°C. The hot mixture is delicately poured through a funnel, keeping a small fall height, into a macroscopic scale mold consisting of an association of two small, medium or large cones (see Figure 2.8). Finally, the sample is left at least for 7 hours to completely cool down at ambient temperature so that all the paraffin has hardened and the solid bonds formed. Typical examples of these resulting solid bonds are shown in Figure 2.3. If the paraffin content is low enough, typically $X_p < 1$ %, only pendular shapes are observed. Beyond this range, there will be an increasing fraction of funicular bridges. This observation is fully consistent with the observation of capillary bridges in a saturated soil (Mitarai and Nori 2006).

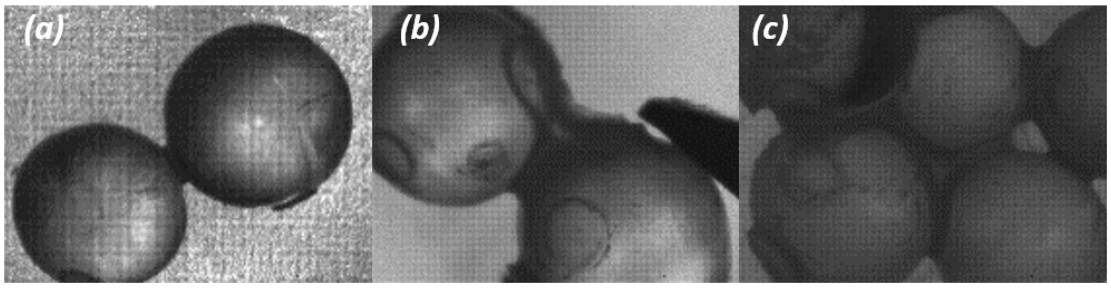

Figure 2.3. – Types of bonds observed between beads after extraction: (a) a typical narrow pendular bond for $X_p < 1$ %; (b) pendular and (c) funicular shapes found for $X_p \geq 1$ %.

Because of the price of the beads (up to around 45 euros/kg) and the amount of waste potentially generated, we developed an appropriate method to recycle our cemented grains by removing the added paraffin. The process of recycling a sample consists of four steps: the first step is to immerse the sample in a commercial sunflower oil [3]. Then, the sample and oil mixture is heated on the stove while stirring and mixing so that the paraffin does not burn, which covers the beads surface with a dark yellow to brown color. Once the temperature of the mixture reaches 110°C, the temperature of the stove is lowered to this value, while stirring continuously for 10 min to be sure that the paraffin is completely melted in the oil and separated from the beads. The second step is removing the oil from the surface of the beads by filtering them, then adding soap and starting to scrub the beads until a thick foam appears. The third step is to rinse the beads with hot water to get rid of the soap and oil. It is useful to repeat the second and third steps twice, or more if necessary, to ensure that the oil has

2. more precisely ρ_{gs} or ρ_{gb} depending on whether the beads are made of silicate or borosilicate glass

3. It was indeed observed in a previous work (PhD thesis of F. Brunier-Coulin) that paraffin bonds lose their adhesion with glass after immersion in a mineral oil.

been completely removed from the outer surface of the beads, especially for small-size beads. Finally, we place the cleaned sample in the oven to dry. After removal from the oven, calcareous deposits may be present between small-size beads (less than $d = 1.4$ mm). These are easily destroyed by hand after the system has cooled for a few minutes. One can also check that the oil has been properly removed by checking that the final product is neither sticky nor yellowish in colour (if not, go back to step 2). The borosilicate beads should still be changed after several recycles to ensure good repeatability of the different tests as a difference in colour has been observed after too many uses.

Figure 2.4. – Recycling process: (left) beads immersed in sunflower oil; (right) recycled glass beads.

2.1.3. Macro-tensile test

2.1.3.1. Description of the setup

Prior to this thesis work, a traction device had already been first developed by F. Brunier-Coulin (Brunier Coulin 2016) to measure the resistance to separation of two sets of granular materials made cohesive by solid bridges, as shown in Figure 2.5. To this end, two open conical containers are brought into contact in a horizontal plane at their minimum section. The material is then poured from the top when the intergranular bridges are still in the liquid state. After solidification of these, a tensile force is applied vertically upwards by gradually filling a water tank connected to the upper part of the sample by a cable and two pulleys while the lower part remains screwed on the support. When the two parts of the sample separate, the loading is

stopped immediately to measure the mass of water in the container and the residual mass of the lifted part. The difference between these two masses provides us with the yield load of the sample. The shape of the device makes it possible to concentrate the stresses at the contact section of the two cones and to generate the rupture in this zone. The critical tensile stress is deduced from the ratio of the yield force to the total area of the failure zone considered as a plane.

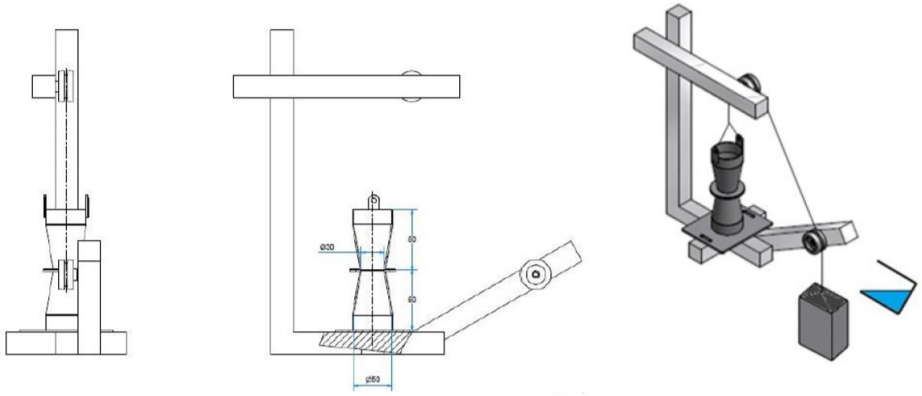

Figure 2.5. – Macro-tensile setup developed by F. Brunier-Coulin. Figure extracted from (Brunier Coulin 2016).

This device, which requires a rather delicate prior calibration of the pulley system, has made it possible to perform interesting measurements (Brunier-Coulin, Cuéllar, and Philippe 2020) but with limited precision. In the course of the present work, significant improvements were therefore made in the way the tension force is generated. As can be seen in Figure 2.6, a spring is connected on one side to the upper part of the mold and on the other side, via a hook, to a force sensor, which is attached to a displacement bench. The top end of the spring can be elevated at a constant velocity defined initially before starting the test via computer software, the force exerted on the upper cone and measured by the sensor being thus imposed by the progressive extension of the spring.

The displacement and the force are recorded during a test as illustrated in Figure 2.7. After an initial regime where the spring extension is not linear, we next observe a linear increase of the tensile force until the sample ultimately breaks when the two cones detach, resulting in a sudden drop in force. The yield tensile force F_T exerted on the sample is the difference between the maximum force and the residual force after rupture, corresponding to the weight of the upper cone, which remains suspended with the grains it contains.

We can finally deduce the critical stress σ_T from:

$$\sigma_T = \frac{F_T}{A} = \frac{F_T}{\frac{\pi}{4}D^2}, \tag{2.1}$$

where A is the area at the neck cross-section (diameter D) of the macroscopic device.

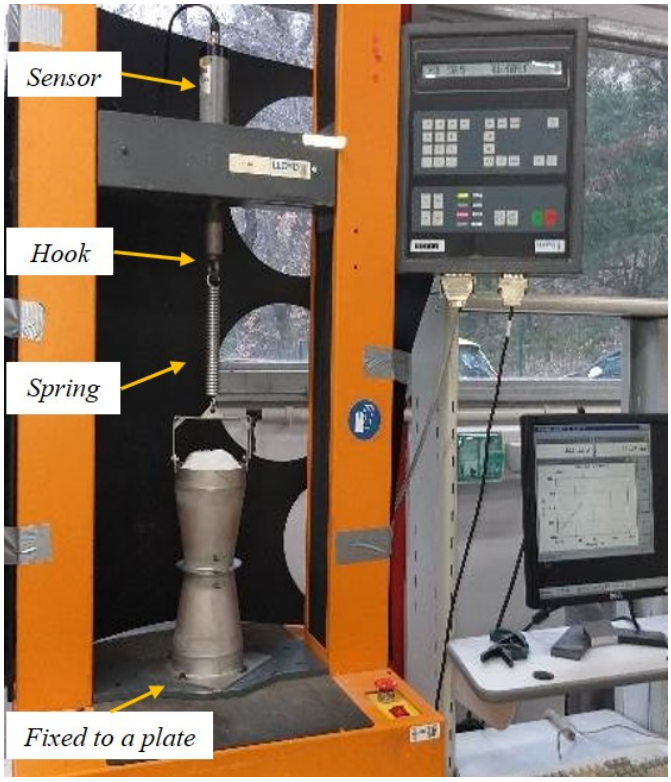

Figure 2.6. – Traction bench for the macroscopic scale tests.

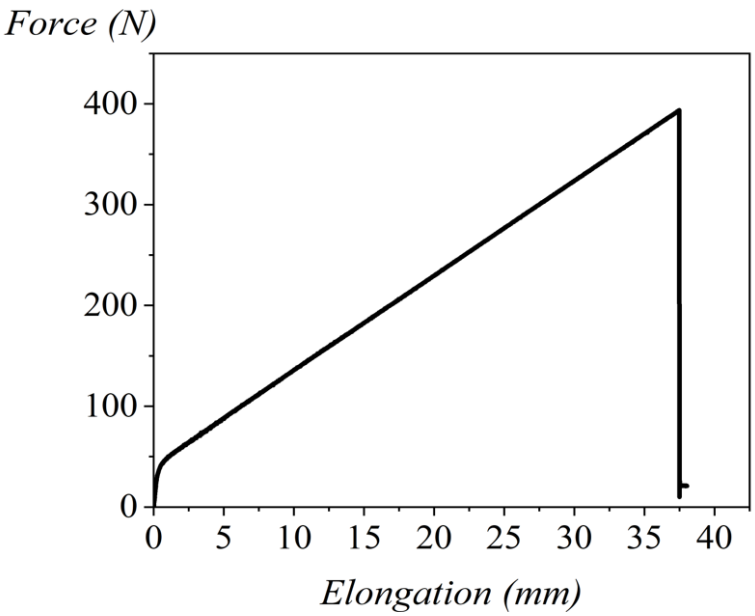

Figure 2.7. – Typical recorded measurements obtained from macro-tensile test.

Note that the force imposed on the macroscopic cone is simply equal to the elongation of the spring multiplied by its stiffness.

Another improvement is the ability to change the size of the cones, which are now available in three different dimensions as shown in Figure 2.8.

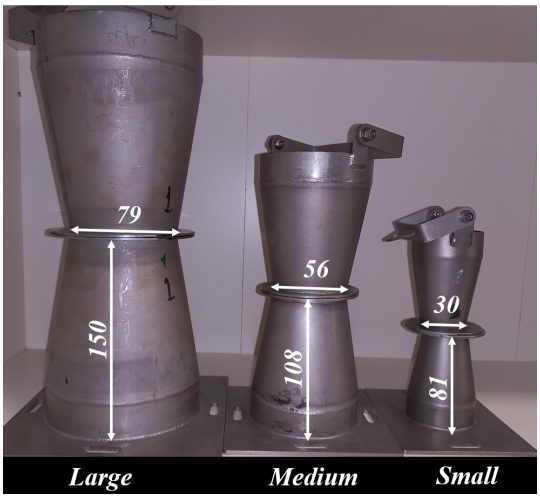

Figure 2.8. – The three sizes of the macro-scale tensile devices (dimensions of the cone height and neck diameter D are in millimeters).

Depending on the cementation strength of the sample and especially the size of the cones, the yield force can differ significantly. We used the same spring with stiffness equals to 9.52 N/mm, but one could easily change it to vary the stiffness, and adapted the displacement velocity, from 0.3 mm/min for high tensile forces down to 0.1 mm/min for the lower ones, usually for the small and medium cones.

It should also be noted that an artifact was observed during some of the first tests. More specifically, a tensile force of zero was obtained, indicating that a crack already exists at the device's neck prior to the start of the test. After several repetitions and checks, we discovered that the bottom plate fixation should be strictly planar from the start (i.e. before pouring the sample in the macroscopic scale and before the sample dries), because any subsequent deformation in this location will severely damage the sample at the contact section between the two cones.

All the macro-tensile tests performed during the present study are summarized in Table 2.1.

2.1.4. Micro-tensile test

This work aims to experimentally characterise the strength provided by bond cementation not only at the scale of a representative soil sample, as discussed in the previous section, but also at the grain level, in order to link the two scales. In addition, a detailed knowledge of microscopic quantities is essential for a thorough physical understanding of the destabilisation mechanisms of the cemented soil through the breaking of adhesive bonds, as during the erosion process, where the eroded material is detached grain by grain, or in the form of aggregates from the bed, which will then be transported by the flow. Determining the micro characterization of the bonds

Particle diameter (mm)	Surface roughness	Paraffin mass content (%)	Glass type
0.6 ±0.13	P	0.2	S
	P	0.5	S
	P	0.7	S
1.40 ± 0.15	P	0.2	S
	P	0.5	S
	P	0.7	S
3.0 ± 0.3	P	0.2	S
	P, M	0.5	S, BS
	P	0.7	S
	P	1.0	S
4.0 ± 0.3	P	0.2	S
	P	0.5	S
	P	0.7	S
	P	1.0	S
5.0 ± 0.2	P, M	0.5	BS
7.0 ± 0.3	P, M	0.5	BS

Table 2.1. – Parameters for the macro-tensile characterization tests. P: polished; M: matt; S: silicate glass; BS: borosilicate glass.

allows us to understand better how particles are attached and how erosion takes place depending on the effective bond strength within a cemented granular soil. To determine the latter, several tests were carried out at the micro-scale under different mechanical solicitations: tensile, shear, bending and torsion. Among the purposes of this work is to propose a general local cohesion law for solid bridges under all types of solicitation that can be used to calibrate discrete numerical models.

Here again, as for the macroscopic case, a previous microscopic traction device had already been developed and used in the laboratory (Brunier-Coulin, Cuéllar, and Philippe 2020). From there, several improvements were made to obtain the different devices presented here, which now make it possible to reach higher stress levels and to test all mechanical loads (tension, shear, bending, torsion).

2.1.4.1. Tensile device using a balance

With the goal of characterizing the bond strength at the grain scale, we use a first tensile test, very similar to the previous macro-scale device, but involving a unique solid bridge between two glass beads. To this end, starting from a sample on which a macroscopic test has been performed (see section 2.1.3), a pair of beads bonded by a solid bridge is very gently extracted at the cross-section of the breakage plane between the two cones. Then, as shown in Figure 2.9, the tensioning system is maintained vertically, with the lower bead glued to the surface of a wood using a drop of strong glue (Loctite brand Super Glue-3), while the upper bead is held between the jaws of an

inverted bulldog tweezers. The bulldog tweezers are connected to an inverted balance, via a very soft spring hand made by a steel wire to sharply reduce the variation in the force applied to the bridge by elongation of the spring. The test is indeed carried out by recording the mass variations with the balance while slowly lowering the bottom stage. Two different springs have been used, one for debonding forces less than 1 N having an effective stiffness equal to 0.027 N/mm (used for 4 mm and lower particle sizes) and a second one with an effective stiffness 0.31 N/mm for forces higher than 1 N (used for 5 and 7 mm particles).

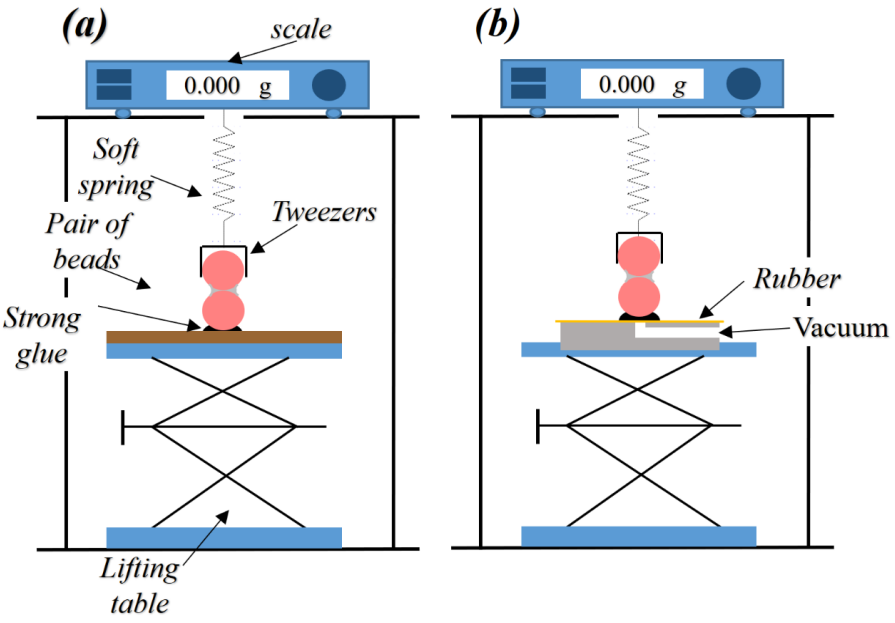

Figure 2.9. – Sketches of the micro-tensile scale devices with (a) the superglue method and (b) the suction system.

Once the bonded beads are correctly positioned, we can start the test by progressively moving downwards the lower bench, causing the spring to elongate and the force, applied to the upper particle and measured by the inverted balance, to gradually increase until the bond breaks. To collect the results, the scale is connected to a computer and the measurements are recorded over time. From the scale acquisition, the sudden decrease in mass Δm is determined as the difference between the maximum value recorded and the residual one, which corresponds to the mass of the remaining ensemble of spring, tweezers, upper bead and possible rest of the solid bridge. Finally, the yield tensile force reads $F_t = \Delta m g$ where $g = 9.81$ m/s^2 is gravity. A typical curve of force over time with resulting F_t is presented in Figure 2.10, where the slope of the increasing part of the graph is checked to be equal to the spring stiffness.

A significant issue regarding this device is the time required to perform a tensile test. Indeed, to reach a tensile force higher than 0.3 N, about 25 minutes are needed for complete drying of the glue because otherwise the failure may occur at this lower gluing contact. We improved this drawback by adding a thin rubber and a vacuum

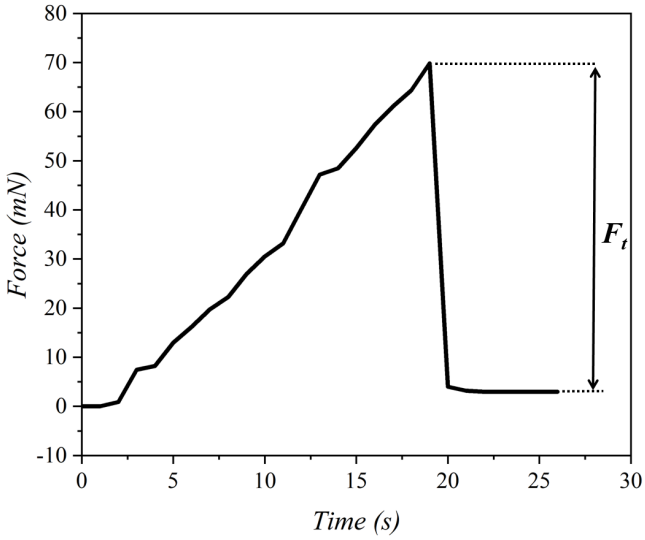

Figure 2.10. – Typical time evolution of the force measured during the test, giving the micro-tensile force F_t

system under the lower bead. The procedure is as follows: first, we grab one particle from the pair of beads with the tweezers and align both vertically. Then, we glue the lower bead to the rubber, which will shrink and stick to it. Finally, we place the bead and the rubber on the vacuum pit, thus inducing a substantial suction force. In this condition, tensile forces can reach up to 4 N, depending on the selected suction pressure and the bulldog tweezers. The average time for this test is reduced to 15 minutes, drying of the glue on the elastic rubber being faster. Both of the fixing systems were used to study the tensile force at a microscopic scale and are sketched in Figure 2.9. Note also that there is no significant fluctuation in the recorded data due to the sensitivity of the balance or the lowering speed of the lifting table, which was controlled manually.

By varying the particle diameter and the mass paraffin content, we have performed many different tests, all listed in Table 2.2.

2.1.4.2. A more compact device for *in operando* tomography

To study in more detail the geometrical characteristics of a solid bridge between two particles and its different modes of rupture, we had the opportunity to perform micro-tomographic visualisations at the MATRIX[4] platform of the laboratory CEREGE in Aix-en-Provence. For this purpose, we developed an adapted micro tensile setup that could be placed in the tomography chamber for *in operando* use, i.e. acquisitions of tomography scans in the course of a test.

Figure 2.11 presents the x-ray tomography device with the laser source used for the acquisition (RX source: target W, acceleration voltage 40 kV, power 10 W). Here,

4. https://www.cerege.fr/fr/laboratoires-et-plateformes/plateforme-matrix

Particle diameter (mm)	Surface roughness	Paraffin mass content (%)	Glass type
1.40 ± 0.15	P	0.2	S
	P	0.5	S
	P	0.7	S
3.0 ± 0.3	P	0.2	S
	P, M	0.5	S
	P	0.7	S
	P	1.0	S
4.0 ± 0.3	P	0.2	S
	P	0.5	S
	P	0.7	S
	P	1.0	S
5.0 ± 0.2	M	0.5	S
	M	1.0	BS
7.0 ± 0.3	M	0.4	BS
	P, M	0.5	BS

Table 2.2. – Parameters for the micro-tensile characterization tests. P: polished; M: matt; S: silicate glass; BS: borosilicate glass.

2D radiography images are recorded with an exposure time chosen to be one second and a field view of 1024 x 1024 pixels^2. The sample is placed between the source and the camera, on a circular turntable equipped with a clamping ring, that can translate along the x, y, and z axes, and rotate around z. In the present case, a thin metallic hollow tube is fixed in the clamping ring while a couple of particles previously extracted from a cemented specimen is glued on the top of the tube through the bead underneath. There, the waiting time for hardening is reduced to 14 minutes compared to our previous experimental protocol (see section 2.1.4.1) in order to perform more experiments over the allotted time. It should also be noted that the turntable is only moved or rotated after the rupture, so as not to impose a load on the system or damage the bond.

As can be seen in Figure 2.11, the space available for positioning the sample to be scanned is rather small and does not allow us to keep our initial set-up with the inverted balance in order to carry out the acquisitions during a test. To this end, our setup has been modified to fit into the limited space of the tomography chamber. Keeping the tensioning system consisting of the tweezers and the spring (the one with a stiffness equal to 0.31 N/mm), the scale has been replaced by a much more compact force sensor. The latter is mounted on a motor-driven translation plate. Then, the test is carried out by recording the force variation due to the motorized lifting movement of the upper plate at a constant speed. A sketch of the new setup is provided in Figure 2.12.

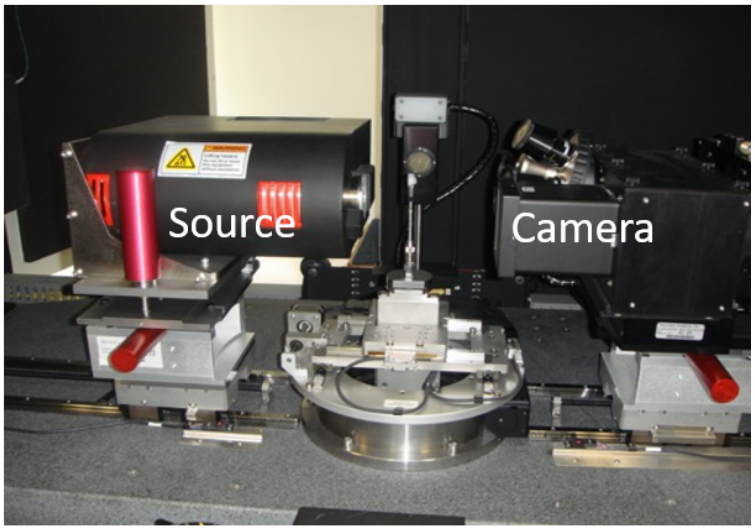

Figure 2.11. – The X-ray tomography platform MATRIX at the CEREGE laboratory.

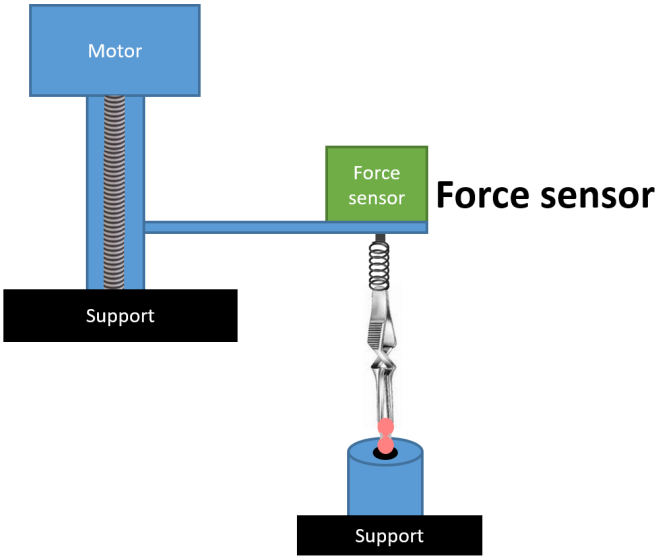

Figure 2.12. – New micro-mechanical characterization setup.

2.1.4.3. Adaptation to different loading types

Based on the latter setups, we finally proposed some additional adaptations in order to study other loading types on a bond between two particles: shear, bending, and torsion. As illustrated in Figure 2.13, these adaptations consist of modifying the orientation of the bond, possibly with the addition of a lifting arm provided by a wooden rod, while continuing to use the progressive tensioning system, in order to apply forces and moments independently along different directions of the axis of the

beads.

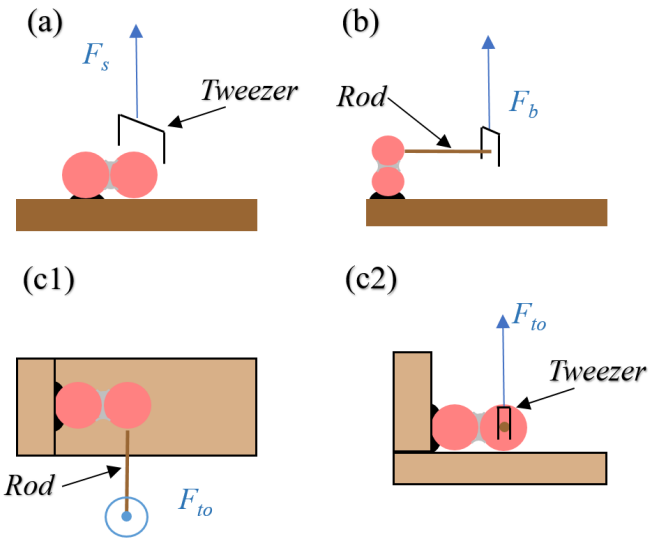

Figure 2.13. – Sketches of the different microscopic setups for (a) shear, (b) bending and (c1) torsion in top view and (c2) in side view.

The shear setup is close to the tensile one, except that the pair of bonded beads is now placed perpendicular to the tweezers, inducing a shearing load at the interface between the paraffin bridges and the particles (see Figure 2.13a). The experimental procedure is as follows: first, one bead of the bonded pair is grabbed by the tweezers with an axis perpendicular to the latter before connecting it to the spring. Then, the bottom stage is elevated to be in contact with the second bead, fixed by a drop of super glue (Loctite brand Super Glue-3) and left drying for 25 minutes.

For bending and torsion loads, the corresponding moments are applied through a wooden rod, initially glued to one of the two beads (see Figure 2.14). The ensemble of bead pair and wooden rod is then installed according to the configurations shown in Figures 2.13b and 2.13c. To prepare an experiment, the following procedure is adopted: first, the rigid wood rod is glued perpendicular to the axis of the bonded pair beads and left for 15 minutes to dry. Then, the tweezers are used to grab the end of the rigid wood while aligning the pair of beads perpendicular (for a bending moment) or parallel (for a torsion moment) to the tweezers. Finally, the tweezers are connected to the spring and a drop of glue is placed at the bottom stage, which will be later elevated to be put in contact with the bead. It is important to note that small additional normal and shear forces are applied in the case of bending and torsion moments, respectively. These forces are, however, very weak, so that they are neglected and not considered as a contributing factor to the bond rupture.

Again, the results are obtained in the form of the evolution of the applied force as a function of time, with a sharp drop at the moment of bond rupture. Whereas for shear load we observed a similar linear behavior as expected from previous tensile tests (see Figure 2.10), the response can be more complex for bending and torsion as

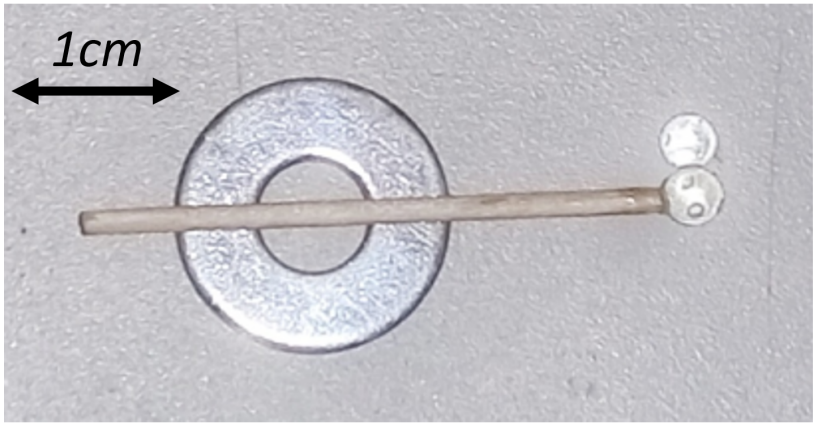

Figure 2.14. – Rigid wood rod glued to one of the pair of beads.

illustrated in Figure 2.15. Such a signal, marked by an abrupt but partial drop in force and a lower rate of subsequent evolution, was observed in many tests carried out in this study. In all cases, the microscopic force at rupture is defined as the difference between the maximum value and the residual one, denoted as F_s, F_b and F_{to} for shear, bending and torsion, respectively.

With the aim of elucidating the movements of particles responsible for this unexpected bending or torsion force evolution, we have placed flags as markers on the two beads and the rod (see Figure 2.16 in the case of bending). The simultaneous elongation of the spring and displacement of the flags are then recorded using two high-resolution cameras, namely Optronis Cyclone-25-150-M camera (with an objective lens 105 mm f/2.8) and XIMEA XiQ camera (with an objective lens 1:1.4/25 mm), respectively. The results of this refined analysis will be presented in section 3.1.2.

By varying the particle diameter and the mass paraffin content, we have performed several shear, bending and torsion tests as listed in Table 2.3.

Particle diameter (mm)	Surface roughness	Mass paraffin content (%)	Glass type	Number of tests
3.0 ± 0.3	P	0.5	S	40
	P	1.0	S	40
4.0 ± 0.3	P	0.5	S	30
	P	1.0	S	40
5.0 ± 0.3	P, M	0.2	BS	30
7.0 ± 0.3	P, M	0.5	BS	50

Table 2.3. – List of experiments performed for shear, torsion and bending load. P: polished; M: matt; S: silicate glass; BS: borosilicate glass.

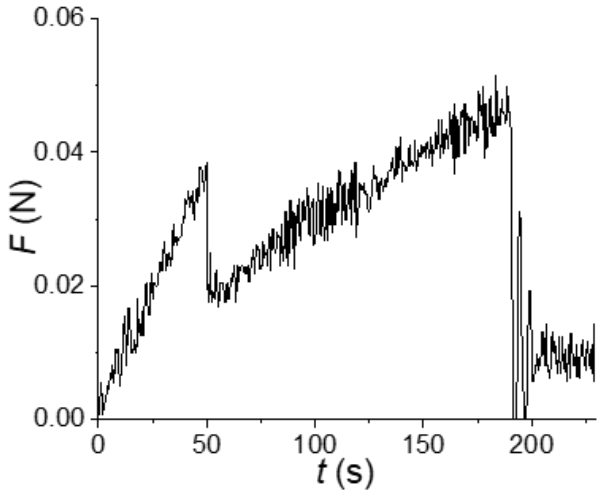

Figure 2.15. – Typical time evolution of the force measured during a torsion test of 7mm glass beads with 0.5 % paraffin content.

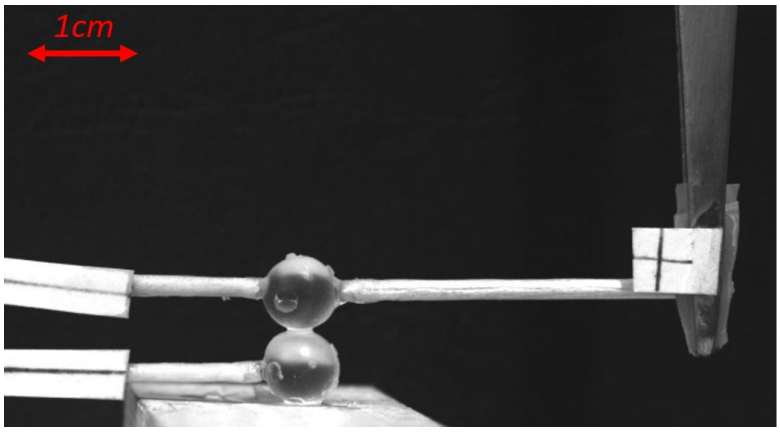

Figure 2.16. – Example of flags installed for a bending test.

2.1.5. Localized hydraulic load

2.1.5.1. Unsuccessful implementation using RIM visualization technique

Description of the target setup This experimental setup aims to study the "hydraulic failure", i.e. substantial grain removal by fluidization or erosion, of an immersed cemented granular material subject to a localized hydrodynamic load. In the implemented physical model, the injection of fluid is directed upward and perpendicularly to the bottom surface of a horizontal layer of cemented soil, resulting in mobilization of only a portion of the particle medium. The liquid is locally injected through an inlet below the sample with a constant flow rate.

The optical technique of Refractive Index Matching (RIM) coupled with the Planar Laser-Induced Fluorescence (PLIF) allows the internal probing of an immersed

granular medium during some hydro-mechanical processes as fluidization, scouring, erosion or hydraulic failure without perturbing it. These techniques have been used previously in our team during some experimental studies (Beguin, Philippe, and Faure 2013; Philippe and Badiane 2013; Brunier-Coulin, Cuéllar, and Philippe 2017; Mena, Luu, Cuéllar, et al. 2017; Mena, Brunier-Coulin, Curtis, et al. 2018). The transparency of the medium achieved by RIM makes it possible to visualize a chosen 2D sheet illuminated by a planar laser, here a green laser module (class 3B, 100 mW, supplied by Coherent) with a wavelength of 532 nm and a convex lens of 60^o opening. Thanks to previous dilution of a fluorescent dye in the liquid, the liquid phase within the mixture gets excited by the laser emission and re-emits light at a slightly longer wavelength, which can then be isolated from the primary laser source by use of a specific high pass filter (590 nm). The images are taken using our previous XIMEA XiQ camera mounted on an adjustable tripod. The imposition of the filter is crucial to separate the scattered light from the fluoresced one so that, as shown in Figure 2.17, the acquired image contains a high contrast between bright and dark areas corresponding to the liquid and solid (i.e. beads) phases, respectively.

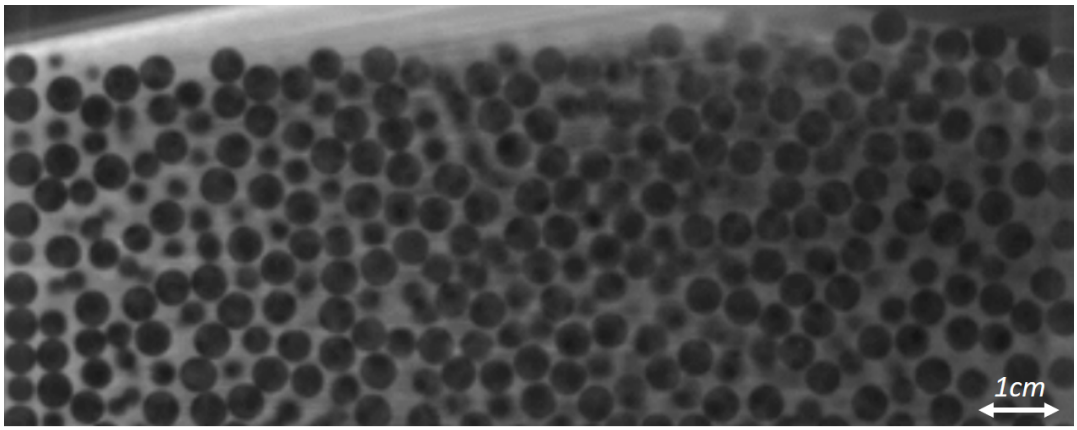

Figure 2.17. – Typical visualization of a 2D internal plane within a granular sample using the RIM-PLIF techniques.

The first limitation of this technique is the progressive reduction of light intensity as it passes through the medium, which has a major impact on the final image quality and generates luminosity gradients. To overcome this difficulty, it is possible to use several lasers. Mena and co-authors used for instance two laser sheets to compensate for this loss of intensity (Mena, Brunier-Coulin, Curtis, et al. 2018). The second drawback is a restriction on both the particle size and the distance between the wall and the illuminated laser plane. Indeed, even if the refraction is weak, it is not totally eliminated and the number of refraction interfaces encountered in the medium must be limited to avoid the image becoming too blurred.

The experimental setup used in the present study is an upgrade of a previous device that has been employed to study the fluidization of a cohesionless granular material (Mena, Luu, Cuéllar, et al. 2017; Mena, Brunier-Coulin, Curtis, et al. 2018; Philippe and Badiane 2013). The actual version is presented in Figure 2.18 where the numbers mark

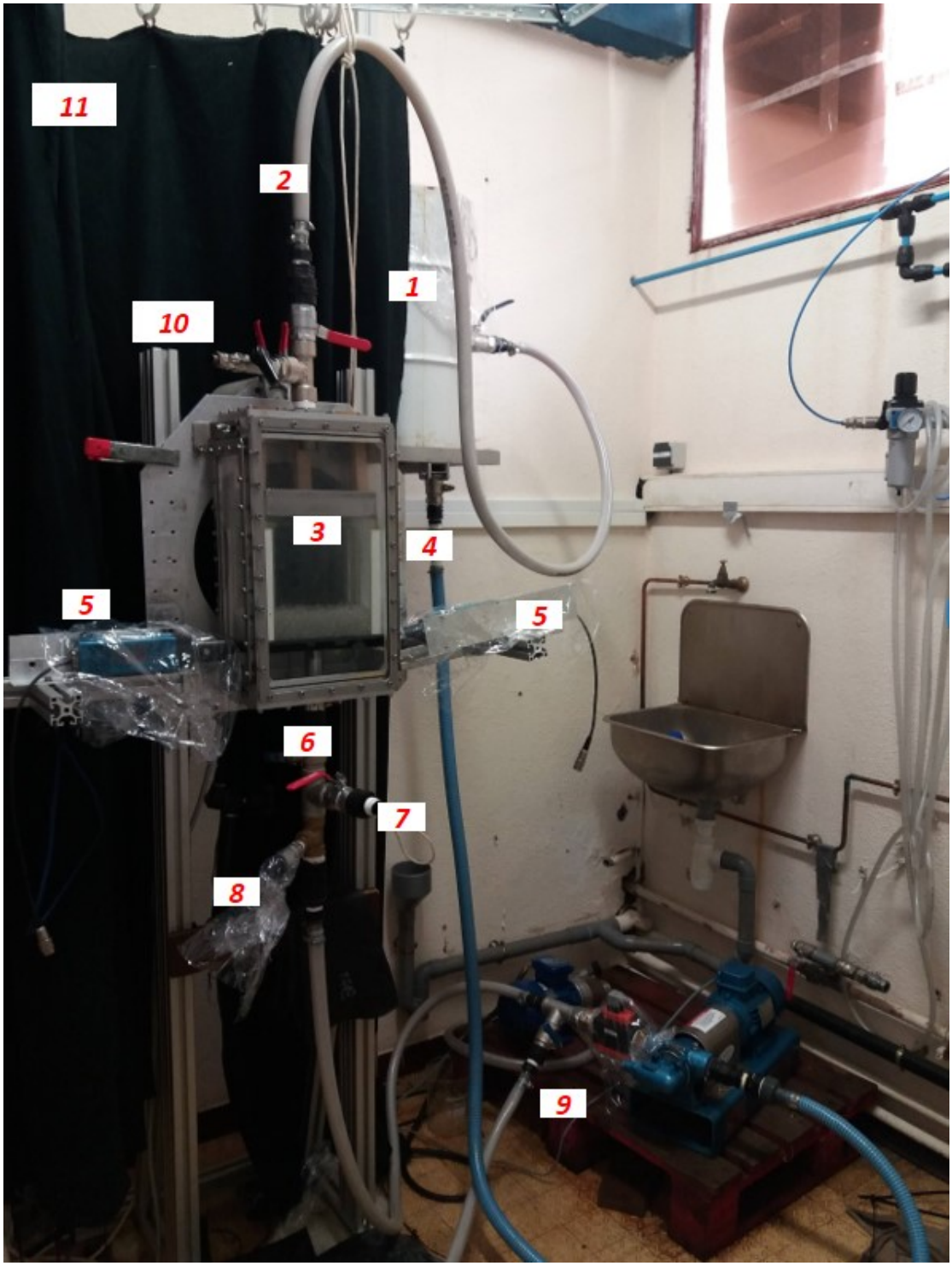

Figure 2.18. – Localized hydraulic load setup using RIM-PLIF techniques.

the following parts of the equipment: (1) metal tank with plastic film inside, (2) outlet pipe of the cell, (3) cell box, (4) inlet pipe of the gear pump, (5) lasers (coherent, PL 532

nm 100 mW), (6) inlet pipe of the cell, (7) outlet valve, (8) static pressure sensor with an absolute uncertainty of 1 kPa (model DTRANS P30 manufactured by Jumo), (9) gear pump (model MS7124 supplied by Lambert Moteur SAS), (10) air and pressure sensor valve, and finally (11) curtains to protect the cell from external light sources. The cell size is $L = 20$ cm, $w = 10$ cm and $h = 30$ cm, made with plexiglass and stainless steel walls of thickness 2.5 cm, all sides being removable. Inside this cell, a removable glass box is used to hold a cemented granular sample, having a 1-inch (2.5 cm) circular hole in the center of its underside, with the same injection diameter D_i as the inlet nozzle. Then the inlet nozzle was placed inside the hole to ensure that the liquid actually flows through the sample as shown in Figure 2.19.

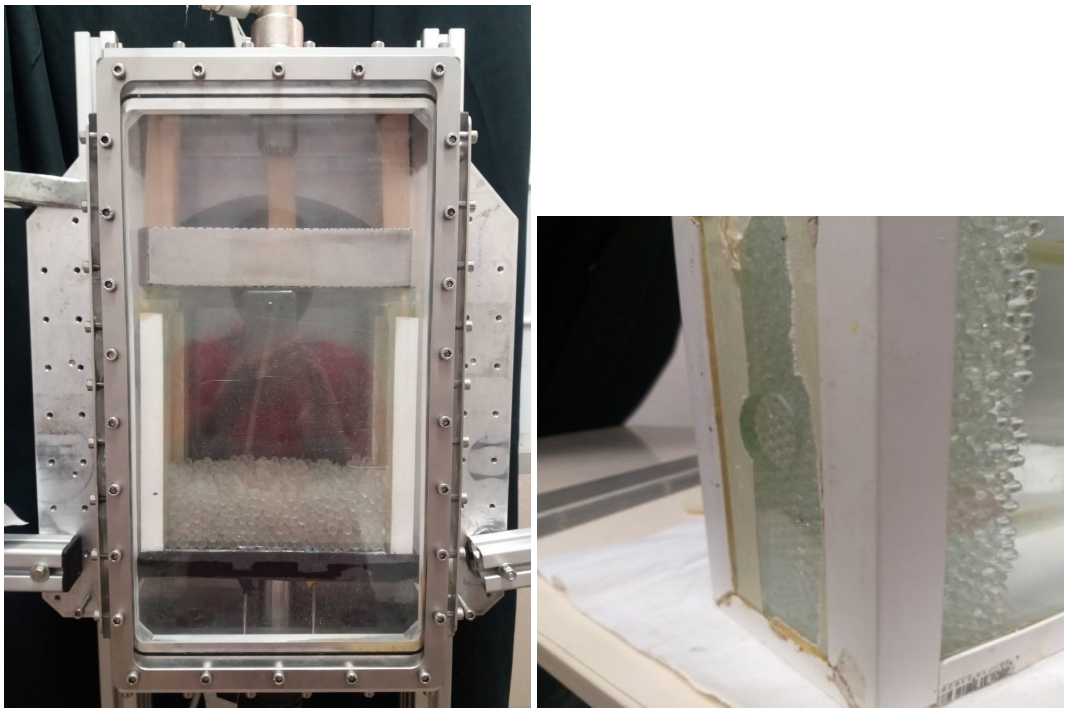

Figure 2.19. – Close up view of the cell (left) and of the glass box used with a 1-inch hole (right).

It is necessary to change the size of the pipes, joints, and valves to 1 inch to achieve high flow rates without exceeding the capacity of the sections. The gear pump is used to supply a constant flow from the tank to the cell, monitored by a controller (Leroy Somer Digidrive), which allows the flow to be manually adjusted up to 32 l/min. The flow rates are converted from the frequency value using a calibration curve measured specifically for this pump. The pressure gradient is deduced from the difference between the two measurements recorded by the pressure sensors, at the inlet and outlet pipe necks of the cell. Note that it is essential to place a filter mesh on the neck of the inlet and outlet pipes in the cell box to prevent the beads from flowing to the gear pump and damage it.

Experimental procedure To prepare each experiment, the glass box was prior dried well from any liquid, then placed inside the cell with the inlet nozzle inserted 1 cm into the glass box. All the faces of the cell are closed except the top cover, from where the hot sample mixture (glass beads and paraffin prepared according to the procedure described in section 2.1.2) is delicately poured through a funnel. The hot sample is dropped into the glass box, keeping the falling height and flow rate constant. After which, the top plate is left open for 7 hours for complete hardening, avoiding any presence of humidity that could affect the bond formation or degrade the optical quality of the liquid.

Once the installation is completed, the first essential step is to eliminate the air bubbles present in the inlet and outlet pipe of the gear pump because it is not possible to remove some trapped air bubbles once the sample gets saturated. The bubble elimination is done by inducing a flow circulation of RIM mixture in a closed loop between the tank and the gear pump through valve number 7 while closing the valve at the inlet of the cell. An important piece of the gear pump should be excluded from the flow path, where a latex membrane with a metallic piece is installed as shown in Figure 2.20. This will prevent part of the mixture from circulating in a closed loop in the pump in case of high pressure, which was also a source of air bubbles. From that moment on, the safety of the gear pump is removed, so it is important to proceed with precaution since any closed valve at the inlet or the outlet pipes will damage it.

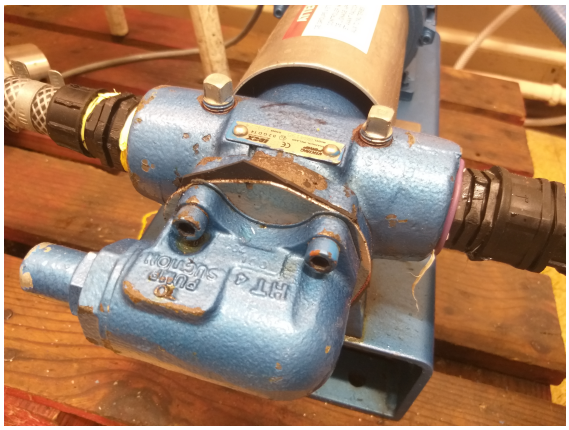

Figure 2.20. – Installation of a latex membrane to exclude the safety block of the gear pump.

The next important step is the sample saturation. To this end, the RIM mixture is very slowly introduced, by means of a gravity flow, into the system to avoid any air trapping inside the cemented grains. The flow rate is controlled by the difference between the level of the tank and the position of the cell, in addition to the valves at the inlet and outlet pipe of the cell. Note that the use of both the valve at the outlet pipe of the cell and the one numbered 10 in Figure 2.18 is important. Initially, they are closed during the saturation, leading to an air pressure built up inside the cell that can decrease the flow rate, which is controlled by closing and partly opening valve number 10. These two valves were particularly used to saturate very small size particles. Full

saturation is reached when the liquid starts pouring from valve 10. Then the second pressure sensor is installed on this valve and stops the leakage.

The final step is to position the camera on a tripod perpendicular to the plane formed by the laser sheet, with the high-pass filter fixed right in front of the camera lens. We can then launch the camera software to record the image sequence at each flow rate, starting from a very small flow rate and gradually increasing it every 20 seconds until failure is observed.

Difficulties encountered in the experiments We have performed several tests by varying the particle diameter $d \geq 3$ mm and paraffin content $X_p \geq 0.1$ %. They have been done with and without insertion of the internal glass box, meaning that the cemented granular sample was placed either in the glass box or directly in the cell to test the corresponding impact and expected improvement.

As presented in section 2.1.1.3, two different mixtures for the RIM experiments have been selected and tested. The RIM mixture #1 consists of 99.2 % DMSO and 0.8 % distilled water, in mass. The first tests presented in the following were implemented with this RIM mixture and for the parameters listed in Table 2.4.

Particle diameter (mm)	Surface roughness	Paraffin mass content (%)	Glass type
3.0 ± 0.3	P	0.1	S
	P	0.5	S
	P	1.0	S
5.0 ± 0.3	P, M	0.2	BS
	P, M	0.5	BS
7.0 ± 0.3	P, M	0.2	BS

Table 2.4. – Parameters used for the first series of RIM experiments. P: polished; M: matt; S: silicate glass; BS: borosilicate glass.

During these tests, it was progressively noted that the RIM mixture #1 has a chemical effect on the plastic pipes due to the high concentration of DMSO, which makes the pipes softer and more susceptible to burst during a test. The pressure reached in the pipes is 6 kPa with a capacity to sustain up to 10 kPa. These pipes became weaker over time and blisters appeared in some places (see Figure 2.21). Another deterioration was observed on the rubber joints that made the system leaking, as they elongated and lost their stiffness. The joints and the pipes were thus changed as soon as a leak was detected. Similarly, the glued plastic corners of the glass box were not resistant enough to DMSO and became a very soft material after being immersed for only 4 hours. The gear pump also started to corrode over time and the resulting rust dust got suspended in the liquid, with a direct impact on the refractive index and the color of the RIM mixture (see Figure 2.21). Above all, the paraffin bridges between the particles themselves were damaged by DMSO when the paraffin content was less than 0.2 %.

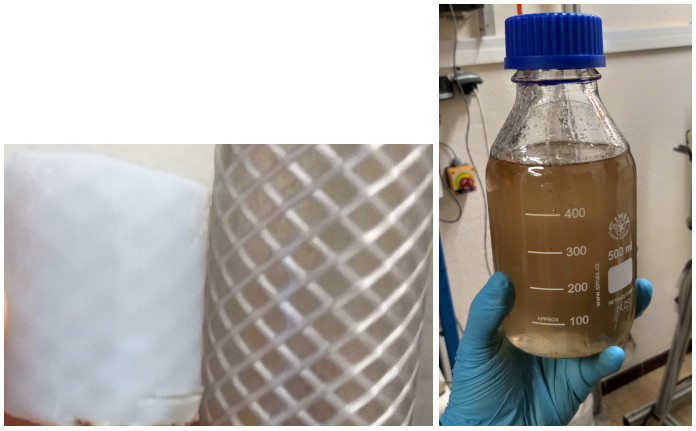

Figure 2.21. – Long-term chemical action of DMSO on a plastic pipe (left) and presence of rust in the liquid due to the oxidization of the pump (right).

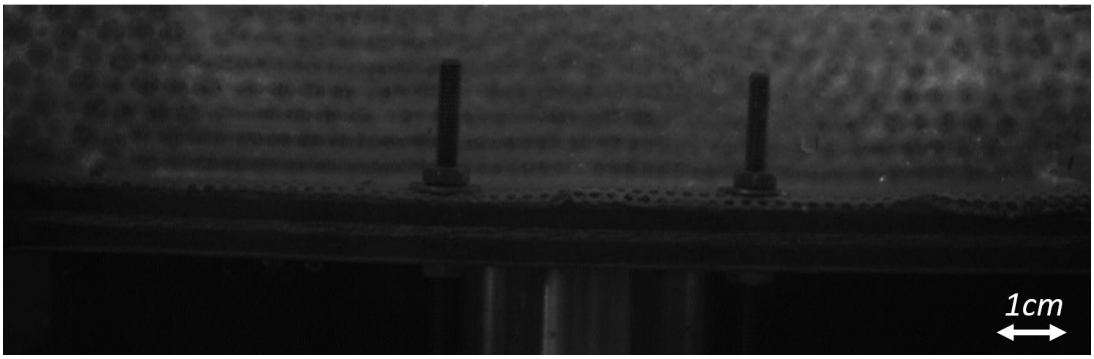

Figure 2.22. – Image of the laser sheet path through a cemented layer of 5 mm beads.

While this chemical action of the liquid is difficult to manage on its own, two major limitations were encountered during these tests: (i) the low quality of the internal visualization of the cemented granular layer; (ii) the impossibility for the flow to fluidize the cemented layer or even to dislodge the slightest grain. As displayed in Figure 2.22, there is a high dispersion of the laser as it goes through the medium. This is mainly due to the presence of the paraffin bonds, whose refractive index differs from the common one of the RIM technique. Thus, the image quality is only sufficient at the left and right boundaries of the cell, but it becomes blurred at the center of the layer. We managed to slightly improve the visualization by focusing the laser sheet at the center of the layer as shown in Figure 2.23. Another way to improve the quality of the RIM image would be the use of larger beads, implying in return that a higher pressure gradient would be required for bond breakage. In the end, in all these experiments, we were never able to observe any hydraulic failure, meaning that the pressure gradient provided by the pump with this liquid was definitely too small.

After noting all the above problems, we decided to discard this RIM mixture #1 and move towards another one, RIM mixture #2 as presented in section 2.1.1.3, that is more viscous and thus more likely to succeed in eroding the cemented layer. The

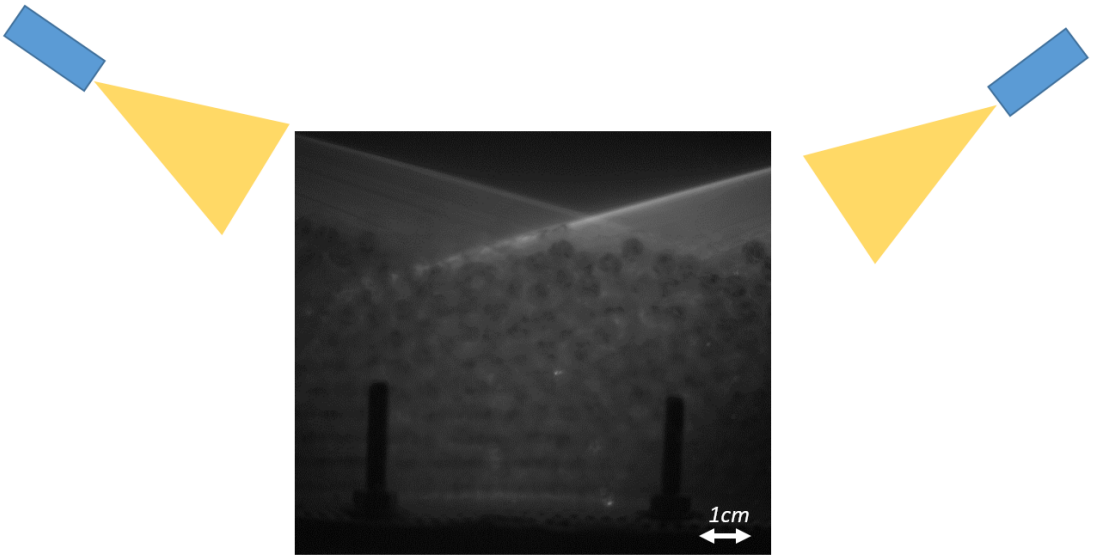

Figure 2.23. – Typical visualization after focusing the laser sheet path at the center of a cemented layer of 5 mm beads.

complementary advantage of this mixture is its smaller concentration in DMSO, which reduced and almost eliminated all the previous problems related to corrosion and plastic deterioration. The tests that were carried out using RIM mixture #2 are listed in Table 2.5.

Particle diameter (mm)	Surface roughness	Paraffin mass content (%)	Glass type
0.1 ± 0.025	P, M	0.2	S
1.4 ± 0.15	P	0.2	S
3 ± 0.3	P, M	0.1	S
5 ± 0.3	P, M	0.1	BS

Table 2.5. – Parameters for the second series of RIM experiments. P: polished; M: matt; S: silicate glass; BS: borosilicate glass.

During this second experimental campaign, we have succeeded in decreasing the mass paraffin content to 0.1 % and substantially increasing the eroding hydraulic pressure gradient. Unfortunately, that was still insufficient to generate the failure of the 5 mm beads layer with paraffin mass content of 0.1 %. Nevertheless, we observed an unexpected behavior when we used 1.4 mm and 3 mm glass beads with 0.2 % and 0.1 % mass paraffin content. Indeed, as illustrated in Figure 2.24, instead of an erosion that would occur from the bottom injection, we observed a complete block uplift where exclusively the bonds between the walls and the contacting glass beads were ruptured, freeing the cemented layer from its attachment to the walls. The sample thus behaved as a block that was lifted due to the hydraulic load. In this case, it appears therefore that the system was controlled by the boundaries. In order to prevent the

sample from such block lifting, we found a solution consisting in coating the lateral walls using hot paraffin before the preparation of the cemented layer.

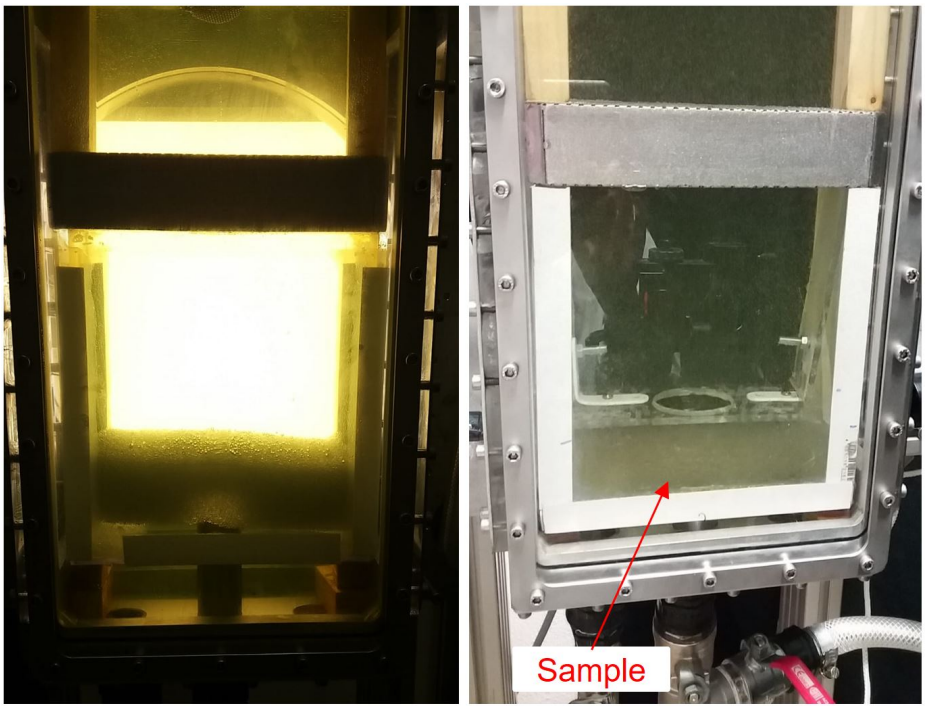

Figure 2.24. – (Left image) Block uplift for a sample with d = 1.4 mm glass beads and X_p = 0.2 % mass paraffin content. (Right image) Plate with a central circular hole installed on top of the cemented glass beads layer, yet no rupture was observed.

Then, keeping a sample with beads large enough to implement the RIM technique, we tested several configurations in order to induce a focused flow at the center of the sample, capable of generating a hydraulic failure. For instance, we have fixed a plate with a central circular hole at the top surface of the sample, as presented in Figure 2.24. The installation of the plate with four wooden wedges is done carefully so that no damage is made to the sample before the test. However, even using this trick, nothing was observed at the center of the sample, except some erosion of particles in contact with the boundary wall. Figure 2.25 shows complementary the impact of an unintentional pre-damage of the sample, during the installation of the wooden wedges and plate, at the right side before submitting it to a localized flow rate. This fracture created a preferential path for the flow, with erosion remaining limited to this zone. We have also tried to overcome the block uplift by using inclined walls of a box. Unfortunately, we observed some scouring of the glass beads at the bent walls and then a block uplift happened all the same (see Figure 2.25).

From there, we decided to work with smaller beads (0.1, 1.4 and 3 mm), thus excluding the use of the RIM technique, but offering a greatly reduced permeability and therefore increased pressure gradients. We also kept the use of the plate with the cen-

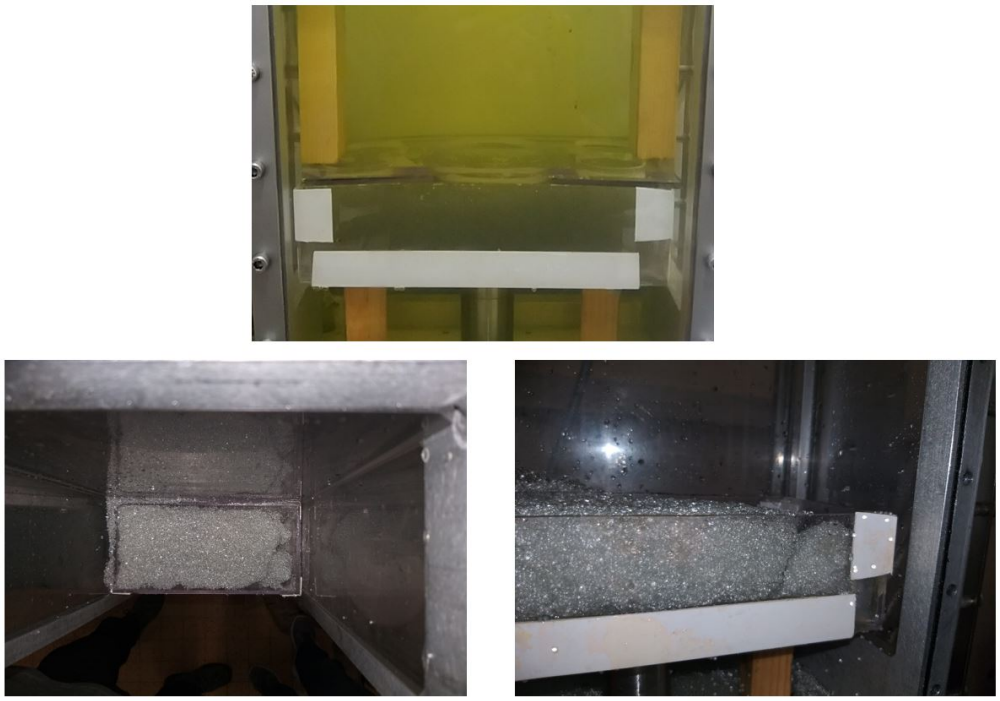

Figure 2.25. – Effect of initiating a fracture in the sample, during the installation of the rod and plate, on the hydraulic failure of the sample with $d = 1.4$ mm glass beads and $X_p = 0.2$ % mass paraffin content.

tral circular hole to focus the hydraulic flow. In this configuration, a local fluidization close to the injection finally occurred, as displayed in Figure 2.26. Unfortunately, we also faced a clogging of the filter with the 0.1 mm particles whose size gets close to the filter meshing size. The clogging led to a pressure build up inside the cell that caused damage of one of the cell's walls.

In conclusion with these numerous tests, we can infer that the implementation of the coupled RIM and PLIF optical techniques does not appear applicable to our artificial cemented materials.

2.1.5.2. Alternative visualization technique

Description of the setup and experimental procedure As an alternative to the RIM optical techniques, we have selected a simpler visualization based on back-lighting using a led panel placed at the back of the sample. As the camera records the transmitted light through the width of the sample, any substantial particle movement or fracture opening inside the sample will induce a detectable change. As seen in Figure 2.27, a cavity or a void appearance becomes brighter than other regions. Moreover, a non-RIM and DMSO-free mixture can be used, eliminating the previous issues and allowing us to test beads of all sizes while the paraffin content can be lowered down to 0.033 %.

The adapted experimental setup is presented in Figure 2.28. It is almost the same

Figure 2.26. – Hydraulic failure within a sample with d=0.1 mm glass beads and X_p = 0.2 % mass paraffin content.

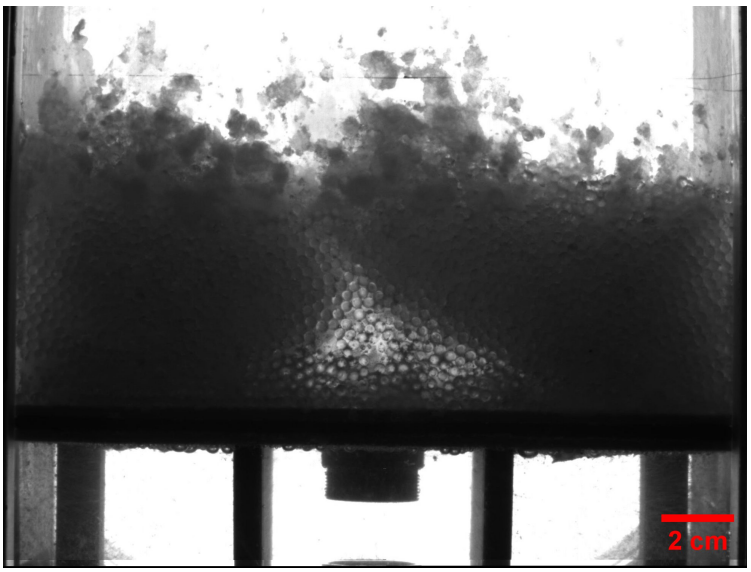

Figure 2.27. – Typical back-light visualization of a cemented granular sample using a led panel.

as the one using the RIM-PLIF techniques except for three changes. The first modification, already introduced, is the replacement of the two lasers with the led panel (supplied by Inspire Gdansk, model 1800 Lumen, size 29.5 x 29.5 cm^2). The second modification is the paraffin coating presented before that is now systematically added to the walls and the bottom plate to prevent block uplift. The last modification was

done later after facing further experimental difficulties due to fracturing of the sample caused by movement or deformation at its boundaries. The solution found was to position the sample on a plate with 6 legs as shown in Figure 2.29. This plate was designed and printed in our lab using a 3D printer, and its legs are fixed to the bottom cover of the cell by screws. It is crucial to have a very rigid plate, of 1 cm thickness in the present case, for its deformation to be negligible, avoiding any paraffin bond breakage.

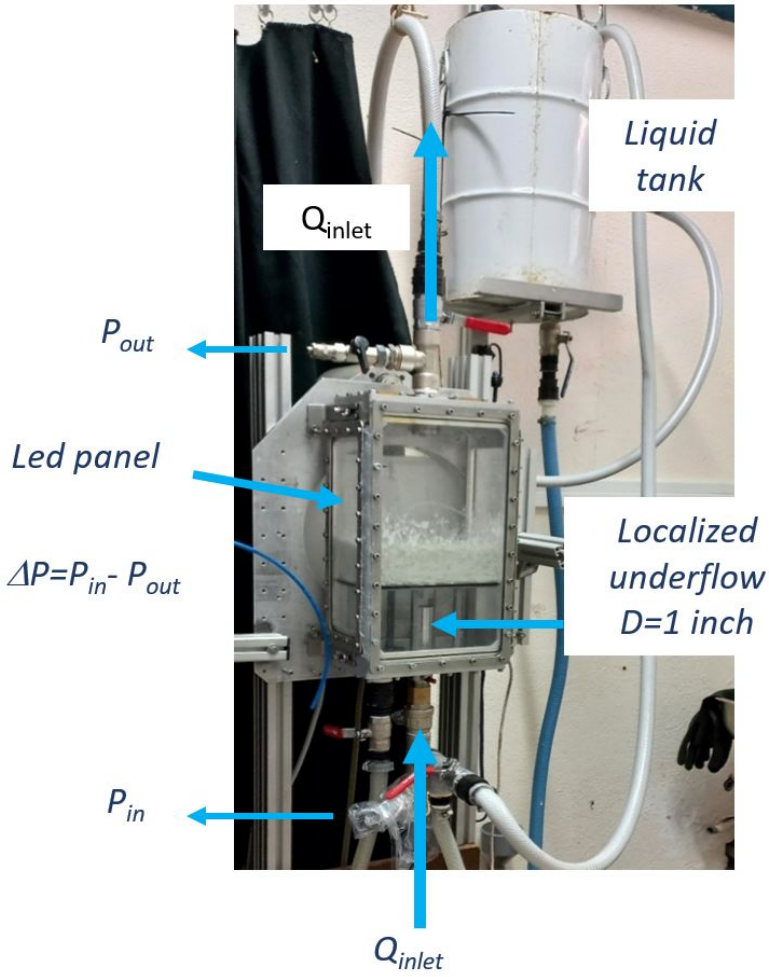

Figure 2.28. – New version of the localized hydraulic load setup using a back-light led panel.

In the end, the following protocol is used to carry out an experiment. We start by coating the walls of the cell with paraffin. Then, the sample preparation, cooling and saturation are the same as described previously, except that the layer is constructed directly on the plate with legs. Acquisition is launched by the camera software that records the image sequence at each flow rate, starting from a very small value and gradually increasing it every 20 seconds until failure.

Figure 2.29. – Plate with legs fixed to the bottom of the cell.

2.2. Numerical methods for cemented soils

This section presents a part of this work, complementary to the experiments described above and dedicated to a numerical investigation of the hydraulic failure of a cemented granular material under localised liquid flow. This study was based on a code already developed within our research group, coupling the two methods presented extensively in the State of the Art: LBM and DEM, with, for the latter, a specific model of solid adhesion described below.

2.2.1. Extension of the cemented bond model to the 3D numerical models

As already introduced in Chapter 1, Benseghier and co-authors have extended the 2D bond model proposed by Delenne (J.-Y. Delenne, El Youssoufi, Cherblanc, et al. 2004), which was based on experimental data with rods of a given diameter (Benseghier, Cuéllar, Luu, Bonelli, et al. 2020). Thereby, the thresholds presented previously, F_n^{rupt}, F_t^{rupt} and M_b^{rupt}, were assumed to depend on a single cementation force C through Eq. 1.36 (Benseghier, Cuéllar, Luu, Bonelli, et al. 2020).

Anticipating the result that will be presented in forthcoming Chapter 3 for the scaling law of the yield tensile force which gives a quadratic dependence on grain size, an equivalent relationship can be assumed in 2D where the shear force, tensile force and bending moment are expressed in terms of a 2D bond strength parameter σ_b as follows:

$$F_n^{rupt} = \sigma_b d, \qquad F_t^{rupt} = C_t \sigma_b d, \qquad M_b^{rupt} = C_b \sigma_b d^2, \tag{2.2}$$

where C_t and C_b are the assumed proportionality coefficients in shear force and bending moment, chosen equal to 0.5 and 0.25, respectively, according to Eq. 1.36.

The 3D solid bond model is based on the same elastic rheology associated now

with four degrees of freedom: the ones of the 2D bond model plus a fourth degree of freedom which corresponds to the torsion moment (Sanayei, Farhat, Luu, et al. 2021). The torsion threshold is assumed proportional to a torsion coefficient C_{to}, similarly to the bending moment. The forces and moments can be applied simultaneously at the interaction point and can be calculated only for small displacements and rotation via linear elastic rheology. The tensile-compression force, shear force, bending moment and torsion moment are associated by normal, shear, bending and torsion stiffness: k_n, k_t, k_b and k_{to}.

$$\begin{pmatrix} F_n \\ F_t \\ M_b \\ M_{to} \end{pmatrix} = \begin{pmatrix} k_n & 0 & 0 & 0 \\ 0 & k_t & 0 & 0 \\ 0 & 0 & k_b & 0 \\ 0 & 0 & 0 & k_{to} \end{pmatrix} \begin{pmatrix} \delta_n \\ \delta_t \\ \gamma_b \\ \gamma_{to} \end{pmatrix}$$

Similarly to the 2D model and consistent with the forthcoming experimental scaling law for tensile force, a 3D bond strength parameter σ_b is introduced through the following relations:

$$F_n^{rupt} = \sigma_b d^2,\ F_t^{rupt} = C_t \sigma_b d^2,\ M_b^{rupt} = C_b \sigma_b d^3,\ M_{to}^{rupt} = C_{to} \sigma_b d^3. \tag{2.3}$$

The extension of the bond failure condition to 3D is done by introducing a fourth parameter to the yield surface criterion as follows:

$$\zeta = \left(\frac{F_n}{{F_n}^{rupt}}\right) + \left(\frac{F_t}{{F_t}^{rupt}}\right)^2 + \left(\frac{M_b}{{M_b}^{rupt}}\right)^2 + \left(\frac{M_{to}}{{M_{to}}^{rupt}}\right)^2 - 1. \tag{2.4}$$

For $\zeta < 0$, the bond is still intact while the rupture occurs when $\zeta \geq 0$.

2.2.2. Simulation of a localized hydraulic failure in 2D numerical model

This section is specifically devoted to the 2D numerical simulation of a localized hydraulic failure of a cemented granular soil layer using the 2D DEM-LBM code presented previously. The DEM is enriched with the 2D bond model, with values of σ_b, C_s, and C_b calibrated from our micro-mechanical tests with adaptation to 2D, to take into account the adhesive force of a bond between the particles. For the LBM, a fluid density on a lattice is simulated with streaming and collision (relaxation) processes using the particle distribution functions f_α. Thus, the boundary conditions can not be directly imposed, but are implemented by setting the desired values of the distribution functions at the boundary nodes. Figure 2.30 presents the different boundary conditions to be used for our 2D numerical simulations and described just after: non-slip, outflow, and imposed velocity. A comprehensive study was conducted by changing many parameters: particle diameter, viscosity, inlet velocity profile, inlet nozzle diameter, bed height, and simulation duration. In particular, three different inlet velocity profiles were studied: uniform, triangular and parabolic (i.e. plane

Poiseuille flow).

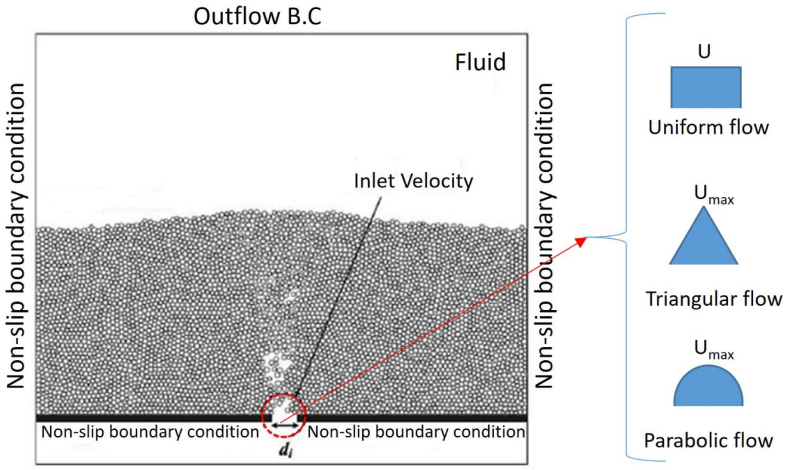

Figure 2.30. – Configuration of the 2D numerical simulations with prescribed boundary conditions.

Non-slip or bounce back boundary condition A non-slip boundary must be imposed between the fluid and a solid wall, where the wall is located in the middle between fluid and solid nodes (see Figure 2.31).

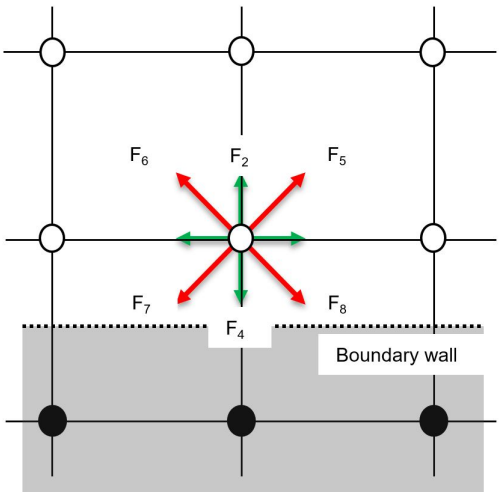

Figure 2.31. – Non-slip boundary condition at a wall located between the solid nodes (black solid circles) and the fluid nodes (open circles). The grey shaded domain stands for the wall position.

To this end, the wall boundary nodes reflect back the incoming distribution functions of neighboring fluid nodes into the opposite direction. The halfway bounce back has been implemented in our model (Zou and X. He 1997), given that it has proven to

give a second-order numerical accuracy. The explicit form of the halfway bounce back is illustrated in Figure 2.31 and the following general expression was proposed:

$$f_{\overline{\alpha}}(x_b, t+\Delta t) = f_{\alpha}^{out}(x_b, t). \tag{2.5}$$

Pressure and velocity boundary condition The same authors have proposed a method to impose a pressure and velocity boundary condition (Zou and X. He 1997), which is based on the assumption that the non-equilibrium part of the distribution function in the direction perpendicular to the boundary (i.e. f_2 and f_4) is kept constant. The corresponding relation reads (Zou and X. He 1997):

$$f_2 - f_2^{eq} = f_4 - f_4^{eq}. \tag{2.6}$$

To impose a pressure boundary condition at the top of a domain, the density needs to be specified (remembering that $\rho = \rho_0 = P_0/{c_s}^2$) while the velocity reads $u = [0, v]$. Using the previous equations 1.43 and 1.44, one can obtain the following relations:

$$f_4 + f_7 + f_8 = \rho_0 - (f_0 + f_1 + f_2 + f_3 + f_4 + f_5 + f_6), \tag{2.7}$$

$$f_8 + f_7 + f_4 = \rho_0 v - (f_6 + f_5 + f_2), \tag{2.8}$$

$$0 = f_5 + f_5 + f_1 - (f_3 + f_6 + f_7). \tag{2.9}$$

In this system containing 3 equations for 4 unknowns (namely f_7, f_4, f_8, and v), a solution can be found by introducing the additional equation 2.6 (Zou and X. He 1997) which finally gives:

$$v = 1 - \frac{f_1 + f_3 + f_0 + 2f_2 + 2f_5 + 2f_6}{\rho_0}, \tag{2.10}$$

$$f_4 = f_2 - \frac{2}{3}\rho_0 v, \tag{2.11}$$

$$f_7 = f_5 + \frac{1}{2}(f_1 - f_3) - \frac{1}{6}\rho_0 v, \tag{2.12}$$

$$f_8 = f_6 - \frac{1}{2}(f_1 - f_3) - \frac{1}{6}\rho_0 v. \tag{2.13}$$

Similarly, the velocity boundary condition is implemented by simply changing the control variable, where the velocity is now imposed whereas the density is unknown, keeping the assumption that the velocity component parallel to the boundary is always zero: $u = [0, v]$. Thus, the unknown quantities are ρ, f_4, f_7 and f_8. Rearranging the previous equations, we obtain the following relations:

$$\rho = 1 - \frac{f_1 + f_3 + f_0 + 2f_2 + 2f_5 + 2f_6}{1 + v_o}, \tag{2.14}$$

$$f_4 = f_2 - \frac{2}{3}\rho v, \tag{2.15}$$

$$f_7 = f_5 + \frac{1}{2}(f_1 - f_3) - \frac{1}{6}\rho v, \tag{2.16}$$

$$f_8 = f_6 - \frac{1}{2}(f_1 - f_3) - \frac{1}{6}\rho v. \tag{2.17}$$

2.2.3. Simulation of a localized hydraulic failure in 3D numerical model using waLBerla framework

The 2D numerical simulation can quickly become insufficient to study the complex phenomena of hydraulic failure, including fluidization, erosion and particle transport. As already explained, the 2D approach uses the trick of the hydraulic radius to create flow paths in the cemented soil, but this is not realistic and may induce local behavior not representative of the real situation. Therefore, we would like to move towards 3D modelling using the waLBerla [5] framework, which is a modern open-source software that supports complex multi-physics simulations. It is specifically designed to address the computational power challenge in computational sciences and engineering, as a framework for massively parallel high-performance computing systems (Balcan, Gonçalves, H. Hu, et al. 2010; Godenschwager, Schornbaum, Bauer, et al. 2013). Additionally, waLBerla's main focus is computational fluid dynamics simulations with several LBM models (BGK, TRT and MRT) and it has the benefit of including a rigid particle dynamics module to simulate particulate systems with the discrete element method (DEM). Also, it enables the efficient simulations of large-scale coupled fluid-particle systems. WaLBerla has been continuously developed since 2007. It was released open-source in version 3.1 in 2017 and published under NU GPL v3 License with tutorials and documentation. Both solvers (LBM and DEM) are implemented inside the same framework, which allows direct access and update of all underlying data structures. The Eulerian fluid grid is divided into fluid cells and solid cells. The particles are mapped onto the Eulerian fluid grid by flagging the cells inside a particle as solid. As in 2D numerical simulation, the hydrodynamic interaction force acting on the individual particles can be computed using the momentum exchange approach, which is subsequently used in the DEM to update the particle position and velocity (Aidun, Lu, and Ding 1998).

As can be noted, waLBerla framework contains all the necessary functions for an effective 3D simulation of the localised hydraulic failure or fluidization of a granular soil. Figure 2.32 presents the specific configuration developed for it, including the boundary conditions (non-slip, outflow, and velocity imposed). The additional work related to the introduction of the solid bond model in the DEM part and the overall coupling was carried out during the twin PhD thesis of Mohammad Sanayei, under

5. https://walberla.net/

the close supervision of Pablo Cuéllar, in the context of the bilateral COMET [6] project between France and Germany (BAM in Berlin and RUB in Bochum). The tool should be operational rather soon and some very preliminary results will be presented in Chapter 4.

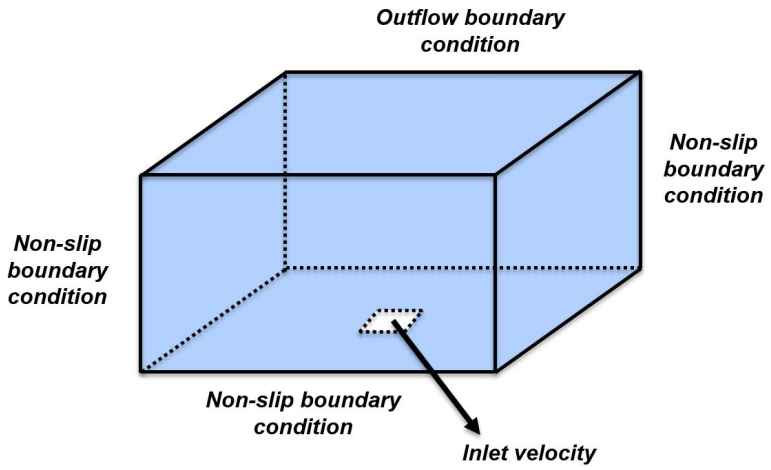

Figure 2.32. – Configuration envisaged and already coded to simulate the localized hydraulic failure of a cemented granular layer with the LBM-DEM coupling of waLBerla framework.

6. https://www6.paca.inrae.fr/recover/Qui-sommes-nous/Nos-equipes/G2DR/COMET

3. Micro-Macro mechanical characterization

Sommaire

This chapter is devoted to the experimental results of the mechanical characterization of our artificial cemented granular material. It first consists in the micro-tests outcomes, including a campaign of micro-tomography visualizations and a theoretical framework to interpret the adhesive force measurements. Then the characterization of the tensile force at the macro scale is presented. Finally, a discussion is proposed to determine the possible roots for the observed intrinsic dispersion and to link the micro and macro scales.

3.1. Micro-scale experimental results

3.1.1. Tensile test

As presented in section 2.1.4, the balance setup is mostly used in our study, with a set of experiments for each type of loading. We performed a parametric study by varying the volumetric paraffin content and the particle diameter. The largest number of micro-mechanical tests on the bonded bead pairs were carried out under tension load, in order to obtain the yield tensile force F_t that quantifies the paraffin bond strength for each test. The results obtained for shear, bending and torsion loads will be presented in a second step.

3.1.1.1. Dispersion

One of the most important results we observed during these tests was the huge and systematic dispersion of the measurements obtained. As exemplified in Figure 3.1, the distribution of the F_t values is extremely wide, although we have done 30 identical tests using exactly the same protocol and extracting the 30 bonded bead pairs from the same macroscopic sample. Moreover, as can be noted, a large amount of tests would be required for the distribution to converge to a definite statistical law.

This very high dispersion in bond strength has been reported in previous investigations (Jarray, Shi, Scheper, et al. 2019; Ham, Martinez, G. Han, et al. 2022). A more detailed discussion about the possible roots for it will be presented in section 3.3.1.

To partially overcome this issue, we had to systematically carry out a large number of repetitions of the measurements, at least 10 and often up to 30, in order to obtain a sufficiently representative mean value for the bond strength. Note also that the error bars used in the following do not correspond to the standard deviation σ of the distribution obtained but to its standard error E, defined by:

$$E = \frac{\sigma}{\sqrt{N}}, \tag{3.1}$$

where N is the population of the distribution.

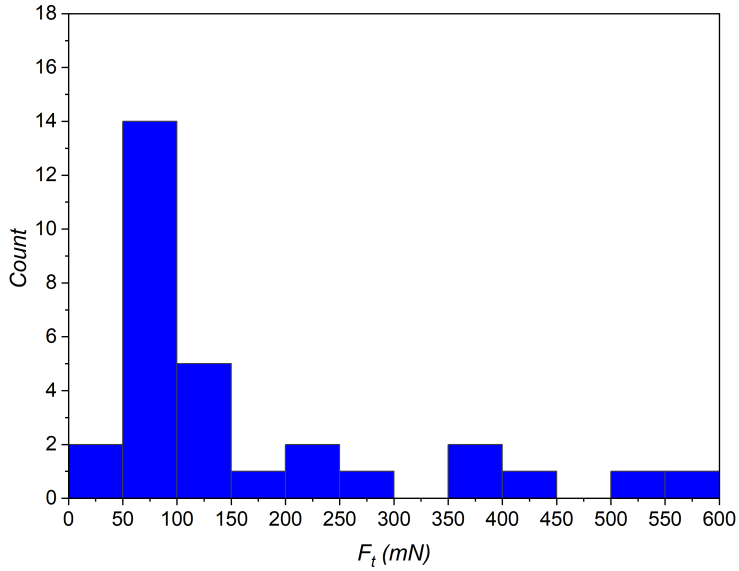

Figure 3.1. – Dispersion of the micro tensile force F_t for a sample made of 4 mm beads with 0.015 paraffin volume content.

3.1.1.2. Influence of particle diameter and paraffin content

Figure 3.2 summarises all our measurements (about 350 individual tests), showing the variation of the yield tensile force with the paraffin volume content ξ_p for different particle diameters d. Each point is obtained by averaging over at least ten measurements, with standard deviations that can exceed 50 % whereas the standard errors are typically around 20 %.

As observed on the graph, increasing the amount of paraffin strengthens the binding regardless of particle size. Furthermore, for the same paraffin content, increasing the particle diameter increases the micro tensile force. It is also worth noting that the standard deviation and standard error increase with both particle size and paraffin content.

Some complementary comments can be made:

- We identified two limitations for the smallest particle size $d = 1.4$ mm. First, when $X_p = 0.2$ %, the bonds became so weak that the extraction of pairs of beads was nearly too challenging. In contrast, for $X_p = 1$ %, we observed the frequent occurrence of paraffin bonds involving more than two beads as previously illustrated in Figure 2.3. This regime of funicular capillary bridges appearing during the preparation of the material at higher paraffin contents is in fact found more generally whatever the diameter of the beads. For paraffin contents less than 1 %, the bonds are solely pendular with a shape that remains almost cylindrical, as previously mentioned in chapter 2.
- Finally, regarding specifically the mean tensile force values obtained for the 7 mm

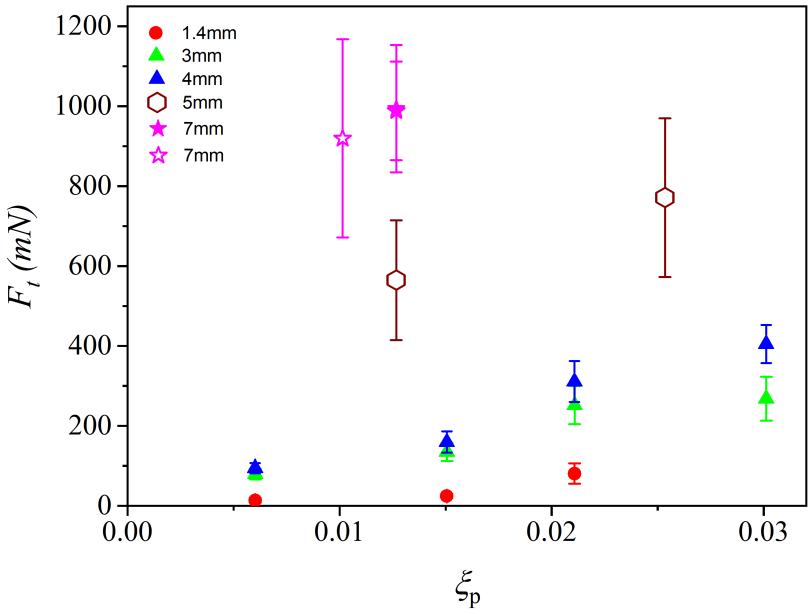

Figure 3.2. – Micro-tensile force F_t as a function of paraffin volume content ξ_p for different bead diameters, from 1.4 to 7 mm. The filled symbols correspond to polished silicate beads while the hollow ones correspond to the matt borosilicate beads.

beads for which the two types of surface finishing (i.e. polished vs matt) could be compared, there is no discernible variation to be attributed to particle roughness in terms of mean value. On the other hand, the error bars seem to be slightly larger when the roughness gets higher.

3.1.1.3. Impact of loading rate and cooling temperature

A series of tests were carried out with the second micro-tensile device, where the velocity of the spring extension, and thus the rate of loading, is constant, controlled by a motor (see section 2.1.4.2). Figure 3.3 presents the loading rate effect on the bond strength using a set of 4 tensile tests conducted per each loading rate with bead pairs extracted from an artificial cemented sample made of 4 mm particles with 0.03 % of paraffin volume content. The results reveal that, at small loading rates, typically below 0.1 mm/sec, there is a slight variation of the yield tensile force but still compatible with an almost constant value, around 600 mN. On the contrary, at higher loading rates, typically above 0.15 mm/sec, a substantial increase is found, with the bond strength being nearly 2 to 3 times larger than the preceding yield value. In our study, the speed is always fixed between 0.05 and 0.1 mm/sec, where the loading rate has a weak impact.

The effect of the cooling techniques has also been investigated by: allowing the

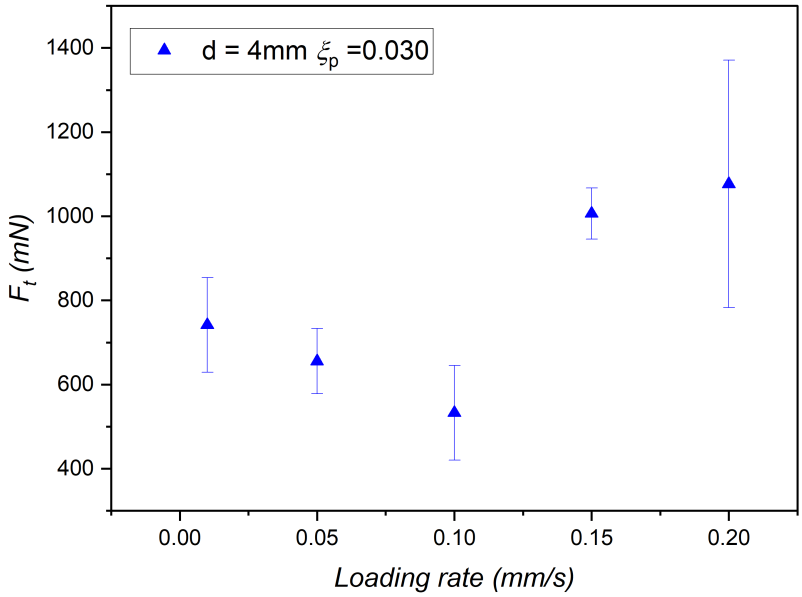

Figure 3.3. – Effect of the loading rate on the micro yield tensile force.

sample to cool and solidify (i) in the macroscopic device at room temperature (test 1), (ii) in a casserole pan at room temperature (test 2), or (iii) in a casserole pan using an accelerated cooling procedure (test 3). By looking at the corresponding results presented in Table 3.1 below, we can notice that cooling the sample at room temperature is associated to a smaller mean value of F_t either within the macroscopic device (test 1) or within the casserole pan (test 2). The difference between tests 1 and 2 lies mainly in the contact surface between the sample and air, which is significantly larger in the large pan compared to the neck cross-section of the macroscopic device, and in the thickness of the sample, only 4 cm in the pan while the macroscopic device has a height of 10.8 cm. Note that in the table, we additionally specify the location of the sample extraction area: at the neck between the two cones for test 1 and either at the surface or the bottom of the pan for tests 2 and 3. We notice that the micro tensile force is almost the same between test 1 and test 2 with extraction at the upper surface. On the contrary, a higher bond strength is found when the sample extraction is performed from the bottom of the casserole pan, possibly due to some infiltration of the liquid paraffin to the bottom of the casserole pan during the slow cooling. The accelerated cooling procedure in test 3 is conducted by placing the casserole pan inside a cold bucket and leaving it there until the next day. When we compare the results of tests 2 and 3, we can see that, except the value found at the surface in test 2, all data are consistent. Overall, the bond strength seems to increase with the cooling rate (test 1 < test 2 < test 3). However, the dispersion of the results highlighted above, as well as the low statistics involved here, do not allow a totally definitive conclusion to be

drawn on the possible impact of the cooling procedure. Apart from a few exceptions, the test 1 procedure was the one used in our tests.

	Test 1	Test 2		Test 3	
	Neck section	Surface	Bottom	Surface	Bottom
Mean F_t (mN)	162	186	293	275	292
Standard error (mN)	27	40	53	38	41
Average F_t (mN)	162	237		282	

Table 3.1. – Influence of the cooling procedure on the yield micro-tensile force.

3.1.2. Shear, bending, and torsion micro-tests

3.1.2.1. Dispersion

Thanks to the adaptations of the microscopic setup presented in the previous chapter and sketched in Figure 2.13, an additional substantial number (about 180) of bond strength tests were carried out also for shear, bending and torsion loads. Here again, a parametric analysis was performed with different particle sizes (3, 4 and 7 mm) and two distinct mass paraffin contents (0.5 % and 1 %).

The corresponding yield values are the shear force and the bending and torsion moment, with the moment being equal to the force multiplied by the length of the lever arm plus the radius of the glass bead. The bending moment M_b causes bending stress to be induced in the paraffin bond, which is aligned in the normal axis of the bond's cross-section to the bending moment. Note that the bond is subjected to a very small compression force which is negligible. The torsion moment M_{to} is the twisting along the axis of a paraffin bond. It is worth noting that the bond in our tests is subjected to a relatively tiny shear force.

Similarly to the micro tensile measurements, a huge and perhaps even wider dispersion of the yield shear force is found, as shown in Figure 3.4. The same conclusion can be made for the bending moment in Figure 3.5 and for the torsion moment in Figure 3.6.

3.1.2.2. Relevance of the yield moment for bending and torsion

As mentioned earlier, the relevant mechanical quantity for bending and torsion is assumed to be the moment, not the force. This means in particular that the location of the point of application of the force on the rod is crucial, a larger force being required when the point of application gets closer to the particle's center. A series of tests was carried out specifically to check this statement and thus validate the relevance of the moment for bending and torsion. To this end, as sketched in Figure 3.7, two different points of application of the force on the wooden rod were used, and also two different rod lengths. The values of the moments are indeed almost the same, especially for bending, whatever the lever arm and the rod length as presented in Table 3.2.

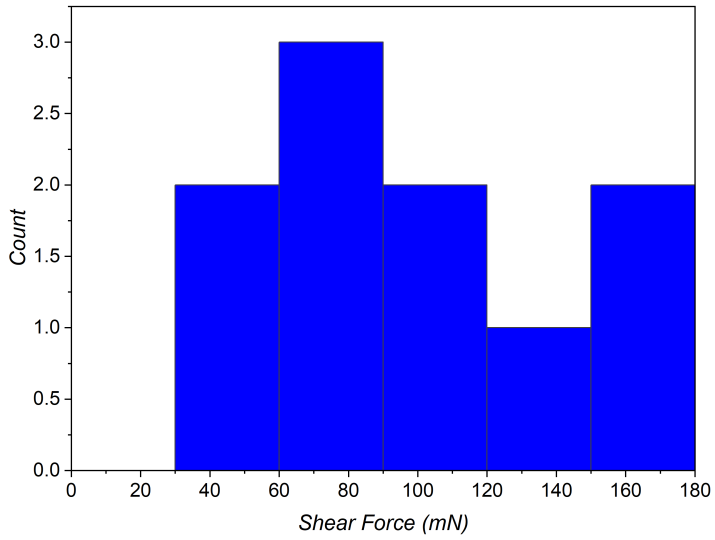

Figure 3.4. – Typical dispersion of the yield shear force of bonds for bead diameter of 3 mm and paraffin volume content of 0.015.

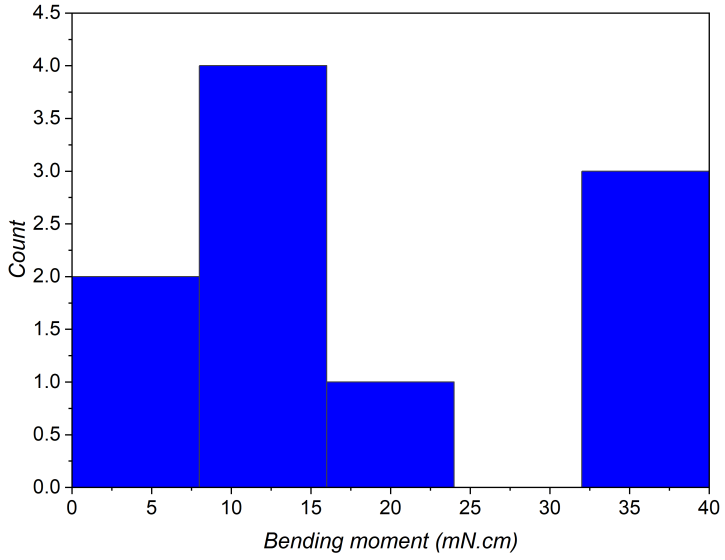

Figure 3.5. – Typical dispersion of the yield bending moment of bonds for bead diameter of 3 mm and paraffin volume content of 0.015.

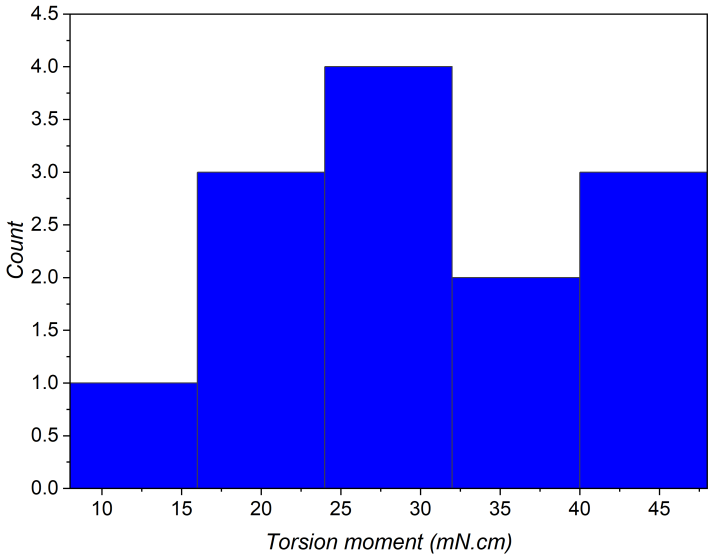

Figure 3.6. – Typical dispersion of the yield torsion moment of bonds for bead diameter of 3 mm and paraffin volume content of 0.015.

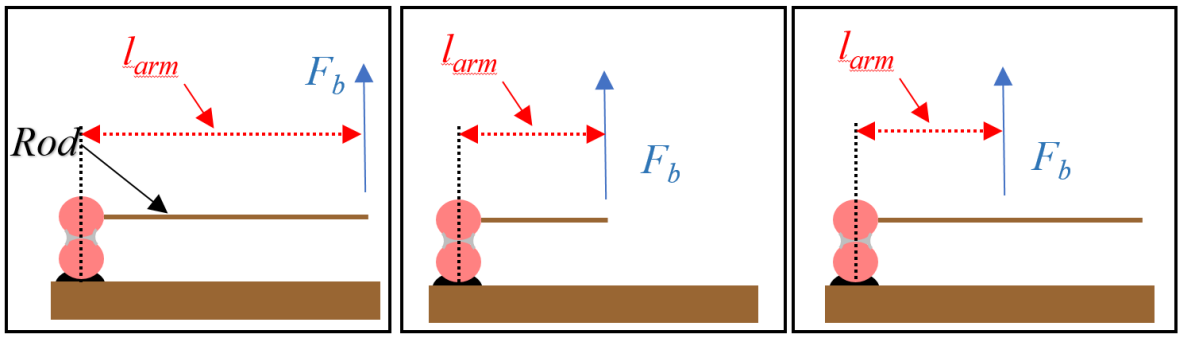

Figure 3.7. – Different points of application of the force for the case of bending and torsion: (left) full stick edge of lever arm, (middle) half stick edge of lever arm, and (right) full stick half the lever arm.

3.1.2.3. Further investigation of bending and torsion by image processing

As presented in the previous chapter and illustrated in Figure 2.15, an unexpected time evolution of the spring force is found in most cases for bending and torsion micro-tests. Here we present the results of a deeper investigation that allows us to interpret this development. For this purpose, some standard bending and torsion tests were carried out but coupled with high resolution image acquisitions of both the spring and the bead pair under load, as detailed previously in section 2.1.4.3.

The image sequence of the spring during a test allows, by simple image processing using the software tool ImageJ, to measure the extension of the spring and to ascertain

		Bending		Torsion	
Rod length (cm)	Lever arm (cm)	Force (mN) (mN)	Moment (mN.m)	Force (mN)	Moment (mN.m)
4.5	4.5	41	1.85	47	2.12
2.25	2.25	80	1.80	88	1.98
4.5	2.25	83	1.87	67	1.51

Table 3.2. – Forces and moments obtained, for different lever arms and rod lengths in the case of bending and torsion loads, for bead diameter of 7 mm and paraffin volume content of 0.013.

that the force recorded by the sensor corresponds to Hooke's law. Note that, as the spring is manufactured and positioned by hand, its stiffness is not always exactly the same and its actual value is only obtained after prior adjustment. Moreover, adding flags glued to the two beads and the wooden rod as presented in Figure 3.8, another post-processing on the second image sequence allows in particular to measure the angle between the rod and the horizontal in order to study its evolution over time.

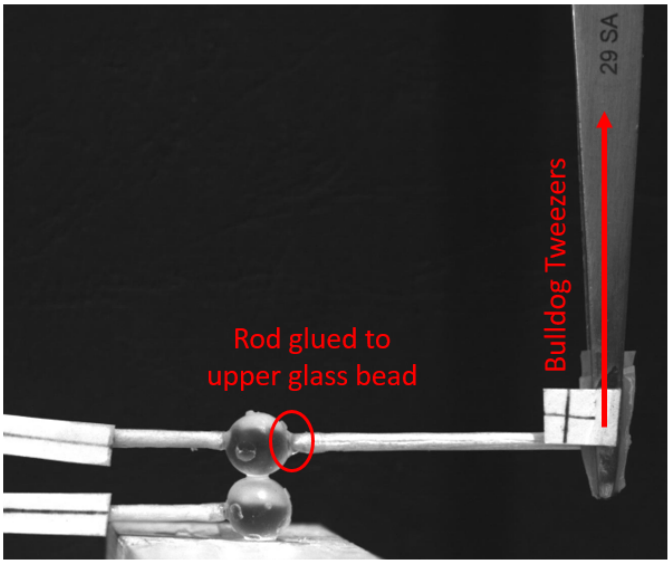

Figure 3.8. – Fixation of the rod to the upper glass bead and positions of the flags.

To begin, we examined the minority case (in about 40 % of our tests), presented in Figure 3.9, where the evolution of the force is similar to those observed for both tension and shear, namely a monotonic increase up to an abrupt drop that can be associated with an instantaneous rupture of the solid bond.

The force-displacement graph can be recovered using the spring elongation and stiffness ($F = k\Delta l$), where the spring elongation is obtained using ImageJ. When we plot in Figure 3.9 the recorded measurement by the sensor and the one recovered using the elongation of the spring $\Delta l(t)$, we indeed found a very good agreement of both curves. Using the implanted flag, we also checked that the upper bead bearing

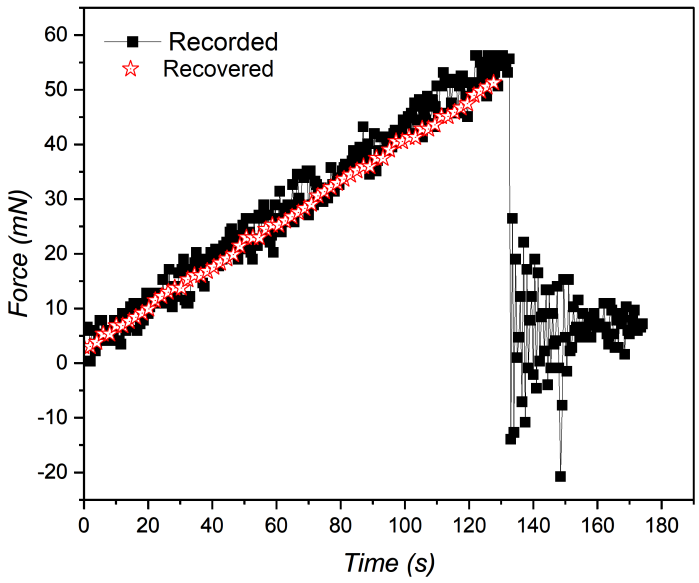

Figure 3.9. – Comparison between the recorded measurement and the recovered one using the post-processing images of the spring elongation for a bending test for 7 mm particles and 0.5% paraffin content.

the wood rod remains motionless and does not rotate during the test. It is important to note that we had to wait 20 minutes for the glue to dry before starting the test, otherwise, the glue being not yet solidified, we could observe a solid rotation of the whole bonded bead pair as a rigid system, consistently with what was observed in the X-ray tomography study (see Figure 3.17 in the next section 3.1.3). For this typical test, the rupture observed at the end of the test is an adhesive one, where an instantaneous crack propagation occurs at the interface between the paraffin and glass bead (the different types of rupture have been initially presented in Figure 1.15).

Next, we examined, in the same way, the unexpected non-monotonic force signal with an intermediate drop and two distinct slopes before and after this drop, as shown in Figure 3.10 and found in about 60 % of our tests. This typical force signal has been systematically observed in the case of mixed bond ruptures (defined in Figure 1.15).

By post-proceeding the image sequence of the spring elongation during the test, we could again observe a good agreement between the recovered values and the measured instantaneous force reduction during the initial linear phase. This adjustment remains acceptable for the second linear increase. This result means that the drop is due to a corresponding decrease in the elongation of the spring. To address this issue, we must consider three probable causes for it: rod bending, loss of rod fixation (either by sliding with respect to the tweezers or at the glued contact with the upper glass bead), and lastly rotation of the upper bead by inclination of the rod.

First, since we have used a metallic rope linking the bulldog tweezers to the spring, the reason for the sudden displacement could be only related to the rod. However,

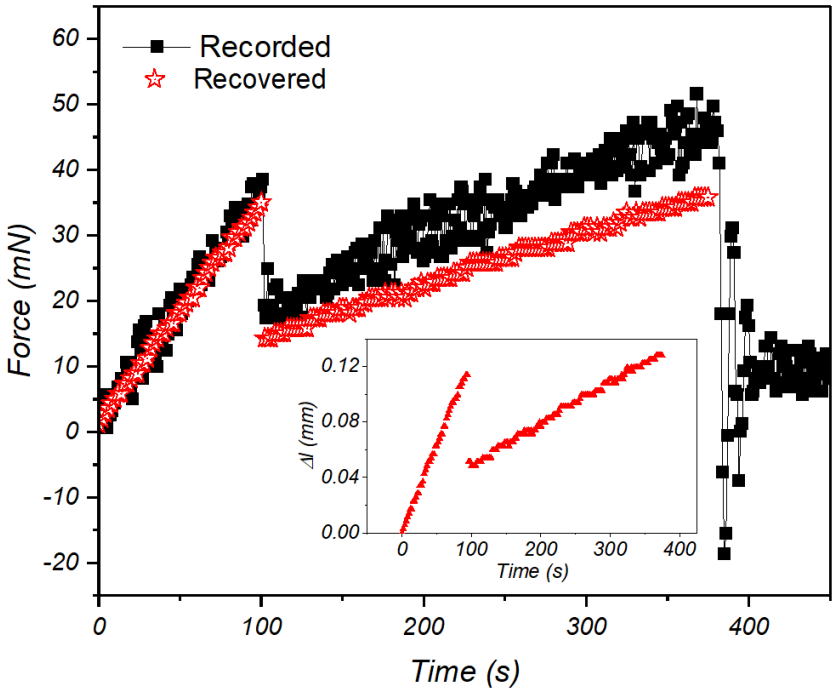

Figure 3.10. – Comparison between the recorded measurement and the recovered one using the post-processing images of the spring elongation in the case of unexpected force signal for a bending test for 7 mm particles and 0.5% paraffin content. Inset: Elongation of the spring as a function of time.

because of the high rod's stiffness in comparison to the force magnitude, any substantial buckling deformation must also be excluded. Secondly, we did not observe any movement or detachment of the glue in the image sequence recorded during the test. It was furthermore really difficult to separate by hand the rod from the glass bead (in the configuration of Figure 3.8). The last point is thus to check that there is actually a rotation of the rod, leading to a reduction in the length of the spring. This is done with some image processing from the sequence recorded with the camera focused on the bonded beads. Figure 3.11 presents successive stages of bond rupture for the test of Figure 3.10. The analysis of the sequence did indeed reveal a variation in the inclination θ of the rod during the test, as shown in Figure 3.12. We first observe a zero value for θ, then an instantaneous jump, but limited in amplitude, at $t \approx 100\ s$, followed by a regular increase until a value of about $3-3.5°$ at which the bridge finally breaks.

In summary, by bringing together all the different information (processing of the image sequences from the two cameras and direct visualisation of the images), it is possible to explain what is happening in this particular test, which is however perfectly representative of all the tests in which such an intermediate crisis has been observed. At the beginning, the evolution is normal, with the slope of the first linear part being exactly equal to the stiffness of the spring (see Fig. 3.10). Then, at $t \approx 100\ s$, a crack was

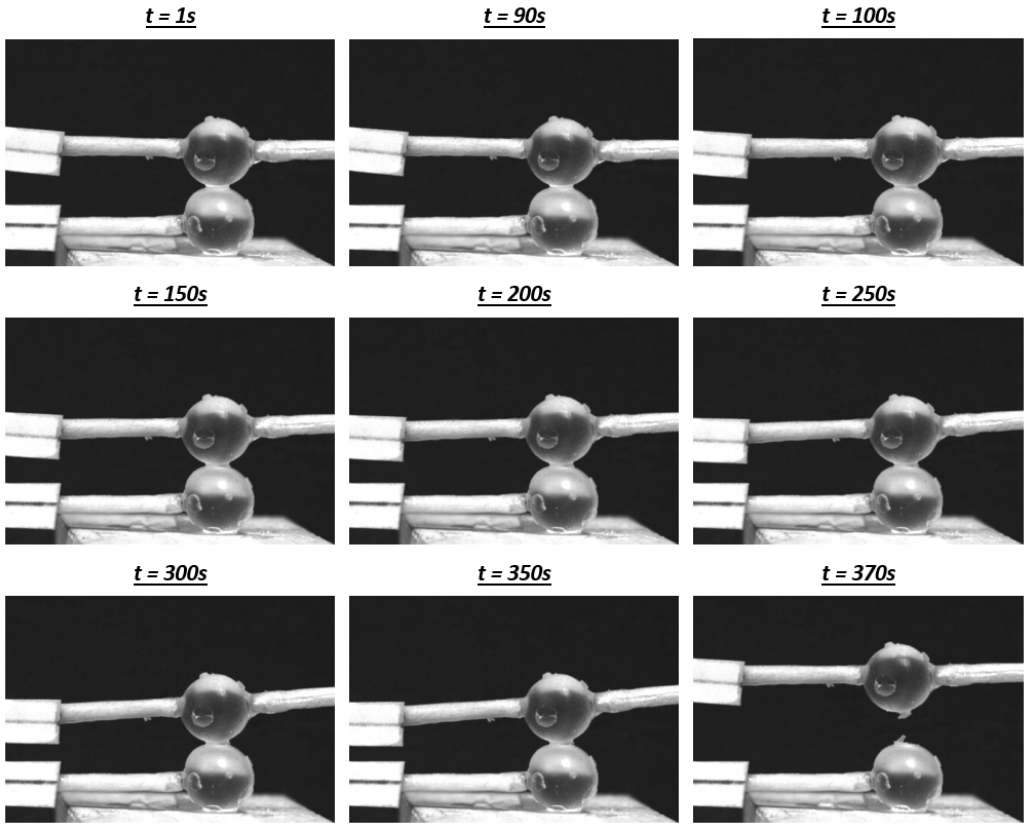

Figure 3.11. – Snapshots of the rotation of the upper glass bead in the case of unexpected force signal.

suddenly initiated in the bond, typically at the contact between the bottom of the glass beads and the paraffin, where the peak stress is expected. Consequently, there was a sudden jump in the rod inclination, which led to a decrease in the elongation of the spring and thus to the observed drop in the force signal. Then, for $t > 100\ s$, the slope of the second almost linear part in Fig. 3.10 gets smaller since the progressive inclination of the rod was limiting the further elongation of the spring and thus the loading rate. The fact that the rod inclination is continuously increasing in Fig. 3.12 means that the initiated fracture was propagating even though the loading has dropped, thus weakening the paraffin bond which eventually failed generating a mixed type rupture as can be seen in the last picture in Fig. 3.11.

The final conclusion is that for some tests (about 40 % in this study) the paraffin bond is not damaged during loading until it breaks instantly by adhesive rupture. In the other cases, there is at some point a partial damage, related to the initiation of a tiny fracture, which, by a geometrical feedback effect induced to the insertion of a spring in our experimental device, significantly reduces the force applied and thus considerably delays the final mixed-type rupture of the bond.

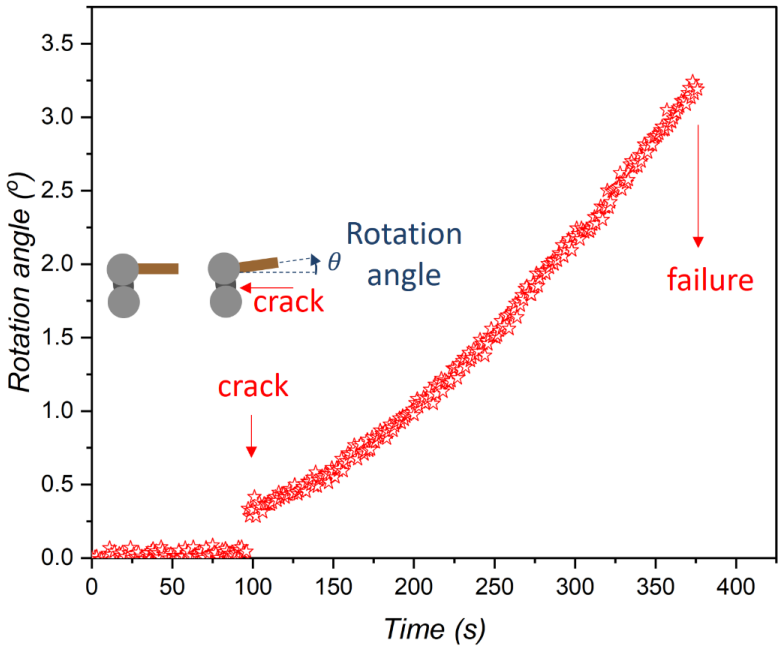

Figure 3.12. – Rotation of the upper glass bead in the case of a typical unexpected force signal.

3.1.2.4. Overall proportionality assumption

Since the observed evolutions for the critical values of the other types of loading show the same trends as for tension, and in order to reasonably simplify the theoretical model we wish to propose for the failure of an adhesive solid bond between particles, we propose to assume a direct proportionality with the yield tensile force. Note that this assumption is consistent with our previous numerical modeling studies with cemented granular soils (Benseghier, Cuéllar, Luu, Bonelli, et al. 2020).

In practice, the yield shear force F_s is supposed proportional to the micro tensile force F_t with the corresponding coefficient C_s, as follows:

$$F_s = C_s F_t. \tag{3.2}$$

For both bending moment M_b and torsion moment M_{to}, an additional length is required, which is obviously the particle diameter d, in order to propose similar relations with the introduction of the coefficients C_b and C_{to}:

$$M_b = C_b d F_t, \tag{3.3}$$

$$M_{to} = C_{to} d F_t. \tag{3.4}$$

Figure 3.13 depicts the corresponding linear regressions (with zero intercept) for all the data (see Table 2.3). The agreement between the proportionality model and the mean values is acceptable, especially in view of the dispersion observed for the three

quantities, and similarly for the yield tensile force, whose standard errors are shown in the graph. The coefficients found are $C_s = 0.41$ for shear with $R^2 = 0.903$, $C_b = 0.37$ for bending with $R^2 = 0.919$, and $C_{to} = 0.46$ for torsion with $R^2 = 0.959$, respectively. It is critical to note that the forces to be measured to quantify torsion are extremely small, which increases the uncertainty.

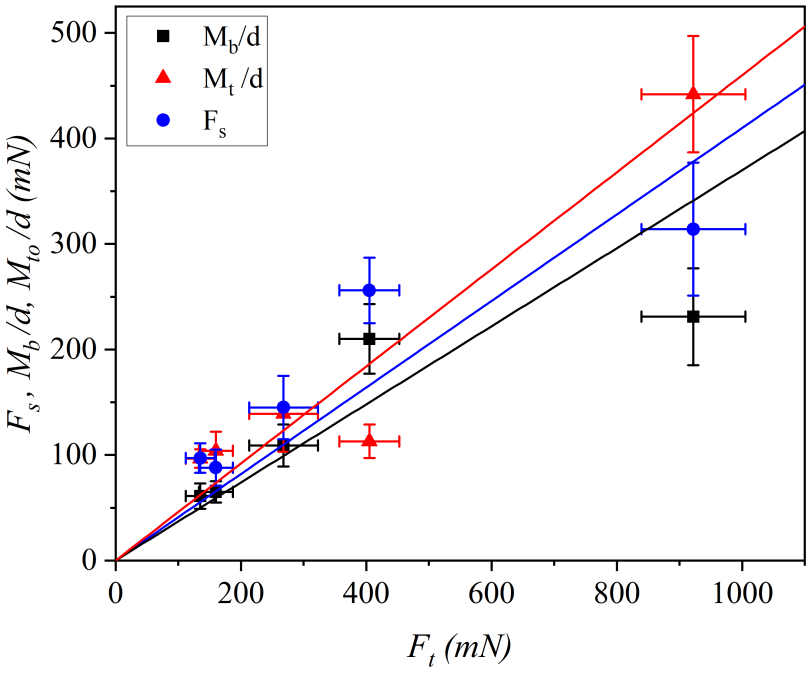

Figure 3.13. – Linear regressions with zero intercept for the critical values of the shear force F_s, the bending moment M_b/d, and the torsion moment M_{to}/d as a function of the yield tensile force F_t.

3.1.3. X-ray tomography study

In this section, we present a complementary study of the bond rupture under the different solicitations considered before, using X-ray tomography imaging. As presented in chapter 2 (see section 2.1.4.3), we had the opportunity to conduct an experimental campaign in the MATRIX platform at CEREGE laboratory (Aix-en-Provence), which aimed to reproduce *in operando* the micro-mechanical characterization of our artificial cemented soil. In practice and as already presented, we have changed the initial balance setup to a new setup involving a force sensor (see Figure 2.12) that fits into the tomography chamber. The main objective of these additional experiments is to discuss the origin of the large statistical dispersion found in our measurements by correlating the force time evolution with the type of rupture observed (adhesive,

cohesive, mixed). By optimising the spatial and temporal resolution range of the micro-tomographic acquisition, we propose to perform a step-by-step monitoring of the detachment between two bonded particles. The tomography setup parameters are as follows: For a resolution of pixel size 3.64 µm and an acquisition rate of 1 s, we succeeded in performing several 2D X-ray radiographs during a micro-mechanical test. Two complete 3D constructions requiring several hours of acquisition were done additionally.

d (mm)	Surface roughness	X_p (%)	Tensile	Shear	Bending	Torsion	Binder
7.0 ± 0.3	P	0.5	2	-	-	-	PP
	M	0.5	3	2	1	2	PP
	M	0.5	2	2	-	-	PG
	M	0.5	2	2	-	-	PH

Table 3.3. – Parameters of the experiments performed within the X-ray tomography device. P: polished; M: matt; PP: pure paraffin; PG: paraffin mixed with graphite powder; PH: paraffin mixed with hollow micro-spheres. Note that the numbers in the table correspond to the number of tests performed.

We carried out a two days campaign exclusively on 7 mm glass beads with 0.5 % paraffin mass content with at least two experiments per type of solicitation, namely for the tensile, shear, bending, and torsion tests. The tests performed are summarized in Table 3.3. Figure 3.14 displays a typical 2D imaging by radiography for an adhesive bond, where the rupture by tension occurs at the contact surface between the lower glass bead and the paraffin bridge. Note that very similar images are found for shear-induced rupture. Regarding the shear load, Figure 3.15 presents the results of two identical tests where the shear force follows the same curve against the displacement of the upper translation plate, with a slope consistently equal to the stiffness of the spring. This expected finding has also been observed for all the tensile tests performed *in operando*.

In contrast, we do not find a similar evolution or a linear increase of force with displacement neither in torsion nor in bending tests. As shown in Figure 3.16, the slope of the torsion test 2 is consistent with the spring stiffness, but this is not the case for test 1. In fact, from the pictures acquired by the tomography imaging and displayed in Figure 3.17, we can see that the pair of bonded beads and the rod as a whole rotates as the displacement of the upper plate increases. This rotation affects the loading rate as well as the form of the curve, resulting in a non-linear trend involving a decrease in the force recorded. This behavior was found to be due to an insufficient drying time for the glue fixing the sample to the bottom support. The entire system is then stuck by the glue but not resistant enough to prevent rolling.

As can be seen in the previous images, the paraffin bonds appeared with a rather low grey level, difficult to discern from the ambient air, even after optimising the exposure setting. This limitation in the tomography visualization is due to the huge difference

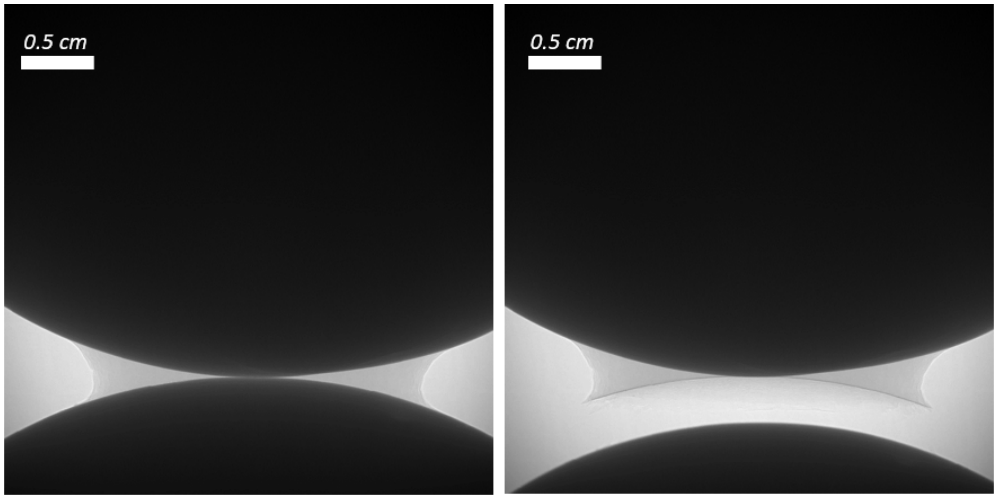

Figure 3.14. – 2D visualization of an adhesive rupture of the bond after a tensile test on a pair of matt beads of 7 mm with 0.5 % pure paraffin.

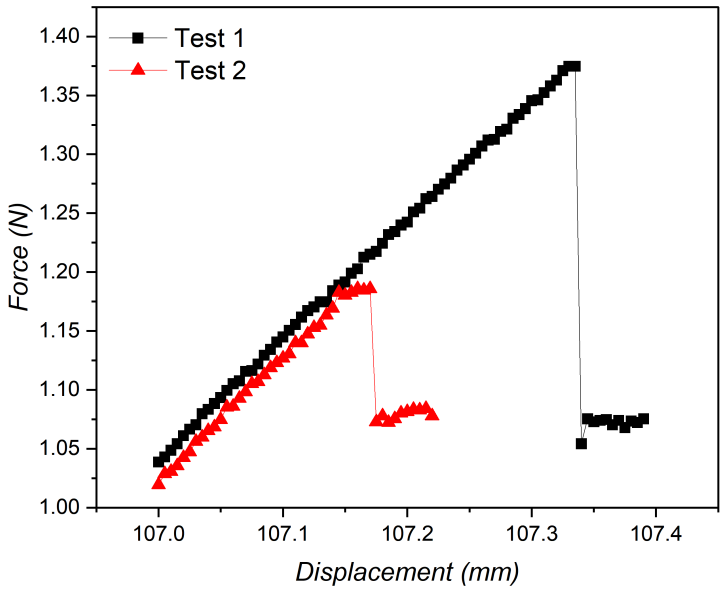

Figure 3.15. – Shear force recorded measurements for a pair of matt glass beads of 7 mm with 0.5 % pure paraffin.

in X-ray absorption between the glass beads and the paraffin. In an effort to overcome it, we tried adding to the liquid paraffin small solid particles with a high absorption capacity, either powder of graphite or hollow glass micrometer spheres, prior solidification of the bonds. Figure 3.18 displays a comparison of bond imaging for pure paraffin and with both graphite powder and hollow micro-spheres addition. Unfortu-

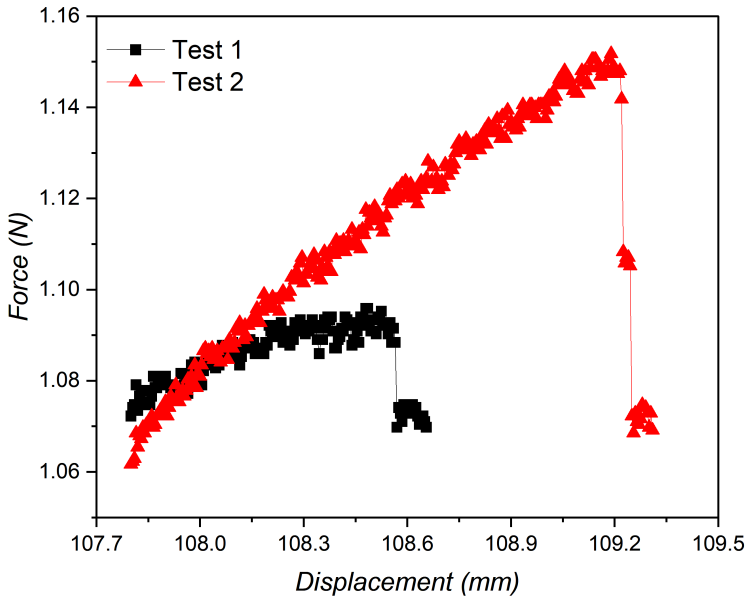

Figure 3.16. – Torsion force recorded measurements for a pair of matt glass beads of 7 mm with 0.5 % pure paraffin.

nately, in both cases, the improvement is not very significant. As shown in Figure 3.19, the hollow micro-spheres did increase a little the contrast of the bond, which looks darker. However, when we zoomed in, we can detect some black spot representing the micrometer particles that seem therefore inhomogeneously dispersed. A more systematic experimental study would be necessary to conclude on the effectiveness of these contrast agents, in particular by varying their concentration and improving the preparation method for better homogeneity.

Finally, we carried out a few full 3D tomographic reconstructions of bonds after rupture. One acquisition typically takes 4 to 7 hours. Figures 3.20 and 3.21 show an adhesive rupture and a mixed rupture, respectively. The latter, which exhibits a rupture that occurred partly within the bond itself (as previously sketched in Figure 1.12), has been observed only once, for the bending test with 7 mm glass beads and 0.5% PP. From the previous 2D pictures, and even more so, these high-resolution 3D images, we can confirm both, that the particles were initially in contact based on the presence of the central dome, and that there is no paraffin covering the particles outside the bond itself. Note finally that, as particularly visible on the 3D view of the adhesive rupture, the edge of the paraffin bridge forms a very thin layer, which probably flowed to a flattened crown after its detachment from the upper particle.

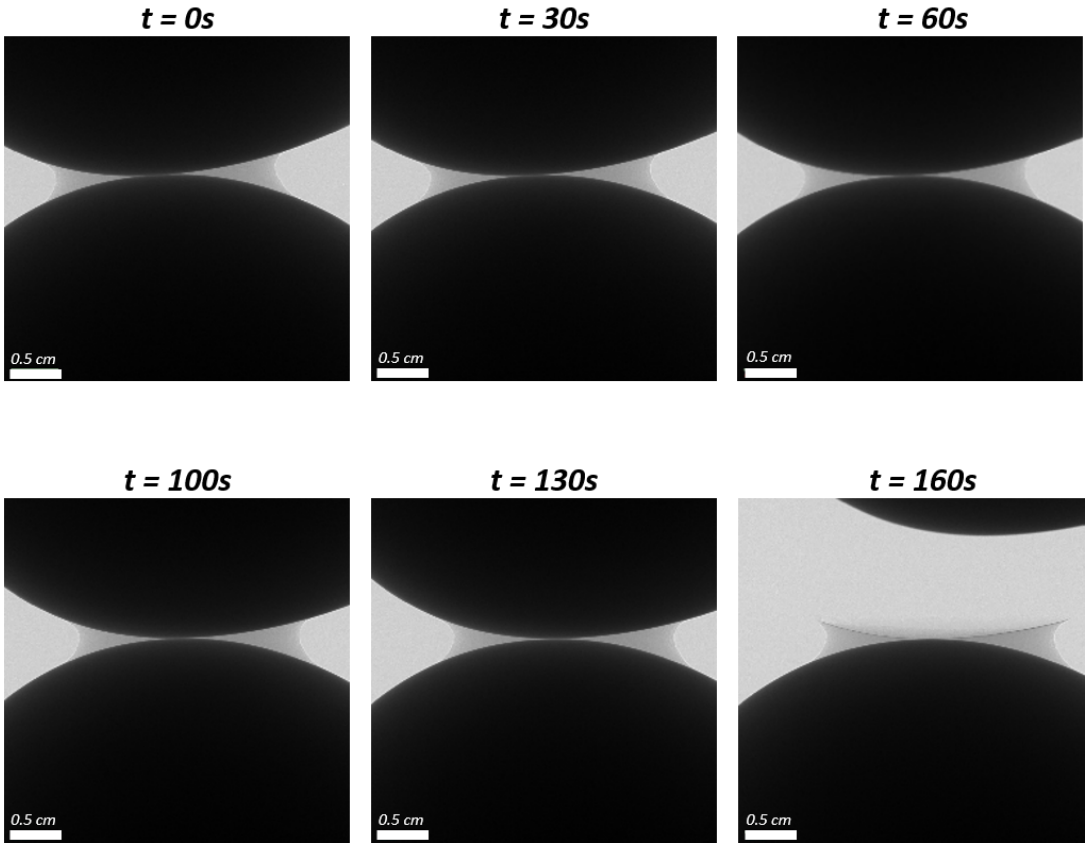

Figure 3.17. – Successive scans showing the solid rotation of the whole system (both beads with bond) under the action of the torsion moment applied by the rod on a pair of matt glass beads.

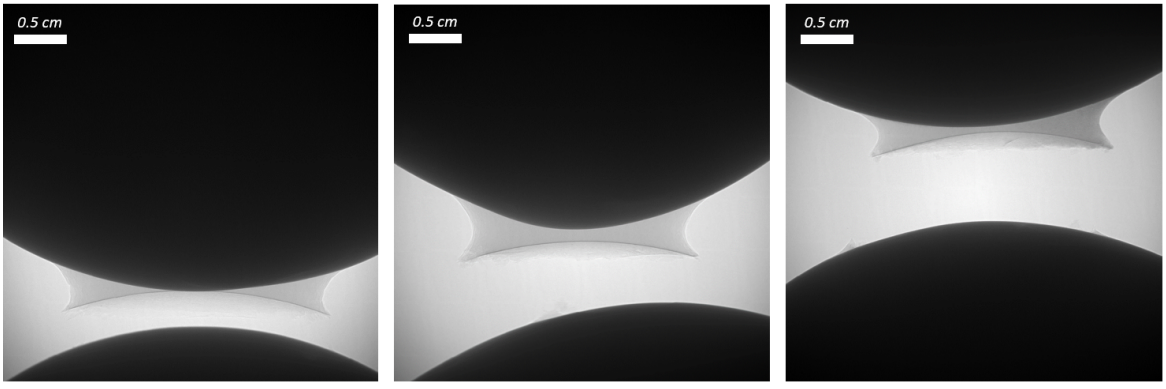

Figure 3.18. – Comparison on the contrast of bond between using: (left image) Pure paraffin (PP); (middle image) paraffin mixed with about 0.8 % of graphite powder (PG); (right image) paraffin mixed with about 0.5 % of hollow micro-spheres (PH).

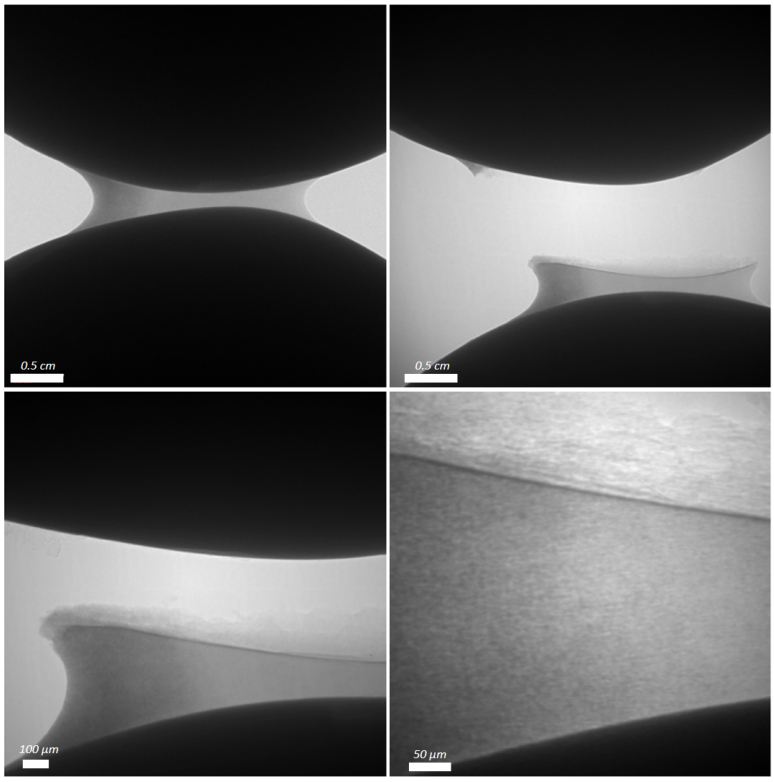

Figure 3.19. – Effect of adding about 0.5 % of hollow micro-spheres in paraffin on the contrast of the bond.

3.1.4. Theoretical framework

3.1.4.1. Proposal of a scaling law for adhesion debonding

This section proposes a theoretical model for the tensile force required to separate a paraffin bridge from a glass bead by considering an adhesive rupture between the two solid bodies in contact, considered both as perfectly rigid. Therefore, this approach clearly differs from the usual Johnson-Kendall-Roberts (JKR) contact model, which is preferentially suited for soft bond contacts (Kendall 1971; Chung and Chaudhury 2005; Yamaguchi, Biswas, Hatano, et al. 2020), to be much in line with some analytical elements originally developed by Ingles (Ingles 1962) for a rigid bond and with other more recent modelings (Brendel, Török, Kirsch, et al. 2011; Ergenzinger, Seifried, and Eberhard 2011; Affes, J.-Y. Delenne, Monnerie, et al. 2012; Horabik and Jozefaciuk 2021). The theoretical framework proposed considers the following assumptions:

1. The mechanical load is assumed to be small enough so that the elastic deformation of the solid bridge can be neglected. This hypothesis will be verified afterwards. Note also that the deformation of the particles is even smaller since the beads are stiffer than the bridge. The glass particles Young's modulus $E_g \sim 65-70$ GPa is indeed much higher than the paraffin wax's one $E_p \sim 100-200$ MPa.

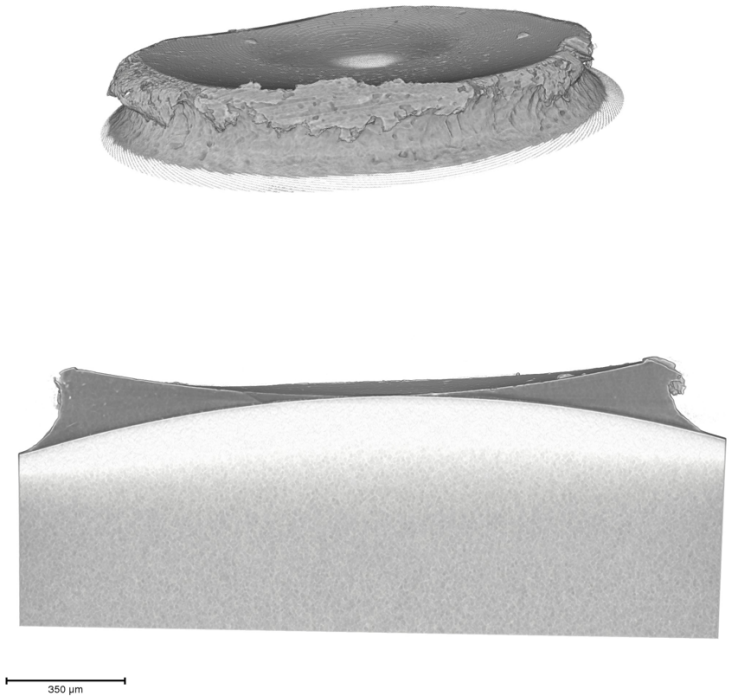

Figure 3.20. – 3D view of an adhesive bond rupture after a shear test.

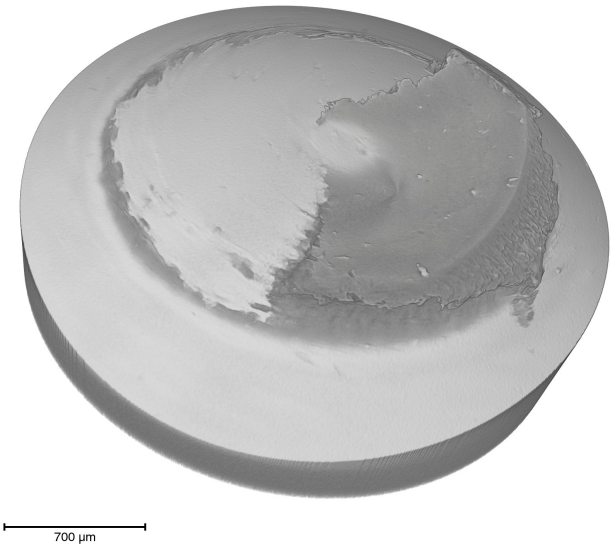

Figure 3.21. – 3D view of a mixed bond rupture after a bending test using 7mm matt glass beads with 0.5% PP

2. By considering two perfectly rigid bodies A and B sharing a common contact surface $d\Sigma$, we assume that the elementary force $\vec{dF}$ needed to perpendicularly debond the interface, i.e. to separate the two bodies, simply reads $\vec{dF} = \sigma_{AB}\vec{d\Sigma}$, where $\vec{d\Sigma}$ is the normal vector to $d\Sigma$ and σ_{AB} is the corresponding adhesive strength between solids A and B, also sometimes called adherence (Topin, J.-Y. Delenne, Radjai, et al. 2007).

3. The shape of a solid bridge is represented by a simplified geometry made of a cylindrical lateral envelope at the region of contact between the two bonded particles which are taken spherical. Moreover, all the bridges are assumed to be strictly identical while the particles they connect are supposed to be exactly in contact, consistently with our previous observations. Therefore, the volume of a bridge is that of a cylinder to which it is necessary to subtract 2 spherical caps as shown in Figure 3.22. Considering the mode of preparation of our samples, this implies that there is a perfectly uniform distribution of the liquid paraffin within the glass beads. We will further consider that the totality of the introduced paraffin is ultimately located in the bridges, neglecting any coating on the surface out of the contacts. This appears certainly too schematic but nevertheless rather compatible with the observed visualizations, where no paraffin layer was visible on the surface of the beads, even in the micro-tomographic views.

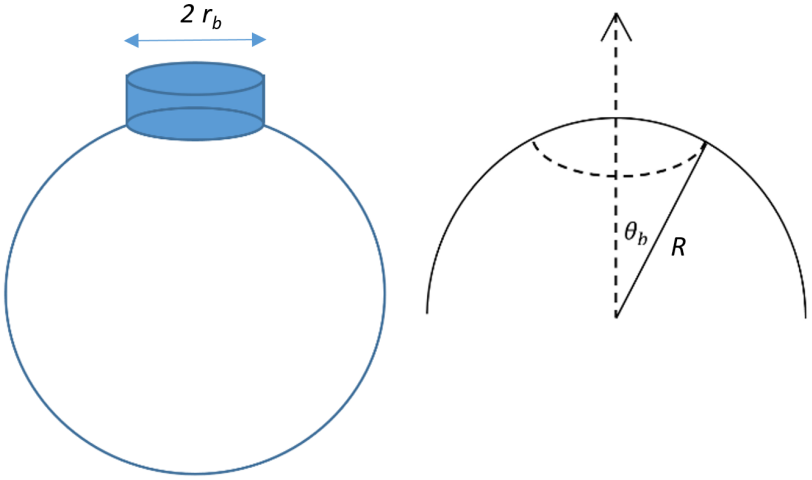

Figure 3.22. – Scheme for modeling a paraffin bridge in contact with a particle.

Based on the second hypothesis and with the introduction of the adhesive strength σ_{gp} between glass and paraffin, the force required to detach a paraffin bridge (parameterised by the angle θ_b as shown in Figure 3.22) from the surface of a glass sphere of radius R is obtained by integration over the contact surface:

$$F_t = \int_0^{\theta_b}\int_0^{2\pi} \sigma_{gp} R^2 \sin\theta\cos\theta\, d\theta\, d\varphi = \sigma_{gp}\pi R^2 (\sin\theta_b)^2 = \sigma_{gp}\Sigma_b, \qquad (3.5)$$

where Σ_b is the cross-section of the cylindrical bridge whose radius is $r_b = R\sin\theta_b$. One can alternatively express F_t in a dimensionless form:

$$\overline{F_t} = \frac{F_t}{\sigma_{gp}\pi R^2}. \tag{3.6}$$

Note that a very similar expression as Eq. 3.5 is expected for a cohesive rupture, i.e. when the rupture occurs within the paraffin bridge itself. One can indeed consider that the failure surface is almost normal to the z-axis, and its area would therefore correspond approximately to Σ_b. Then σ_{gp} needs to be replaced by the intrinsic cohesive strength of paraffin, σ_{pp}, which is usually referred to as the ultimate tensile strength. For full consistency, the relation $\sigma_{gp} < \sigma_{pp}$ must be verified.

The relation between the paraffin volume content ξ_p and the bond angle θ_b is obtained relying on the third assumption, considering that liquid paraffin is exclusively located within the bonds, the latter being all identical, and that the glass spheres connected by each bond are in actual contact. The shape of a bond is consequently a cylinder minus two spherical caps and, after minor calculations, the corresponding volume V_b reads:

$$V_b = \frac{2\pi}{3}R^3(1-\cos\theta_b)^2(1+2\cos\theta_b). \tag{3.7}$$

This expression can also be written in a dimensionless form as:

$$\overline{V_b} = \frac{3V_b}{4\pi R^3} = \frac{1}{2}(1-\cos\theta_b)^2(1+2\cos\theta_b). \tag{3.8}$$

In a given sample, denoting by N the number of spherical glass beads (of same radius R) with a mean coordination number Z, the total number of bonds is $\frac{Z}{2}N$. Then, we can determine in the sample the volume of paraffin V_p and glass V_g, respectively:

$$V_p = \frac{Z}{2}NV_b, \tag{3.9}$$

$$V_g = N\frac{4}{3}\pi R^3. \tag{3.10}$$

This gives the following expression for the paraffin volume content ξ_p:

$$\xi_p = \frac{V_p}{V_g} = \frac{Z}{2}\overline{V_b}. \tag{3.11}$$

Considering $\overline{F_t}$ and $\overline{V_b}$, there is no obvious one-to-one relationship. However, the following combination can be used:

$$\frac{\overline{F_t}^2}{\overline{V_b}} = \frac{2\sin^4\theta_b}{(1-\cos\theta_b)^2(1+2\cos\theta_b)} = 2\left(1+\frac{\cos^2\theta_b}{1+2\cos\theta_b}\right). \tag{3.12}$$

Then, since θ_b cannot much exceed $\frac{\pi}{6}$ (limit case of a pendular bridge in a locally ordered arrangement of spheres), we can use the following approximation for $\theta \in \left[0, \frac{\pi}{6}\right]$:

$$\frac{\overline{F_t}^2}{\overline{V_b}} = 2.63 \pm 0.04. \tag{3.13}$$

This minor approximation finally allows the following explicit semi-theoretical law to be proposed for the adhesive bond force with an accuracy of ±0.8%:

$$F_t = \sigma_{gp} 1.62\pi \sqrt{\frac{2}{Z}} \sqrt{\xi_p} R^2. \tag{3.14}$$

The two only unknowns in this expression are σ_{gp}, the adhesive strength at the interface between glass and paraffin, and Z, the mean coordination number of the beads within the cemented sample.

3.1.4.2. Comparison to experimental results

As can be seen in Figure 3.23, the theoretical expression provides a good agreement with the experimental data when the mean values of F_t previously presented in Fig. 3.2 are now plotted as a function of $\xi_p^{1/2} R^2$. A linear regression with a 0-intercept gives a proportionality coefficient that is equal to 0.70 ± 0.03 MPa with a relatively high R-square value of 0.978.

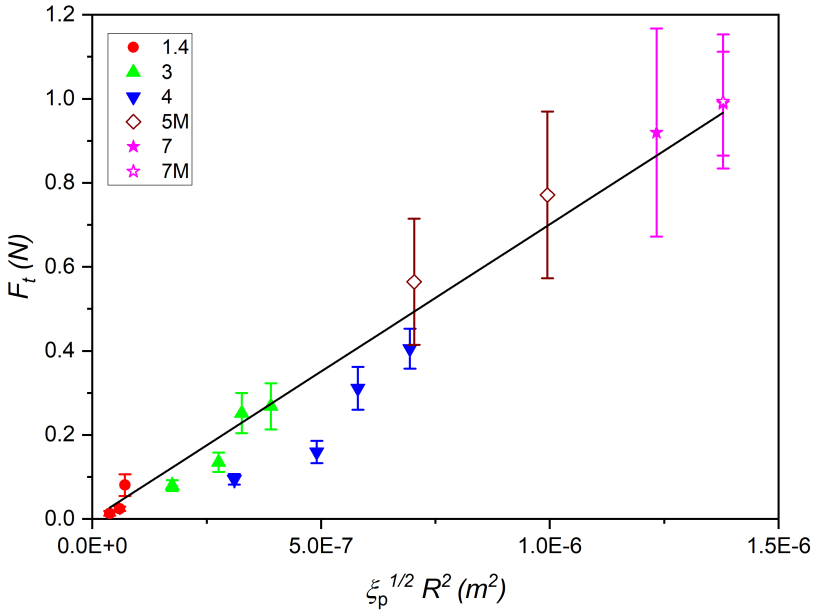

Figure 3.23. – Micro-tensile force F_t as a function of $\xi_p^{1/2} R^2$. The solid line stands for a linear regression with 0-intercept, $y = \alpha x$, giving $\alpha = 0.70 \pm 0.03$ MPa with a goodness of fit $R^2 = 0.978$. Closed and open symbols stand for polished and matt particles, respectively.

Prior to deducing the value of σ_{gp} from the slope, we need beforehand to estimate the typical value of the mean coordination number Z in a cemented granular material. Note first that the latter is obviously higher than in a dry granular medium since bonds can exist even if the connected grains are not perfectly in contact. An arbitrary choice of either $Z = 9$ or $Z = 8$ was previously proposed in a theoretical model of cemented granular materials (Dvorkin, Nur, and H. Yin 1994) while, in the different but related case of unsaturated mono-size grains connected by pendular water bridges, values of the coordination number tending towards 7.6 (Gröger, Tüzün, and Heyes 2003) and about 8 (Richefeu, El Youssoufi, and Radjaı 2006) have been reported. A previous work by the author and colleagues has also suggested a value around 8 (Farhat, Luu, Philippe, et al. 2021) for our cemented materials (detailed in forthcoming section A.2), not far from a measure of 7.4 obtained for a rather similar artificial system made of beads bonded by solidified polymer bridges (Schmeink, Goehring, and Hemmerle 2017).

In the end, by imposing $Z = 8$ as an arbitrary but somehow reasonable choice, one finally yields: $\sigma_{gp} = 0.275 \pm 0.012$ MPa.

Several back assessments can be made on the basis of this quantitative value. It can first be checked that this adhesive strength is consistently much smaller than the cohesive strength, or ultimate tensile strength, of paraffin for which values found in the literature (at ambient temperature and for different types of paraffin wax) indicate $\sigma_{pp} \approx 0.6$ MPa (Pal and Ravikumar 2019), $\sigma_{pp} \approx 1$ MPa (DeSain, Brady, Metzler, et al. 2009), or $\sigma_{pp} \approx 2$ MPa (Seyer and Inouye 1935), all these values being effectively greater than σ_{gp}. Additionally, the bond strain can be estimated from Hooke's law of elasticity, with a typical Young's modulus value of $E_p \sim 100 - 200$ MPa for pure paraffin wax (Pal and Ravikumar 2019; DeSain, Brady, Metzler, et al. 2009). The corresponding strain reads $\epsilon = \sigma_{gp}/E_p$ and is found very small, around 10^{-3}, confirming that the bond remains almost perfectly rigid during a micro-tensile test.

3.2. Macro-scale experimental results

3.2.1. Tensile test

To measure the overall cementation strength of our artificial cemented soil at the macro-scale, we performed traction tests using our different cells constituted each of two conical parts as previously presented in section 2.1.3 (see Figures 2.8 and 2.6). Using the small (S), medium (M), and large (L) bi-conical cells, we conducted a parametric study by varying both the particle size and the paraffin content of the samples. From the recorded force at rupture (i.e. when the two cones split up), denoted by F_T, we can calculate the macro tensile stress σ_T by simply dividing this yield force by the failure section at the neck of the device, $(\pi/4)D^2$, where the minimum cone frustrum diameters are D=30, 56 and 79 mm, respectively.

On the one hand, as expected, we observe in Figure 3.24 that increasing the paraffin mass content from X_p= 0.2 to 0.7 % regardless of the diameter of the glass beads or the

conical cell used, enhances the yield macro tensile strength σ_T. If we look at the 4 mm beads (see Figure 3.24d), it seems however that σ_T tends to saturate above $X_p \approx 0.8$ %. On the other hand, when considering different macroscopic devices (S, M & L) for a

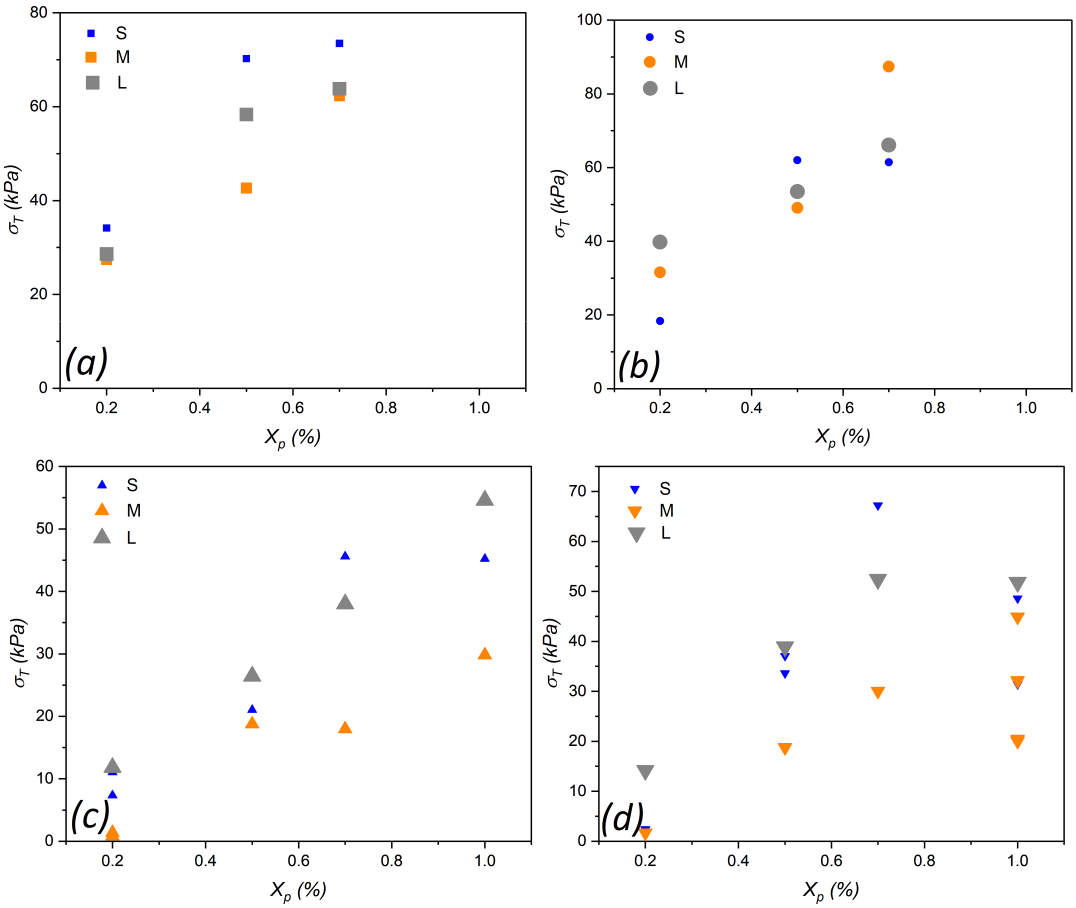

Figure 3.24. – Yield macro tensile stress *versus* paraffin mass content for the three different cone sizes and for several different particle diameters: (a) $d = 0.6$ mm, (b) $d = 1.4$ mm, (c) $d = 3$ mm, and (d) $d = 4$ mm.

same paraffin content and a same particle diameter, we can evidence a discrepancy in the value of the macro tensile stress which should be the same whatever the size of the device. This result seems to indicate that there are some finite-size effects. Note that the scattering is greater for the 3 and 4 mm glass beads.

In Figure 3.25, we gather all the data by plotting the yield macro tensile strength σ_T as a function of the paraffin volume content ξ_p. Taking into account the wide dispersion of the data, we observe that the measurements of σ_T for the 3 mm and 4 mm particles almost match. The same applies to the data for the 0.6 mm and 1.4 mm particles. While in the micro-scale study the micro-tensile force increases with particle size at the same paraffin content, we can see in comparison that the macro tensile stresses for both the 3 mm and 4 mm particles are lower than for the 0.6 mm and 1.4 mm particles. This trend could be explained by the fact that, for the same size

of device, there are a greater number of small particles (namely d=0.6 and 1.4 mm) than larger particles (namely d=3 and 4 mm) at the neck contact area between the two cones.

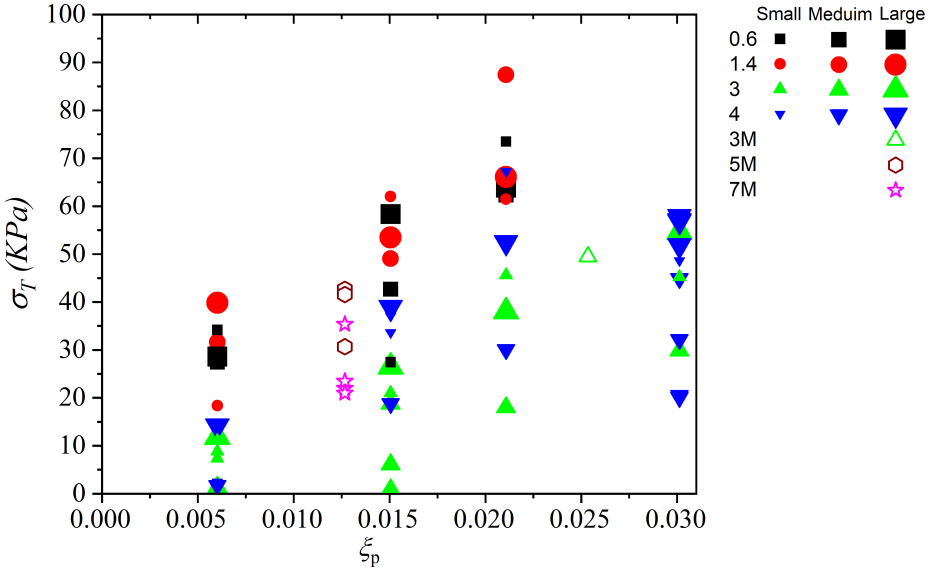

Figure 3.25. – Yield macro tensile stress σ_T as a function of the paraffin volume content ξ_p for different glass bead diameters, from 0.6 to 7 mm, and the three cone sizes (corresponding to the symbol sizes). Closed and open symbols stand for polished and matt particles, respectively.

3.2.2. Impact of loading rate and creep testing

Among the different control parameters in this macro tensile characterization setup, we briefly looked at the impact of the loading rate and the effect of creeping. The previous macroscopic tensile tests were carried out with a jack speed ranging between 0.25 and 1 mm/min. As can be seen in Figure 3.26, the yield macro tensile stress σ_T almost fluctuates in this range around a constant value (regarding the high dispersion of the measurements). However, σ_T increases significantly (by a factor of about 2) when we impose a loading rate above 2 mm/min. It is worth noting that this behaviour is much reminiscent of that observed at the microscopic scale and presented previously in Figure 3.3.

We also performed three identical creep tests by applying a constant tensile force chosen close but below the expected yield value. Figure 3.27 shows the time evolution of the macroscopic force during each experiment, repeated with the same particle diameter d = 4 mm and paraffin content X_p = 1 %. We systematically observe an instantaneous failure with no evolution of displacement versus time, which is consistent with the micro and macro tensile tests, without any detectable variation of the force

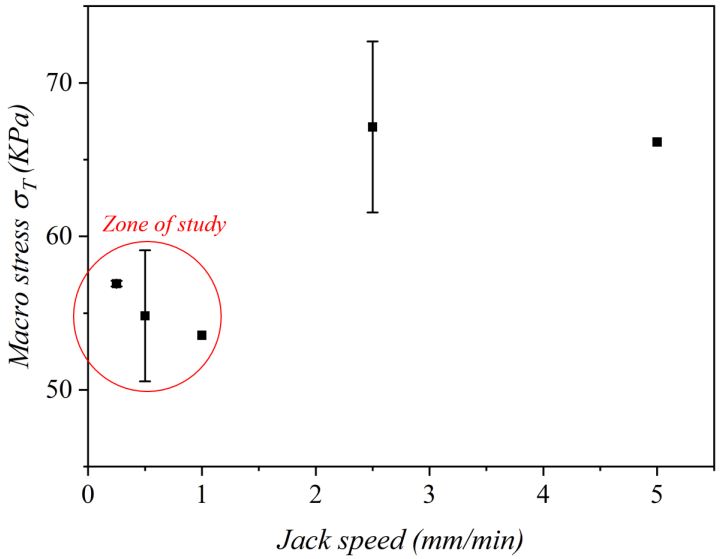

Figure 3.26. – Yield macro tensile stress σ_T as a function of the jack speed of the upper plate for a sample with 4 mm beads and $X_p = 1.0$ %. Each point stands for an average of at least two measurements.

prior to failure. However, the duration of the plateau before the cone separation is variable, highlighting the random nature and high variability of the failure process. In conclusion, it appears that there is no open damage or cracks progressing in the bond, similarly to what has been already suggested by the X-ray tomography scans.

3.3. Discussion

3.3.1. Intrinsic dispersion

For the two micro and macro-mechanical characterizations of our cemented granular material, the measurements have shown to be subject to huge variability and statistical fluctuations. In this section, we propose a discussion on the possible roots for this intrinsic dispersion.

At the bond scale

It should be remembered that the rupture of a solid bond can be of three different types, namely the adhesive, cohesive and mixed ones. A wide dispersion in the bond tensile strength has been also observed elsewhere, for bio-cemented soil (Ham, Martinez, G. Han, et al. 2022), which is independent of the type of rupture (mixed, adhesive and cohesive), as shown in Figure 1.14. Apart from the limited number of illustrations by our high resolution 3D tomography imaging (see Figures 3.20 and 3.21), we also systematically identified the rupture type after each micro-tensile characterisation using a microscope. Figure 3.28 displays the typical images acquired that allow us

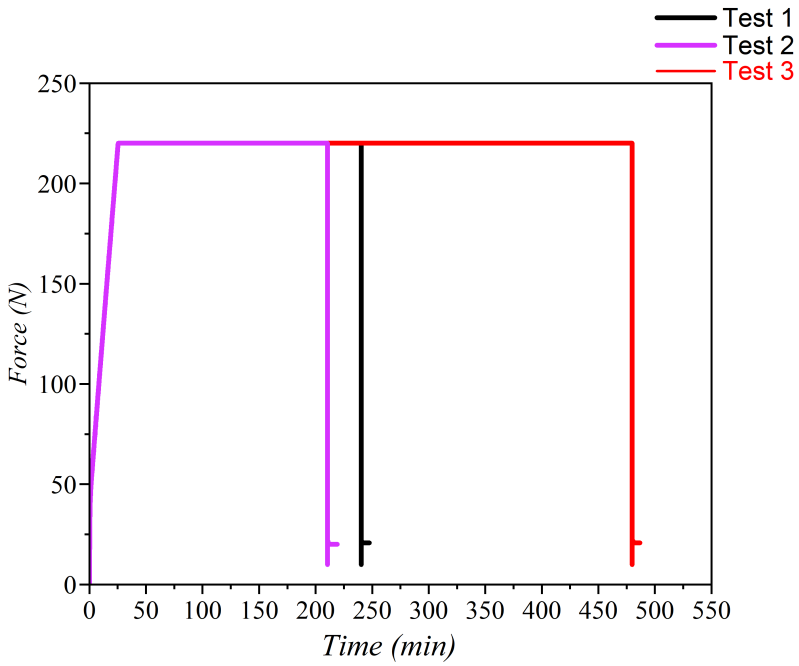

Figure 3.27. – Repeated tests for three creeping experiments.

to examine the shape of the broken bond. The paraffin left on the glass beads after rupture is indeed used to differentiate the three different rupture types. The adhesive rupture is defined when there is an almost perfectly clean surface on one of the two beads (implying the presence of the quasi-intact bridge on the other bead). The cohesive rupture occurs within the bulk of the bond, which is split in two parts, resulting in a relatively even distribution of the remaining paraffin deposit on the surface of both particles. For the mixed rupture, only a part of the bond is completely detached from the beads, with a fraction of the contact area being clean. While the purely adhesive case is easily identified, it is more difficult to distinguish certain cohesive cases from the mixed ones. This visual discrimination is therefore not fully objective and subject to some bias interpretation by the operator.

Several factors influence the type of rupture that is observed: Firstly, the size of the particle; secondly, the surface roughness of the glass beads (polished or matt); and thirdly, the loading type used to break the bond (tensile, shear, bending, or torsion). In all of the experiments, we observed almost 100% of purely adhesive ruptures in tensile and shear tests for particles smaller than 5 mm in diameter with a polished surface finish. This is no longer the case for the tests with 5 and 7 mm particles, where the mixed type of rupture is also found, as evidenced by the more detailed analysis, to be presented just below, which was carried out for a series of micro-tensile tests on 7 mm particles with two different surface roughnesses (polished and matt). Finally, for all bending and torsion tests, it seems that, whatever the size of the particles or the surface finish, about 40 % of the ruptures are adhesive, the others being mixed.

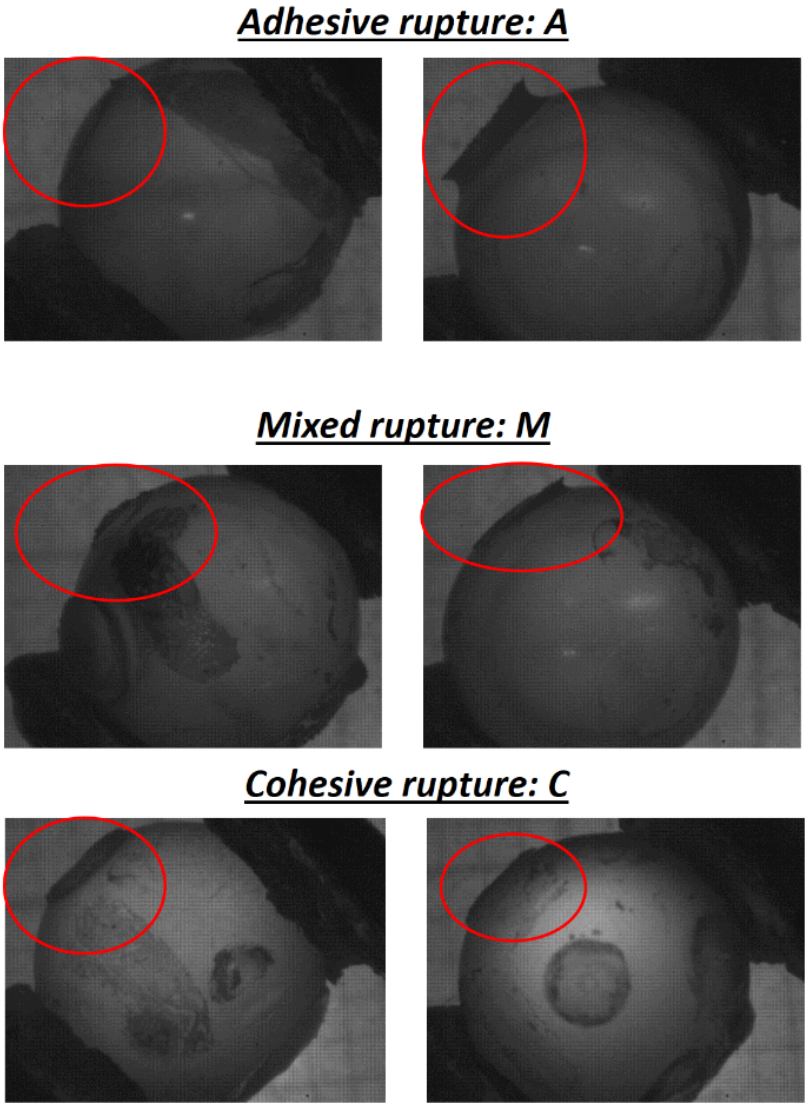

Figure 3.28. – Microscope images illustrating the three different types of rupture after the micro-tensile tests with beads of 7 mm diameter and a paraffin content of $X_p = 0.5$ %.

By correlating the types of failure with the beads surface roughness, we have noted that around 90 % of the bond ruptures for the polished particles are adhesive, the rest being mixed. For the matt beads, the ruptures are mostly mixed, with some rare cases of the two other types. From the microscope observation, we are also able to estimate the size of each paraffin bond and check, as suggested by the theory (see Eq. 3.5), if the yield force does increase with the bond cross-section. This analysis shows, rather unexpectedly, that the bond strength does not seem to be correlated with either the bond radius or the type of rupture. Indeed, as shown in Figure 3.29, we observe a scatter plot for the yield tensile force *versus* the bond radius, regardless of

the rupture type and the bead surface finish. The blue solid line indicates the mean value calculated for the bond radius square, equal to 1.12 mm^2.

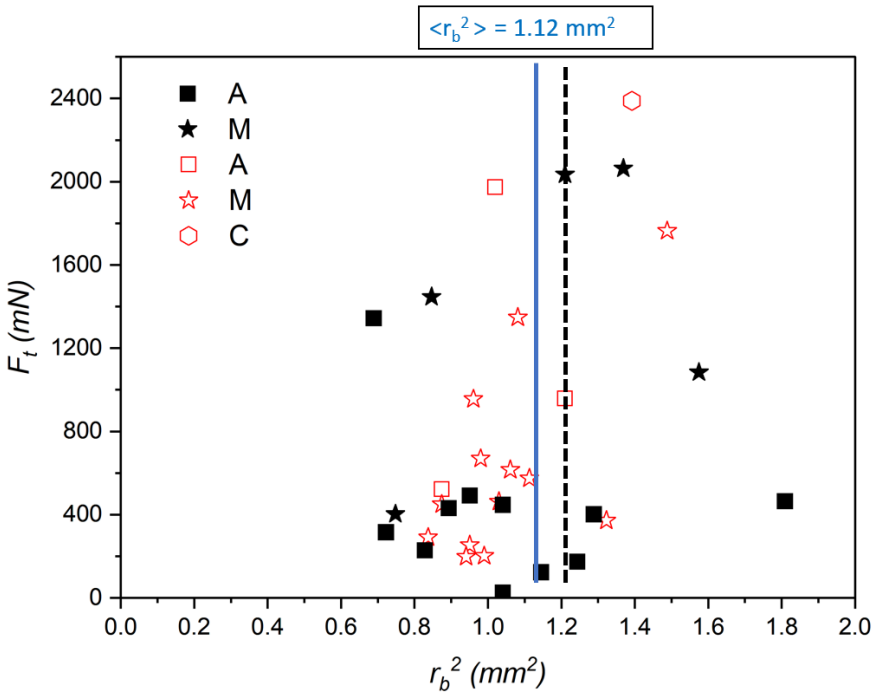

Figure 3.29. – Yield micro-tensile force as a function of the square of the bond radius for 7 mm beads and $X_p =$ 0.5 % with the distinction of the surface finish, either polished (closed symbols) or matt (open symbols), and of the different bond rupture types observed (A = adhesive, M = Mixed and C = cohesive). Dashed line presents the mean bond radius obtained by using the theory. The blue line presents the mean $r_b{}^2$ of the experiments.

Based on the previous theory (see Figure 3.22), one can estimate the radius of the bond and compare it to this experimental mean value. From section 3.1.4.2, the bond radius is indeed given by $r_b = R\sin\theta_b$ while θ_b is related to the paraffin volume content through Eq. 3.8 and Eq. 3.11. In the present situation, knowing that $X_p = 0.5$ %, we can then deduce a value of about 18° for θ_b, which is verified to be well below $\frac{\pi}{6}$ (i.e. 30°) as assumed in the theory. And finally, for 7 mm beads, we find a theoretical prediction of 1.21 mm^2 for the square of the bond radius which is consistently close to the mean value estimated from the direct visualisation. This quite good agreement gives relevance to the proposed geometric model for the paraffin bonds.

However, this analysis does not enable correlations to be highlighted with different parameters bearing an intrinsic dispersion (surface condition, bridge size) and therefore unfortunately does not provide any interesting conclusion regarding the dispersion of the microscopic measurements.

At the sample scale

As we have seen, a large intrinsic dispersion of the yield values is observed for bond rupture in our micro-scale measurements for the tensile and shear force, as well as for bending and torsion moments. At the macro-scale, all of these solicitations are applied simultaneously in the bond population at the cone's neck, leading to an expected significant level of uncertainty on the macro-tensile test results. Moreover, the great dispersion measured at the macro-scale, even greater than that at the micro-scale, could also come from some finite size effects. Indeed, among all experiments carried out, we varied both the particle size of the cemented granular samples and the size of the conical devices. Consequently, the experiments involved different numbers of grains in the rupture zone with, in some cases, very little statistical averaging and high influence of the boundaries. The latter could be a major contributing factor to the data scatter. Further, there are some notable variations in the fracture geometry as illustrated in Figure 3.30 that presents several examples of post-failure surfaces at the device's neck after the cones separation. It can be seen that, depending on the case, the surface obtained is not always flat but there can be a 3D effect with more or less convex parabolic shapes. The hypothesis of using the neck cross-section in the calculation of the stress at failure thus leads to an overestimation of the latter for all cases of parabolic shape. In order to correct these calculations, and more broadly to propose a comprehensive study (including, for example, the influence of the paraffin content in addition to that of the particle size), further systematic experiments would be necessary.

Figure 3.30. – Different shapes of the surface rupture obtained with the large macroscopic cone: (left) almost planar rupture for a sample of 0.6 mm beads with $X_p = 0.5$ %; (middle) parabolic shape for a sample of 1.4 mm beads with $X_p = 0.2$ %; (right) moderately parabolic shape for a sample of 7 mm beads with $X_p = 0.5$ %.

3.3.2. Micro-macro relationship

From the previous measurements of cementation strength using tensile tests at both the grain micro-scale and the sample macro-scale, we can experimentally propose a micro-macro relationship. As mentioned in chapter 1 (see section 1.2.1.3), Rumpf (Rumpf 1962) originally derived a homogenisation law that linearly relates the macroscopic yield stress to the inter-particle cohesion-type force. More recently, Richefeu

and co-authors (Richefeu, El Youssoufi, and Radjaı 2006) developed an expression for the macroscopic stress σ_T that is linked to the micro-tensile force F_t through the grain radius R, the mean coordination number Z and the mean solid volume fraction ϕ, such as (reminder of Eq. 1.8):

$$\sigma_T = \frac{3Z\phi}{2\pi}\frac{F_t}{(2R)^2}.$$

On our side, we previously derived in section 3.1.4.2 the following semi-theoretical law from our experimental results (reminder of Eq. 3.14):

$$F_t = \sigma_{gp} 1.62\pi \sqrt{\frac{2}{Z}}\sqrt{\xi_p} R^2,$$

where ξ_p is the paraffin volume content and σ_{gp} the adhesive strength at an elementary interface between glass and paraffin.

Thus, by inserting Eq. 3.14 into Eq. 1.8, we obtain the following micro-macro relationship:

$$\sigma_T = 0.86\phi\sigma_{gp}\sqrt{Z}\sqrt{\xi_p}. \tag{3.15}$$

This expression does not involve anymore the glass bead radius and solely depends on the paraffin volume content ξ_p. Figure 3.31 compares this theoretical relation to the previous data plotted in Figure 3.25, by using a coordination number $Z = 8$, a solid volume fraction ϕ equal to 0.61, and the value of σ_{gp} previously deduced from linear regression on the micro-data. Given the very wide dispersion of data, it is impossible to conclude on the relevance of the model. All we can say is that the order of magnitude appears to be correct, with perhaps some overestimation of the macro tensile stress.

Note that a preliminary study based on a preliminary series of experiments was reported at the conference Powders and Grains in 2021 and is summarized in Appendix A. The analysis presented therein was based on a pioneering and entirely empirical version of the law predicting the yield micro-tensile force F_t. The latter has been clarified by the contribution of new experiments as detailed in section 3.1.4.1. Nevertheless, the previous approach to proposing a micro-macro relationship was very similar, including a discussion about the coordination number.

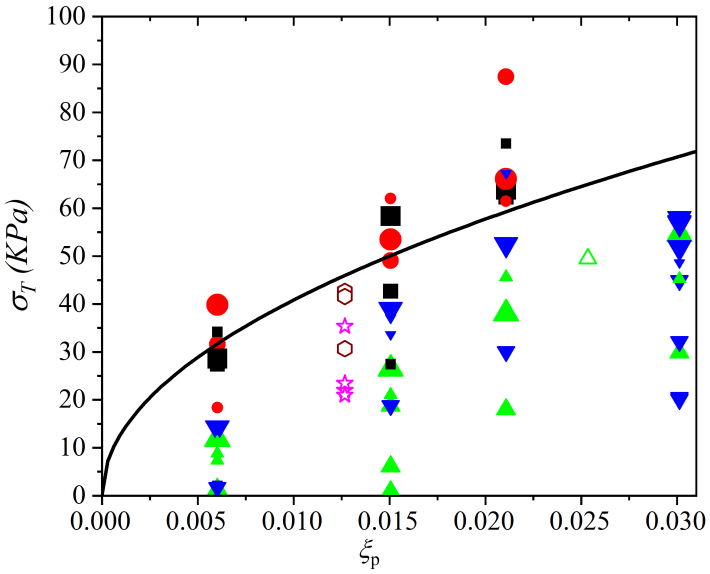

Figure 3.31. – Same data and notations as in Figure 3.25 with addition of the black curve corresponding to the theoretical prediction in Eq. 3.15.

4. Localized hydraulic failure of a cemented granular layer

Sommaire

Introduction

This chapter is dedicated to the study of the conditions for hydraulic failure of a horizontal layer of cemented grains subjected to a localized upward water flow, from both experimental and numerical approaches. The first part is devoted to the experiments, by presenting the methodology used and the description of the various types of failure regime observed. The second part deals with 2D numerical simulations performed with our in-house DEM-LBM code, including a comparison between the numerical parametric study results and the experiments, and lastly a brief presentation of the forthcoming 3D extension of this numerical study using the WalBerla open-source code.

4.1. Experimental results

4.1.1. Phenomenology

Earlier in the manuscript, we presented the experimental procedure dedicated to the hydraulic failure tests on a cemented granular layer. A typical experiment basically consists of imposing, by successive steps, a gradual increase of the flow rate Q at the bottom injection, at a controlled rate induced by a gear pump, while the corresponding hydraulic pressure difference is measured by sensors. At the moment a fracture within the sample occurs, a significant pressure difference drop is observed, allowing the so-called failure onset to be determined precisely in terms of critical hydraulic pressure difference and flow rate, denoted by ΔP_c and Q_c, respectively. To explore the phenomenology, we have tested several cemented samples with different micro-mechanical properties by varying the beads diameter (from 0.7 to 1.4 mm) and the inter-particle adhesion (bonds of paraffin with mass content from 0.033 to 0.7 %). Note that the interstitial flow rate and the pressure of the liquid are related through the hydraulic conductivity that depends on both the geometry (i.e. reduced diameter injection) and the permeability of the cemented granular material used.

The experimental campaign carried out showed four distinct behaviors when submitting an immersed soil layer to a bottom localized injection: (i) a static regime, referring to no movement in the sample; (ii) a block rupture, when a median crack appears at the inflow; (iii) a fluidized path regime, namely a progressive burrowing along the walls; (iv) a block uplift, by sliding at the walls after prior breakage of the concerned bonds.

4.1.1.1. Static regime

The static regime is the first sample behavior observed, at a low enough flow rate, for all the experiments conducted throughout this investigation. In this condition, the viscous forces exerted by the flow through the porous medium are insufficient to compensate both the bonds strength and the buoyant weight of the cemented

granular sample. The layer thus stays static when the imposed flow rate is less than a critical value Q_c. Figure 4.1 illustrates the latter static regime case.

Figure 4.1. – Example of a static regime for a sample with $d = 3$ mm, $Q = 2$ l/min and $X_p = 0.2$ %. Note that the dark spots on the window are paraffin coatings as will be explained later.

4.1.1.2. Block rupture

The block rupture, illustrated in Figure 4.2, is one of the types of failure that occurs for a cemented granular material when the flow rate reaches its critical value Q_c, i.e. when the pressure starts to drop, as visible in Figure 4.3. By that time, the pressure difference had increased sufficiently to break the bonds above the injection hole and create a vertical fracture. A cavity then develops in the center of the sample. This kind of failure occurs suddenly. No movement was recorded by the camera in this zone prior to the rupture. Only minor degradation of the bonded grains in contact with the corners of the walls could be seen. Once ruptured, the sample is divided into two rigid blocks by a median cavity with an almost triangular shape. The onset of the fracture initiates a gradual decay of the hydraulic pressure difference.

4.1.1.3. Fluidized path

The second type of failure for a cemented granular material is the development of a fluidized path along the walls, as pictured in Figure 4.4. This case has been observed for the same diameter of glass beads but with a lower paraffin content than for the previous block rupture. Furthermore, the hydraulic pressure difference required to destabilise this layer is almost half the critical one for block rupture. Note that we have

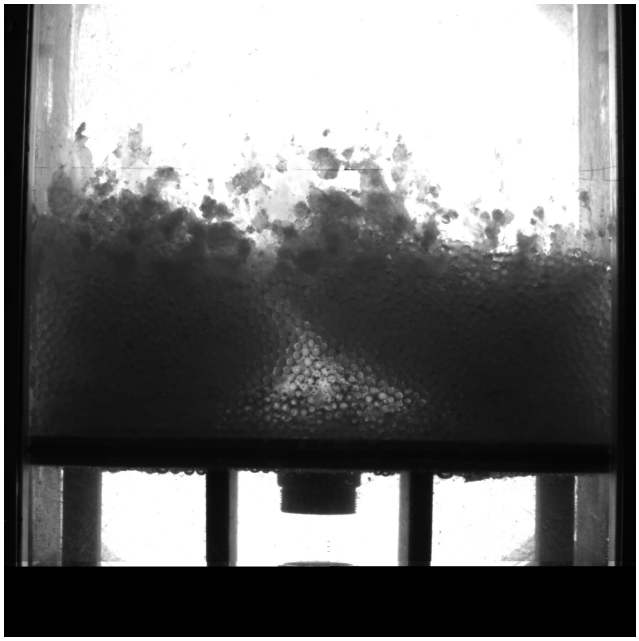

Figure 4.2. – Example of a hydraulic failure by block rupture for a sample with $d = 3$ mm, $Q_c = 27.5$ l/min and $X_p = 0.2$ %.

almost reached the maximum flow rate of the pump, and consequently the upper limit of our range of exploration for this study. As shown in Figure 4.5, the hydraulic pressure difference decrease is much more limited. A further comment can be made from Fig. 4.3 and Fig. 4.5 where it can be seen that the flow rate of the pump remains perfectly constant during each step, even when the pressure difference decreases, thanks to the use of a volumetric (gear) pump rather than, for instance, a centrifugal one.

4.1.1.4. Block uplift

The block uplift, which is the last and rather unexpected type of failure observed, is similar to a rigid body being lifted up by the hydraulic flow. For this, a prior debonding is required in all the contacts between the cemented sample and its boundaries (lateral and bottom plate). Because the drag force on the entire block is greater than its buoyant weight once the adhesive bonds to the walls are broken, the block takes off to a certain extent, as displayed in Figure 4.6. Figure 4.7 depicts the sudden hydraulic pressure difference decrease caused by the sample destabilization by uplift. However, we can see that the hydraulic pressure difference then becomes constant, indicating that the sample has come to a stop and it is in equilibrium at a specific level.

This behavior highlights the weakness or highest exposure of the paraffin bridges that connect a glass bead to a wall and can be attributed to a lack of adhesive strength between the plexiglass wall and the glass bead, combined to a preferential flow path along the wall that induces a greater drag force. This behavior also reflects a strong control by the boundary conditions. As this type of destabilisation was found almost

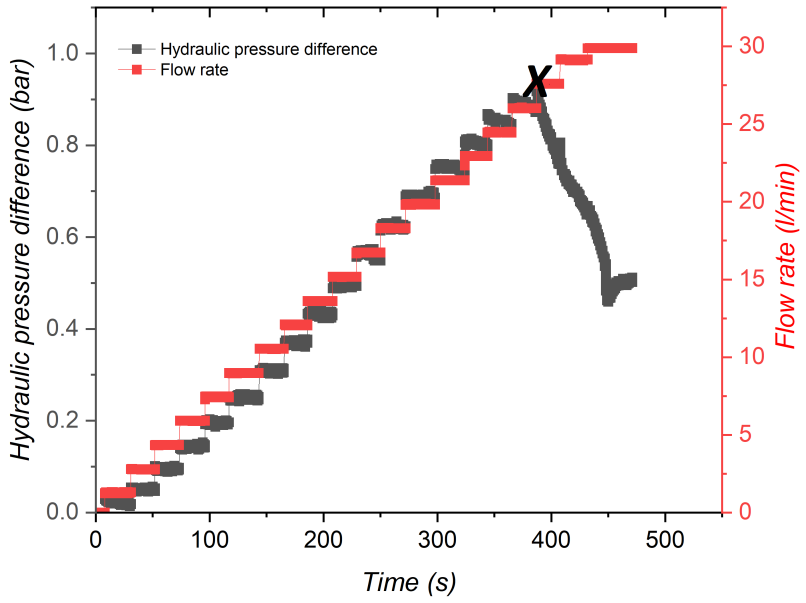

Figure 4.3. – Temporal evolution of the hydraulic pressure difference and the flow rate, for the block rupture displayed in Figure 4.2. The black cross indicates the failure onset. The critical flow rate required to have the block rupture destabilization is $Q_c = 27.5$ l/min.

systematically in the first experiments we conducted, we decided for the following tests to have a paraffin-coating of the walls prior preparation of the cemented layer, as previously mentioned in section 2.1.5.1, in order to inhibit this type of failure by reinforcing paraffin bridges at the boundaries.

For the few un-coated wall experiments, one can try to predict the macroscopic force necessary to break all the bonds in contact with the side walls and the bottom plate, referring to the theory of the adhesive bond proposed in section 3.1.4.2. This involves taking into account the number N_w of bonds at the lateral walls that must be broken by shear F_s and the number N_b of bonds at the bottom plate that must be broken by tension force F_t. The resulting vertical macroscopic force is calculated as follows:

$$F_{flow} = N_b F_t + N_w F_s = \frac{\phi S_b}{\pi R^2}\left(1 + C_s \frac{S_w}{S_b}\right) F_t,$$

where S_b is the surface of the bottom plate and S_w is the total surface of the sample in contact with the lateral wall. Assuming, by way of substantial simplification, that the pressure at the base of the sample is almost uniformly distributed, the hydraulic pressure difference required to have a block uplift simply reads $\Delta P_c = \frac{F_{flow}}{S_b}$. Based on this calculation, we can compare this theoretical prediction to the measured critical hydraulic gradient ΔP_c. As presented in Table 4.1, our estimation is in good agreement

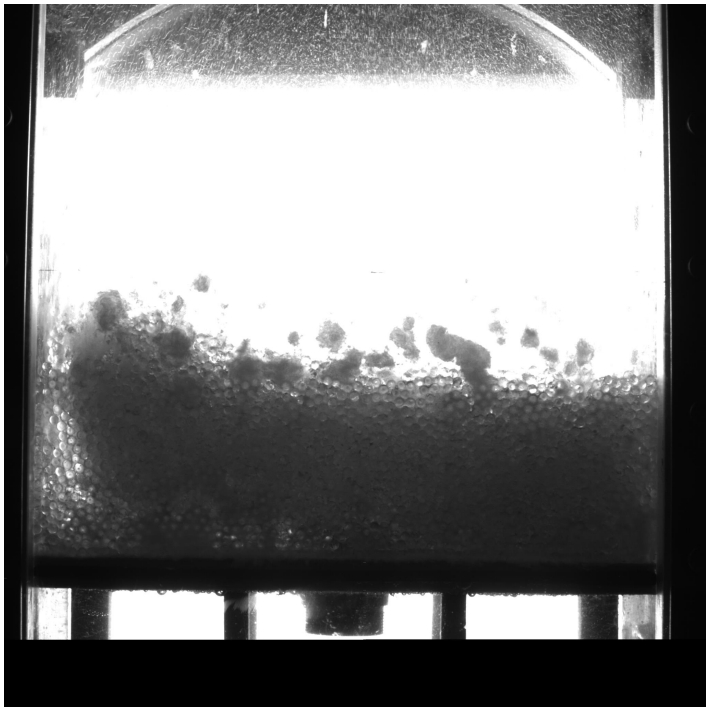

Figure 4.4. – Example of a hydraulic failure by a fluidized path (at the left side wall) for a sample with $d = 3$ mm, $Q_c = 22.5$ l/min and $X_p = 0.1$ %.

with the un-coated wall experiments.

d (mm)	Paraffin content (%)	ΔP_c experimental (kPa)	ΔP_c theoretical (kPa)
1.4	0.2	20.6	20.4
3	0.2	18.8	20.4

Table 4.1. – Comparative table for theoretical and experimental critical hydraulic pressure difference ΔP_c in the case where the walls are not coated by paraffin.

Finally, it should be noted that this pre-coating of walls remains however insufficient in preventing the sample from block uplift when we increase significantly either the particle diameter, the paraffin content, or the sample height.

4.1.2. Results of parametric study

With the same approach as proposed in several previous works of localized fluidization in granular materials (Philippe and Badiane 2013; Zoueshtiagh and Merlen 2007; Mena, Luu, Cuéllar, et al. 2017; Mena, Brunier-Coulin, Curtis, et al. 2018), but with addition here of cemented bonds between the grains, we aim at experimentally investigating the threshold values inducing the hydraulic failure in terms of critical flow rate Q_c and critical pressure difference ΔP_c, by means of a parametric study for

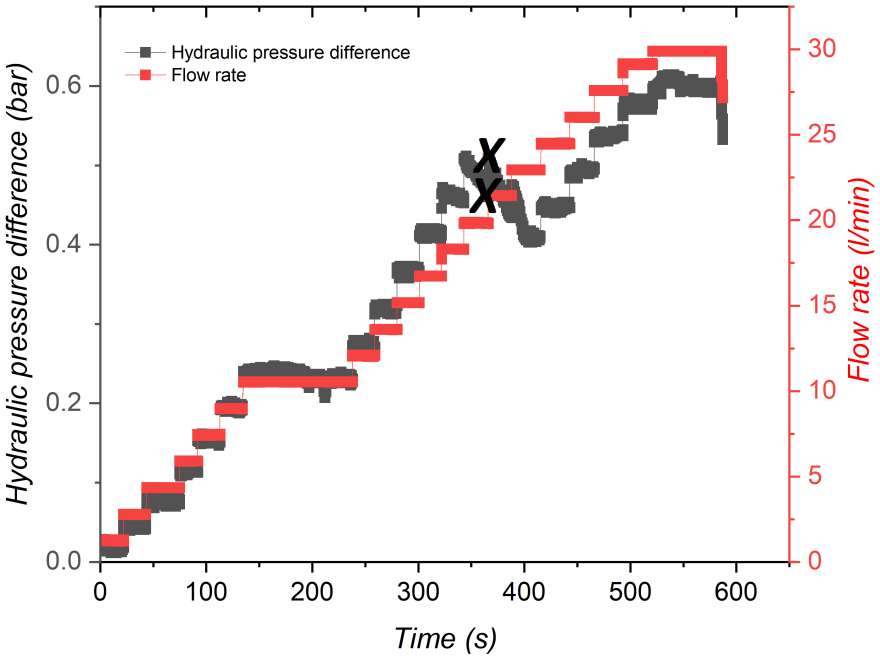

Figure 4.5. – Temporal evolution of the hydraulic pressure difference and the flow rate, for the fluidized path displayed in Figure 4.4. The black cross indicates the failure onset. The critical flow rate required to have the fluidized path destabilization is $Q_c = 22.5$ l/min.

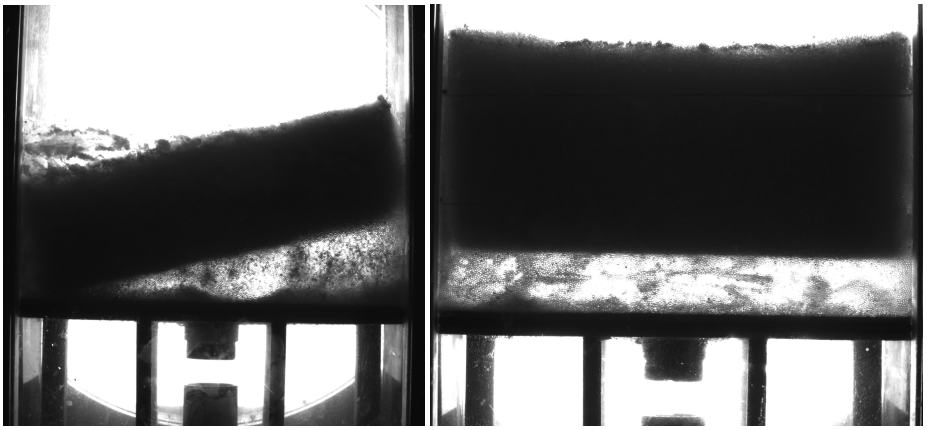

Figure 4.6. – Example of two block uplifts: (left) for $d = 0.7$ mm and $X_p = 0.7$ % for a 5 cm height sample; (right) $d = 0.7$ mm and $X_p = 0.1$ % for a 8 cm height sample.

various glass bead diameters (0.7, 1.4 and 3 mm), paraffin contents (0.033, 0.05, 0.1, 0.2 and 0.7 %) and sample bed heights (5 and 8 cm), as presented in Table 4.2.

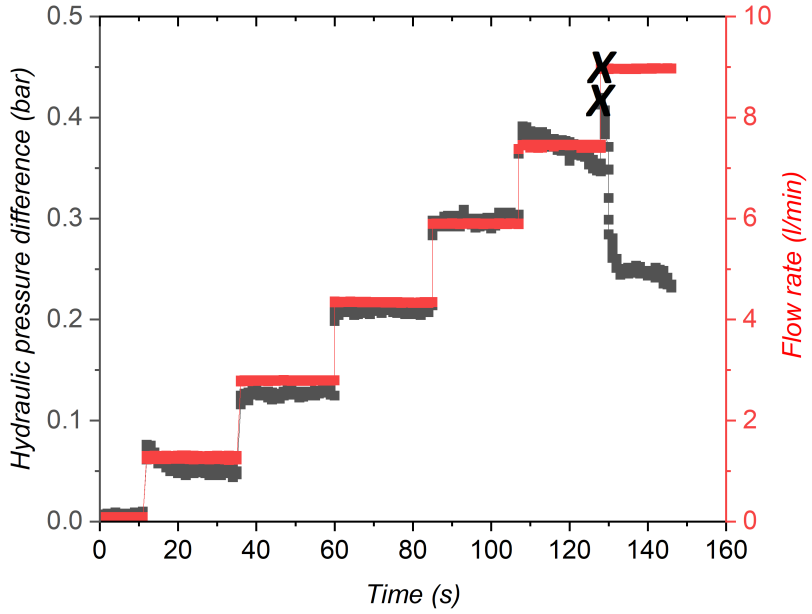

Figure 4.7. – Temporal evolution of the hydraulic pressure difference and the flow rate, for an 8 cm height sample with $d = 0.7$ mm and $X_p = 0.1$ %, corresponding to the block uplift displayed in Figure 4.6. The black cross indicates the failure onset.

Figures 4.8, 4.9 and 4.10 plot the flow rate Q as a function of the pressure difference ΔP for the different experiments listed in Table 4.2. On all these graphs, we observe a linear growth of the hydraulic pressure difference as the flow rate is increased, until the sample destabilises. The occurrence of one of the three types of failure, as described above, is then detected by a simultaneous pressure drop. At that moment, we acquired both the critical flow rate Q_c and the critical hydraulic pressure difference ΔP_c. Note that unfortunately there is no clear distinction between the conditions for block rupture and fluidized path.

Figures 4.8 and 4.9 show that when the paraffin content or the sample height increases, the destabilisation observed becomes the block uplift. When the paraffin content and the bed height are smaller, it gets more difficult to predict which failure will occur. However, the most likely types of destabilization to be obtained are either the fluidized path or the block rupture. In Figure 4.10, we studied the repeatability of these experiments by performing the same test twice ($d = 3$ mm, $X_p = 0.033$ % and $H = 5$ cm). As expected, there is some uncertainty in the slope of the initial growth and in the threshold value.

On the previous graphs, we can note that for $Q < Q_c$ and $\Delta P < \Delta P_c$, there is an initial linear increase of the flow rate as a function of the ΔP, which refers to the static regime. From these measurements, we can then estimate the hydraulic conductivity K of the

d (mm)	Paraffin mass content (%)	Height (cm)	Hydraulic conductivity (m/s×10^{-3})
0.7	0.05	5	0.124
0.7	0.1	5	0.123
0.7	0.1	5	0.103
0.7	0.7	5	0.111
0.7	0.1 (long test)	5	0.128
0.7	0.1 (shock load)	5	0.088
0.7	0.4 (around the center)	5	0.096
0.7	0.05 (at the center)	5	0.096
0.7	0.1 (bottom) 0.4 (upper)	3 cm (bottom layer) 3 cm (upper layer)	0.125 0.125
1.4	0.05	5	0.124
1.4	0.1	5	0.123
1.4	0.2	5	0.122
1.4	0.7	5	0.135
3	0.033	5	0.158
3	0.033	5	0.121
3	0.1	5	0.123
3	0.2	5	0.120

Table 4.2. – Parameters of all the hydraulic failure experiments.

cemented granular material, which is proportional to the slope coefficient between Q and ΔP based on the assumption that Darcy's law is valid. The corresponding values are given in Table 4.2. Note that the K values for the two repeated tests ($d = 3$ mm, $X_p = 0.033$ % and $H = 5$ cm) are consistently very close. Furthermore, even when the paraffin content varies for a same glass bead diameter, the K values are relatively close. Consequently, the induced increase in bond size does not have much impact on the hydraulic conductivity.

After failure, while $Q = Q_c$, we observe that ΔP decreases. Knowing the paraffin content, one can determine the micro-tensile force using the theoretical prediction proposed in the previous section (see Eq. 2.4). Hence, Figure 4.11 presents the critical hydraulic pressure difference ΔP_c versus the micro-tensile force F_t. As shown, it appears that the critical pressure difference has a continuous growth tendency with the micro-tensile force. But it is difficult and rather speculative to conclude if there is any general trend of the data.

However, much more interesting results can be obtained by introducing the dimensionless numbers of fluid mechanics adapted to the case of fluidization of a bed of particles. As already discussed in the State of the Art, one can find, both for a uniform and a localized fluidization of a granular bed (Mena, Brunier-Coulin, Curtis, et al. 2018), a unique relation between the two relevant dimensionless groups, namely the inlet particle Reynolds number and either the Archimedes number Ar or the Galileo

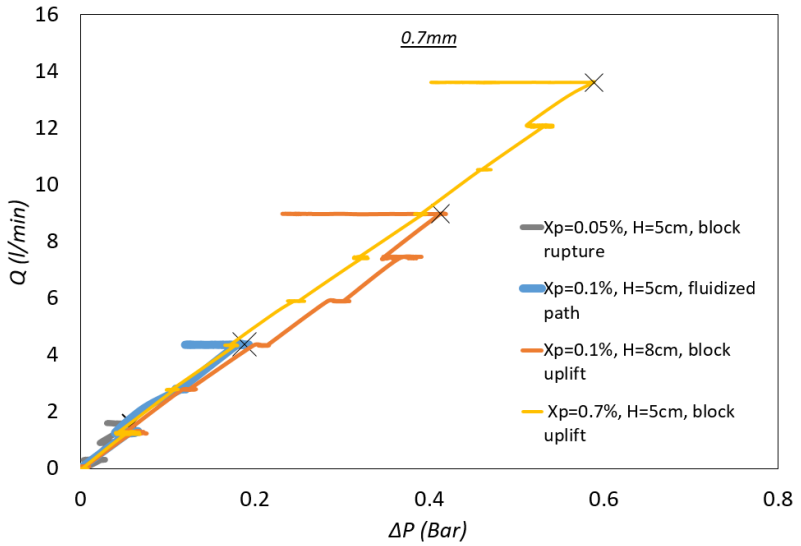

Figure 4.8. – Flow rate Q versus hydraulic pressure difference ΔP for a sample of beads with diameter $d = 0.7$ mm, various paraffin contents X_p=0.05, 0.1 and 0.7 %, and two bed heights $H = 5$ and 8 cm. The critical flow rate Q_c and the critical hydraulic pressure difference ΔP_c are indicated by the black crosses.

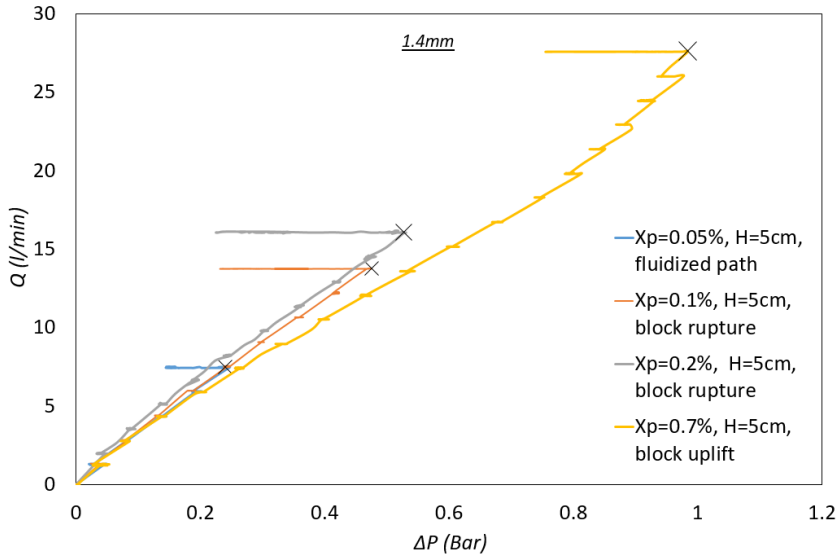

Figure 4.9. – Flow rate Q versus hydraulic pressure difference ΔP for a sample of beads with diameter $d = 1.4$ mm, various paraffin contents X_p=0.05, 0.1, 0.2 and 0.7 %, and a bed height $H = 5$ cm. The critical flow rate Q_c and the critical hydraulic pressure difference ΔP_c are indicated by the black crosses.

number Ga since $Ar \propto Ga^2$ (see Eq. 1.23), which both compare the buoyant weight to the viscous effects. As a reminder, the Galileo number is given by the following

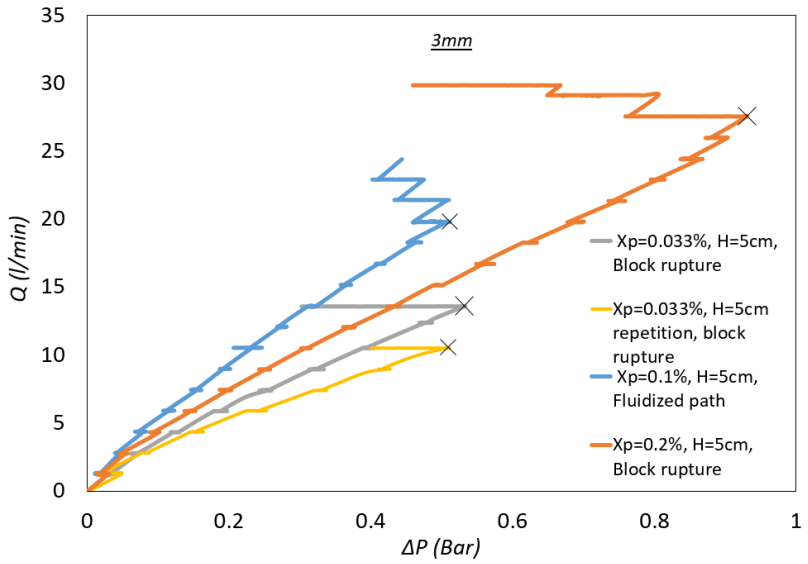

Figure 4.10. – Flow rate Q versus hydraulic pressure difference ΔP for a sample of beads with diameter $d = 3$ mm, various paraffin contents X_p=0.033, 0.1 and 0.2 %, and a bed height $H = 5$ cm. The critical flow rate Q_c and the critical hydraulic pressure difference ΔP_c are indicated by the black crosses.

equation for a cohesion-less granular system:

$$Ga = \frac{\sqrt{\rho_l(\rho_g - \rho_l)g\omega_g}}{\eta_l}, \tag{4.1}$$

where ω_g is the volume of the grain, ρ_l the liquid density, ρ_g the grain density, η_l the liquid viscosity, and g the earth's gravity. Here, the Reynolds number is defined at the inlet of diameter D_i, using the mean velocity $V = \frac{4Q}{\pi(D_i)^2}$. The critical Reynolds number is then equal to $Re^* = \frac{\rho_l V d}{\eta_l}$.

In the present case where the granular bed is cemented, the buoyant weight of a grain, $(\rho_g - \rho_l)g\omega_g$, is completely insignificant when compared to the adhesive bond force F_t. Since the competition is now between adhesive and viscous effects, we therefore propose the usual Galileo number to be replaced by an adhesive Galileo number defined as follows:

$$Ga_{adh} = \frac{\sqrt{\rho_l F_t}}{\eta_l}. \tag{4.2}$$

One can alternatively define an adhesive Archimedes number as:

$$Ar_{adh} = \frac{\rho_l F_t}{\eta_l^2}. \tag{4.3}$$

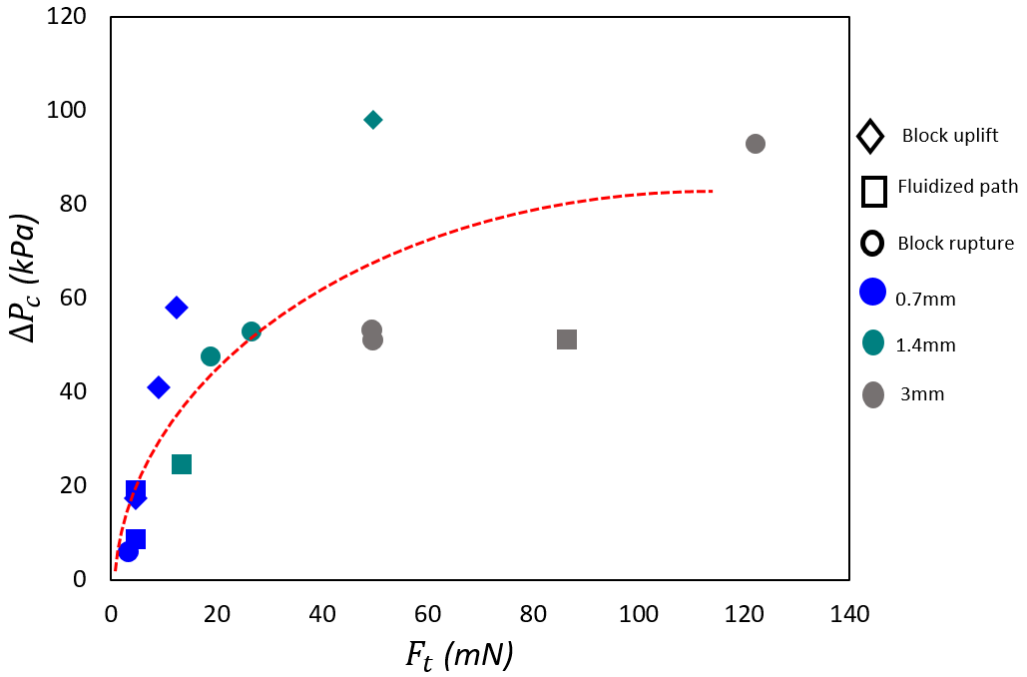

Figure 4.11. – Critical hydraulic pressure difference ΔP_c as a function of the yield micro-tensile force F_t for different bead diameters: $d = 0.7$ mm, $d = 1.4$ mm and $d = 3$ mm, with bed height H= 5 cm. The three types of hydraulic failure (block uplift, fluidized path and block rupture) are indicated by distinct symbols. The red line is a guide for the eyes suggesting a speculative trend.

Figure 4.12 then shows the adhesive Archimedes number Ar_{adh} as a function of the critical Reynolds number Re^* for all the experiments performed with our cemented layers. We do find a satisfactory trend of the data within the entire range of measurements, rationalizing the fact that, at higher Archimedes numbers, higher critical Reynolds numbers are required to destabilize the cemented granular material.

To understand the origin of this dimensionless relationship, we can consider the force balance on a grain at the onset of its destabilisation. Indeed, at the exact critical condition, the drag force F_d exerted by the flow on the particle should be of the same order of magnitude as the adhesive micro tensile force F_t. Since the critical Reynolds number reached is much higher than 1, the viscous expression by Stokes is no longer valid for the drag coefficient C_d and one must use an empirical expression as the one proposed by Dallavalle and already introduced in Eq. 1.16. Assuming that $F_d = \alpha F_t$, with α a dimensionless number of order ~ 1, we obtain the following relation from Eq. 1.13:

$$Ar_{adh} = \frac{\pi}{8\alpha}\left(\sqrt{24Re^*} + \sqrt{0.44}Re^*\right)^2. \tag{4.4}$$

This formula remains broadly consistent with our data, and the best agreement (dashed line in Figure 4.12) is obtained for $\alpha \approx 0.03$, a number that is actually some-

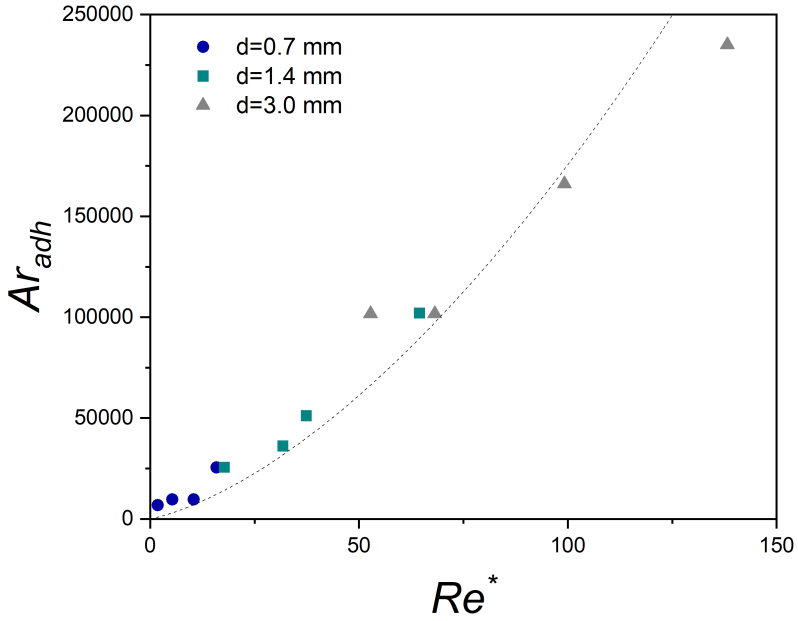

Figure 4.12. – Adhesive Archimedes number Ar_{adh} as a function of the critical Reynolds number Re^* for all the experiments. The dashed line stands for Eq. 4.4 with $\alpha = 0.03$.

what lower than expected. This discrepancy is however partly understandable. Firstly, because the liquid velocity around a particle is not equal to the injection velocity V but to the interstitial velocity, which is higher than the previous one by a factor of $\frac{1}{\epsilon} \approx 2.5$ where $\epsilon \approx 0.4$ is the bed's porosity. On the other hand, as already mentioned, paraffin bonds do not only break by traction. Yet the critical values for the other loads (i.e. shear, bending and torsion) are lower by a factor of about 0.4. We therefore expect a value around 0.06 for the coefficient α, which, although still a bit too high, is already closer to the value obtained here.

Finally, our present results in the case of cemented material can be compared in Figure 4.13 with those obtained for localized fluidization of granular material and presented in Figure 1.30 (Mena, Brunier-Coulin, Curtis, et al. 2018 and Philippe and Badiane 2013), together with the corresponding Darcy and Ergun laws.

Note that to make this comparison possible, it is necessary to specify the pre-factors not taken into account in the dimensionless numbers. Indeed, $(\rho_g - \rho_l)gd^3$ is used for the buoyant weight of a spherical particle in the definition of the Archimedes number (see Eq. 1.23). A $\frac{\pi}{6}$ factor is therefore missing, whereas our adhesive Archimedes number is built directly on the adhesive bond force F_t. We have therefore multiplied the Ar_{adh} values by the inverse coefficient $\frac{6}{\pi}$ before comparing the data. As can be seen in Figure 4.13, with the exception of the smallest values of the Reynolds number, the data seem to be rather comparable which is quite remarkable and even surprising

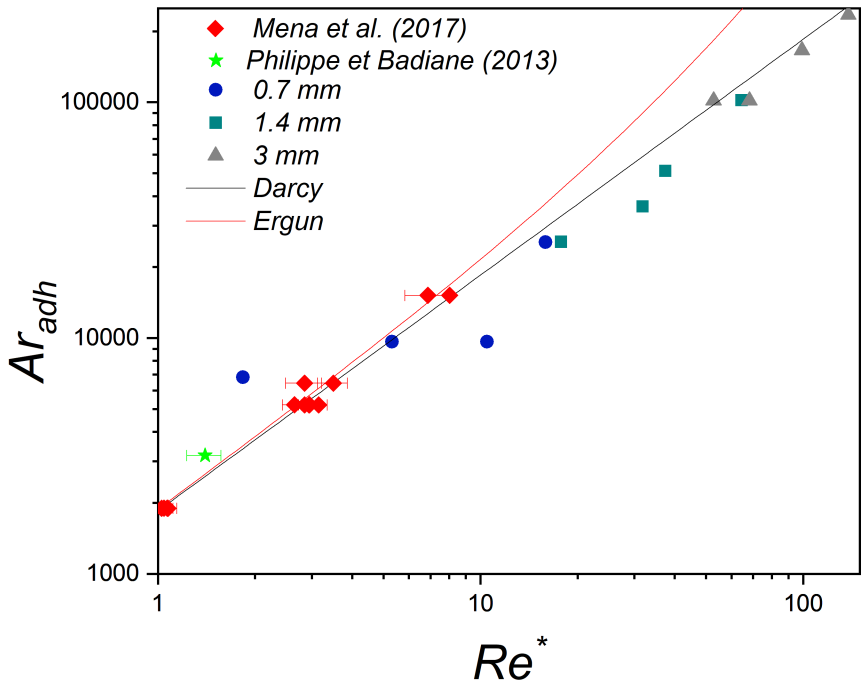

Figure 4.13. – Same data as in Fig. 4.12, multiplied by $\frac{6}{\pi}$ and plotted in log-log scale. Experimental data obtained in previous works have been added (Mena, Brunier-Coulin, Curtis, et al. 2018 and Philippe and Badiane 2013). The two lines stand for the Darcy (grey) and Ergun (red) laws.

given the strong differences in the destabilisation modes: granular fluidization *versus* hydraulic failure by either block uplift, fluidized path, or block rupture.

4.1.3. Additional experiments

For further exploration, we also investigated the hydraulic failure process induced by other flow protocols and sample configurations. On the one hand, we sought to cause a localized erosion by making specific cemented samples composed of zones with distinct bond strength. First, we created a central domain around the injection port where beads of d=7 mm are bonded with a very small paraffin content of $X_p = 0.05$ %, surrounded by grains heavily cemented with $X_p = 0.4$ %. As pictured in Figure 4.14, while the paraffin is still liquid, a paper is folded into a cylindrical shape allowing the beads cemented with 0.4 % of paraffin to be poured around. Then, the sample with 0.05 % is placed inside the cylinder paper. The folded paper is thus removed by gently raising it upward, before the solidification of the bridges. Figure 4.15 shows that the central cylindrical weakest zone indeed endures a block uplift, indicating the importance of the boundary effect. With the same idea, we tested a sample of beads with $d = 7$ mm and composed by two strata of distinct bond strength, namely

$X_p = 0.1$ % for the bottom layer and $X_p = 0.4$ % for the upper layer. For this sample configuration, after an initial static regime, we observed the uplift of the strongest layer followed by a block uplift of the whole sample. Figure 4.16 presents the flow rate versus pressure difference measurements for these two additional experiments. As expected, one recovers the same evolution than observed previously (see Fig. 4.8 and Fig. 4.9).

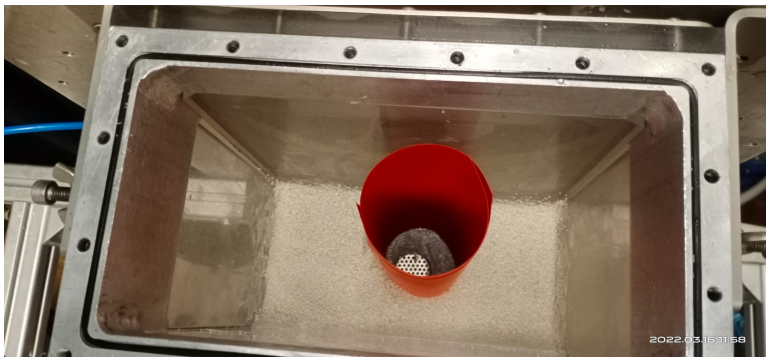

Figure 4.14. – Procedure for the construction of a cemented granular layer composed of beads with $d = 0.7$ mm and paraffin content of $X_p = 0.4$ % around the orifice and $X_p = 0.05$ % at the center.

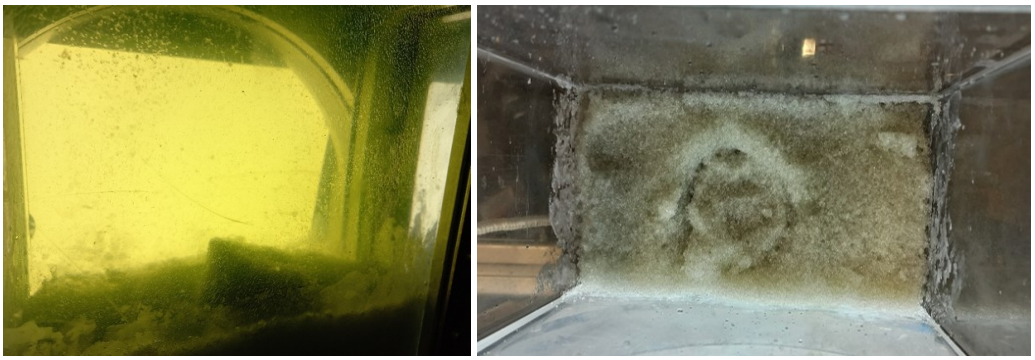

Figure 4.15. – Cylindrical block uplift of the central weaker zone.

On the other hand, using a usual homogeneously cemented sample, we tested two other flow solicitations, namely a shock load of the flow and the opposite long constant flow rate. The hydraulic response for the first short-time solicitation experiment, displayed in Figure 4.16, exhibits a relatively slow decrease of ΔP that begins at $Q = 4.0$ l/min. At that moment, we could observe a block rupture. Then, the hydraulic pressure drops to zero as the sample was elevated in the liquid. After reaching an equilibrium state in the cell, the sample recovered some resistance. Lastly, on another sample we imposed a constant flow rate of $Q = 2.8$ l/min for 2 hours. This long duration flow test resulted in the development of a fluidized path. As presented in Figure 4.16, the hydraulic response displays a non-monotonic increase, composed of successive short pressure drops, until a final consequent fall in the pressure signal.

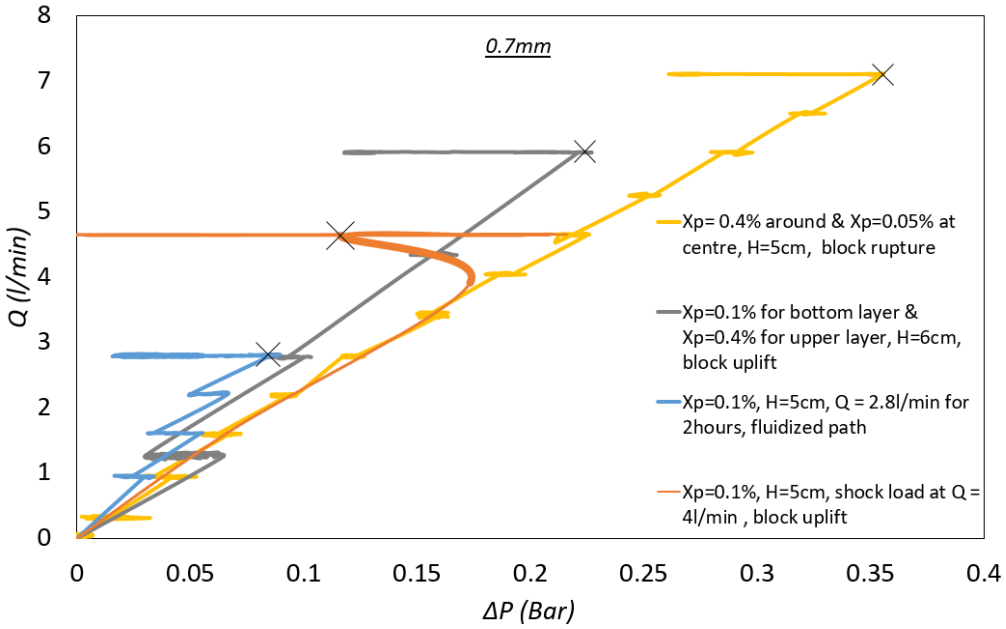

Figure 4.16. – Flow rate Q versus hydraulic pressure difference ΔP for samples of beads with $d = 0.7$ mm with specific cementation and injection flow conditions (see details in text).

4.2. 2D numerical results

As explained in chapter 2, we complemented the above experimental study of the hydraulic failure of a cemented granular soil with two series of numerical simulations using 2D LBM-DEM modeling. The first one, which was used to get familiar with the code, extended the analysis of localized fluidization of a granular soil carried out during the Ph.D. thesis of J. Ngoma. Afterwards, the solid bridge model was added in order to perform a parametric investigation of the destabilization of a cemented granular material subject to a preferential flow path, in which we will describe the observed phenomenology as well as the governing parameters, mainly the flow rate, for the material's failure.

4.2.1. Localized fluidization of a granular layer

4.2.1.1. Agreement with previous results

Earlier in chapter 1, we discussed the phenomenology observed for the numerical destabilization of a granular layer, with three different regimes: static, cavity, and chimney regimes, and the previous 2D LBM-DEM numerical modeling in our group that allowed to reproduce these findings (Ngoma, Philippe, Bonelli, J.-Y. Delenne, et al. 2014; Ngoma, Philippe, Bonelli, J.-Y. Delenne, et al. 2015; Ngoma, Philippe, Bonelli, Radjaı, et al. 2018).

Here, starting from the same code, we introduced several improvements, following

the work by Z. Benseghier (Benseghier, Cuéllar, Luu, Bonelli, et al. 2020). The previous periodic condition between top and bottom boundaries with a uniform flow has been replaced by an outflow boundary condition at the top and, at the bottom boundary, an imposed velocity profile at the inlet and zero velocity elsewhere. A comparison of our numerical model is accomplished by running four different simulations with the same input parameters (inlet velocity and viscosity and boundary conditions) as in the previous studies by J. Ngoma (Ngoma, Philippe, Bonelli, J.-Y. Delenne, et al. 2014; Ngoma, Philippe, Bonelli, J.-Y. Delenne, et al. 2015; Ngoma, Philippe, Bonelli, Radjaı, et al. 2018). The input parameters of the first three series of simulations are presented in Table 4.3.

Parameters	Values
Spherical grains diameter d (mm)	$1.6-2.4$
Grains density (kg/m^3)	2500
Normal contact stiffness (N/m)	10^5
Friction coefficient	0.3
Restitution coefficient	0.2
Fluid density (kg/m^3)	1000
Kinematic viscosity ν_f (m^2/s)	2.0×10^{-6}
Hydraulic radius coefficient	0.8
Spatial resolution	10
Gravity (m/s^2)	9.81
Duration of simulation (s)	10
Number of DEM cycles	2
Layer thickness (mm)	88
Inlet diameter (mm)	8

Table 4.3. – General parameters selected for our numerical simulations.

As summarized in Table 4.4, the three different steady state regimes (static, cavity, and chimney) already presented in Figure 1.34 are consistently observed, but for slightly different inlet velocities due to the change in the imposed inlet flow condition. However, the results are thus rather close to the previous ones obtained by J. Ngoma.

Simulation number	Inlet velocity (m/s)	Simulations by J. Ngoma.	Present simulations
1	0.15	Static	Static
2	0.29	Static	Cavity
3	0.40	Cavity	Chimney
4	0.60	Chimney	Chimney

Table 4.4. – Types of fluidization observed for different inlet velocities with the numerical code developed by J. Ngoma and with the actual improved one.

Note furthermore that, running the same simulation with an inlet velocity of 0.32 m/s

but for an extended duration, up to 170 seconds, our 2D numerical model was unable to replicate the experimental observation (Mena, Brunier-Coulin, Curtis, et al. 2018; Mena, Luu, Cuéllar, et al. 2017) where a transition from cavity regime to chimney regime is achieved for a longer time (few seconds to hours).

4.2.1.2. Identification of the relevant injection flow control parameter

As mentioned earlier, J. Ngoma's simulations were conducted with the inlet velocity used as a control parameter but with a single (uniform) injection velocity profile and almost exclusively for the same diameter D_i. Yet, however, the experiments have shown that the flow rate is the relevant control parameter, whatever the combination of diameter and mean velocity at inlet (Mena, Luu, Cuéllar, et al. 2017; Mena, Brunier-Coulin, Curtis, et al. 2018; Ngoma, Philippe, Bonelli, J.-Y. Delenne, et al. 2015). Indeed, the injection velocity has no visible effect on the onset for initiation of the fluidization regime. It only influences the transient duration phase but not the size of the fluidized chimney, which is nearly the same regardless of the injection diameter D_i.

With our 2D numerical simulations, we have implemented different inlet velocity profiles, namely parabolic (Poiseuille), triangular and uniform, to investigate their impact on the fluidization threshold and thus discriminate between the maximal profile velocity and the flow rate as a control parameter. As exhibited in Table 4.5, our numerical model recovered the same result as in the experiments, where the governing parameter is the flow rate regardless of the inlet velocity profile applied at injection.

Profile	Parabolic	Triangular	Uniform
Maximal inlet velocity (cm/s)	3.7	5.0	2.5
Inlet flow rate (cm^2/s)	1.97	2.0	2.0

Table 4.5. – Critical values of maximal inlet velocity and flow rate in the chimney regime for three different velocity profiles.

4.2.2. Localized hydraulic failure of a cemented granular layer

4.2.2.1. General phenomenology observed

Moving from the frictional to the cemented case, the phenomenology is no longer the same but there have been hardly any studies addressing this situation, with the exception of two which are far from comprehensive (Cui 2013; Cui, Li, Chan, et al. 2014). This statement has motivated the work presented here in which several sets of 2D simulations were performed to explore the influence of various parameters on the numerical destabilization of the cemented granular material: the grain diameter d, which is chosen as either 2 or 5 mm; the bond strength σ_b, which ranges from 0 to 2500 N/m; the thickness H of the cemented granular layer, which is 5, 10, or 15 cm;

and finally the viscosity of the fluid equal to either 24 or 75 cP [1]. The inlet diameter is fixed to 9.6 mm and the density of the beads is now set to 2230 kg/m^3. The full set of parameters used for these simulations is given in Table 4.6.

d (mm)	2			5		
H (cm)	5	10	15	5	10	15
σ_b (N/m)	0	0	0	0	0	0
	250	250	250	-	-	100
	-	-	500	200	200	200
	-	-	750	-	-	300
	1000	1000	1000	-	-	400
	-	-	1250	-	-	500
	-	-	1500	-	-	600
	-	-	1750	-	-	700
	-	-	2000	-	-	800
	-	-	2250	-	-	900
	-	-	2500	1000	1000	1000

Table 4.6. – Parameters used to simulate localized hydraulic failure in a cemented granular layer with two different values of viscosity, 24 and 75 cP.

For each simulation of this series, a uniform profile is imposed at the inlet of fixed diameter, with a velocity, and thus a flow rate Q, that is kept constant for 10 s. Note that the grains are artificially fixed for 0 s $< t <$ 2 s to wait for the flow to be well established before the release of the bed. The phenomenology observed, which will be described in detail just below, highlights two successive regimes and three different scenarios for the destabilization of the cemented sample. First, a static regime is met when there is no motion within the sample but possibly bond degradation. Next, there is a failure regime which includes the following modes of destabilization for the cemented bed: a fracture scenario in which two cracks are formed initiated from the inlet injection by progressive ruptures of bonds; a fluidized chimney scenario where the grains are set in motion in the same way as for a granular material, with almost homogeneous debonding of the entire sample; a mixed destabilization scenario, in-between fluidized chimney and fracture propagation.

Static regime

For all of the simulations carried out during this parametric study, the static regime was the first to be detected, at flow rates lower than the critical one denoted Q_c, where the viscous forces are not strong enough to compensate for both the bonds forces and the buoyant weight of the cemented layer. During pressurization, the sample layer lets the fluid pass through its pores with minimum sample expansion and remains static throughout the simulation while the imposed flow rate is smaller than Q_c. However,

1. As a reminder 1 cP = 10^{-3} kg/m/s.

even if the grains do not move, there is a possibility of bond degradation inside the sample. This damage by bond rupture in the static regime will be discussed in more detail in the forthcoming section 4.2.2.3. Two illustrations of the static regime are provided in Figure 4.17, where almost no damage occurred, and in Figure 4.18, where several bonds have been broken during the flow solicitation.

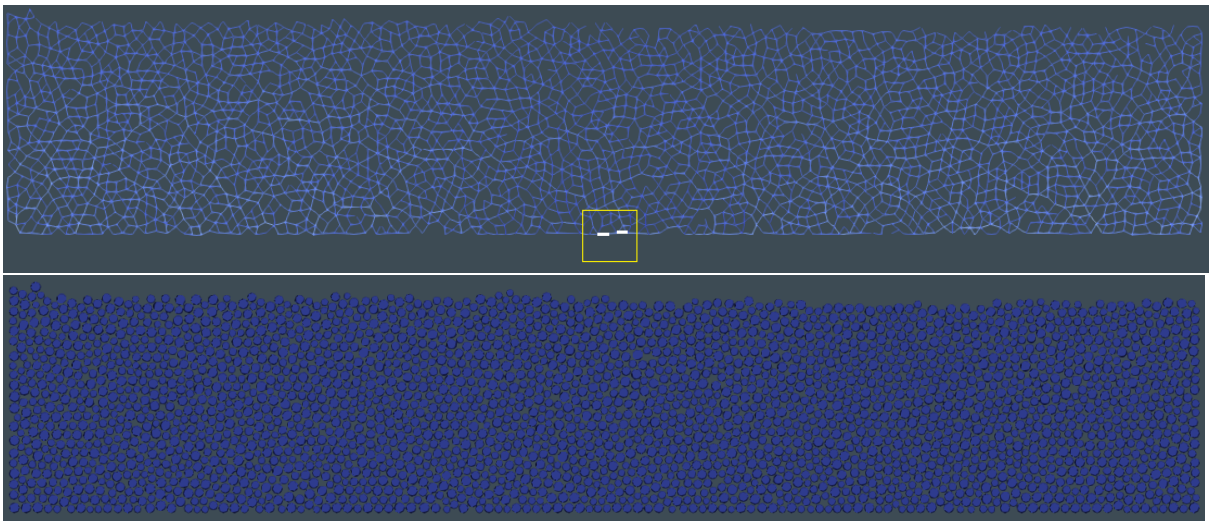

Figure 4.17. – Example of static regime without damage for a sample with $d = 2$ mm, $H = 5$ cm and $\sigma_b = 1000$ N/m, subjected to an inlet flow rate $Q = 2.11$ cm^2/s during 10 s: (Top) Adhesive bonds at $t = 10$ s where the white segments within the yellow box correspond to the only two broken bonds; (Bottom) Grain's velocity at $t = 10$ s, represented in a scale ranging from 0 (blue) to the inlet fluid velocity 0.022 m/s (red), where the maximal value found here, around 4×10^{-4} m/s, is obviously negligible.

Failure regime

When the flow rate is above its critical value, $Q \geq Q_c$, a destabilization of the cemented layer occurs but develops according to three distinct scenarios, described below.

- Fracture scenario

In this scenario, the destabilization is initiated under pressure difference and flow rate drag force by rupture of the bonds above the injection hole and along two almost symmetrical paths as seen in Figure 4.19. These fractures happen quickly and unexpectedly, with no early warning signs as grain motions in this zone prior to the sudden rupture at critical Q_c and ΔP_c. A drop in the hydraulic pressure difference is found following the development of these fractures. The observation of this scenario depends mainly on the cementation bond strength, but also on the grain size, and the

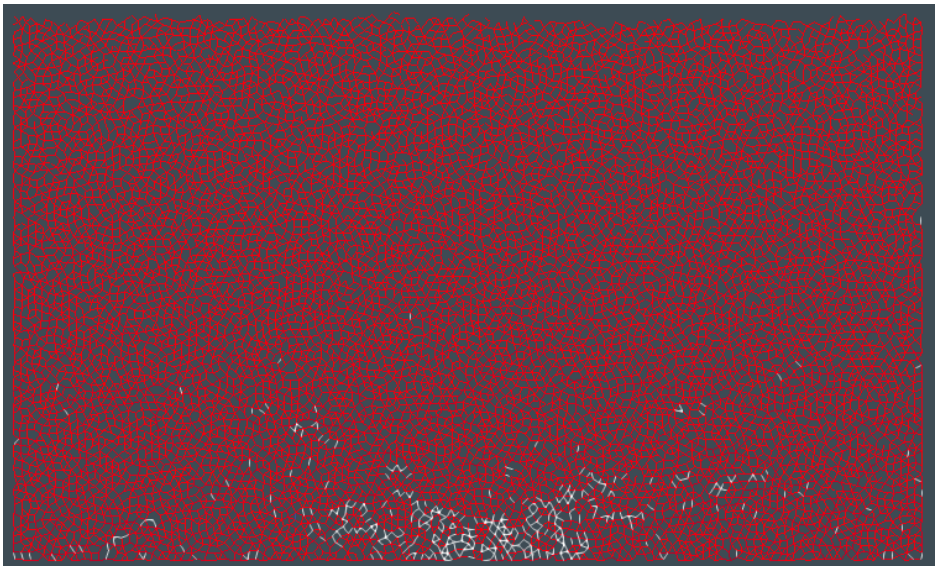

Figure 4.18. – Example of static regime with damage for a sample with $d = 2$ mm, $H = 15$ cm and $\sigma_b = 750$ N/m, subjected to an inlet flow rate $Q = 2.88$ cm^2/s during 10 s. The red segments correspond to intact bonds and the white ones to broken bonds.

bed height. The flow rate seems to control the length of the routes. However, for a flow rate much higher than Q_c, we can have a transition to the mixed destabilization scenario for a given sample.

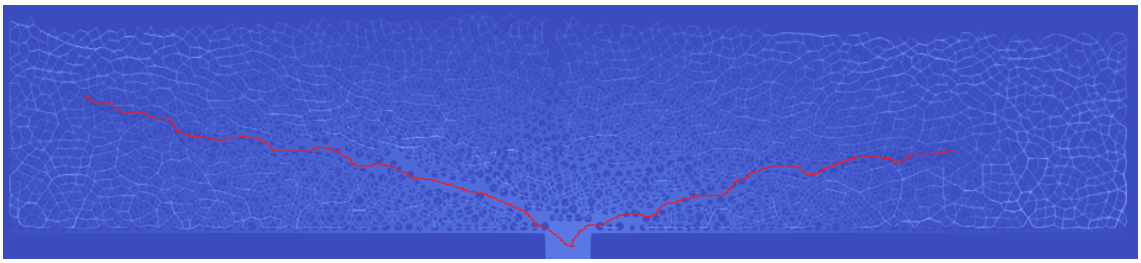

Figure 4.19. – Example of fracture scenario for a sample with $d = 2$ mm, $H = 5$ cm and $\sigma_b = 1000$ N/m, subjected to an inlet flow rate $Q = 3.55$ cm^2/s during 10 s. The two red lines identify the fractures induced by the hydrodynamic load.

- Fluidized chimney scenario

A fluidized chimney is observed when a prior quasi-homogeneous debonding of all or most of the bonds between the grains takes place as a result of the fluid's hydrodynamic force, at a critical Q_c and ΔP_c. As a result of reaching this debonded stage, the sample transforms to the granular situation, where a chimney is known to be

found. As depicted in Figure 4.20, the fluidization zone expands swiftly above the inlet injection hole, quickly reaching the sample's top by generating a chimney of fluidized grains. The balance of two separate fluxes achieves a steady state: the upward flux of grains carried out by the flow in the core section of the chimney, and the downward flux of outlying grains that constantly refuel the system.

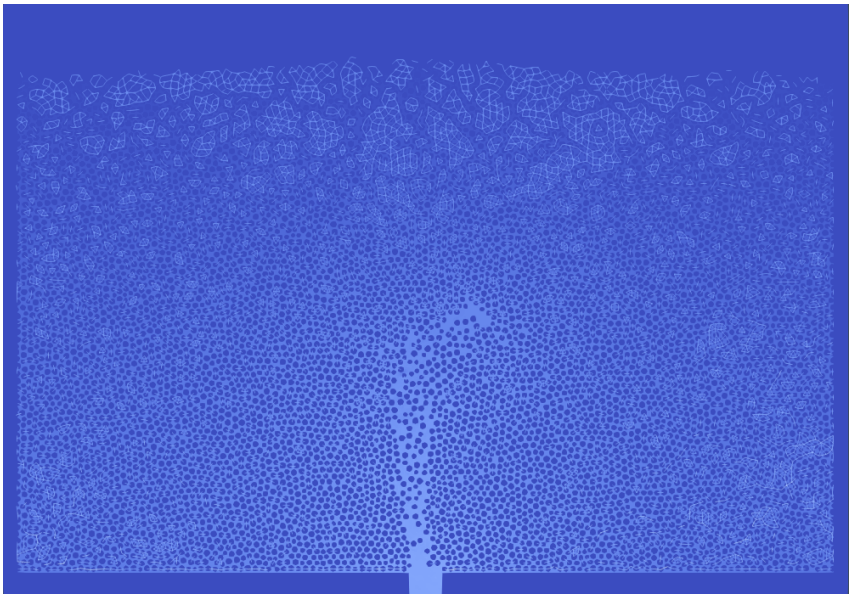

Figure 4.20. – Example of a fluidized chimney scenario for a sample with $d = 2$ mm, $H = 15$ cm and $\sigma_b = 250$ N/m, subjected to an inlet flow rate $Q = 6.43$ cm^2/s during 10 s.

- Mixed destabilization scenario

Finally, a third type of destabilization is observed, which we will denote mixed because it presents both a fluidized zone and a propagation within the cemented bed by small successive fractures along an inclined direction. Such a scenario is illustrated in both Figures 4.21 and 4.22, at different time steps in this latter example to exhibit the step-by-step expansion. Note that secondary transverse fractures also develop by the end of the simulation.

4.2.2.2. Critical conditions and phase diagram

Impact of the various parameters on the critical conditions

As previously described, the static regime is the first stage encountered before reaching a critical inlet flow rate above which the cemented bed gets destabilized. A parametric investigation was carried out to determine which subsequent scenario of destabilization occurs by varying the grain diameter (2 and 5 mm), the bed height (5, 10, and 15 cm), liquid viscosity (24 and 75 cP), and cementation bond strength σ_b

Figure 4.21. – Example of a mixed destabilization scenario for a sample with $d = 2$ mm, $H = 5$ cm and $\sigma_b = 250$ N/m, subjected to an inlet flow rate $Q = 1.92$ cm^2/s during 10 s.

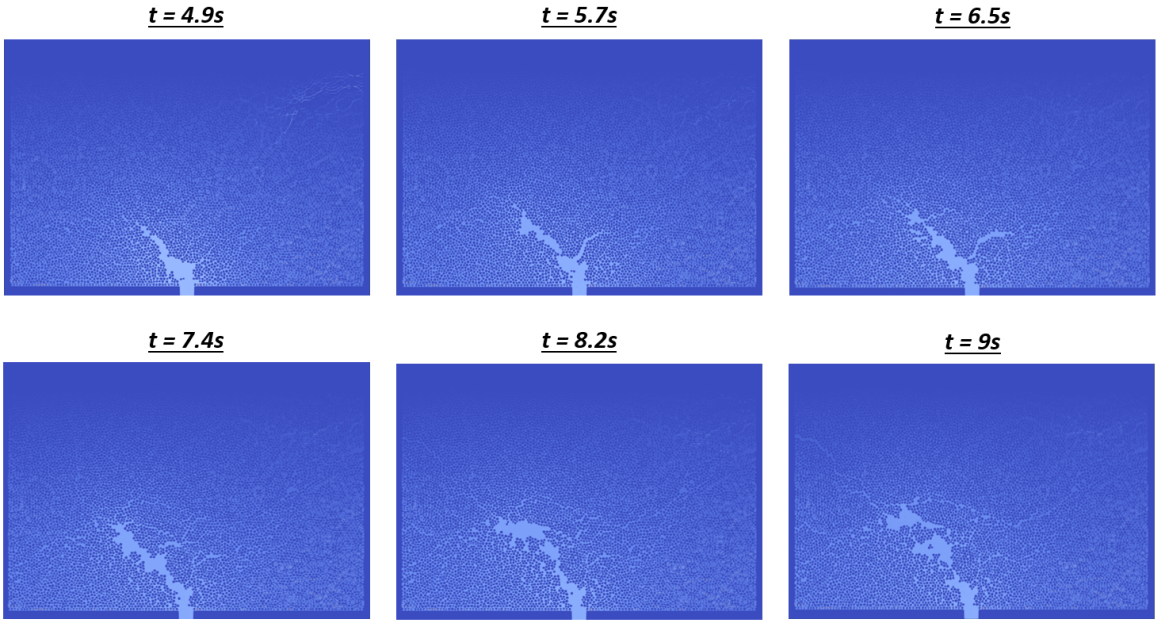

Figure 4.22. – Example of a mixed destabilization scenario at different time steps of the simulation for a sample with $d = 2$ mm, $H = 15$ cm and $\sigma_b = 1000$ N/m, subjected to an inlet flow rate $Q = 6.72$ cm^2/s during 10 s.

(up 1000 N/m). Table 4.7 depicts the three scenarios (fracture, fluidized chimney, and mixed) met in the 14 simulations performed with these parameters.

First, we note that mixed or fluidized chimney scenarios are favored as expected for weak bond strengths (200 and 250 N/m). On the contrary, the high value of σ_b corresponds to fracture scenarios, except for one mixed case. Additionally, we observe that increasing the bed height causes a transition of the scenario from fracture to mixed and finally to the fluidized chimney. Finally, here, there is no impact of viscosity on the selection of the destabilization type. Figure 4.23 nevertheless shows that increasing viscosity reduces the critical inlet flow rate required for sample destabilization whatever the grain size.

Concerning the dependence on the height H of the cemented bed, Figures 4.24 and

			Scenario of destabilization		
d (mm)	Viscosity (cP)	σ_b (N/m)	$H = 5$ cm	$H = 10$ cm	$H = 15$ cm
2	24	250	M	FC	FC
		1000	F	F	M
	75	1000	F	-	-
5	24	200	M	FC	FC
		1000	F	F	F
	75	1000	F	-	-

Table 4.7. – Different destabilization scenarios (F: fracture, FC: fluidized chimney, M: mixed) observed according to bed height H, particle diameter d, bond strength σ_b, and viscosity.

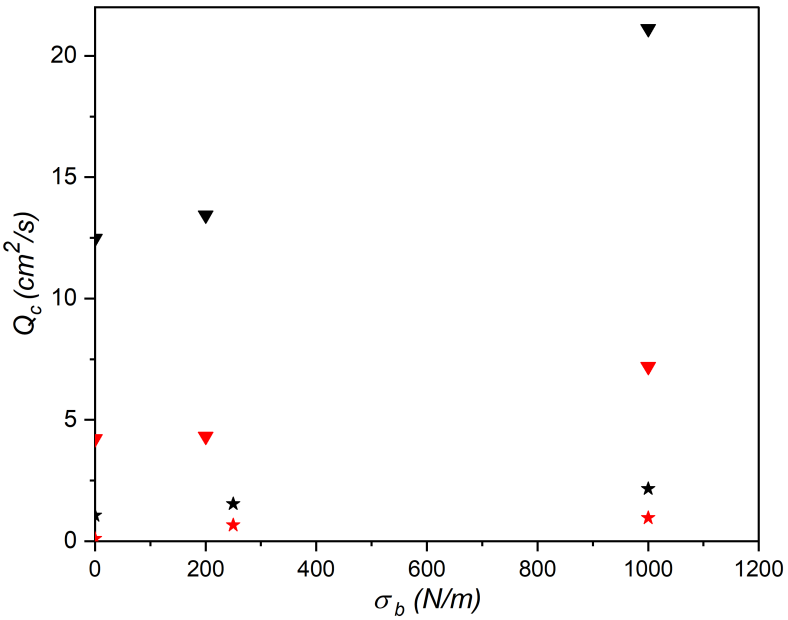

Figure 4.23. – Influence of viscosity on the critical inlet flow rate as a function of bond strength σ_b, for two different grain diameters of 2 mm (star symbols) and 5 mm (down triangle symbols) and for a bed height $H = 5$ cm. The red symbols stand for a viscosity of 75 cP, whereas the black ones are for a viscosity of 24 cP.

4.25 reveal that the critical inlet flow rate Q_c increases with H, regardless of the particle size (2 mm or 5 mm). There is however far much limited impact at $\sigma_b = 1000$ N/m for the large particles (see Fig. 4.25).

Finally, taking a closer look at the influence of the cementation bond strength, we can see on these two figures that there is an initial increase in the critical inlet flow rate with σ_b and then a stagnation, or even, if the height is greater than or equal to 10 cm,

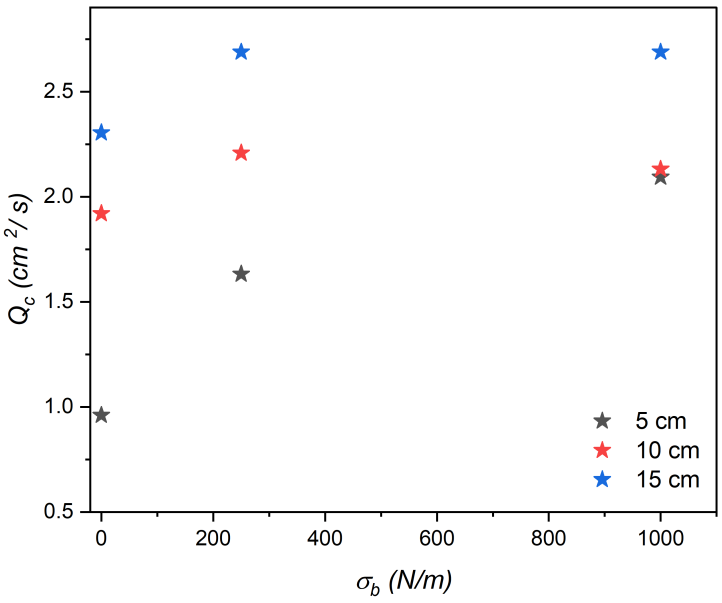

Figure 4.24. – Critical inlet flow rate as a function of bond strength for a sample with $d = 2$ mm and height of 5, 10, and 15 cm.

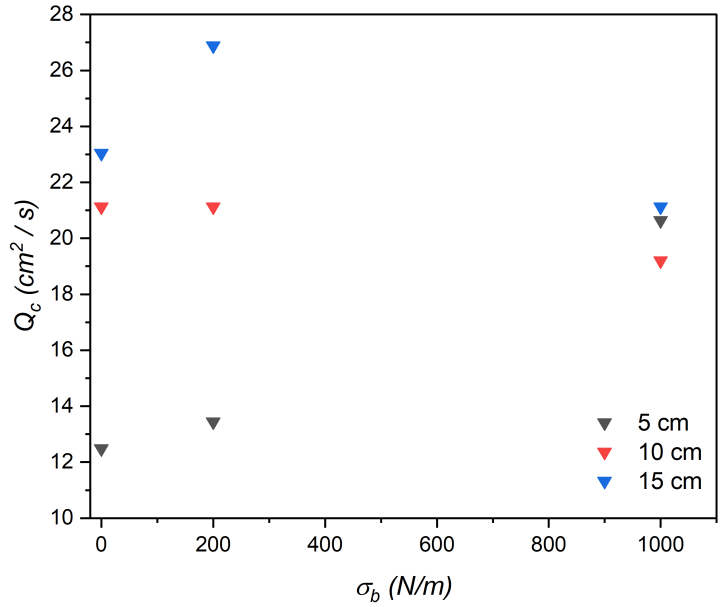

Figure 4.25. – Critical inlet flow rate as a function of bond strength for a sample with $d = 5$ mm and height of 5, 10, and 15 cm.

a decrease for the highest bond strength. This behaviour has been further explored in the following section based on the construction of phase diagrams.

Phase diagrams for the different regimes and scenarios

We have conducted more simulations, using either constant or gradually increasing flow rate, to determine the critical inlet flow rate Q_c specifically for a bed of height $H =$ 15 cm by varying the particle diameter (2 and 5 mm) and the bond strength σ_b. Figures 4.26 and 4.27 provide two phase diagrams summarizing the various observed regimes, including the domain where damage occurs in the static regime and also the destabilization scenarios of the failure regime, observed for inlet flow rates ranging from 0 to 4.03 cm^2/s and from 0 to 43.2 cm^2/s for $d = 2$ mm and $d = 5$ mm, respectively.

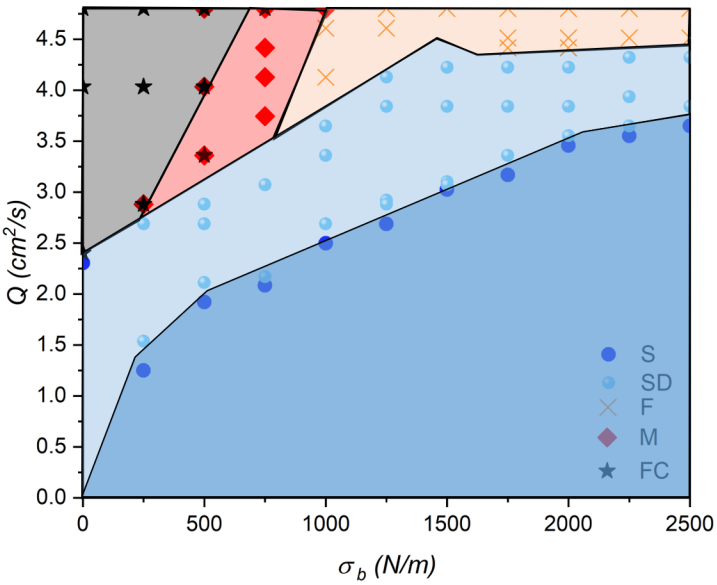

Figure 4.26. – Phase-diagram summarizing the different regimes with the destabilization scenarios for a sample with $d = 2$ mm and $H = 15$ cm. S: static without damage; SD: static with damage; F: Fracture; M: Mixed; and FC: Fluidized chimney.

Firstly, it should be noted that it is sometimes difficult to discern or define the boundaries between fluidized chimney, mixed, and fracture destabilization scenarios. Furthermore, it can be particularly difficult to distinguish between a sample that is still static but has undergone much localized damage as the initiation of a fracture, and a sample that will be considered definitely fractured. The plotted boundaries are thus positioned roughly. Although very different from a quantitative point of view, the two phase diagrams for the different grain diameters are quite similar from a qualitative point of view. Interestingly, we see that increasing the inlet flow rate, while maintaining the cementation bond strength and the bed height constant, results in a

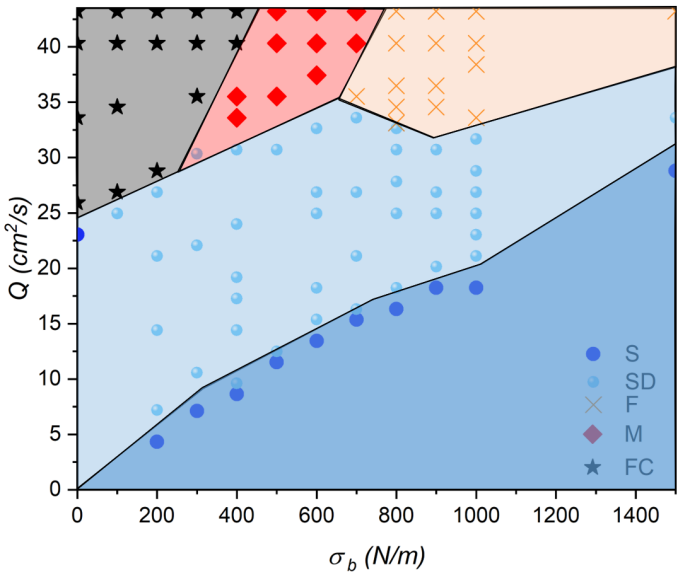

Figure 4.27. – Phase-diagram summarizing the different regimes with the destabilization scenarios for a sample with $d = 5$ mm and $H = 15$ cm. S: static without damage; SD: static with damage; F: Fracture; M: Mixed; and FC: Fluidized chimney.

transition from one type of destabilization to another, from fracture to mixed or from mixed to fluidized chimney.

Concerning the frontier between static (including damage) and failure regimes, we partially confirm the previous result showing that the initial growth of Q_c with σ_b does not continue but saturates and even decreases, as evident in the diagram for the series with $d = 2$ mm in Figure 4.26. A slightly different trend is found for the other series $d = 5$ mm. Indeed, there is clearly an initial increase, but it is followed by a small decrease, before again observing an increase in the resistance of the medium with σ_b (see Fig. 4.27). In both series, the three destabilization scenarios are successively met along this frontier between static and failure regimes. The local decline of the boundary for $d = 5$ mm is experienced just after the transition from the mixed scenario to the fracture scenario, in the range $700 < \sigma_b < 900$ N/m.

4.2.2.3. Analysis of damage in the static regime

In this last section, we focus on the static regime in the situation where the inlet flow rate is too small to destabilize the cemented bed but high enough to induce damage through bond ruptures within the sample as shown in the previous phase diagrams.

Figure 4.28 shows, for increasing values of the bond strength, the spatial distribution of the broken bonds in a sample with $d = 5$ mm and $H = 15$ cm, after solicitation during 10 s at a constant inlet flow rate of 28.8 cm^2/s. The broken bonds are presented in white color while the intact ones are in red. For weak cementation, one can observe a rather homogeneous debonding through the whole sample. After reaching a higher

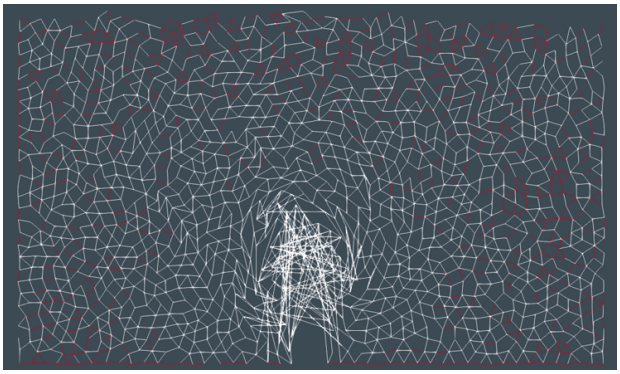

(a) $\sigma_b = 100 N/m$

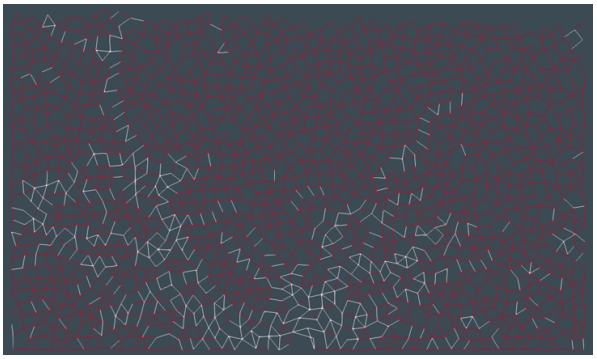

(b) $\sigma_b = 500 N/m$

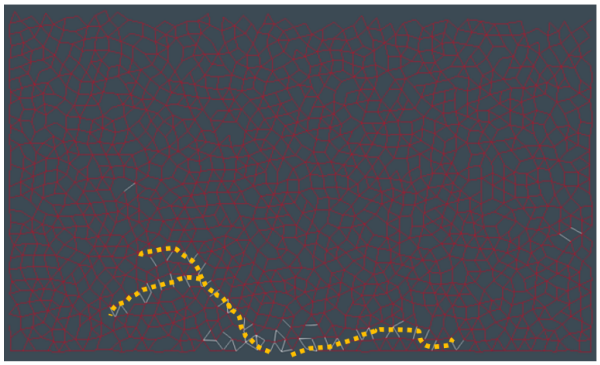

(c) $\sigma_b = 900 N/m$

Figure 4.28. – Distribution of the broken bonds in a sample with d = 5 mm and H = 15 cm subjected to an inlet flow rate Q = 28.8 cm^2/s during 10 s, for different bond strengths: (a) σ_b = 100 N/m; (b) σ_b = 500 N/m; (c) σ_b = 900 N/m. The intact bonds are in red, the broken ones in white and the yellow dotted curves tracers stand for fracture paths.

level of the bond strength (here $\sigma_b \approx 500$ N/m), the number of broken bonds is much more reduced and tends to follow fracture paths. Increasing the cementation bond strength further reduces the length of these fractures and their inclination. This spatial distribution of damage reflects the type of destabilisation observed at higher flow

rates: homogeneous debonding, heterogeneous debonding and localized debonding along cracks correspond to the early stage of fluidized chimney, mixed and fracture destabilisation scenarios, respectively. It should be highlighted that we are still in the static regime with a damaging case but no visible evolution in the sample in terms of strain and grain displacement. However, a slight transitory bed inflation is observed, as shown in Figures 4.29 and 4.30 for the same sample with $d = 5$ mm and another one with $d = 2$ mm. It is recalled that the grains are artificially fixed for 0 s $< t <$ 2 s, which explains that the bed height first remains constant. Obviously, the subsequent dilation of the bed substantially depends on the cementation bond strength. Indeed, both the duration of the transient and the final steady dilation reached decrease for stronger bonds down to an asymptotic dilation curve which is most likely due to the elasticity of the bonds which remains unchanged. However, it could be relevant in the future to fine-tune the solid bond model by directly linking bond elasticity to bond strength. For the three weakest bond strengths in the 5 mm cemented bed, it can be seen that the dilation is not fully stabilized yet. This is a typical case where it is difficult to distinguish between severe damage that leaves however the sample in the static regime and very slow destabilization in the failure regime according to a fluidized chimney scenario in this example (see the phase diagram in Figure 4.27).

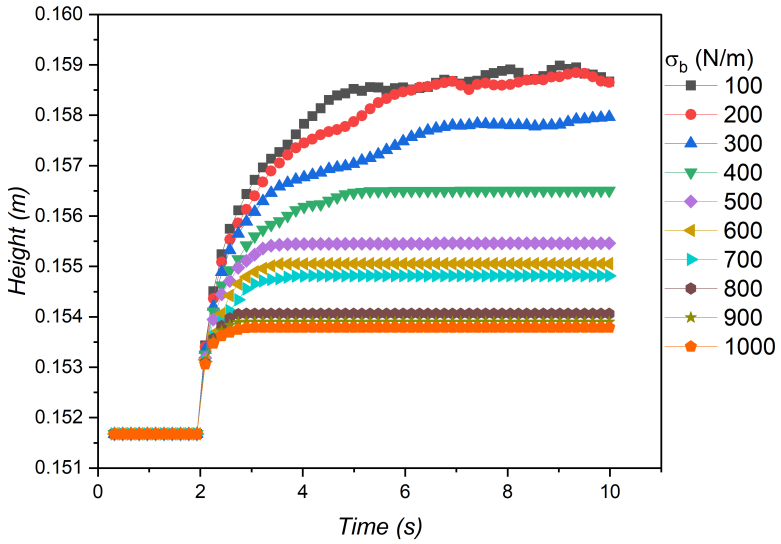

Figure 4.29. – Bed height versus time in a sample with $d = 5$ mm and $H = 15$ cm subjected to an inlet flow rate $Q = 28.8$ cm^2/s during 10 s, for bond strength varying from 100 to 1000 N/m.

The influence of the bond strength is also clearly observed in the number of broken bonds, which is progressively reduced by increasing σ_b as shown in Figures 4.31 and 4.32. At the release of the previously fixed grains (i.e. at $t = 2$ s), an instantaneous damage occurs, involving an increasing number of bond ruptures when σ_b is de-

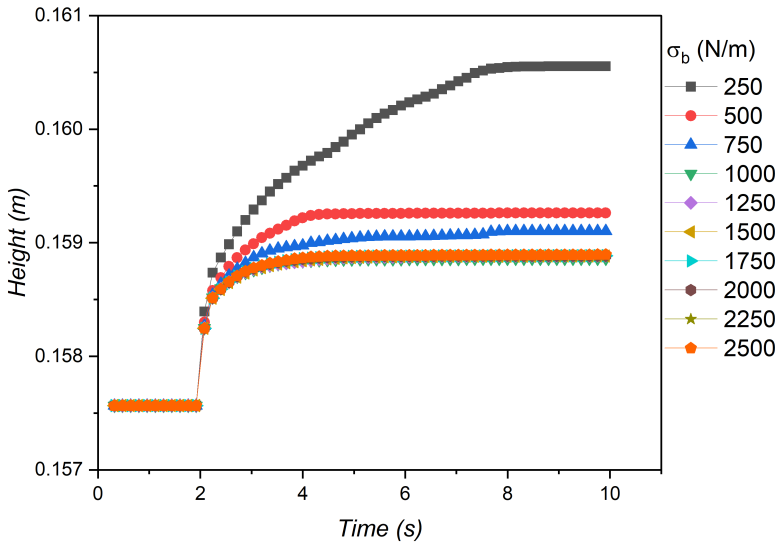

Figure 4.30. – Bed height versus time in a sample with $d = 2$ mm and $H = 15$ cm subjected to an inlet flow rate $Q = 2.88$ cm^2/s during 10 s, for bond strength varying from 250 to 2500 N/m.

creased, corresponding to the homogeneous debonding already mentioned. This is particularly noticeable for the 5 mm sample in Figure 4.29 while not a single bond is broken in the 2 mm bed for σ above 750 N/m. Next, for $t > 2$ s, there is almost no more damage for sufficiently high bond strengths, typically above $\sigma_b \approx 700$ N/m for $d = 5$ mm and $\sigma_b \approx 250$ N/m for $d = 2$ mm, respectively.

The graphs in Figures 4.33 and 4.34 are obtained by plotting for each of the two previous series of simulations the cumulative damage as the fraction of broken bonds compared to the initial bond population. The damage decreases quite rapidly with increasing strength of the bonds until a limit value ($\sigma_b \approx 800$ N/m for both $d = 5$ mm and $d = 2$ mm) beyond which it reaches almost zero, meaning that roughly no bonds are broken. In the damage range, a homogenous debonding of the sample is found for low cementation bond strength while, for intermediate σ_b values, one observes cracks in terms of bond ruptures localization but without significant straining of the sample. As can be seen in Figure 4.33, a complete damage equal to 1 is expected to be reached at very low bond strength which means that the bed is no more cemented but purely frictional, ready to be fluidized through a chimney. On the contrary, in Figure 4.34 with $d = 2$ mm, damage remains much smaller than 1. We also observe in this graph that the damage curve is slightly shifted to the low bond strength values when the imposed flow rate is smaller, going from 2.88 cm^2/s to 2.40 cm^2/s.

While maintaining the constant inlet flow rate of the two previous series of simulations, the mean pressure at the inlet can be calculated and its variation is shown in Figures 4.35 and 4.36 for different σ_b. To start with, a comment can be made on the

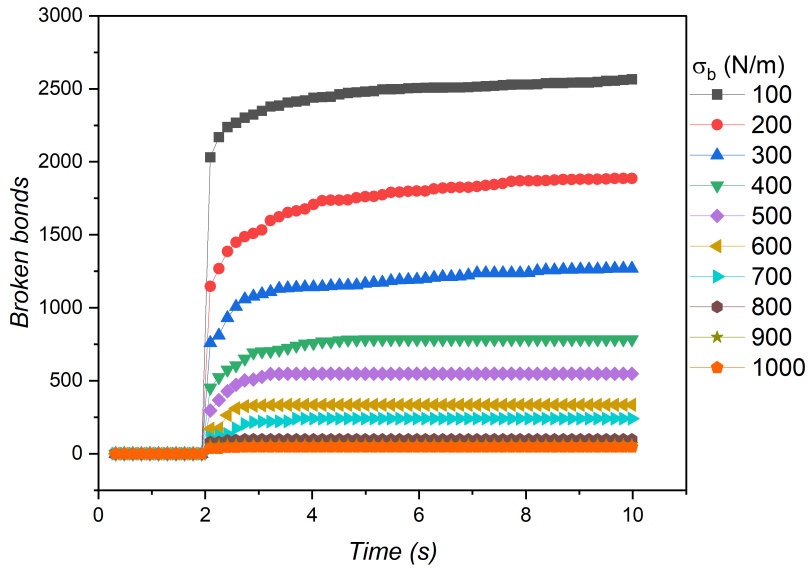

Figure 4.31. – Number of broken bonds versus time in a sample with $d = 5$ mm and $H = 15$ cm subjected to an inlet flow rate $Q = 28.8$ cm^2/s during 10 s, for bond strength varying from 100 to 1000 N/m.

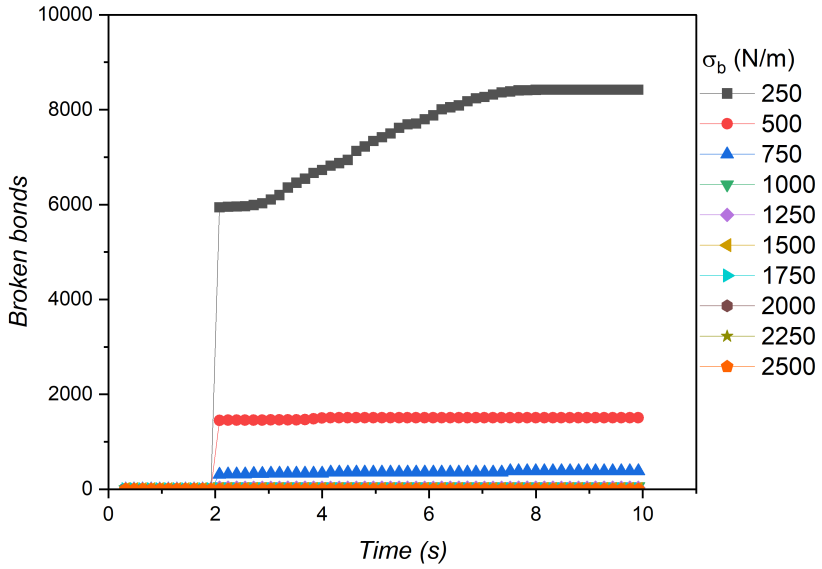

Figure 4.32. – Number of broken bonds versus time in a sample with $d = 2$ mm and $H = 15$ cm subjected to an inlet flow rate $Q = 2.88$ cm^2/s during 10 s, for bond strength varying from 250 to 2500 N/m.

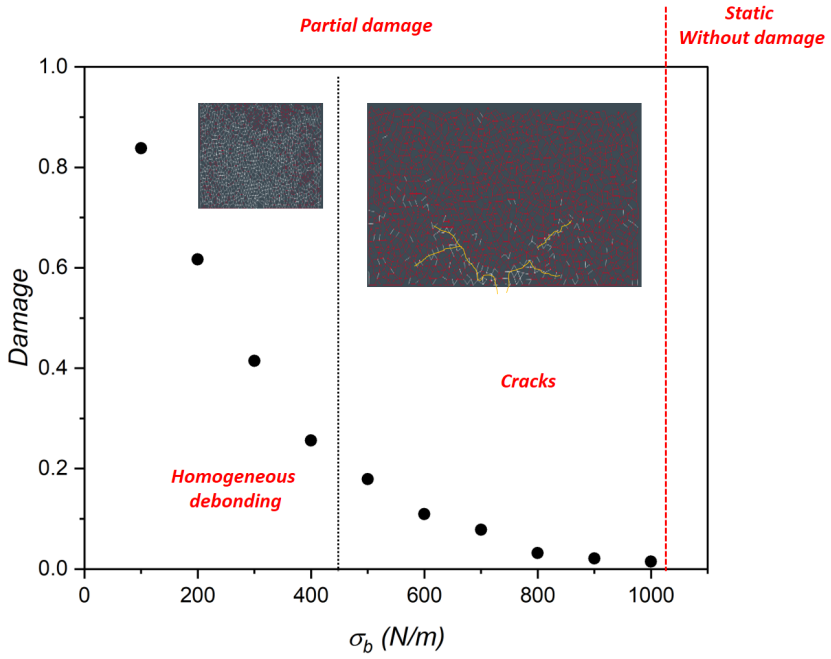

Figure 4.33. – Damage in a sample with $d = 5$ mm and $H = 15$ cm subjected to an inlet flow rate $Q = 28.8$ cm^2/s during 10 s as a function of bond strength.

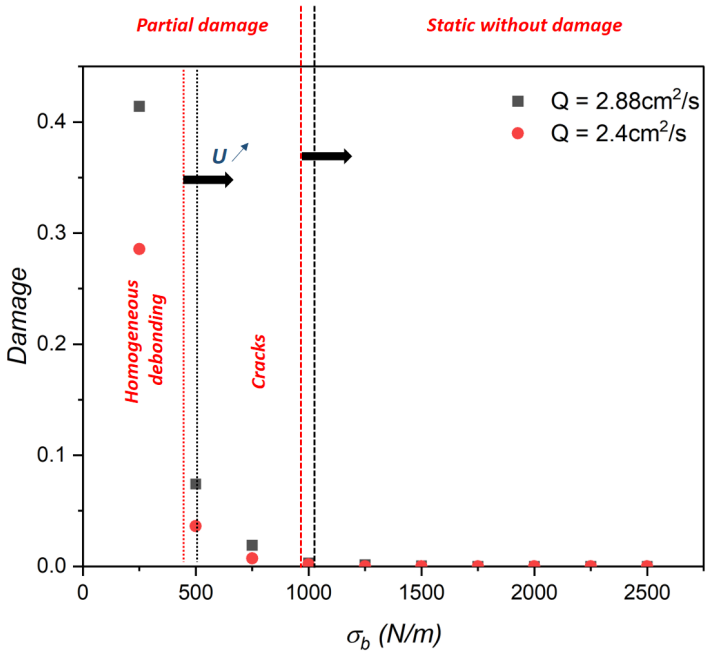

Figure 4.34. – Damage in a sample with $d = 2$ mm and $H = 15$ cm subjected to an inlet flow rate of either $Q = 2.88$ cm^2/s (black square symbols) or $Q = 2.40$ cm^2/s (red circle symbols) during 10 s as a function of bond strength.

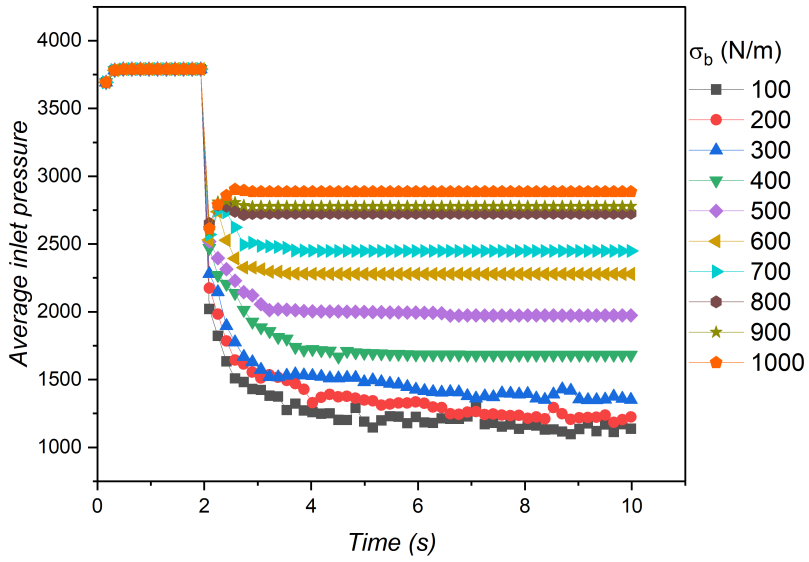

Figure 4.35. – Mean inlet pressure versus time in a sample with $d = 5$ mm and $H = 15$ cm subjected to an inlet flow rate $Q = 28.8$ cm^2/s during 10 s, for bond strength varying from 100 to 1000 N/m.

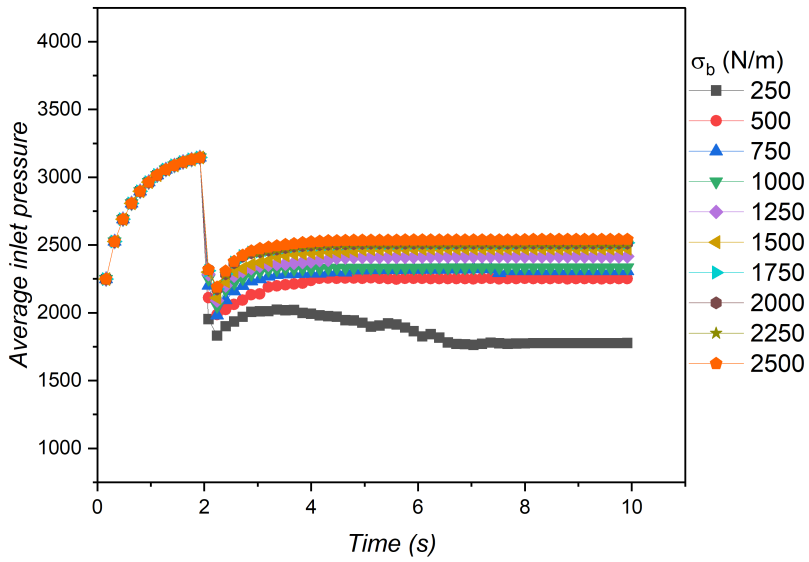

Figure 4.36. – Mean inlet pressure versus time in a sample with $d = 2$ mm and $H = 15$ cm subjected to an inlet flow rate $Q = 2.88$ cm^2/s during 10 s, for bond strength varying from 250 to 2500 N/m.

first two seconds during which the grains are fixed: the time required for the flow to be well established and for the pressure to stabilize is very short for the 5 mm bed but much longer for the 2 mm one, where the steady state of the flow is not fully reached after 2 s. This is most likely due to the difference in hydraulic conductivity between the two beds, which is directly related to the size of the grains. After grain release at $t = 2$ s, a sudden drop in pressure is observed, which can be explained by the expansion of the bed already discussed above. Then, below a threshold in bond strength, the pressure keeps decreasing slowly to almost reach a steady value while, above this threshold, it is increasing again before stabilizing at a final constant value. Note that the threshold values found for the two samples are exactly the ones as highlighted previously regarding the temporal evolution of bond ruptures and damage. Finally, it should be pointed out that the perfectly stationary state observed after this more or less long transitory phase confirms that the bed remains truly static. With the exception, as already mentioned, of the simulations for the 5 mm bed with the 3 weakest bond strengths, which could possibly be considered as evolving towards the failure regime.

4.2.3. Discussion

Comparison with experimental results

Although the numerical modeling is done in 2D, we can see that there are points of agreement with the experiments on the hydraulic failure of cemented granular layers previously presented. With regard to the different types of destabilization, we first obtained a similar static regime when the imposed flow rate is low enough. In this case, the numerical study could interestingly provide complementary information on the state of internal cementation by recording the broken bonds within the hydraulically stressed sample. It should be remembered that one of the initial targets of the experimental study was to use the RIM visualization technique in order to explore the microstructure evolution of a model of cemented soil during its erosion. As explained in section 2.1.5.1, despite our efforts, we had unfortunately not succeeded in setting up a system suitable for this type of visualization.

Using this 2D numerical modeling, by intentionally implementing a strong cementation, we also succeeded in simulating a destabilization scenario somehow reminiscent to the block rupture behavior often observed during the experiments, even if there are clear differences in the orientation of the fractures and the shape of the area that is finally lifted by the flow. The type of destabilization along a preferential path for low bond strengths is also found in both numerical and experimental approaches. However, while the simulations produce a central fluidized chimney (both in the fluidized chimney and mixed scenarios), the experimental observation shows a fluidized path that develops along the walls. The two processes therefore remain quite different, with a strong influence of the boundary conditions in the experiments and a very restrictive limitation to 2D geometry in the simulations.

2D limitations and transition to 3D simulations

The 2D frame of our numerical model is most likely at the origin of part of the differences observed between the experimental and modeling results. In practice, the initial choice to develop an in-house 2D code was motivated by the possibility of ensuring computation times accessible by the technology available at that point in our research team. The computational efficiency thus enabled us to explore the phenomenology in wide range of parameters, in particular, to propose phase diagrams. Nevertheless, it is important to recognize the limitations of this approach. Typically, in a densely packed 2D granular sample, the disks are supposed to be in true contact. For our immersed situation, in order to allow the fluid to circulate throughout the pores, we had to introduce the so-called hydraulic radius, which represents a slightly smaller radius for the grains in the LBM calculations than the real radius value for the DEM calculations. This 2D geometry also reduces the degrees of freedom accessible by the system by limiting for example the rearrangements between neighboring grains. Moreover, the bottom injection of the fluid flow through a small cross-section in a plane, rather than in a volume, necessarily induces a slower decrease in velocity away from the source than in the real 3D case.

As presented in chapter 2 (see section 2.2.3), in the context of the bilateral COMET project between France and Germany, a 3D numerical modeling of immersed cemented grains has been developed, in parallel to the present study, during the twin PhD thesis of Mohammad Sanayei (at BAM [2] in Berlin and RUB [3] in Bochum). As part of my co-tutelle PhD thesis and French-German co-supervision, I spent several weeks at BAM, under the local supervision of Dr. Pablo Cuéllar, in order to learn the basics of their massively parallel 3D extension using a LBM-DEM coupling of waLBerla [4] framework, in collaboration with Christoph Rettinger, from the Department Computer Science of FAU [5]. Based on the newly developed code which implements similar boundary conditions as the real experimental ones (see previous Figure 2.32), I carried out two very preliminary simulations, for a granular and for a cemented sample. For these first 3D numerical simulations using WaLBerla and shown in Figure 4.37, we selected a shallow sample to reduce the calculation time. The main parameters are $d = 0.5$ mm, $\rho_g = 1010$ kg/m^3, $\sigma_b = 8 \times 10^6$ N/m^2 and $\nu = 10^{-6}$ m^2/s, with a 3D domain of dimension $1 \times 1 \times 1$ cm^3. It is still too early to make broad statements, but we observed that the two cases, as expected, behave differently. In contrast to the granular sample, where the flow erodes the grains away, the flow in the cemented granular layer prefers to flow towards the sample's border walls and under the grains. Based on these initial encouraging results, further 3D simulations will be carried out, with the ultimate objective of a direct comparison with our experiments.

2. https://www.bam.de
3. https://www.ruhr-uni-bochum.de/en
4. https://walberla.net/
5. https://fau.eu/

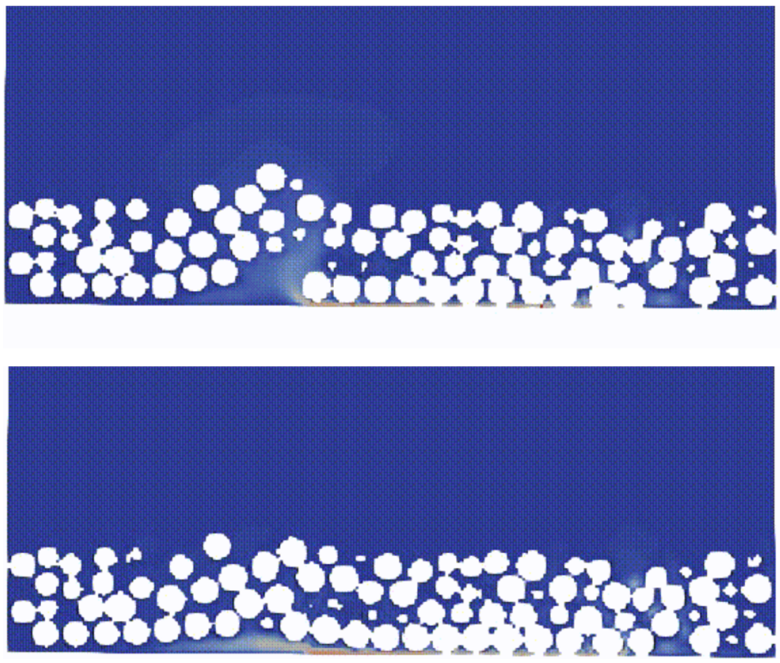

Figure 4.37. – Cross-section of 3D destabilization of (top) a granular and (bottom) a cemented granular sample by a localized inlet flow rate. The flow velocity is indicated by a range of colors, with red indicating the highest value and blue indicating the lowest value.

Conclusion and perspectives

Conclusion

The goal of this thesis was to investigate, mainly experimentally and numerically for a complementary part, the hydromechanical instability and the elementary mechanisms of destabilization of cemented granular materials using a micro-macro approach. This study notably aimed to address the specific problem of the safety of hydraulic structures, such as dams and embankments, threatened by the phenomenon of erosion. Despite the difficulties encountered, in particular for some experimental aspects, interesting advances have been made and the main findings are summarized below.

Micro-macro mechanical characterization

Our research first focused on the experimental micro-macro mechanical characterization of artificial cemented granular materials, made of spherical glass beads bonded with paraffin bridges. By varying the properties (particle size, surface finishing, and paraffin content) of this artificial material, we tested a large range of sample parameters. On the one hand, we investigated several solicitations at the micro-scale to study the bond strength, starting from tensile and shear forces to bending and torsion moments. Despite the large dispersion detected (standard error nevertheless less than 20 %), the micro-tensile force was found to increase with both the paraffin content and the glass bead diameter. By means of X-ray tomography and specific experiments with image processing, we examined three different modes of bond rupture: (i) adhesive rupture, when a full debonding at the bead surface occurs; (ii) cohesive rupture, when the bridge itself is fractured; (iii) mixed rupture, which combines the two others. Typically, around 90 % of the bond ruptures are adhesive ones for the polished particles, whereas, for the matt beads, the ruptures are mostly mixed. Only some rare cases of cohesive ruptures have been observed for matt beads with large diameter. An interesting finding was that, within the intrinsic dispersion, the micro-tensile strength does not seem to be affected neither by the size of the paraffin bridge nor by the type of the rupture. To interpret our measurements, we have succeeded in deriving a theoretical law that links the micro-tensile force to paraffin volume content, coordination number, and grain diameter. Finally, we proposed to linearly relate the critical values of shear force, bending moment, and torsion moment to the yield micro-tensile force, using coefficients obtained by fitting our whole set of data and thus offering a calibrated 3D model for grain cementation through solid bonds.

On the other hand, we performed macro-tensile tests for which high variability was measured, even larger than at the micro-scale. Beyond this dispersion, resulting from both the above scattering in the particle-particle cohesion strength and a suspected finite size effect related to the macro-devices, the macro-tensile strength was found, as expected, to increase with the paraffin content. A proposal of a theoretical law based on the micro-scale one was derived by the use of a homogenization law proposed by Richefeu and co-authors (Richefeu, El Youssoufi, and Radjaı 2006) and in the continuation of Rumpf's initial work. This theoretical expression suggests a dependence solely on the paraffin volume concentration and not on the size of the glass beads. An observation of an instantaneous brittle failure during several creep tests indicated the absence of damage progressing in the sample by bond ruptures. Finally, complementary tests showed that the macro-tensile force could be affected by the rate of loading, and the non-repeatability of the creep tests highlighted the random nature of the failure process.

Localized hydraulic failure of a cemented granular layer

In the second part of our work, we carried out several experimental campaigns on submerged cemented granular materials subjected to a localized flow loading from bottom injection. Globally, all of these experiments showed that cemented beds made of larger beads and higher paraffin content required a greater flow rate to be destabilized. Four distinct modes of hydraulic failure were observed: (i) a static regime, with no movement in the sample; (ii) a block rupture, characterized by the appearance of a median crack above the flow inlet; (iii) a fluidized path rupture, by progressive burrowing along the walls towards the inlet; and (iv) a block uplift rupture, when the sample slides upward at the lateral walls following prior bond breakage at its boundaries. To relate these experiments to our previous micro-mechanical characterization, we plotted the critical hydraulic pressure, acquired at each hydraulic failure experiment, as a function of the yield micro-tensile force. The resulting and rather speculative trend showed that the hydraulic threshold indeed increased with the cemented soil cohesion, regardless of the destabilization mode. Finally, in consistency with previous data from experiments on granular localized fluidization (Mena, Luu, Cuéllar, et al. 2017), it was possible to satisfactorily gather all the data, approximately on Ergun's law, when considering the relevant dimensionless numbers, namely the inlet particle Reynolds number and the Archimedes number, the latter being adapted to the cemented case by considering the micro-tensile force instead of the grain buoyant weight.

In addition, we succeeded in simulating several types of localized hydraulic failures in cemented granular beds using a homemade 2D numerical code based on an LBM-DEM coupling method. The governing parameters for the onset of erosion were found to be the flow rate (regardless of the inlet velocity profile applied at the inlet injection), the particle diameter, the bond strength, and the bed height. A rather similar phenomenology was thus observed, including the following scenarios reminiscent to the experiments: (i) the so-called static regime, with possible partial damage by

rupture of a fraction of the solid bridges; (ii) the fracture scenario, that refers to a destabilization of the cemented bed through almost symmetric inclined cracks initiating from the inlet ; (iii) the fluidized chimney scenario, that refers to a localized destabilization of the grains, from the inlet, in somehow the same way as with purely granular material; (iv) the mixed scenario, that is a combination of the two previous ones. Using phase diagrams, we finally discussed the influence of both inlet flow rate and bond strength on the failure modes. Overall, we got an interesting though limited agreement between the 2D numerical part and the experimental findings. However, the discrepancy provides an incentive to improve the modeling by pursuing a 3D extension. In collaboration with the BAM, some preliminary and rather promising 3D simulations using the WaLBerla framework have been successfully performed at the very end of this thesis.

Perspectives

A 3D DEM inhouse code of the macro scale tensile cone test was developed by Mohammad Sanayei and Pablo Cuéllar at BAM using C++ language. This code shares exactly the same parameters than our experiments: cone sizes, particle diameters and 3D solid bond model previously proposed with the coefficients obtained from the micro-scale experimental tests. This numerical replicate will be used to investigate the origins of the huge dispersion observed experimentally: Distributed yield values; finite size effect; impact of polydispersity.

The present investigation also opens up numerous perspectives on the problem of hydraulic fracturing of cemented soil by localized flows. From an experimental point of view, we encountered many limitations, notably the fact that the sample was highly controlled by the boundary of the system, that make this present work a first, still exploratory step, which calls for further development. For future work, the setup could be optimized to allow better repeatability and to make accessible a more controlled range of study parameters that would eventually reveal intermediate or new failure regimes. The validity of Ergun's law is particularly meant to be included in future objectives by performing additional systematic experiments. Exploring different protocols, such as imposing a constant flow rate for a longer duration would also be relevant for studying possible damage effect in the long term. Minor improvements to the adhesive solid bond model could also be considered, and calibrated using experimental data, for example concerning bond elasticity. Finally, the 3D numerical tool in development announces the hoped-for possibility to perform more realistic simulations. With a more comprehensive purpose, the experimental and numerical modelings initiated during this thesis are intended to be extended to the broader framework of research on erosion and hydro-mechanical instabilities in such cemented soils.

Bibliography

[Aff+12] R. Affes, J.-Y. Delenne, Y. Monnerie, et al. “Tensile strength and fracture of cemented granular aggregates”. In: *Eur. Phys. J. E* 35 (2012), p. 117 (cit. on p. 101).

[Ai+11] J. Ai, J.-F. Chen, J.-M. Rotter, et al. “Assessment of rolling resistance models in discrete element simulations”. In: *Powder Technology* 206.3 (2011), pp. 269–282 (cit. on p. 29).

[ALD98] C.-K. Aidun, Y. Lu, and E.-J. Ding. “Direct analysis of particulate suspensions with inertia using the discrete Boltzmann equation”. In: *Journal of Fluid Mechanics* 373 (1998), pp. 287–311 (cit. on p. 81).

[Akr+22] S. Akrami, A. Bezuijen, F.-S. Tehrani, et al. “The effect of relative density in the response of sand to internal fluidization”. In: *Acta Geotechnica* (2022) (cit. on p. 42).

[AC14] M.-O.-A. Alsaydalani and C.-R.-I. Clayton. “Internal fluidization in granular soils”. In: *Journal of Geotechnical and Geoenvironmental Engineering* 140.3 (2014), p. 04013024 (cit. on pp. 42, 43, 45).

[ATH03] E. Asghari, D.-G. Toll, and SM. Haeri. “Triaxial behaviour of a cemented gravely sand, Tehran alluvium”. In: *Geotechnical Geological Engineering* 21 (2003), pp. 1–28 (cit. on pp. 15–17).

[Bal+10] D. Balcan, B. Gonçalves, H. Hu, et al. “Modeling the spatial spread of infectious diseases: The GLobal Epidemic and Mobility computational model”. In: *Journal of computational science* 1.3 (2010), pp. 132–145 (cit. on p. 81).

[Bat72] G.-K. Batchelor. “Sedimentation in a dilute dispersion of spheres”. In: *Journal of fluid mechanics* 52.2 (1972), pp. 245–268 (cit. on p. 26).

[Bea88] J. Bear. *Dynamics of fluids in porous media*. Courier Corporation, 1988 (cit. on pp. 11, 25, 26, 41).

[BPF13] R. Beguin, P. Philippe, and Y.-H. Faure. “Pore-scale flow measurements at the interface between a sandy layer and a model porous medium: Application to statistical modeling of contact erosion”. In: *Journal of Hydraulic Engineering* 139.1 (2013), p–1 (cit. on pp. 26, 66).

[Ben+20a] Z. Benseghier, P. Cuéllar, L.-H. Luu, S. Bonelli, et al. “A parallel GPU-based computational framework for the micromechanical analysis of geotechnical and erosion problems”. In: *Computers and Geotechnics* 120 (2020), p. 103404 (cit. on pp. 32, 33, 35, 38, 77, 95, 132).

[Ben+20b] Z. Benseghier, P. Cuéllar, L.-H. Luu, S. Delenne J.-Y.and Bonelli, et al. "Relevance of free jet model for soil erosion by impinging jets". In: *Journal of Hydraulic Engineering* 146.1 (2020), p. 04019047 (cit. on p. 36).

[Bol+07] E. Bollaert, A. Schleiss, L.-G. Castillo, et al. "Scour of rock due to the impact of plunging high velocity jets Part I: A state-of-the-art review". In: *Journal of Hydraulic Research* 45.6 (2007), pp. 853–858 (cit. on p. 1).

[Bon12] S. Bonelli. *Erosion of geomaterials*. John Wiley & Sons, 2012 (cit. on p. 1).

[BB11] S. Bonelli and N. Benahmed. "Piping flow erosion in water retaining structures". In: (2011) (cit. on p. 7).

[Bou+07] D.-F. Boutt, B.-K. Cook, B.-J.-O.-L. McPherson, et al. "Direct simulation of fluid-solid mechanics in porous media using the discrete element and lattice-Boltzmann methods". In: *Journal of Geophysical Research: Solid Earth* 112.B10 (2007) (cit. on p. 38).

[BFL01] M. Bouzidi, M. Firdaouss, and P. Lallemand. "Momentum transfer of a Boltzmann-lattice fluid with boundaries". In: *Physics of fluids* 13.11 (2001), pp. 3452–3459 (cit. on p. 38).

[Bre+11] L. Brendel, J. Török, R. Kirsch, et al. "A contact model for the yielding of caked granular materials". In: *Granular Matter* 13 (6 2011), pp. 777–786 (cit. on pp. 29, 30, 101).

[Bro70] R.-L. Brown. *JC Richards in Principles of Powder Mechanics*. 1970 (cit. on p. 11).

[Bru16] F. Brunier Coulin. "Étude des mécanismes élémentaires de l'érosion d'un sol cohésif". Theses. 2016, p. 159. URL: https://hal.inrae.fr/tel-02605448 (cit. on pp. 54, 55).

[BCP17] F. Brunier-Coulin, P. Cuéllar, and P. Philippe. "Erosion onset of a cohesionless granular medium by an immersed impinging round jet". In: *Physical Review Fluids* 2.3 (2017), p. 034302 (cit. on p. 66).

[BCP20] F. Brunier-Coulin, P. Cuéllar, and P. Philippe. "Generalized Shields criterion for weakly cohesive granular materials". In: *Phys. Rev. Fluids* 5 (3 2020), p. 034308 (cit. on pp. 51, 55, 58).

[Bud88] D.-A. Budd. "Aragonite-to-calcite transformation during fresh-water diagenesis of carbonates: Insights from pore-water chemistry". In: *Geological Society of America Bulletin* 100.8 (1988), pp. 1260–1270 (cit. on p. 19).

[Cas+17] L.-A. Casella, E. Griesshaber, X. Yin, et al. "Experimental diagenesis: insights into aragonite to calcite transformation of Arctica islandica shells by hydrothermal treatment". In: *Biogeosciences* 14.6 (2017), pp. 1461–1492 (cit. on p. 19).

[CCB14] E. Catalano, B. Chareyre, and E. Barthélemy. "Pore-scale modeling of fluid-particles interaction and emerging poromechanical effects". In: *International Journal for Numerical and Analytical Methods in Geomechanics* 38.1 (2014), pp. 51–71 (cit. on p. 34).

[CCB13] E. Catalano, B. Chareyre, and E. Barthélémy. "DEM-PFV analysis of solid-fluid transition in granular sediments under the action of waves". In: *AIP Conference Proceedings*. Vol. 1542. 1. American Institute of Physics. 2013, pp. 1063–1066 (cit. on p. 34).

[CC70] S. Chapman and T.-G. Cowling. *The mathematical theory of non-uniform gases: An account of the kinetic theory of viscosity, thermal conduction and diffusion in gases*. Cambridge University Press, 1970 (cit. on p. 35).

[Che+20] X. Chen, L.-G. Wang, J.-P. Morrissey, et al. "DEM simulations of agglomerates impact breakage using Timoshenko beam bond model". In: *Granular Matter* 24 (3 2020), p. 74 (cit. on p. 16).

[CC05] Chung and Chaudhury. "Soft, J.-Y. and Hard Adhesion, M.-K." In: *The Journal of Adhesion* 81.10-11 (2005), pp. 1119–1145 (cit. on pp. 29, 101).

[CS11] B.-D. Collins and N. Sitar. "Stability of Steep Slopes in Cemented Sands". In: *Journal of Geotechnical and Geoenvironmental Engineering* 137.1 (2011), pp. 43–51 (cit. on p. 15).

[Cui13] X. Cui. "Numerical simulation of internal fluidisation and cavity evolution due to a leaking pipe using the coupled DEM-LBM technique". PhD thesis. University of Birmingham, 2013 (cit. on pp. 39, 43–45, 133).

[Cui+12] X. Cui, J. Li, A. Chan, et al. "A 2D DEM–LBM study on soil behaviour due to locally injected fluid". In: *Particuology* 10.2 (2012), pp. 242–252 (cit. on pp. 38, 39, 43, 45).

[Cui+14] X. Cui, J. Li, A. Chan, et al. "Coupled DEM–LBM simulation of internal fluidisation induced by a leaking pipe". In: *Powder Technology* 254 (2014), pp. 299–306 (cit. on pp. 45, 133).

[CS79] P.-A. Cundall and O.-D.-L. Strack. "A discrete numerical model for granular assemblies". In: *geotechnique* 29.1 (1979), pp. 47–65 (cit. on p. 27).

[Dar56] H. Darcy. *Les fontaines publiques de la ville de Dijon: Exposition et application des principes à suivre et des formules à employer dans les questions de distribution d'eau: Ouvrage terminé par un appendice relatif aux fournitures d'eau de plusieurs villes, au filtrage des eaux et à la fabrication des tuyaux de fonte, de plomb, de tôle et de bitume*. Vol. 2. V. Dalmont, 1856 (cit. on p. 25).

[Del+04] J.-Y. Delenne, M.-S. El Youssoufi, F. Cherblanc, et al. "Mechanical behaviour and failure of cohesive granular materials". In: *International Journal for Numerical and Analytical Methods in Geomechanics* 28.15 (2004), pp. 1577–1594 (cit. on pp. 19, 21, 29, 30, 32, 77).

[DeS+09] J. DeSain, B. Brady, K. Metzler, et al. “Tensile Tests of Paraffin Wax for Hybrid Rocket Fuel Grains”. In: *45th AIAA/ASME/SAE/ASEE Joint Propulsion Conference & Exhibit*. 2009 (cit. on pp. 51, 106).

[Dur97] J. Duran. “Sables, poudres et grains”. In: (1997) (cit. on p. 11).

[DNY94] J. Dvorkin, A. Nur, and H. Yin. “Effective properties of cemented granular materials”. In: *Mechanics of Materials* 18 (1994), pp. 351–366 (cit. on p. 106).

[ESE11] C. Ergenzinger, R. Seifried, and P. Eberhard. “A discrete element model to describe failure of strong rock in uniaxial compression”. In: *Granular Matter* 13.4 (2011), pp. 341–364 (cit. on pp. 29, 30, 33, 101).

[Fan+03] X. Fan, P. Ten, C. Clarke, et al. “Direct measurement of the adhesive force between ice particles by micromanipulation”. In: *Powder technology* 131.2-3 (2003), pp. 105–110 (cit. on p. 19).

[Far+21] A. Farhat, L.-H. Luu, P. Philippe, et al. “Multi-scale cohesion force measurements for cemented granular materials”. In: *EPJ Web Conf.* 249 (2021), p. 08008 (cit. on p. 106).

[Di-94] R. Di-Felice. “The voidage function for fluid-particle interaction systems”. In: *International Journal of Multiphase Flow* 20.1 (1994), pp. 153–159 (cit. on pp. 23, 33).

[FF07] R. Fell and J.-J. Fry. “The state of the art of assessing the likelihood of internal erosion of embankment dams, water retaining structures and their foundations”. In: *Internal erosion of dams and their foundations, edited by: Fell, R. and Fry, JJ, Taylor and Francis, London* (2007), pp. 1–24 (cit. on p. 7).

[FHO07] Y.-T. Feng, K. Han, and D.-R.-J. Owen. “Coupled lattice Boltzmann method and discrete element modelling of particle transport in turbulent fluid flows: Computational issues”. In: *International Journal for Numerical Methods in Engineering* 72.9 (2007), pp. 1111–1134 (cit. on p. 43).

[FM04] Z.-G. Feng and E.-E. Michaelides. “The immersed boundary-lattice Boltzmann method for solving fluid–particles interaction problems”. In: *Journal of computational physics* 195.2 (2004), pp. 602–628 (cit. on p. 43).

[Fis26] R.-A. Fisher. “On the capillary forces in an ideal soil; correction of formulae given by WB Haines”. In: *The Journal of Agricultural Science* 16.3 (1926), pp. 492–505 (cit. on p. 14).

[FFS00] M. Foster, R. Fell, and M. Spannagle. “The statistics of embankment dam failures and accidents”. In: *Canadian Geotechnical Journal* 37.5 (2000), pp. 1000–1024 (cit. on pp. 1, 5, 6).

[Fou+05] Z. Fournier, D. Geromichalos, S. Herminghaus, et al. “Mechanical properties of wet granular materials”. In: *Journal of Physics: Condensed Matter* 17.9 (2005), S477 (cit. on p. 14).

[FDG97] J.-J. Fry, G. Degoutte, and A. Goubet. “L’érosion interne: typologie, détection et réparation”. In: *Barrages & réservoirs* 6 (1997), p. 126 (cit. on p. 7).

[GPN20] A. Gans, O. Pouliquen, and M. Nicolas. “Cohesion-controlled granular material”. In: *Physical Review E* 101.3 (2020), p. 032904 (cit. on pp. 13, 17).

[GA77] J. Garside and M.-R. Al-Dibouni. “Velocity-voidage relationships for fluidization and sedimentation in solid-liquid systems”. In: *Industrial & engineering chemistry process design and development* 16.2 (1977), pp. 206–214 (cit. on p. 27).

[Ge+18] R. Ge, M. Ghadiri, T. Bonakdar, et al. “Experimental study of the deformation and breakage of 3D printed agglomerates: Effects of packing density and inter-particle bond strength”. In: *Powder Technology* 340 (2018), pp. 299–310 (cit. on p. 16).

[Gib01] A.-D. Gibilaro. *Fluidization dynamics*. Elsevier, 2001 (cit. on pp. 23, 24, 27).

[Gir+11] M.-C. Girard, C. Walter, J.-C. Rémy, et al. *Sols et environnement-2e édition-Cours, exercices et études de cas-Livre+ compléments en ligne: Cours, exercices corrigés et études de cas*. Dunod, 2011 (cit. on p. 5).

[God+13] C. Godenschwager, F. Schornbaum, M. Bauer, et al. “A framework for hybrid parallel flow simulations with a trillion cells in complex geometries”. In: *Proceedings of the International Conference on High Performance Computing, Networking, Storage and Analysis*. 2013, pp. 1–12 (cit. on p. 81).

[GTH03] T. Gröger, U. Tüzün, and D.-M. Heyes. “Modelling and measuring of cohesion in wet granular materials”. In: *Powder Technology* 133.1 (2003), pp. 203–215. ISSN: 0032-5910. DOI: https://doi.org/10.1016/S0032-5910(03)00093-7. URL: http://www.sciencedirect.com/science/article/pii/S0032591003000937 (cit. on p. 106).

[GM12] E. Guazzelli and J.-F. Morris. *A Physical Introduction to Suspension Dynamic*. Cambridge University Press, 2012 (cit. on p. 26).

[Ham+22] S.-M. Ham, A. Martinez, G. Han, et al. “Grain-Scale Tensile and Shear Strengths of Glass Beads Cemented by MICP”. In: *Journal of Geotechnical and Geoenvironmental Engineering* 148.9 (2022), p. 04022068 (cit. on pp. 17–20, 84, 109).

[HFO07] K. Han, Y.-T. Feng, and D.-R.-J. Owen. “Coupled lattice Boltzmann and discrete element modelling of fluid–particle interaction problems”. In: *Computers & structures* 85.11-14 (2007), pp. 1080–1088 (cit. on p. 39).

[He+17] Y. He, D.-Z. Zhu, T. Zhang, et al. “Experimental Observations on the Initiation of Sand-Bed Erosion by an Upward Water Jet”. In: *Journal of Hydraulic Engineering* 143.7 (2017), p. 06017007 (cit. on p. 42).

[HT06] D. Hlushkou and U. Tallarek. “Transition from creeping via viscous-inertial to turbulent flow in fixed beds”. In: *Journal of Chromatography A* 1126.1-2 (2006), pp. 70–85 (cit. on p. 26).

[HJ21] J. Horabik and G. Jozefaciuk. “Structure and strength of kaolinite–soil silt aggregates: Measurements and modeling”. In: *Geoderma* 382 (2021), p. 114687 (cit. on pp. 29, 30, 101).

[Hu+22] R. Hu, X. Wang, H. Liu, et al. “Scour Protection of Submarine Pipelines Using Ionic Soil Stabilizer Solidified Soil”. In: *Journal of Marine Science and Engineering* 10.1 (2022) (cit. on p. 16).

[Ing62] O.-G. Ingles. “Bonding forces in soils, Part 1: Natural soils - The physical factors responsible for cohesive strength”. In: *Proceedings, Australian Road Research Board Conference, Vol 1, Part 2*. 1962, pp. 999–1013 (cit. on pp. 16, 17, 21, 101).

[Ism+02] M.-A. Ismail, H.-A. Joer, W.-H. Sim, et al. “Effect of Cement Type on Shear Behavior of Cemented Calcareous Soil”. In: *Journal of Geotechnical and Geoenvironmental Engineering* 128.6 (2002), pp. 520–529 (cit. on p. 15).

[Isr11] J.-N. Israelachvili. *Intermolecular and surface forces*. Academic press, 2011 (cit. on p. 12).

[Jar+19] A. Jarray, H. Shi, B.-J. Scheper, et al. “Cohesion-driven mixing and segregation of dry granular media”. In: *Scientific reports* 9.1 (2019), pp. 1–12 (cit. on pp. 14, 17, 19, 84).

[JYL07] M. Jiang, H.-S. Yu, and S. Leroueil. “A simple and efficient approach to capturing bonding effect in naturally microstructured sands by discrete element method”. In: *International Journal for Numerical Methods in Engineering* 69.6 (2007), pp. 1158–1193 (cit. on p. 30).

[Jia+13] M.-J. Jiang, J. Liu, Y. Sun, et al. “Investigation into macroscopic and microscopic behaviors of bonded sands using distinct element method”. In: *Soils and Foundations* 53.6 (2013), pp. 804–819 (cit. on pp. 29, 30).

[Jia+11] M.-J. Jiang, H.-B. Yan, H.-H. Zhu, et al. “Modeling shear behavior and strain localization in cemented sands by two-dimensional distinct element method analyses”. In: *Computers and Geotechnics* 38.1 (2011), pp. 14–29 (cit. on p. 29).

[JYH06] M.-J. Jiang, H.-S. Yu, and D. Harris. “Bond rolling resistance and its effect on yielding of bonded granulates by DEM analyses”. In: *International Journal for Numerical and Analytical Methods in Geomechanics* 30.8 (2006), pp. 723–761 (cit. on p. 29).

[JKR71] K.-L. Johnson, K. Kendall, and A.-D. Roberts. “Surface energy and the contact of elastic solids”. In: *Proceedings of the royal society of London. A. mathematical and physical sciences* 324.1558 (1971), pp. 301–313 (cit. on p. 29).

[JS11] J.-W. Jung and J.-C. Santamarina. “Hydrate adhesive and tensile strengths”. In: *Geochemistry, Geophysics, Geosystems* 12.8 (2011) (cit. on pp. 15, 19).

[Ken71] K. Kendall. “The adhesion and surface energy of elastic solids”. In: *Journal of Physics D: Applied Physics* 4.8 (1971), pp. 1186–1195 (cit. on pp. 29, 101).

[KR89] A.-R. Khan and J.-F. Richardson. “Fluid-particle interactions and flow characteristics of fluidized beds and settling suspensions of spherical particles”. In: *Chemical Engineering Communications* 78.1 (1989), pp. 111–130 (cit. on p. 27).

[Kir+11] R. Kirsch, U. Bröckel, L. Brendel, et al. “Measuring tensile, shear and torsional strength of solid bridges between particles in the millimeter regime”. In: *Granular Matter* 13.5 (2011), pp. 517–523 (cit. on pp. 19, 29).

[Koh+04] M.-M. Kohonen, D. Geromichalos, M. Scheel, et al. “On capillary bridges in wet granular materials”. In: *Physica A: Statistical Mechanics and its Applications* 339.1-2 (2004), pp. 7–15 (cit. on p. 14).

[Kou+22] H. Kou, H. Jing, C. Wu, et al. “Microstructural and mechanical properties of marine clay cemented with industrial waste residue-based binder (IWRB)”. In: *Acta Geotechnica* 17.5 (2022), pp. 1859–1877 (cit. on p. 16).

[LGB08] D. Lachouette, F. Golay, and S. Bonelli. “One-dimensional modeling of piping flow erosion”. In: *Comptes Rendus Mécanique* 336.9 (2008), pp. 731–736 (cit. on p. 33).

[LL00] P. Lallemand and L.-S. Luo. “Theory of the lattice Boltzmann method: Dispersion, dissipation, isotropy, Galilean invariance, and stability”. In: *Physical review E* 61.6 (2000), p. 6546 (cit. on p. 37).

[Li13] J. Li. “Numerical investigations of the coupled DEM-LBM technique with application to leakage-soil interaction due to a leaking pipe”. PhD thesis. University of Birmingham, 2013 (cit. on p. 43).

[LJG04] W. Lick, L. Jin, and J. Gailani. “Initiation of movement of quartz particles”. In: *Journal of Hydraulic Engineering* 130.8 (2004), pp. 755–761 (cit. on p. 12).

[Lin+16] H. Lin, M.-T. Suleiman, D.-G. Brown, et al. “Mechanical Behavior of Sands Treated by Microbially Induced Carbonate Precipitation”. In: *Journal of Geotechnical and Geoenvironmental Engineering* 142.2 (2016), p. 04015066 (cit. on p. 17).

[Luu+19] L.-H. Luu, G. Noury, Z. Benseghier, et al. “Hydro-mechanical modeling of sinkhole occurrence processes in covered karst terrains during a flood”. In: *Engineering Geology* 260 (2019), p. 105249 (cit. on p. 39).

[MFC21] S.-F.-V. Marques, L. Festugato, and N.-C. Consoli. “Stiffness and strength of an artificially cemented sand cured under stress”. In: *Granular Matter* 23 (2021), p. 35 (cit. on p. 15).

[Men+18] S.-E. Mena, F. Brunier-Coulin, J.-S. Curtis, et al. “Experimental observation of two regimes of expansion in localized fluidization of a granular medium”. In: *Physical Review E* 98.4 (2018), p. 042902 (cit. on pp. 39, 42, 66, 121, 124, 128, 129, 133).

[Men+17] S.-E. Mena, L.-H. Luu, P. Cuéllar, et al. “Parameters affecting the localized fluidization in a particle medium”. In: *AIChE Journal* 63.5 (2017), pp. 1529–1542 (cit. on pp. 39–42, 66, 121, 133, 153).

[Mer+14] F. Mercier, S. Bonelli, P. Philippe, et al. “On the numerical modelling of the Hole Erosion Test”. In: *Scour and Erosion: Proceedings of the 7th International Conference on Scour and Erosion, Perth, Australia, 2-4 December 2014*. CRC Press. 2014, p. 309 (cit. on p. 33).

[MCO12] G. Michlmayr, D. Cohen, and D. Or. “Sources and characteristics of acoustic emissions from mechanically stressed geologic granular media - A review”. In: *Earth-Science Reviews* 112.3 (2012), pp. 97–114 (cit. on p. 15).

[Mik+16] H. Mikulčić, J.-J. Klemeš, M. Vujanović, et al. “Reducing greenhouse gasses emissions by fostering the deployment of alternative raw materials and energy sources in the cleaner cement manufacturing process”. In: *Journal of Cleaner Production* 136 (2016), pp. 119–132 (cit. on p. 16).

[MN06] N. Mitarai and F. Nori. “Wet granular materials”. In: *Advances in Physics* 55.1-2 (2006), pp. 1–45 (cit. on p. 53).

[Mus37] M. Muskat. “The flow of fluids through porous media”. In: *Journal of Applied Physics* 8.4 (1937), pp. 274–282 (cit. on p. 25).

[Ngo+14] J. Ngoma, P. Philippe, S. Bonelli, J.-Y. Delenne, et al. *Interaction between two localized fluidization cavities in granular media : Experiments and numerical simulation*. International Symposium on Geomechanics from Micro to Macro. 2014 (cit. on pp. 39, 131, 132).

[Ngo+15] J. Ngoma, P. Philippe, S. Bonelli, J.-Y. Delenne, et al. “Transient regime to fluidized chimney within a granular bed by means of a 2D DEM/LBM modelling”. In: *IV International Conference on Particle-based Methods – Fundamentals and Applications - PARTICLES 2015*. IV International Conference on Particle-based Methods – Fundamentals and Applications PARTICLES 2015 E. Oñate, M. Bischoff, D.R.J. Owen, P. Wriggers & T. Zohdi (Eds). Barcelona, Spain: International Center for Numerical Methods in Engineering (CIMNE), 2015, pp. 519–528 (cit. on pp. 45, 131–133).

[Ngo+18] J. Ngoma, P. Philippe, S. Bonelli, F. Radjaı, et al. “Two-dimensional numerical simulation of chimney fluidization in a granular medium using a combination of discrete element and lattice Boltzmann methods”. In: *Physical Review E* 97.5 (2018), p. 052902 (cit. on pp. 39, 44, 46, 131, 132).

[Oli18] M.-V.-P. Oliveira. “Nova Algodões: entre o vivido e o projetado: articulação polıtica dos atingidos pelo rompimento da barragem Algodões I, em Cocal, no Piauı”. In: (2018) (cit. on p. 6).

[OLF11] D.-R.-J. Owen, C.-R. Leonardi, and Y.-T. Feng. “An efficient framework for fluid–structure interaction using the lattice Boltzmann method and immersed moving boundaries”. In: *International Journal for Numerical Methods in Engineering* 87.1-5 (2011), pp. 66–95 (cit. on p. 43).

[PR19] Y. Pal and V. Ravikumar. “Mechanical Characterization of Paraffin-Based Hybrid Rocket Fuels”. In: *Materials Today: Proceedings* 16 (2019), pp. 939–948 (cit. on p. 106).

[Par65] E. Partheniades. “Erosion and Deposition of Cohesive Soils”. In: *Journal of the Hydraulics Division* 91.1 (1965), pp. 105–139 (cit. on p. 9).

[PB13] P. Philippe and M. Badiane. “Localized fluidization in a granular medium”. In: *Physical Review E* 87.4 (2013), p. 042206 (cit. on pp. 39–41, 66, 121, 128, 129).

[Phi+17] P. Philippe, P. Cuéllar, F. Brunier-Coulin, et al. “Physics of soil erosion at the microscale”. In: *EPJ Web of Conferences*. Vol. 140. EDP Sciences. 2017, p. 08014 (cit. on p. 32).

[PC97] P. Pierrat and H.-S. Caram. “Tensile strength of wet granula materials”. In: *Powder Technology* 91.2 (1997), pp. 83–93. ISSN: 0032-5910. DOI: https://doi.org/10.1016/S0032-5910(96)03179-8. URL: http://www.sciencedirect.com/science/article/pii/S0032591096031798 (cit. on pp. 21, 170).

[PMC01] O. Pitois, P. Moucheront, and X. Chateau. “Rupture energy of a pendular liquid bridge”. In: *The European Physical Journal B-Condensed Matter and Complex Systems* 23.1 (2001), pp. 79–86 (cit. on p. 14).

[PHC01] A.-V. Potapov, M.-L. Hunt, and C.-S. Campbell. “Liquid–solid flows using smoothed particle hydrodynamics and the discrete element method”. In: *Powder Technology* 116.2-3 (2001), pp. 204–213 (cit. on p. 34).

[PC04] D.-O. Potyondy and P.-A. Cundall. “A bonded-particle model for rock”. In: *International Journal of Rock Mechanics and Mining Sciences* 41.8 (2004), pp. 1329–1364 (cit. on pp. 29, 30).

[PAF01] O. Pouliquen, B. Andreotti, and Y. Forterre. “Les milieux granulaires: entre fluide et solide”. In: *Cours de l’ENSTA* (2001) (cit. on p. 12).

[Pow04] W. Powrie. *Soil Mechanics: Concepts and Applications, Second Edition*. CRC Press, 2004 (cit. on p. 16).

[PG14] L.-J. Prendergast and K. Gavin. “A review of bridge scour monitoring techniques”. In: *Journal of Rock Mechanics and Geotechnical Engineering* 6.2 (2014), pp. 138–149 (cit. on p. 1).

[QdL92] Y.-H. Qian, D. d’Humières, and P. Lallemand. “Lattice BGK models for Navier-Stokes equation”. In: *EPL (Europhysics Letters)* 17.6 (1992), p. 479 (cit. on p. 35).

[RNS08] K.-K. Rao, P.-R. Nott, and S. Sundaresan. *An introduction to granular flow*. Vol. 490. Cambridge university press Cambridge, 2008 (cit. on p. 11).

[Rap+89] S. Rapagna, R.-D. Felice, L.-G. Gibilaro, et al. "Steady-state expansion characteristics of monosize spheres fluidised by liquids". In: *Chemical Engineering Communications* 79.1 (1989), pp. 131–140 (cit. on p. 27).

[Rei+12] S.-D.-S. Reis, N.-A.-M. Araújo, J.-S. Andrade-jr, et al. "How dense can one pack spheres of arbitrary size distribution?" In: *EPL (Europhysics Letters)* 97.1 (Jan. 2012), p. 18004. DOI: 10.1209/0295-5075/97/18004. URL: https://doi.org/10.1209/0295-5075/97/18004 (cit. on p. 11).

[RZ54] J.-F. Richardson and W.-N. Zaki. "u. wn zaki: Sedimentation and fluidization". In: *Trans. Instn. chem. Engrs. Bd* 32 (1954), p. 35 (cit. on p. 26).

[RER06a] V. Richefeu, M.-S. El Youssoufi, and F. Radjai. "Shear strength properties of wet granular materials". In: *Physical Review E* 73.5 (2006), p. 051304 (cit. on p. 169).

[RER06b] V. Richefeu, M.-S. El Youssoufi, and F. Radjaı. "Shear strength properties of wet granular materials". In: *Phys. Rev. E* 73 (5 2006), p. 051304 (cit. on pp. 21, 106, 114, 153).

[RL07] M. Righetti and C. Lucarelli. "May the Shields theory be extended to cohesive and adhesive benthic sediments?" In: *Journal of Geophysical Research: Oceans* 112.C5 (2007) (cit. on p. 12).

[Rum62] H. Rumpf. *The strength of granules and agglomerates*. New York Wiley Interscience, 1962 (cit. on pp. 21, 113).

[San+21] M. Sanayei, A. Farhat, L.-H. Luu, et al. "Micromechanical framework for a 3d solid cohesion model-implementation, validation and perspectives". In: *Proceeding-VII International Conference on Particle-Based Methods PARTICLES 2021*. 2021, pp. 1–10 (cit. on p. 78).

[SGH17] A. Schmeink, L. Goehring, and A. Hemmerle. "Fracture of a model cohesive granular material". In: *Soft Matter* 13 (5 2017), pp. 1040–1047 (cit. on pp. 18, 106).

[Sch+21] H.-E. Schulz, J.-E. van Zyl, T. Yu, et al. "Hydraulics of Fluidized Cavities in Porous Matrices: Cavity Heights and Stability for Upward Water Jets". In: *Journal of Hydraulic Engineering* 147.10 (2021), p. 04021037 (cit. on p. 42).

[SI35] W.-F. Seyer and K. Inouye. "Paraffin wax: Tensile strength and density at various temperature". In: *Industrial and Engineering Chemistry* 27 (5 1935), pp. 567–570 (cit. on p. 106).

[Söd09] K.-J.-M. Söderholm. "Critical Evaluation of Adhesive Test Methods Used in Dentistry". In: *Journal of Adhesion Science and Technology* 23.7-8 (2009), pp. 973–990 (cit. on p. 19).

[Suc01] S. Succi. *The lattice Boltzmann equation: for fluid dynamics and beyond*. Oxford university press, 2001 (cit. on p. 43).

[Ten+22] A. Tengattini, E. Andò, I. Einav, et al. "Micromechanically inspired investigation of cemented granular materials: part I—from X-ray micro tomography to measurable model variables". In: *Acta Geotechnica* (2022), pp. 1–21 (cit. on pp. 15–18).

[TL18] D. Terzis and L. Laloui. "3-D micro-architecture and mechanical response of soil cemented via microbial-induced calcite precipitation". In: *Scientific reports* 8.1 (2018), pp. 1–11 (cit. on pp. 16, 17).

[TL19] D. Terzis and L. Laloui. "A decade of progress and turning points in the understanding of bio-improved soils: A review". In: *Geomechanics for Energy and the Environment* 19 (2019), p. 100116 (cit. on pp. 16, 17).

[TRL20] A. Theocharis, J.-N. Roux, and V. Langlois. "Elasticity of model weakly cemented granular materials: A numerical study". In: *International Journal of Solids and Structures* 193-194 (2020), pp. 13–27 (cit. on p. 17).

[Tho91] C. Thornton. "Interparticle sliding in the presence of adhesion". In: *Journal of Physics D: Applied Physics* 24.11 (1991), pp. 1942–1946 (cit. on pp. 29, 43).

[TN98] C. Thornton and Z. Ning. "A theoretical model for the stick/bounce behaviour of adhesive, elastic-plastic spheres". In: *Powder Technology* 99.2 (1998), pp. 154–162 (cit. on pp. 29, 43).

[TCC12] A.-T. Tong, E. Catalano, and B. Chareyre. "Pore-scale flow simulations: model predictions compared with experiments on bi-dispersed granular assemblies". In: *Oil & Gas Science and Technology–Revue d'IFP Energies nouvelles* 67.5 (2012), pp. 743–752 (cit. on p. 34).

[Top+07] V. Topin, J.-Y. Delenne, F. Radjai, et al. "Strength and failure of cemented granular matter". In: *The European Physical Journal E* 23 (2007), pp. 413–429 (cit. on pp. 16–18, 103).

[Tra+17] D.-K. Tran, N. Prime, F. Froiio, et al. "Numerical modelling of backward front propagation in piping erosion by DEM-LBM coupling". In: *European Journal of Environmental and Civil Engineering* 21.7-8 (2017), pp. 960–987 (cit. on pp. 30, 31, 39, 45, 47, 48).

[Van+13] V. Van-Beek, A. Bezuijen, H. Sellmeijer, et al. "Erosion in Geomechanics Applied to Dams and Levees". In: (2013) (cit. on pp. 1, 7).

[Van82] M. Van-Dyke. *An album of fluid motion*. Vol. 176. Parabolic Press Stanford, 1982 (cit. on p. 22).

[Van+07] K. Van-Oost, T.-A. Quine, G. Govers, et al. "The impact of agricultural soil erosion on the global carbon cycle". In: *Science* 318.5850 (2007), pp. 626–629 (cit. on p. 1).

[Van+93] L.-C. Van-Rijn et al. *Principles of sediment transport in rivers, estuaries and coastal seas*. Vol. 1006. Aqua publications Amsterdam, 1993 (cit. on p. 1).

[VSP96] I. Vardoulakis, M. Stavropoulou, and P. Papanastasiou. "Hydro-mechanical aspects of the sand production problem". In: *Transport in porous media* 22.2 (1996), pp. 225–244 (cit. on p. 33).

[Wai+09] W.-F. Waite, J.-C. Santamarina, D.-D. Cortes, et al. "Physical properties of hydrate-bearing sediments". In: *Reviews of Geophysics* 47.4 (2009), RG4003 (cit. on p. 15).

[Wan+22] T. Wang, F. Zhang, J. Furtney, et al. "A review of methods, applications and limitations for incorporating fluid flow in the discrete element method". In: *Journal of Rock Mechanics and Geotechnical Engineering* 14.3 (2022), pp. 1005–1024 (cit. on pp. 33, 34).

[WV04] J.-C. Winterwerp and W.-G.-M. Van-Kesteren. *Introduction to the physics of cohesive sediment dynamics in the marine environment*. Elsevier, 2004 (cit. on p. 1).

[Yam+20] Y. Yamaguchi, S. Biswas, T. Hatano, et al. "Failure processes of cemented granular materials". In: *Phys. Rev. E* 102 (5 2020), p. 052903 (cit. on pp. 29, 101).

[Yu+03] D. Yu, R. Mei, L.-S. Luo, et al. "Viscous flow computations with the method of lattice Boltzmann equation". In: *Progress in Aerospace sciences* 39.5 (2003), pp. 329–367 (cit. on p. 38).

[Zha+16] L. Zhang, M. Peng, D. Chang, et al. *Dam failure mechanisms and risk assessment*. John Wiley & Sons, 2016 (cit. on pp. 7, 8).

[Zho+99] Y.-C. Zhou, B.-D. Wright, R.-Y. Yang, et al. "Rolling friction in the dynamic simulation of sandpile formation". In: *Physica A: Statistical Mechanics and its Applications* 269.2-4 (1999), pp. 536–553 (cit. on p. 29).

[ZH97] Q. Zou and X. He. "On pressure and velocity boundary conditions for the lattice Boltzmann BGK model". In: *Physics of fluids* 9.6 (1997), pp. 1591–1598 (cit. on pp. 79, 80).

[ZM07] F. Zoueshtiagh and A. Merlen. "Effect of a vertically flowing water jet underneath a granular bed". In: *Physical review E* 75.5 (2007), p. 056313 (cit. on pp. 39, 40, 121).

ANNEXES

A. Appendix A

A. Empirical scaling laws for cementation strength and coordination number

A.1. Choice and relevance of a micro-scale empirical relation

Figure A.1 displays the yield micro-tensile force F_t for different bead diameters d and mass paraffin content X_p. The graph shows an empirical scaling since all measured values gather together satisfactorily when plotted as a function of X_p multiplied by $d^{3/2}$.

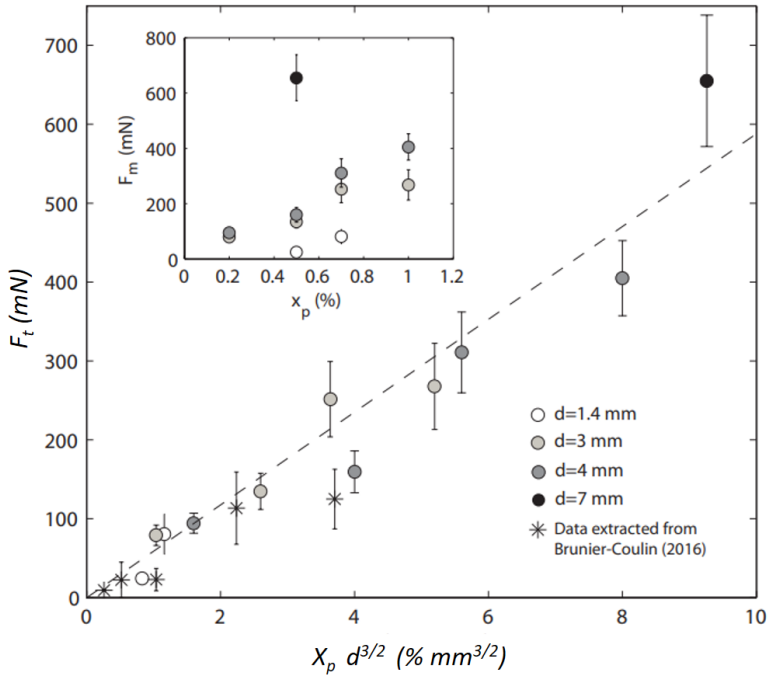

Figure A.1. – Yield micro-tensile force F_t as a function of $X_p d^{3/2}$. The dashed line stands for $y = \alpha x$, with the fit coefficient $\alpha = 58.8 \pm 3.2$ mN/mm$^{3/2}$ and a goodness of fit $R^2 = 0.967$. Inset: F_t as a function of X_p.

We propose to rationalize the whole set of measurements of the macro tensile stress (varying d, X_p and D) in Figure A.2. Relying on the power law given in Figure A.1, σ_T roughly scales with $X_p\ d^{-1/2}$ as a first-order approximation.

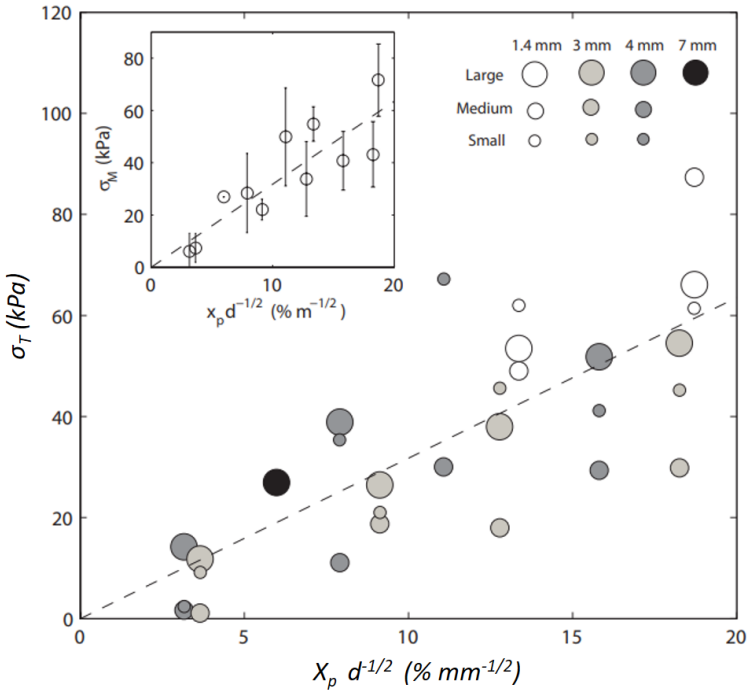

Figure A.2. – Yield macro tensile stress σ_T as a function of $X_p\ d^{-1/2}$. Inset: Averaged values. The dashed line stands for $y = \beta x$, with the fit coefficient $\beta = 3.3 \pm 0.3\ kPa\ \mathrm{mm}^{1/2}$ and a goodness of fit $R^2 = 0.936$.

A.2. Coordination number

In the present study, we intend to interpret our data against the coordination number using the two previous empirical relations of the micro tensile force and the macro tensile stress. Using the micro-macro relation by Richefeu and co-authors (Richefeu, El Youssoufi, and Radjai 2006) expressed in Eq. 1.8, we can deduce the mean coordination number Z in the considered cross-section as:

$$Z = \frac{8}{3\phi}\frac{F_T}{F_t}\left(\frac{d}{D}\right)^2. \tag{A.1}$$

Figure A.3a represents Z calculated from the macro-scale traction data presented above, as a function of the ratio D/d of the macro-device cone's diameter D to the grain's diameter d. Accounting for the large dispersion discussed previously, we obtain values ranging from 1 to 17! There is in particular a noticeable decrease of Z for the lowest paraffin content $X_p = 0.2$ %. This latter behavior is somehow consistent with the numerical study by Richefeu et al. (Richefeu, El Youssoufi, and Radjai 2006), where the coordination number of wet granular materials slightly increases with the water content. Figure A.3b provides a crude average of the previous Z values in six successive ranges of D/d whatever the other parameters (bead diameter, size of the macro-device, paraffin content), showing an almost constant value around 7 ± 2. If

we consider the usual relationship $Z = \pi/(1-\phi)$ found in the literature (Pierrat and Caram 1997), we get $Z = 8.06$ for $\phi = 0.61$ as estimated in our experiments. So, despite the huge dispersion of the data, an incipient agreement with classical approaches seems to emerge without any further calibration.

Finally, we wondered to what extent the finite size could impact the coordination number. To this end, we built a model based on simple considerations to take into account the influence of the lateral wall. Let's first define the total number of grains in the rupture section as $N = \phi\frac{\pi D^2}{\pi d^2}$, and the number of grains in contact with the lateral wall as $N_w = \phi\frac{\pi D}{d}$. Denoting the bulk coordination number by Z^*, we propose to write the mean coordination number Z in the considered cross-section as follows:

$$Z = \frac{N - N_w}{N} Z^* + \frac{N_w}{N}\left(1 + \frac{Z^*}{2}\right). \tag{A.2}$$

In this expression, we considered that: (i) a grain with no contact with the wall has Z^* contacts with other grains ; (ii) a grain in contact with the wall has only one contact (the one with the wall) in the half-space towards the wall and $Z^*/2$ contacts in the opposite half-space. The following alternative expression can also be found:

$$Z = Z^*\left[1 - \pi\frac{d}{D}\left(\frac{1}{2} - \frac{1}{Z^*}\right)\right]. \tag{A.3}$$

By using $Z^* = 8.06$ as estimated above, the present phenomenological model predicts a significant boundary effect only for $D/d < 10$ (dotted line in Fig.A.3b), which is indeed out of our experimental range. This suggests that no relevant finite-size effect is expected here, at least for what concerns the mean coordination number.

A final comparison can be carried out based on the two phenomenological relations found previously, namely $F_t = \alpha X_p d^{3/2}$ and $\sigma_T = \beta X_p d^{-1/2}$. To this end, we need to use SI units (kg, m, s). This gives :

$$Z = \frac{2\pi.1000^{1/2}}{3\phi}\frac{\beta}{\alpha}. \tag{A.4}$$

And finally $Z = 6.1 \pm 0.9$ which is a rather consistent value.

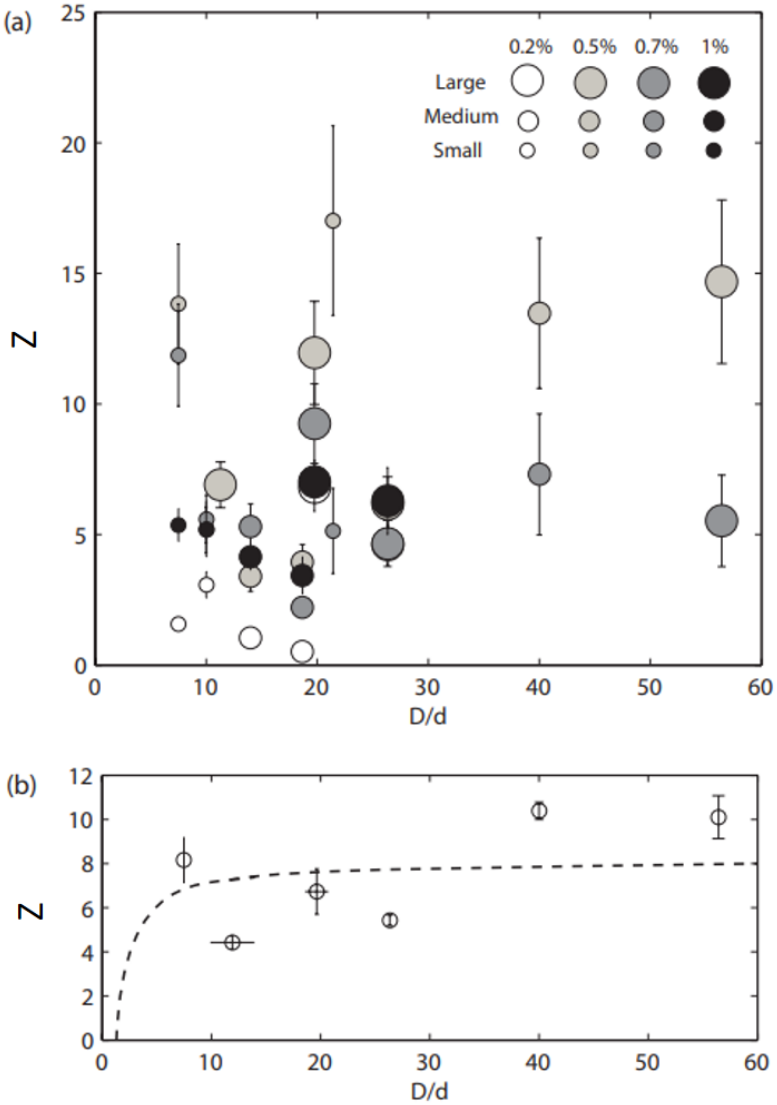

Figure A.3. – (a) Coordination number Z as a function of D/d. The legend indicates the size of the macro-scale device and the paraffin content. (b) Averaged values of Z as a function of D/d. The dotted line stands for the theoretical prediction from Eq. A.2.

Schriftenreihe des Instituts für Grundbau, Wasserwesen und Verkehrswesen der Ruhr-Universität Bochum

Herausgeber: H.L. Jessberger

1 (1979) **Hans Ludwig Jessberger**
Grundbau und Bodenmechanik an der Ruhr-Universität Bochum

2 (1978) **Joachim Klein**
Nichtlineares Kriechen von künstlich gefrorenem Emschermergel

3 (1979) **Heinz-Joachim Gödecke**
Die Dynamische Intensivverdichtung wenig wasserdurchlässiger Böden

4 (1979) **Poul V. Lade**
Three Dimensional Stress-Strain Behaviour and Modeling of Soils

5 (1979) **Roland Pusch**
Creep of soils

6 (1979) **Norbert Diekmann**
Zeitabhängiges, nichtlineares Spannungs-Verformungsverhalten von gefrorenem Schluff unter triaxialer Belastung

7 (1979) **Rudolf Dörr**
Zeitabhängiges Setzungsverhalten von Gründungen in Schnee, Firn und Eis der Antarktis am Beispiel der deutschen Georg-von-Neumayer- und Filchner-Station

8 (1984) **Ulrich Güttler**
Beurteilung des Steifigkeits- und Nachverdichtungsverhaltens von ungebundenen Mineralstoffen

9 (1986) **Peter Jordan**
Einfluss der Belastungsfrequenz und der partiellen Entwässerungsmöglichkeiten auf die Verflüssigung von Feinsand

10 (1986) **Eugen Makowski**
Modellierung der künstlichen Bodenvereisung im grundwasserdurchströmten Untergrund mit der Methode der finiten Elemente

11 (1986) **Reinhard A. Beine**
Verdichtungswirkung der Fallmasse auf Lastausbreitung in nichtbindigem Boden bei der Dynamischen Intensivverdichtung

12 (1986) **Wolfgang Ebel**
Einfluss des Spannungspfades auf das Spannungs-Verformungsverhalten von gefrorenem Schluff im Hinblick auf die Berechnung von Gefrierschächten

13 (1987) **Uwe Stoffers**
Berechnungen und Zentrifugen-Modellversuche zur Verformungsabhängigkeit der Ausbaubeanspruchung von Tunnelausbauten in Lockergestein

14 (1988) **Gerhard Thiel**
Steifigkeit und Dämpfung von wassergesättigtem Feinsand unter Erdbebenbelastung

15 (1991) **Mahmud Thaher**
Tragverhalten von Pfahl-Platten-Gründungen im bindigen Baugrund,
Berechnungsmodelle und Zentrifugen-Modellversuche

Schriftenreihe des Instituts für Grundbau der Ruhr-Universität Bochum

Herausgeber: H.L. Jessberger

16 (1992) **Rainer Scherbeck**
Geotechnisches Verhalten mineralischer Deponieabdichtungsschichten
bei ungleichförmiger Verformungswirkung

17 (1992) **Martin M. Bizialiele**
Torsional Cyclic Loading Response of a Single Pile in Sand

18 (1993) **Michael Kotthaus**
Zum Tragverhalten von horizontal belasteten Pfahlreihen aus langen Pfählen in Sand

19 (1993) **Ulrich Mann**
Stofftransport durch mineralische Deponieabdichtungen:
Versuchsmethodik und Berechnungsverfahren

20 (1992) **Festschrift anlässlich des 60. Geburtstages von**
Prof. Dr.-Ing. H. L. Jessberger
20 Jahre Grundbau und Bodenmechanik an der Ruhr-Universität Bochum

21 (1993) **Stephan Demmert**
Analyse des Emissionsverhaltens einer Kombinationsabdichtung im Rahmen der
Risikobetrachtung von Abfalldeponien

22 (1994) **Diethard König**
Beanspruchung von Tunnel- und Schachtausbauten in kohäsionslosem Lockergestein
unter Berücksichtigung der Verformung im Boden

23 (1995) **Thomas Neteler**
Bewertungsmodell für die nutzungsbezogene Auswahl von Verfahren zur Altlastensanierung

24 (1995) **Ralph Kockel**
Scherfestigkeit von Mischabfall im Hinblick auf die Standsicherheit von Deponien

25 (1996) **Jan Laue**
Zur Setzung von Flachfundamenten auf Sand unter wiederholten Lastereignissen

26 (1996) **Gunnar Heibrock**
Zur Rissbildung durch Austrocknung in mineralischen Abdichtungsschichten
an der Basis von Deponien

27 (1996) **Thomas Siemer**
Zentrifugen-Modellversuche zur dynamischen Wechselwirkung zwischen Bauwerken
und Baugrund infolge stoßartiger Belastung

28 (1996) **Viswanadham V. S. Bhamidipati**
Geosynthetic Reinforced Mineral Sealing Layers of Landfills

29 (1997) **Frank Trappmann**
Abschätzung von technischem Risiko und Energiebedarf bei Sanierungsmaßnahmen für Altlasten

30 (1997) **André Schürmann**
Zum Erddruck auf unverankerte flexible Verbauwände

31 (1997) **Jessberger, H. L. (Herausgeber)**
Environment Geotechnics, Report of ISSMGE Technical Committee TC 5 on Environmental Geotechnics

Schriftenreihe des Instituts für Grundbau und Bodenmechanik der Ruhr-Universität Bochum

Herausgeber: Th. Triantafyllidis

32 (2000) **Triantafyllidis, Th. (Herausgeber)**
Boden unter fast zyklischer Belastung: Erfahrung und Forschungsergebnisse (Workshop)

33 (2002) **Christof Gehle**
Bruch- und Scherverhalten von Gesteinstrennflächen mit dazwischenliegenden Materialbrücken

34 (2003) **Andrzej Niemunis**
Extended hypoplastic models for soils

35 (2004) **Christiane Hof**
Über das Verpressankertragverhalten unter kalklösendem Kohlensäureangriff

36 (2004) **René Schäfer**
Einfluss der Herstellungsmethode auf das Verformungsverhalten von Schlitzwänden in weichen bindigen Böden

37 (2005) **Henning Wolf**
Zur Scherfugenbänderung granularer Materialien unter Extensionsbeanspruchung

38 (2005) **Torsten Wichtmann**
Explicit accumulation model for non-cohesive soils under cyclic loading

39 (2008) **Christoph M. Loreck**
Die Entwicklung des Frischbetondruckes bei der Herstellung von Schlitzwänden

40 (2008) **Igor Arsic**
Über die Bettung von Rohrleitungen in Flüssigböden

41 (2009) **Anna Arwanitaki**
Über das Kontaktverhalten zwischen einer Zweiphasenschlitzwand und nichtbindigen Böden

Schriftenreihe des Lehrstuhls für Grundbau, Boden- und Felsmechanik der Ruhr-Universität Bochum

Herausgeber: T. Schanz

42 (2009) **Yvonne Lins**
Hydro-Mechanical Properties of Partially Saturated Sand

43 (2010) **Tom Schanz (Herausgeber)**
Geotechnische Herausforderungen beim Umbau des Emscher-Systems
Beiträge zum RuhrGeo Tag 2010

44 (2010) **Jamal Alabdullah**
Testing Unsaturated Soil for Plane Strain Conditions: A New Double-Wall Biaxial Device

45 (2011) **Lars Röchter**
Systeme paralleler Scherbänder unter Extension im ebenen Verformungszustand

46 (2011) **Yasir Al-Badran**
Volumetric Yielding Behavior of Unsaturated Fine-Grained Soils

47 (2011) **Usque ad finem**
Selected research papers

48 (2012) **Muhammad Ibrar Khan**
Hydraulic Conductivity of Moderate and Highly Dense Expansive Clays

49 (2014) **Long Nguyen-Tuan**
Coupled Thermo-Hydro-Mechanical Analysis: Experimental and Back Analysis

50 (2014) **Tom Schanz (Herausgeber)**
Ende des Steinkohlenbergbaus im Ruhrrevier: Realität und Perspektiven für die Geotechnik, Beiträge zum RuhrGeo Tag 2014

51 (2014) **Usque ad finem**
Selected research papers

52 (2014) **Houman Soleimani Fard**
Study on the Hydro-Mechanical Behaviour of Fiber Reinforced Fine Grained Soils with Application to the Preservation of Historical Monuments

53 (2014) **Wiebke Baille**
Hydro-Mechanical Behavior of Clays - Significance of Mineralogy

54 (2014) **Qasim Abdulkarem Jassim Al-Obaidi**
Hydro-Mechanical Behavior of Collapsible Soils

55 (2015) **Veselin Zarev**
Model Identification for the Adaption of Numerical Simulation Models - Application to Mechanized Shield Tunneling

56 (2015) **Meisam Goudarzy**
Micro and Macro Mechanical Assessment of Small and Intermediate Strain Properties of Granular Material

57 (2016) **Oliver Detert**
Analyse einer selbstregulierenden interaktiven Membrangründung für Schüttkörper auf geringtragfähigen Böden

58 (2016) **Yang Yang**
Analyses of Heat Transfer and Temperature-induced Behaviour in Geotechnics

59 (2016) **Alborz Pourzargar**
Application of suction stress concept to partially saturated compacted soils

60 (2017) **Hanna Haase**
Multiscale analysis of clay-polymer composites for Geoenvironmental applications

61 (2017) **Kavan Khaledi**
Constitutive modeling of rock salt with application to energy storage caverns

62 (2017) **Nina Silvia Müthing**
On the consolidation behavior of fine-grained soils under cyclic loading

63 (2017) **Elham Mahmoudi**
Probabilistic analysis of a rock salt cavern with application to energy storage systems

64 (2017) **Negar Rahemi**
Evaluation of liquefaction behavior of sandy soils using critical state soil mechanics and instability concept

65 (2018) **Chenyang Zhao**
A contribution to modeling of mechanized tunnel excavation

66 (2019) **Tom Schanz (Herausgeber)**
Innovationen im Spezialtiefbau und in der Umweltgeotechnik,
Geotechnik Beiträge zum RuhrGeo Tag 2014

67 (2019) **Linzhi Lang**
Hydro-Mechanical Behaviour of Bentonite-Based Materials Used for Disposal of Radioactive Wastes

68 (2019) **Usama Al-Anbaki**
Hydraulic Interaction of Soil and Nonwoven Geotextiles under Unsaturated Conditions

69 (2019) **Abhishek Rawat**
Coupled Hydro-mechanical Behavior of a Compacted Bentonite-Sand Mixture: Experimental and Numerical Investigations

Schriftenreihe des Lehrstuhls für Bodenmechanik, Grundbau und Umweltgeotechnik der Ruhr-Universität Bochum

Herausgeber: T. Wichtmann

70 (2019) **Mahmoud Qarmout**
Tunnel face stability using Kinematical Element Method (KEM)

71 (2021) **Raoul Hölter**
Optimal Experimental Design in Geotechnical Engineering.

72 (2022) **Wolfgang Lieske**
Impact of polymer constitution on the hydro-mechanical behaviour of modified bentonite for the application in geotechnical and geoenvironmental engineering

73 (2022) **Patrick Staubach**
Contributions to the numerical modeling of pile installation processes and high-cyclic loading of soils

74 (2022) **Lingyun Li**
On the hydromechanical behaviour of loess and its effect on slope stability under rainfall infiltration

75 (2022) **Debdeep Sarkar**
Influence of particle characteristics on the behaviour of granular materials under static, cyclic and dynamic loading

76 (2023) **Torsten Wichtmann (Herausgeber)**
Umbau des Emscher-Systems - Geotechnische Erfahrungen,
Beiträge zum RuhrGeo Tag 2023

77 (2023) **Abbas Farhat**
Fluidization and erosion of cemented granular materials - Experimental characterization and micromechanical simulation